Chair of Chemistry of Polymeric Materials

Doctoral Thesis

DEVELOPMENT OF STIMULI-RESPONSIVE PHOTOPOLYMERS FOR THE 3D-PRINTING OF FUNCTIONAL ACTIVE DEVICES

Usman Shaukat, MSc

June 2023

AFFIDAVIT

I declare on oath that I wrote this thesis independently, did not use other than the specified sources and aids, and did not otherwise use any unauthorized aids.

I declare that I have read, understood, and complied with the guidelines of the senate of the Montanuniversität Leoben for "Good Scientific Practice".

Furthermore, I declare that the electronic and printed version of the submitted thesis are identical, both, formally and with regard to content.

Date 17.06.2023

Signature Author

Usman Shaukat

Acknowledgments

Completing a scientific thesis like the following requires close and excellent collaboration among numerous individuals. In this chapter, I express my gratitude to all those who have supported and accompanied me during the preparation of this dissertation.

First and foremost, I extend my deepest gratitude to Priv.-Doz. DI Dr. Sandra Schlögl for her exceptional supervision, unwavering patience, valuable assistance, and constant encouragement throughout the entire duration of this thesis.

In addition, I would also like to thank DI Dr. Elisabeth Rossegger for her scientific support, supervision and patience.

Much of my gratitude is devoted to my colleagues at the PCCL and Institute of Chemistry of Polymeric Materials. They did not only enrich my time with their great help, but also ensured a perfect working atmosphere.

I would also like to thank my friends and companions from the bottom of my heart for their support over the past years.

I dedicate this work to my family, as I would not be writing these lines without their support. Thank you!

Abstract

The goal of the thesis was to develop new stimuli-responsive materials processable by digital light processing (DLP) 3D-printing and streamline their applicability for soft-robotic devices. In order to meet the objectives, a primary focus was on the development of photo-curable resins that are 3D-printable and offered a wide variety of thermo-mechanical properties. Secondly, dynamic covalent bonds were introduced undergoing thermally induced transesterification reactions, which rendered robotic systems malleable and healable.

As a first study, a library of dynamic thiol-acrylate networks was developed and structure-property relationships between resin composition, crosslink density, mechanical performance and bond exchange kinetics were established. For this, an acidic organic phosphate was introduced which did not only stabilize the resins but also served as an efficient catalyst, promoting dynamic bond exchange reactions. This breakthrough opened the path to thermally mendable, reprocessable and malleable dynamic photopolymers. The results showcased that the manipulation of the network structure allowed for effective control of the thermo-mechanical characteristics across a broad range. Rapid bond exchange reactions were facilitated by the abundance of –OH and ester groups, in addition to the high polymer chain mobility. Soft devices with thermal mendability and desirable stretchability were successfully DLP 3D-printed. Additionally, multi-material DLP 3D-printing was pursued to fabricate more advanced soft active devices, by combining the advantages of the developed resin formulations. Two different thiol-acrylate resins, with a varying degree of crosslinking, and widely different thermo-mechanical properties were employed to print prototypes, which exhibited great versatility along with shape memory and thermo-activated healing properties.

As a next step, photolatent transesterification catalysts were exploited as they provide a unique method to spatially control dynamic bond exchange reactions in dynamic photopolymers. In non-irradiated condition, the polymer networks containing the latent catalysts behaved like a permanently crosslinked duromer. However, when subjected to UV-light (365 nm), Brønsted acids were released, which efficiently catalyzed transesterification at elevated temperature and allowed for rearrangement of the network's topology above the networks topological freezing temperature (T_v). Moreover, the insensitivity of the photolatent catalysts to visible light (405 nm) enabled the DLP 3D-printing of sophisticated architectures without premature activation of the catalyst. The investigations demonstrated that the speed at which bonds are exchanged depends on the liberated Brønsted acid's stability, the quantum yield of the disintegration

reaction and the counter-anion's size. In areas exposed to UV light, the dynamic thiol-acrylate networks exhibited triple shape memory, while non-UV exposed domains functioned as simple T_g-based shape memory materials. This controlled locking of specific areas during thermal programming geared up exciting possibilities for additive manufacturing of functional devices.

Furthermore, to reduce the environmental foot print of the polymeric materials, bio-based vegetable oils were exploited as building block for dynamic photopolymers. As a sustainable building block, acrylated linseed oil was synthesized and combined with selected thiol crosslinkers. An organic transesterification phosphate catalyst was employed in the resin formulations which catalyzed efficient dynamic exchange reactions of the hydroxy and ester moieties present in the network. Excellent storage stability and photocuring kinetics facilitated the DLP 3D-printing of soft-active actuators with shape memory properties and malleability.

To further reduce the dependence on fossil fuel, a bio-based phosphate ester catalyst along with bio-based reactive diluents was synthetized. This target was attained by using eugenol, which is abundantly available from biologically renewable green sources, as starting material. The resin formulations were optimized towards the processability with DLP 3D-printing, and soft active structures with shape memory and healing properties were fabricated.

The outputs of the current thesis underscored the substantial promise of highly functional materials that respond to an external stimulus, whilst novel material concepts and manufacturing approaches have been integrated which set the stage for various future applications in smart active soft-robotics.

Contents

1. Introduction

The significant advantages of photoinduced polymerization over alternative polymerization and curing methods have garnered substantial attention over the past century. The ability to undergo solvent-free polymerization, in an energy efficient and locally controlled manner has made the process economically feasible in various application fields [1,2]. The ability to induce polymerization only in the illuminated regions of a resin with high precision, has been employed for the manufacturing of printing plates, wiring boards, microelectronic devices, optical disks [2], integrated circuits, and many others [3].

The history of photopolymers originates its roots from 1829, when Joseph Niépce developed a photographic process based on the principals of photopolymers [4,5]. Since antiquity, a photosensitive natural resin known as "bitumen of Judea", which hardens under sunlight, has been applied for the embalming of mummies and caulking of wooden ships by ancient Egyptians [6]. Since that time, the quest of humankind to develop photopolymers has raised the scientific and industrial interests and today we stand at such a point that the imagination of dental, bio-medical, coatings, adhesives, automotive, electronics and semiconductor industry is incomplete without the contribution of photopolymers [7–17].

Most of these applications do not only require advances in the processing technologies but also demand a great diversity of the photopolymers which are tailored, and adopted to the application conditions. The incorporation of adaptable chemistries into photopolymers allows for the creation of smart-intelligent materials that actively respond to an external stimulus and could modify their characteristics and undergo structural re-orientations. Such stimuli are not only limited to light, but also the influence of electric field, magnetic field, pH value, temperature and humidity is able to stimulate a controlled switch in the properties of the materials.

Controlling the nature and timing of responses in the final material could be achieved by comprehending the operational principles of every stimulus and the photopolymer chemistry. The ability of stimuli-responsive polymers to crosslink and de-crosslink, along with a great spatial and temporal control under the applied stimuli induces localized stresses, stiffening or softening, solubility and surface wettability variations, and in certain material dimension leading to micro and macro scale movements. Such responses could open many doors of application by introducing additional functions such as recycling, damage healing and shape memory in advanced materials used in biological or soft-robotic systems [18–22].

In the present work, the development of stimuli-responsive photopolymers has been the primary focus of attention for the additive manufacturing of soft active devices and actuators exhibiting additional functions. Free radical curing of monomers bearing functional groups such as acrylates and methacrylates has been well established for the formation of photopolymers since the past few decades. By the introduction of dynamic covalent bonds in these photopolymers, additional features can be realized, which drastically broaden the application window. Careful selection of monomers with abundance of free hydroxy and ester moieties is targeted within this thesis to form dynamic photopolymer networks undergoing thermo-activated transesterification. To activate such dynamic bond exchange reactions at defined temperatures, organic phosphates were introduced as transesterification catalysts, which show excellent solubility in the photocurable resin systems and do not negatively affect the shelf life or cure rate. By using derivatives with functional methacrylate groups, the catalyst can also be covalently bonded within the photopolymer network [23]. A library of formulations containing multi-functional acrylates and thiols was developed and the impact of the network design (e.g. number of hydroxyl and ester moieties, functionality and spacer length) on the cure kinetics, bond exchange rate and related thermal and mechanical properties of the photopolymers were studied. After development of structure-property relationships and the optimization of the network properties, vat photopolymerization 3D-printing of selected formulations was carried out to print soft actuators, which underwent thermally triggered shape change and - by exploiting the dynamic nature of the hydroxy ester bonds - were able to intrinsically heal macroscopic damages.

Along with printing single materials, the developed resin systems were also applied for the fabrication of multi-material actuators using a multi-vat DLP 3D-printer. By the sophisticated combination of resins yielding soft and stiff photopolymers, multi-material actuators were successfully fabricated which locally varied in their glass transition temperatures (local change of shape recovery) and Young's modulus. In addition, damages inserted in the printed objects were thermally healed by the material reflow induced by the activated bond exchange reactions of the hydroxy ester groups.

Pursuing another approach, multi-material actuators were further DLP 3D-printed by using light sources with different wavelengths instead of changing the vats during the printing process. This required the sequence-dependent orthogonal curing of a photoreactive resin formulation, for which, spatially controlled dynamic photopolymers were prepared by incorporating photolatent catalysts in the dynamic photopolymer networks. Onium salts such

as triphenylsulfonium salts possess the capability to release strong Brønsted acids upon UV exposure and have been well known for the initiation of cationic polymerization [24]. Herein, the released acid was used to catalyze bond exchange reactions (transesterification) in photopolymer networks. The network was formed upon visible light exposure (405 nm). In this wavelength region, the used photolatent transesterification catalysts were transparent and remained non-activated. Upon UV exposure (365 nm), the catalysts are then selectively formed in the exposed areas of the material. In this thesis, the influence of the structure, absorption characteristics and thermal stability of the released acids on the bond exchange rate of dynamic thiol-acrylate photopolymers were studied. In addition, soft active structures were printed with the dual wavelength DLP 3D-printer. By switching the light source during the printing, it was possible to obtain 3D-structures with defined regions which were able to undergo topological network rearrangements and were malleable at elevated temperature.

Advancing from petroleum-based building blocks, further work of this thesis was dedicated to reduce the environmental impact of the dynamic photopolymers by exploiting bio-based building blocks. For this purpose, plant-based oils consisting of epoxy moieties were further modified with acrylic acid to form acrylated vegetable oils. DLP 3D-printable resin formulations were prepared by mixing the modified vegetable oils with thiols and methacrylate-functional phosphate esters. The abundance of ester and hydroxy moieties in acrylated vegetable oils could efficiently engage in thermally induced transesterification reactions forming damage healable photopolymers. In addition, soft actuators were 3D-printed benefiting from the excellent shape memory and actuation properties under external stimuli (heat).

As a next step, efforts were made to develop fully bio-based dynamic photopolymer networks. For this purpose, eugenol acrylate and an organic phosphate (serving as transesterification catalyst) were synthesized from bio-derived sources. The resin formulations were optimized towards DLP 3D-printing and soft active devices were printed. Owed to their abundance of ester and hydroxy groups in the network, the printed structures were able to undergo shape memory and heal inserted damage by the thermally triggered reflow.

These novel approaches developed within this thesis have been fruitful in defining new grounds for the design of advanced functional photopolymers, and have paved the ways towards the 3D-printing of soft active devices with additional functions, which are highly sought after in soft robotics and bio-medical applications.

2. Theoretical background

In this chapter, the theoretical background of photochemistry, photopolymers, photo-polymerization methodologies and additive manufacturing with photopolymerization will be discussed in detail. Furthermore, focus will also be put on covalent adaptable networks, and the principals which govern the chemistry of bond exchange reactions in dynamic polymer networks.

2.1. Photo-matter response

Photoactive substances undergo an excitation and de-excitation corresponding to a distinctive energy transfer. Such photophysical operations involve the transfer of absorbed photon energy between the excited luminophore (acceptor) to the chromophore (donor) by exchanging the energy levels [25].

Furthermore, alterations in the distribution of electrical charges within the molecule are linked to modifications in the dipole moment [26]. The absorption of photon energy is only allowed when there is a nonzero value for the overall transition moment, implying that the disparity in energy between the ground state (E_1) and the excited state (E_2) must match the energy of the absorbed photon [27]. The energy of the photon is expressed by Planck's equation (Eq. 1) [28]

$$\Delta E = h \cdot \nu = \frac{hc}{\lambda} \qquad \text{Eq. 1}$$

where ΔE represents the energy gap between two excited states i.e. E_1 and E_2, ν represents the frequency, h denotes Planck's constant, while λ and c represent the absorbed light's wavelength and speed of the light in vacuum medium, respectively [28,29].

The energy of the incident photon should strictly match with the energy difference of the orbitals. Otherwise, it will be reflected, scattered or transmitted away by the irradiated material. The molecular orbital model also explains the absorption in energy orbitals as presented in the Figure 1. The formation of molecular orbitals of an atom takes places by the linear combination of its valence shell orbitals. Combination of two single orbitals generates two molecular orbitals; a high energy orbital termed as lowest unoccupied molecular orbital (LUMO), and the lower energy orbital called as highest occupied molecular orbital (HOMO). The HOMO is occupied by two electrons having an antiparallel spin direction, and permits the bonding of two atoms, i.e. bonding orbital. In contrast to that, higher energy orbitals are bonded through antibonding orbitals. In non-excited state (ground state), the LUMO is usually unoccupied, but the electronic excitation of a molecule energizes the electrons to occupy the occupied orbital

[30]. The electrons are hence excited from the ground state S_0 to the excited singlet state S_1 [31].
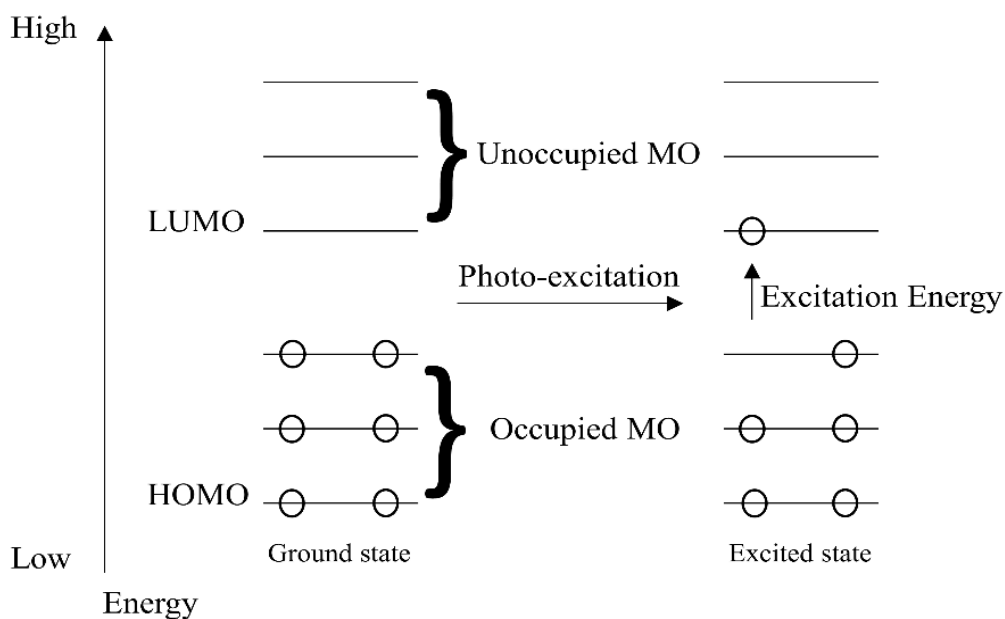
Figure 1. Diagram illustrating the concept of HOMO and LOMO of a molecule [31].

However, the electrons are energetically unstable in the excited state and hence quickly return back to the ground state emitting the absorbed excited energy via numerous radiation and non-radiation mechanisms [32]. Such mechanisms can be characterized from one of the following:

- Radiational relaxation by fluorescence or phosphorescence
- Non-radiational relaxation
- Photochemical reactions

Aleksander Jablonski studied in detail the emission of light and the molecular absorbance process, and presented a schematic demonstration of the possible consequences, when photons are bombarded on a particular molecule. This representation termed as Jablonski diagram demonstrates the molecular energy levels, singlet and triplet states and the corresponding vibrational energy levels, along with photophysical processes like fluorescence.
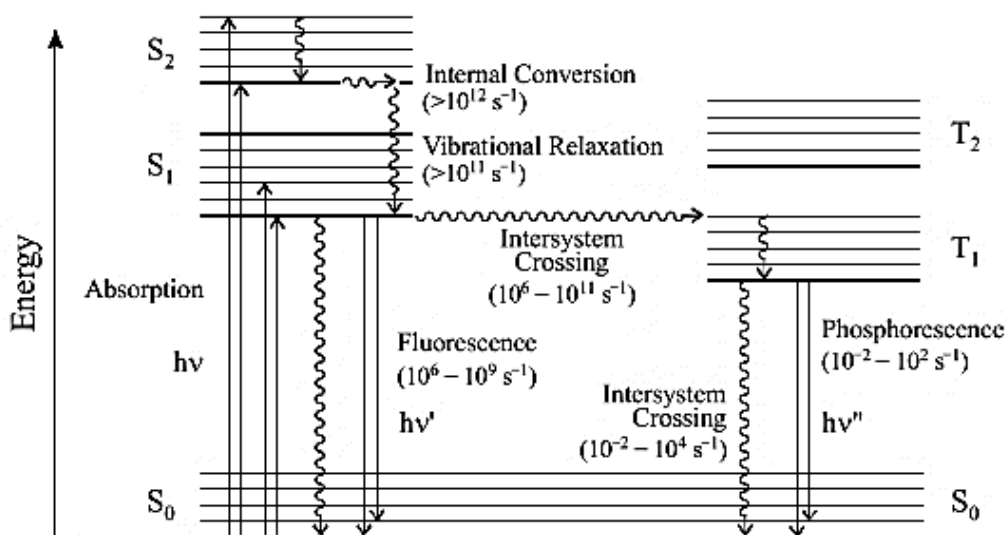
Figure 2. Jablonski diagram, representing transition in an organic compound [33].

The interlevel radiational transitions are represented via straight arrows, while non-radiational transitions are indicated by curly arrows (Figure 2) [33]. Michael Kasha presented a further rule in 1950, to understand the de-excitation mechanisms of photon excited molecules. Kasha stated that the emitting level of a given multiplicity is the lowest excited level of that multiplicity. Which means that the deactivation of lowest vibration level of S_1 or T_1 will generate the luminescence emission and chemical reaction by excited molecules from the same level [26,34]. Furthermore, the quantum yield of the de-excited species will define the moles of activated species upon absorption of photons [33]. The further classification of the deactivation and energy release process can be explained section-wise as follows:

Non-radiational relaxations

Non-radiational transactions involve the de-excitation of the activated orbitals without radiation release. These transitions are primarily based on the internal conversions, vibrational relaxations and intersystem crossing [26]. Intersystem crossing consists of intermolecular spin-prohibited and radiation-free transformations among the isoenergetic states of various multiplicity, i.e. [S_2 › T_1] [35].

Contrary to that, internal conversions are associated with the relaxations from a higher excited level to a lower excitation state within the same multiplicity, i.e. [S_2 › S_1] [35]. While the vibrational relaxations represent the transition from a vibrationally activated state and the $v = 0$ state within a particular electronic state, whereby activated molecules can collide with each other and undergo quenching, releasing the additional energy in the form of heat [36].

Radiational relaxations

Radiative transmission concerns the de-excitation of energy states S_1 and T_1 through luminescence processes, which undergo several deactivation bands rather than a single step. The processes are classified into fluorescence and phosphorescence. Fluorescence process involves the release of photons among similar multiplicity states, and takes places from the lowest vibrational level to the lowest excited state ($S_1 \rightarrow S_0$). Relative to the absorption maximum, the wavelength of the emitted light is shifted towards lower energy and hence higher wavelengths [27].

Phosphorescence is a special relaxation process, which involves the intersystem crossing of the excited electron and spin multiplicity among the singlet (S_1) and the triplet (T_1) states. Phosphorescence takes place from the triplet state (T_1), and the wavelengths are shifted to higher values [$T_1 \rightarrow S_0$] [26].

2.2. Photochemical reactions

During the excitation process, the incident photons are absorbed by the molecules and they reach a higher energy level. The absorbed photon's energy integrates into the total energy of the molecules absorbing it. Based on the nature of lower and upper electronic states, various reactions can take place, which can be briefly described using two principals:

Stark-Einstein's law: This law states that the absorption of each photon takes place by one molecule and hence considers a single-quantum process. The principal is widely implied in photochemistry, but limitations also exist when a very high intensity light source is employed, i.e. lasers, in which the absorption of two or multiple photon takes places [28].

Grotthuss-Draper law: This law describes that the photochemical alterations occur as a consequence of the light absorption by the chemical substance in a reaction system [34].

2.2.1. Photopolymerization reactions

Photopolymerization reactions offer great advantages over conventional polymerization mechanisms, including fast curing rates, mild reaction conditions (even room temperature), high spatial and temporal control of the reaction and low energy consumption [37–39]. Furthermore, the ability of optical sources to form excellent resolution materials with high precision and accuracy, high reaction conversions, low cost of equipment and process machinery also adds to the superiority of photochemistry [40–42]. In particular, energetically unfavorable reactions that require high reaction temperatures to overcome the activation energy

barrier could be executed at room temperature under light exposure [39,43]. This requires, the exploitation of electromagnetic spectrum for photoinitiation, while the choice of suitable light source is also critical to fulfil the energy demands of the targeted photoreactions. On one hand side, the energy of the irradiation rises by decreasing the wavelength, the penetration depth of the optical source decreases drastically on the other hand, limiting the application of photoreaction in thicker materials (Figure 3) [44]. Table 1, shows the respective energies and frequencies of the electromagnetic spectrum of light.
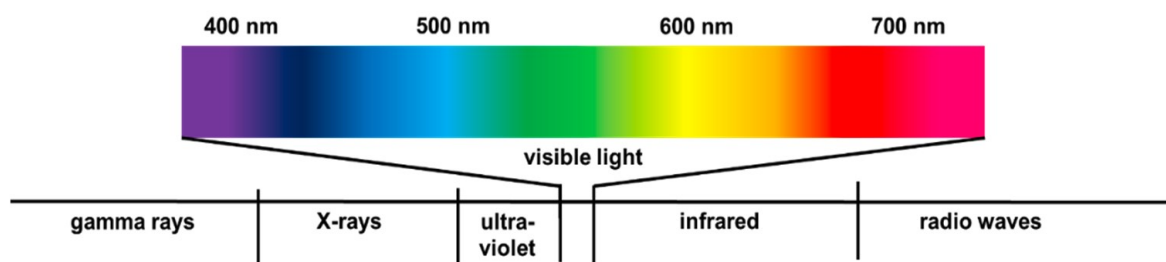
Figure 3. Electromagnetic spectrum of light [45].

Table 1. Energy per mol photon for given wavelength [26,46].

Colors	Frequency (1/s)	Wavelength (nm)	Energy (KJ/mol)
Infrared	3×10^{14}	1000	120
Red	4.3×10^{14}	700	171
Orange	4.8×10^{14}	620	193
Yellow	5.2×10^{14}	580	206
Green	5.7×10^{14}	530	226
Blue	6.4×10^{14}	470	254
Violet	7.1×10^{14}	420	285
Ultraviolet	$>10 \times 10^{14}$	<300	>400

As described earlier, the photoreactions can be triggered in an electronically excited state of molecules. If the irradiated light has an adequate energy, i.e. the spectral emission of the illumination source overlaps the absorption spectra of the targeted molecule, the absorbed

photon would be able to promote an electron from the illuminated molecule in the highest occupied molecular orbital (HOMO) to the lowest unoccupied molecular orbital (LUMO) [47].

The absorption of an illuminated molecule is generally described by the Beer-Lambert law (Eq. 2),

$$A = \varepsilon c d = -\log(\frac{I}{I_0}) \qquad \text{Eq. 2}$$

Where, A represents the absorbance of the irradiation within the material, ε is the molar extinction coefficient, c is the concentration of the absorbing species and d presents the optical path length. Moreover, the terms I_o and I correspond to the incident light intensity and the light intensity that could pass through the material [48].

However, each absorbed photon cannot trigger the desired molecular mechanism. Hence, it is important to keep quantum yield (φ) under consideration (Eq. 3), which describes the frequency of a particular event (N_e) underwent per absorbed photon in the system (N_p).

$$\varphi = \frac{N_e}{N_p} \qquad \text{Eq. 3}$$

Due to the fact that quantum yield and molar absorption are strongly controlled by the wavelength, higher absorption of light is desired throughout the targeted material to experience fast reaction rates. However, photoreactions are limited by the areas of the materials where incident light can be absorbed and diffused. Hence, it is essential to apply adequate concentration of appropriate photoinitiators and pigments in the photopolymerization system [47].

2.2.2. Photoinitiators

Photoinitiators are special chemical compounds having a capability to produce reactive species in the form of cations, anions or free radicals under irradiation of visible (Vis), ultraviolet (UV) or near-infrared (NIR) light. Photoinitiators are the primary working horses in the majority of photopolymerization processes. The commercial availability of a vast variety of photoinitiators in liquid and solid form, has significantly enhanced their application window. The dissolution of photoinitiators in the prepolymer prior to irradiation has to be ensured to obtain an efficiently polymerized product.

Free radical photoinitiators typically follow two different sorts of cleavage mechanisms, that are classified as [47] :

- Norrish type I photoinitiators (α-cleavage): Such photoinitiators follow a unimolecular bond cleavage reaction to generate free radicals.

- Norrish type II photoinitiators (H-abstraction): These photoinitiators engage in bimolecular reactions, producing radical species through the interactions among the excited states of the absorbing molecule and another molecule.

In case of a radical initiator, that forms two identical radicals, the rate of initiation R_i can be described by Eq. 4,

$$R_i = 2f\varphi I_0[I]\varepsilon \qquad \text{Eq. 4}$$

where, f is the radical efficiency, φ indicates the quantum yield, I_o represents the light intensity, ε and the $[I]$ are the molar absorption and the concentration of photoinitiator, respectively. However, Eq. 4 is only valid if the irradiated photopolymer has a lower photo-attenuation over its cross-section [39].

Type I photoinitiators (Figure 4) typically consist of aromatic carbonyl groups, including benzoin and its derivatives, acetophenones, benzyl ketals, O-acyl-α-oxyimino ketones, aminoalkyl phenones, acylphosphine oxides and α-hydroxyalkyl ketones that are capable of producing free radicals by α-cleavage under photo-irradiation [47–50]. Benzoin derivates are most widely employed photoinitiators on account of their high reactivity and quantum efficiency. Although, they suffer from a shorter life span at room temperatures, as the benzylic hydrogen could be abstracted conveniently [51]. On the other hand, acylphosphine oxides offer a great thermal stability and high reactivity from the phosphonyl radicals being generated [52].
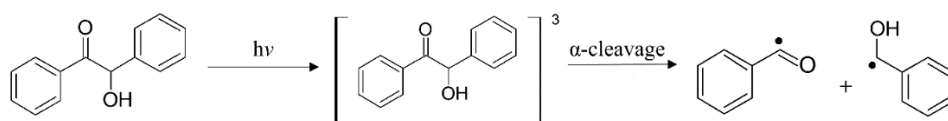
Figure 4. Type I photoinitiation mechanism [51]

Type I photoinitiators (Figure 4) are most utilized for initiating crosslinking reactions in photopolymerization systems where UV/Vis light sources are employed. Photoinitiators having a high molar extinction coefficient and UV absorption range ($\lambda < 400$ nm) are frequently used in vat photopolymerization 3D-printing systems [53].

The wavelength and intensity of the light required to start photocleavage reactions in the photoinitiator depends on its chemical structure. In the case of Irgacure 651 and Irgacure 1173,

the energy is absorbed at relatively lower bands and hence, the π to π* transition takes place in the ultraviolet (UV) range [54]. On the other hand, the photoinitiators based on phosphine oxide exhibit a lower energy level of π*, moving the π to π* peak to higher wavelengths [55].

In comparison to type I photoinitiators, slower initiation and curing rates are offered by type II photoinitiators on account of their bimolecular reaction mechanism. Type II photoinitiators require the participation of a co-initiator, which supports the hydrogen abstraction or electron transfer reaction in the presence of electronically excited initiator molecules (Figure 5 shows the mechanism of type II photoinitiators).
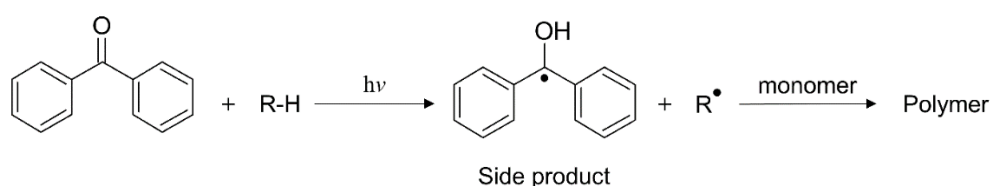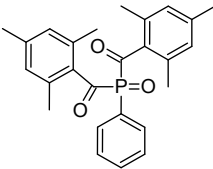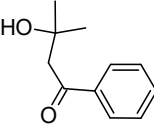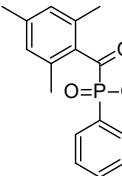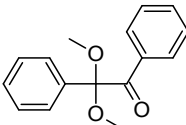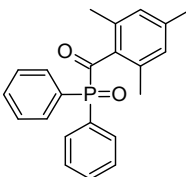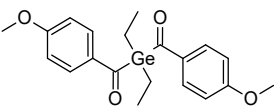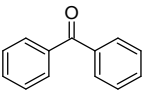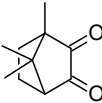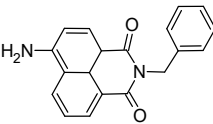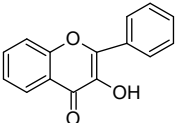
Figure 5. Type II photoinitiation mechanism [51]

Especially the photo-irradiation of aromatic ketones, such as thioxanthones, quinones, benzophenones and benzyls in the presence of hydrogen donors yield ketyl radicals, alongside other radicals obtained from the hydrogen donor [56]. For initiating the crosslinking reactions, hydrogen donor radicals are commonly employed. Due to the steric hindrance and delocalization of unpaired electrons, ketyl radicals exhibit remarkable stability and do not undergo reactions with vinyl monomers.

However, ketyl radicals could terminate the polymerization reactions by forming the ketyl species within the growing polymer network [57]. Onium or bromo salts are often introduced into the compounds to quench the ketyl radicals via bromination and oxidation, hence preventing the chain termination [51]. The choice of the co-initiator is also a decisive factor in defining the rate of photoinitiation. Tertiary amines have higher reactivities in comparison to ethers and alcohols. The majority of the photoinitiators absorb the light in the UV region. The absorption window can be extended to the visible light region by introducing suitable sensitizers. On the other hand, some visible light absorbing Type II photoinitiators are also being frequently applied such as camphorquinone in combination with an amine synergist [58].

In general, the success of the photoinitiator application lies on the suitability of the overlap between the absorption properties and the emission wavelengths of the irradiating light source [59]. Some widely used radical photoinitiators in photopolymerization processes are presented in Table 2.

Table 2. List of radical photoinitiators used in photopolymerization. Reused with permission from [47].

Photoinitiators	Active wavelength	Structure	Literature
Phenyl bis (2,4,6-trimethylbenzoyl) phosphine oxide (BAPO)	295 nm, 370 nm		[60–64]
2-Hydroxy-2-methyl-1-phenyl-propan-1-one (Irgacure 1173)	245 nm, 280 nm, 331 nm		[65]
Ethyl (2,4,6-trimethylbenzoyl) phosphine oxide (Irgacure TPO-L)	275 nm, 379 nm		[66,67]
2,2-Dimethoxy-phenylacetohphenone (Irgacure 651)	252 nm, 340 nm		[63,68,69]
Diphenyl (2,4,6 trimethylbenzoyl) phosphine oxide (Irgacure TPO)	295 nm, 368 nm, 380 nm, 393 nm		[70–72]
Bis (4-methoxybenzoyl) diethylgermanium (Ivocerin)	408 nm		[73,74]
Benzophenone	253 nm		[75]
Camphorquinone	468 nm		[60,76,77]
5-Amino-2-benzyl-1H-benzo isoquinoline-1,3(2H)-dione (NDP2)	417 nm		[60]
3-Hydroxyflavone (3HF)	370-470 nm		[78]

Cationic photoinitiators represent another type of initiators that have been employed greatly in photopolymerization. Such photoinitiators are commonly used to initiate the polymerization reactions in epoxy and vinyl ether-based systems. Crivello et al. reported the application of onium salts for photochemically initiating cationic ring-opening reactions in the late 1970s [7,79]. The initiation depends on the generation of Brønsted acids, which are produced by the cleavage of the excited onium salts, and subsequent reactions with solvent molecules or monomers in the formulations [80]. The strength of the evolving acid is greatly influenced by the chemical structure of the counter anion. The acidity of the photoacids increases with the nucleophilicity and size of the counter-anion [80,81]. Commonly used photoacid generators are diaryliodonium and triarylsulfonium salts, based on their exceptional capability to release acids under light irradiation. Some of the derivates are presented in Figure 6.

(4-n-Decyloxyphenyl)phenyliodonium hexafluoroantimonate IOC-10 SbF$_6$

Di(4-methylphenyl)iodonium hexafluorophosphate

4-Isopropylphenyl-4'-methylphenyliodonium tetrakis(pentafluorophenyl)borate

S-4-Thiophenoxyphenyl-S,S-diphenylsulfonium hexafluoroantimonate
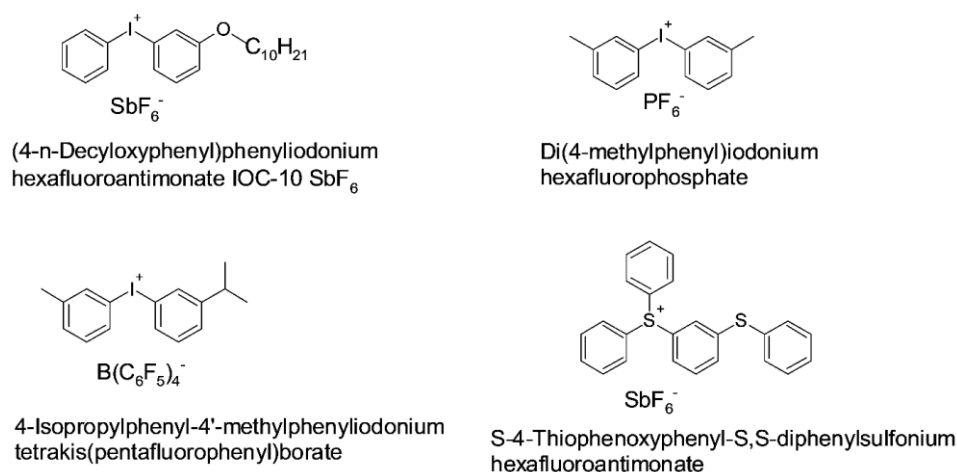
Figure 6. Structure of selected cationic photoinitiators, reproduced with permission from [82].

Under UV exposure, iodonium salts undergo homolytic and heterolytic bond cleavage reactions. In case of the homolytic cleavage reaction, an ayrl radical cation or a radical pair is generated while on the other hand, an aryl cation is produced when the heterolytic cleavage takes place [83]. The reactive groups further react with the solvent or monomer molecules to form strong Brønsted acids, i.e. HF, which are strongly capable of initiating the cationic polymerization [24].

Triarylsulfonium and diaryliodonium salts usually suffer from the limited absorption (absorption maxima lie typically between 200 – 300 nm). One solution to shift the absorption peak to higher wavelengths is to apply radical-induced cationic polymerization [84]. This process requires the combined application of photoacid generators with Type I or Type II photoinitiators, which can produce free radicals under visible light irradiation. Once they are

produced, free radicals get oxidized in the presence of radical cations and aryliodonium salt, which ultimately initiate cationic polymerizations. Another way to shift the absorption wavelength to higher wavelengths involve the application of dyes as sensitizers [47,85].

2.2.3. Photopolymerization reaction mechanisms

Photopolymerization reactions are generally classified into two categories, specifically chain-growth polymerization and step-growth polymerization. Chain-growth polymerization is a type of reaction that produces polymers with high molecular weight in the early stages of the process, with the yield increasing gradually over time. These reactions require the use of radical or ionic initiators to start the process. The initiators react with the monomers and start the growth of the polymer chains, known as the initiation reaction. As the reaction progresses, functional monomers are added one after the other to the active growing chain ends, known as propagation reaction [86]. The polymerization process is terminated either by the combination of active centers or through disproportionation reactions, which involve the rearrangement of atoms to form a saturated and an unsaturated chain end through the exchange of a H-atom [47,87].

Due to the rapid nature of chain-growth polymerization, the resulting material properties can vary significantly. The conversion of low viscous liquids into highly crosslinked networks occurs quickly in a couple of seconds, leading to a diffusion-controlled system, heterogeneous crosslink density [47,88–92], gradients in temperature and concentration and delayed equilibrium properties accomplishment.

To start the process of a free radical polymerization, the addition of a previously mentioned initiators is required. When exposed to light, the excited initiators homolytically cleave and the generated radicals are able to react with unsaturated carbon-carbon bonds in the resin mixture [87,92]. However, if the formulation is heavily pigmented or dyed, the intensity of light and initiation rate may vary [93], making the reactive charge transfer process more difficult and reducing the efficiency of the initiator as primary radicals become trapped and ultimately re-combine [47,90,94].

During the propagation stage of the chain-growth reaction, monomer/oligomer radicals are added to unsaturated carbon-carbon bonds, creating more radicals at the end of the chain [90,95,96]. This leads to an increase in crosslink density over time, which can cause diffusion limitations and the polymer to become vitrified. The propagation step can be mathematically described by Eq. 5 [47,87],

$$R_p = k_p[M][M_n\cdot] \qquad\qquad \text{Eq. 5}$$

where, R_p represents the rate of propagation reaction, k_p as the propagation rate constant, while [$M_n.$] and [M] represent the concentration of overall radicals and the concentration of double bonds, respectively [47].

The reaction can be terminated when two radical species combine. However, the ideal termination kinetics does not takes into account factors such as the length of the chain, trapping of radicals, or heterogeneities in the developing network, and the termination rate (R_T) can be expressed as Eq. 6 [47,87],

$$R_T = 2k_T[M_n.]^2 \qquad \text{Eq. 6}$$

where k_T is the termination rate constant, and [$M_n.$] presents the overall radical concentration. The termination step is often constrained by the diffusion-controlled regime, which can result in the Trommsdorff effect or gel effect [97]. Due to diffusion-controlled mass transfer limitations, the termination process by chain combinations becomes challenging, and the concentration of primary radicals suddenly rises, causing an increase in the polymerization rate and hence the reaction temperature. This temperature rise leads to faster radical formation, and the increasing viscosity of the system makes it difficult to evenly disperse them [98–100]. As a result, radical species can get trapped within the crosslinked networks, and they may remain in the polymer for a long time [47,82,98,99,101].

2.2.4. Radical Polymerization

Free radical polymerization is a chain addition mechanism in which a radical center initiates and propagates the reaction, allowing the polymerization process to take place even at room temperature. This reaction is triggered by the creation of radical species through the use of a photoinitiator that is excited or cleaved by light, starting the addition reactions [41,47]. The resulting highly reactive radicals further attack the monomer molecules, transmitting the active center to them. This leads to the addition of active radical centers to other monomers consisting of unsaturated carbon bonds via electron transfer throughout the activated volume, causing an increase in resin's viscosity and ultimately, gelation [47,87,92].

The reaction is stopped by immobilizing the active centers through a combination of radical species or the deprotonation (hydrogen transfer) of active monomers [87]. Compared to step-growth polymerization, radical induced chain-growth polymerization reactions are much faster, and commonly used building blocks include acrylates, methacrylates, vinyl monomers or even a combination of them [47,92,95,96,102]. The reaction mechanism is presented in detail in Figure 7.
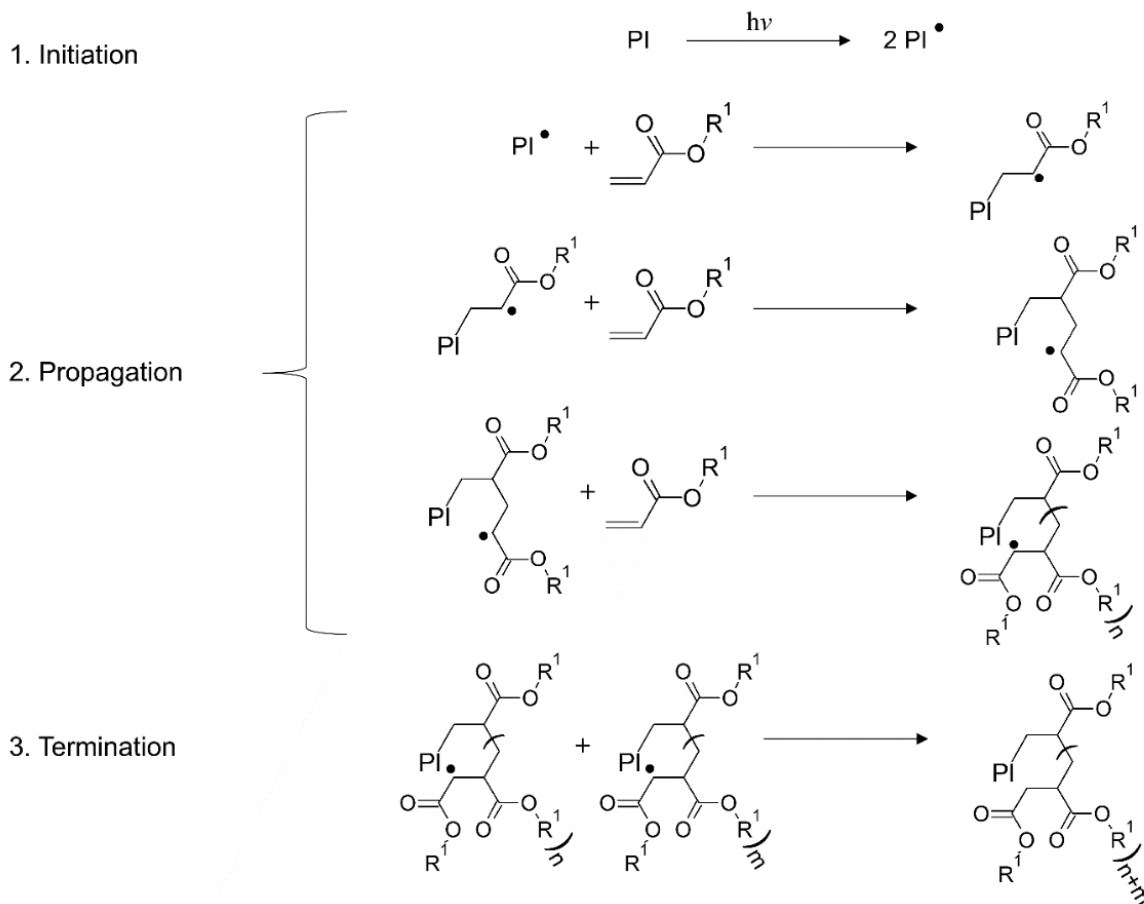
Figure 7. Illustration of the step-by-step progression of radical-induced chain-growth polymerization in acrylates. The termination phase is solely portrayed as a combination step in this representation. Reused with permission [47].

However, such polymer networks have certain limitations, including high shrinkage stresses and network heterogeneities [91,92]. Additionally, the presence of oxygen can inhibit addition reactions by reacting with the radical species and hindering further addition reactions [47].

The properties of a final polymer product are largely determined by the monomers, which are the fundamental building blocks of the polymer network. For successful polymerization, it is crucial that the monomers are compatible with the light source, contain adequate photoinitiators having suitable absorption characteristics and an appropriate light source. Additionally, the cured photopolymers should be dimensionally stable, have the required stiffness, biocompatibility and durability, and are able to withstand environmental conditions including application temperatures and pressures [47,59,103–105]. Figure 8 displays some of the commonly used commercial (meth-)acrylates.
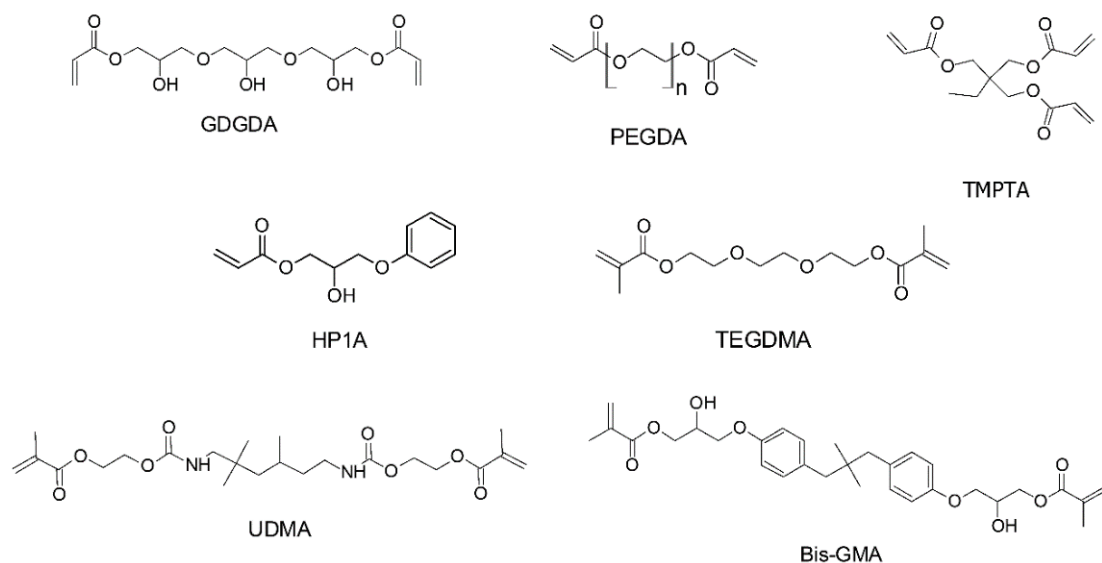
Figure 8. Structures of selected acrylates and methacrylate monomers typically used for photopolymerization. Reused with permission [47].

2.2.5. Cationic polymerization

Cationic polymerization involves a chain-growth process where cationic initiators are employed to activate the monomer via charge transfer. Compared to radical mediated polymerization of (meth)acrylates and vinyl monomers, cationic polymerization has several benefits such as insensitivity to oxygen, lower shrinkage stress, and higher mechanical performance in the evolved networks [106,107]. However, the reaction kinetics of cationic initiated reactions are slower when compared to widely-used radical polymerization. The most widely adopted monomers for cationic polymerization typically include epoxies (Figure 9) and nucleophilic vinyl monomers [107–109].
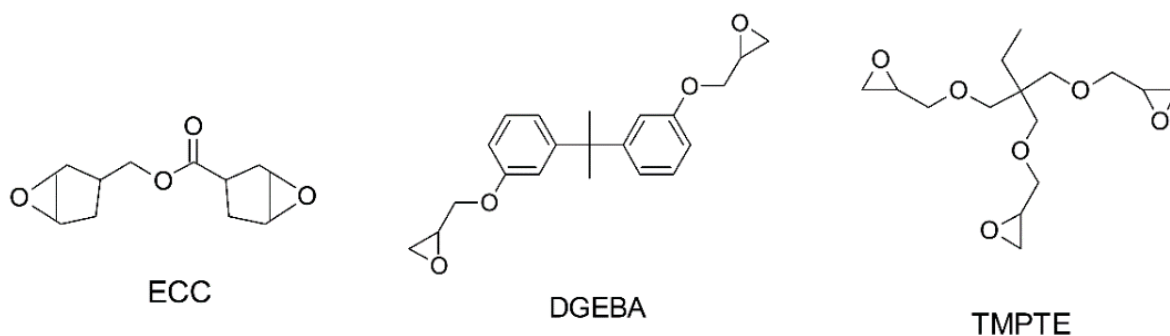
Figure 9. Structures of certain commonly used epoxy monomers for photopolymerization.

Cationic polymerization requires the presence of cationic photoinitiators such as sulfonium salts and aryl iodonium that generate reactive species through photo-illumination [24,108,109]. In

epoxy ring-opening reactions, the cationic initiator attacks adjacent epoxy rings, resulting in the formation of polyether links through cationic ring-opening polymerization (as shown in Figure 10). The chemical reactivity of epoxies varies depending on their functionality and structure, with cycloaliphatic epoxies being particularly reactive to ring-opening reactions due to their dual strained rings [91]. Commercial epoxies such as (3,4-epoxycyclohexane) methyl-3,4-epoxycyclohexylcarboxylate (ECC) [110–113] and bisphenol-A diglycidyl ether (DGEBA) [114] are widely used in photopolymerization reactions [115,116].
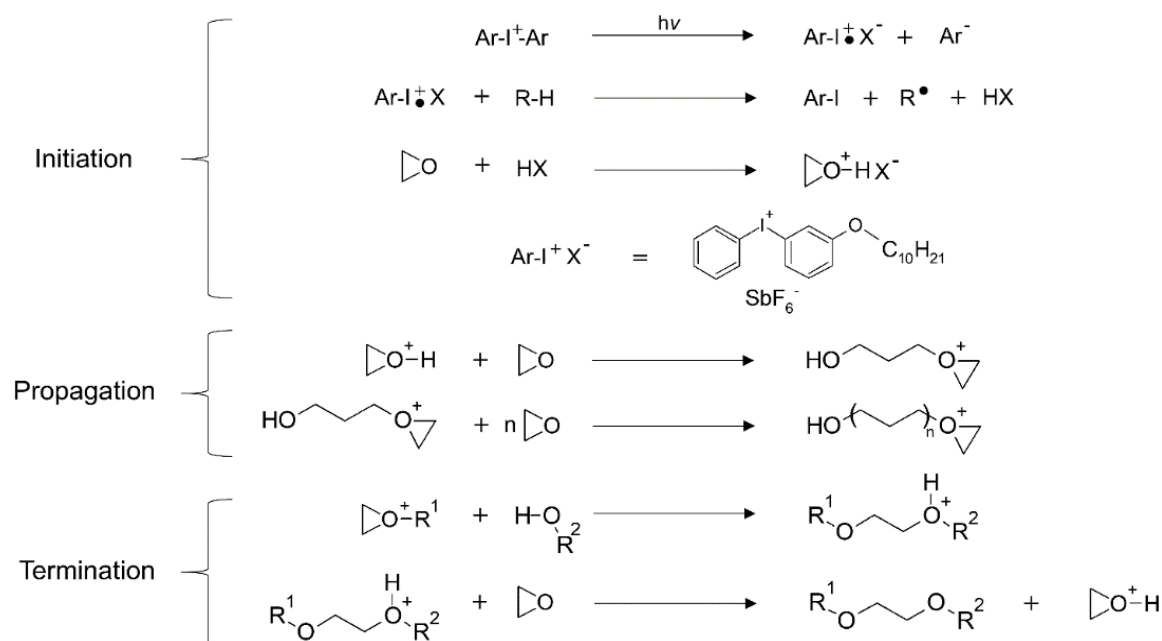
Figure 10. Mechanism of photoacid initiated epoxy polymerization (cationic chain-growth) [117].

In general, it is also important to maintain the lower viscosity of resins in photopolymerization. For example in photopolymerization 3D-printing, it's typically necessary for the liquid resins to have a viscosity below 4 Pa.s [40,118,119]. A higher resin's viscosity can impede the accuracy of the layer thickness printing and prolongs the curing process. Additionally, a higher viscosity resin is not able to evenly disperse over the building platform during consecutive layers printing, resulting in areas with insufficient resin wetting.

2.3. Step-growth polymerization

Similar to chain-growth polymerization reactions, initiators are typically required to start a step-growth polymerization reaction, which proceeds between two or multiple monomers with contrary functionalities in equimolar concentrations. In contrast to chain-growth polymerization, the polymer's molecular weight exhibits a gradual growth during the initial

phases of the reaction, and the formation of the polymer network involves a repetitive occurrence of a single type of reaction [92,95,96,102].

In a step-growth polymerization, the functional groups from the monomers react to form a dimer initially, which subsequently reacts with other monomers to form trimers and tetramers, and the process continuous until complete conversion is achieved [96,102]. The degree of polymerization (D_p) in this reaction can be determined using the Carothers equation (Eq. 7) for a given conversion (p) [120],

$$D_p = \frac{2}{2-pf}$$

Eq. 7

while f presents the average number of functional groups of various monomers. Step-growth polymerization reactions are categorized based on their reaction types, which include polyesterification, polyamidation, polyaddition or polycondensation reactions. However, cycloaddition, electron transfer and radical coupling reactions, and atom transfer radical addition reactions can also attribute to the step-growth polymerization reactions [87,95,96,102].

Step-growth polymerization following a click reaction have unique characteristics such as [23,121–123]:

1) High reaction yields
2) Performance at ambient conditions
3) Insensitivity to water and oxygen
4) No side reactions or simply removable side products
5) Orthogonality and regio-specifity with other reactions

Some well-known examples of click reactions include nucleophilic ring-opening reactions, Diels-Alder reactions, copper-catalyzed azide-alkyne cycloaddition (CuAAC), and thiol-ene/yne reactions [121].

2.3.1. Thiol-ene and thiol-yne chemistries

Photoreactions based on thiol-ene or thiol-meth(acrylate) systems can occur via either radical-induced step-growth polymerization or thiol Michael-addition reactions, as shown in Figure 11 [23,91]. These reactions are commonly known as thiol-ene reactions because the reacting group in acrylate or methacrylates is a -C=C group, exhibiting modular click reaction characteristics [123]. In the free radical thiol-ene reaction, a free radical (such as a thiyl radical) adds to the -C=C groups. In contrast, thiol-Michael addition reactions (TMR) involves the catalyst-

facilitated addition of thiols to an electron-deficient -C=C functional group. Moreover, TMR proceeds through the anti-Markonikov reaction pathway, in which a nucleophilic carbon atom is incorporated into an α,β-unsaturated carbonyl group through 1,4-addition reactions [124].
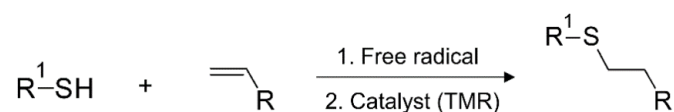
Figure 11. Comparison of the general reaction pathways for thiol addition to "ene" functionalities: contrasting the radical-mediated thiol-ene reaction with the catalyzed thiol-Michael reaction [125].

Although the final product from both reactions may be the same, the processing techniques used are entirely different [123]. A proper understanding of these methods is necessary for successful implementation in photopolymerization. Thiol-Michael reactions can be initiated using a wide variety of catalysts, such as strong bases, metals, Lewis acids and organometallics [126,127]. These reactions can occur even in the absence of light and cause the liquid resins to solidify (gelation), which reduces their shelf-life significantly [128]. Additionally, the fast polymerization kinetics of TMRs make it challenging to control their orthogonality. Therefore, within the context of vat photopolymerization 3D-printing, only the radical-induced thiol-ene step-growth polymerization is discussed in the following sections. From a physical standpoint, most commercially available thiols are in the liquid state, which allows for convenient dissolution and rapid introduction into photocurable resin formulations. Figure 12 and Figure 13 show examples of thiols and alkene monomers.
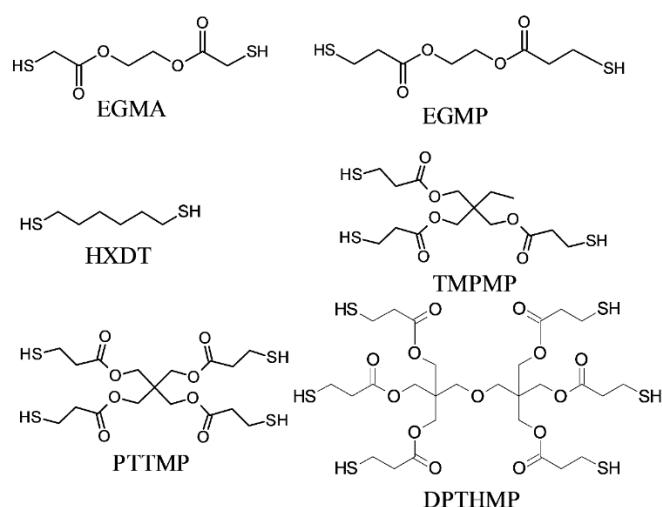
Figure 12. Structures of selected commercially available thiols
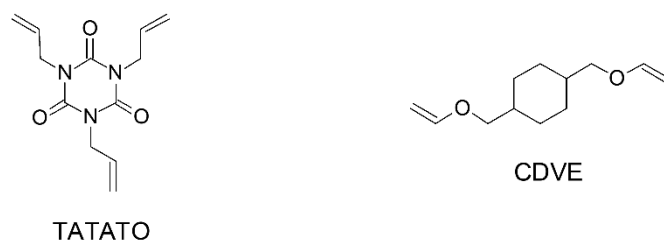
Figure 13. Two examples of the frequently used alkenes

The thiol-ene reaction mixtures undergo a series of stages in their free radical reactions, beginning with the activation of thiols through a H-abstraction reaction with a photoinitiator radical (as shown in Figure 14). This produces thiyl radicals that can consequently attack unsaturated -C=C groups, forming carbon-centered radicals and shifting the active radical centers. These carbon-centered radicals can then abstract a hydrogen atom from another thiol group, and the reaction propagates through further reactions with unsaturated carbon bonds, following a step-growth mechanism [123]. When acrylates or methacrylates are used as the unsaturated (-ene) component, the unsaturated carbonyl moieties can also undergo homo-polymerization via addition reactions (chain-growth), resulting in a mixed-mode reaction mechanism [123], as depicted in Figure 14.
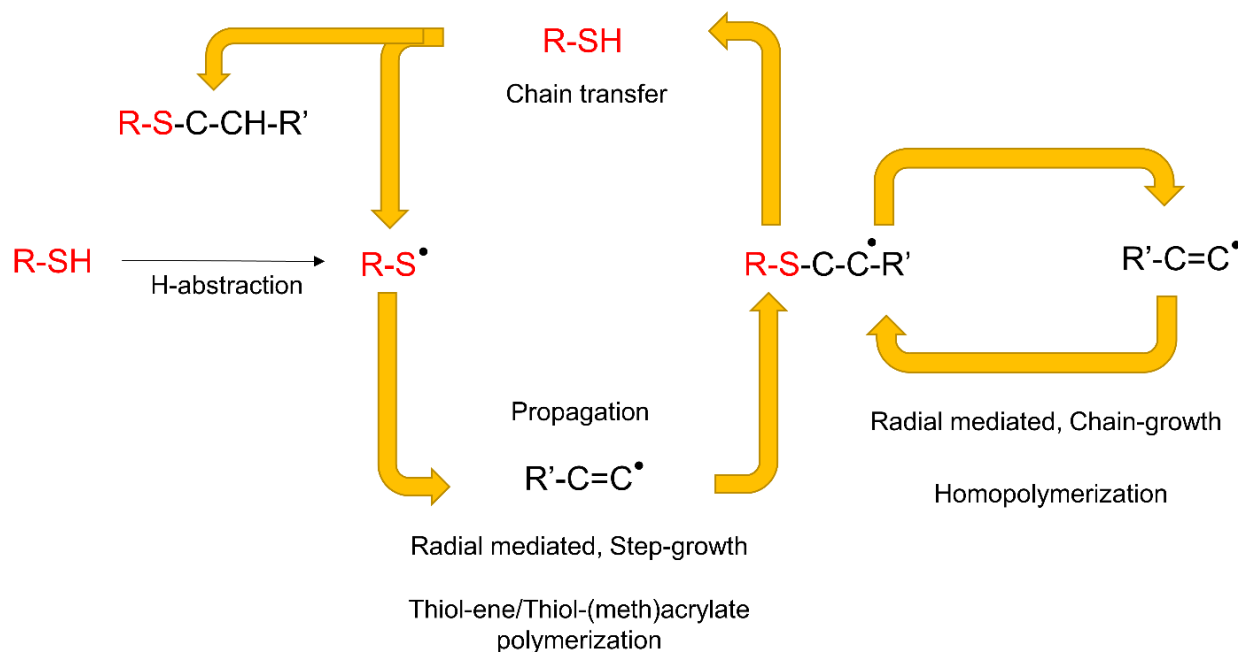
Figure 14. Reaction mechanism following a combination of thiol-ene and acrylate homopolymerization reaction (mix-mode polymerization). Active carbon centers can act as a chain transfer agent and chain propagator throughout the reaction cycle [123].

Free radical thiol-ene reactions have various benefits compared to homo-polymerization reactions based on acrylates or methacrylates. One key advantage is that thiols are capable of generating thiyl radicals by donating hydrogen atoms in the presence of peroxide radicals, making them less susceptible to oxygen inhibition [23,129]. Another advantage is that the thiol-ene reactions result in a gelation at higher reaction conversions due to the step-growth polymerization. As a result, the polymer networks are tougher and experience lower shrinkage stress [130–132].

Furthermore, compared to pure acrylate/methacrylate photopolymers, thiol-ene polymers exhibit a greater degree of biocompatibility [133,134]. These advantages have led to thiol-ene or thiol-(meth)acrylate reactions being recognized as one of the most promising chemistries in vat photopolymerization 3D-printing, and numerous research studies have demonstrated it in recent years [125,128,135–137].

It should be noted that thiol addition reactions are not restricted to -C=C bonds, but they can also take place with -C≡C groups from alkyne monomers [138–140]. The reaction mechanism is identical to that of thiol-ene reactions, but it typically contains a double addition reaction with a thiyl radical, resulting in the formation of a vinyl-sulfide intermediate. Thiol-yne produces polymer networks with a higher glass transition temperatures and higher crosslinking density than thiol-ene reactions [141–143].

2.5. Additive manufacturing

Additive manufacturing, also known as 3D-printing, is a comprehensive technique for processing materials that was discovered in the 1980s and since then has gained significant attention [79,80,144–149]. The technology is currently experiencing significant growth and can be utilized through various methods, including material jetting [81,84], binder jetting [85,150], material extrusion [151–155], powder bed fusion [156,157], vat photopolymerization [40,41,80,158–160], and sheet lamination [79,149,161,162].

In particular, the use of additive manufacturing or 3D-printing for polymers offers numerous advantages over conventional processing techniques for creating 3D-objects with multi-material properties. The process allows for the single-step manufacturing of complex three-dimensional products, significantly shortening processing times, and has gained increasing attention in the last decade [40,79,147,154,163–166].

The desired 3D-shape models are created by evolving structures layer-by-layer or point-by-point via a computerized controlled system. Unlike traditional processing methods that require

the use of molds, dies or lithography masks, 3D-printing technologies use automated machinery to transfer computer-aided designs into sophisticated 3D-structures with minimal loss of material [167–170].

Moreover, the capability of producing technical products under reduced process complexity and lower cost of printing technology has gathered great attention from the industry and academia. Based on the processing principle, over 50 different types of additive manufacturing processes have been so far reported [144]. The choice of the suitable additive manufacturing technology for a particular product depends on the chemical and physical properties of the materials used and the intended final applications of the finished products.

Based on the fact that thermoplastics have the ability to become soft and malleable when heated above their melting point, allows them to be used in extrusion-based additive manufacturing methods. Nevertheless, the inherent mechanical characteristics of 3D-printed objects in their pure state are often unsuitable for structural applications, requiring the inclusion of particular additives, such as reinforcing fillers, to alter their properties. [171,172]. Despite this, 3D-printed thermoplastics can be easily reprocessed and re-melted again due to the absence of covalent bonds.

On the other hand, thermosets and crosslinked polymers produced through 3D-printing cannot undergo reprocessing since chemical crosslinks are created during the printing procedure. Such curing reactions are typically permanent as the materials become insoluble and infusible once covalently crosslinked. Curing reactions are generally initiated by temperature or light. Especially, optically initiated curing reactions offer multiple benefits such as spatial reaction control, rapid curing at mild reaction conditions (room temperature) and reduced energy consumption [37–39]. These facts, make photoreactions well-suitable for additive manufacturing. Vat photopolymerization 3D-printing is the specific methodology that deals with the light-induced curing of the polymer precursors in the division of additive manufacturing. A liquid photocurable resin is photo-illuminated and selectively cured either via point-by-point (stereolithography) or a layer-by-layer (DLP 3D-printing) illumination scheme. Vat photopolymerization technology employees numerous functional monomers such as unsaturated polyesters, epoxy resins, methacrylates, acrylates, phenolic polymers and organosilicons [173]. The utilization of additive manufacturing technology for such systems, can create soft materials and photopolymers that exhibit exceptional mechanical strength and stiffness, comparable to dental resins [174].

However, vat photopolymerization 3D-printing still undergoes numerous challenges. These include the limited functionality of monomers, a restricted range of photopolymers that fully support the printing technology, the loss of reactions' orthogonality, the leaching of material, and the challenge of maintaining long-term properties, as well as the viscosity and printability of precursors with a suitable resolution.

The appealing aspects of vat photopolymerization have on the other hand led to its growing use in materials fabrication and various techniques have been developed to expand its capabilities. The most common technology involve stereolithography (SLA), liquid crystal display (LCD) printing, digital light processing (DLP), continuous liquid interface printing (CLIP), and two photon absorption (TPA) printing [40,80,158]. To enhance comprehension of the process, make the best out of the accessible photopolymers and limit the challenges to the vat photopolymerization 3D-printing technology, it is crucial to have a comprehensive understanding of the technology's mechanism itself alongside the underlying reaction chemistry. Going further, a brief overview of the processing techniques, emphasizing their main features characteristics is provided.

2.5.1. Stereolithography

Stereolithography (SLA) is a sub-process in vat photopolymerization 3D-printing, which uses liquid resins with a suitable viscosity, which are illuminated in a vat with a selected light source, causing a polymerization reaction to occur at specific points (Figure 15). This process is guided by 3D-interpretation software and is carried out point-by-point to create a 3D-structure [8,166,175]. Commonly used liquid resins in SLA technology include methacrylates, acrylates, vinyl and epoxy monomers. The overall characteristics of the printed structures rely on several factors, including the chemical functionality, viscosity of the resin, duration of exposure to light, intensity of light and additional additives incorporated into the formulations. Photoinitiators and light absorbers are also added to the resin formulations to initiate reactions and boost the resolution and surface finish of the 3D-printed articles.
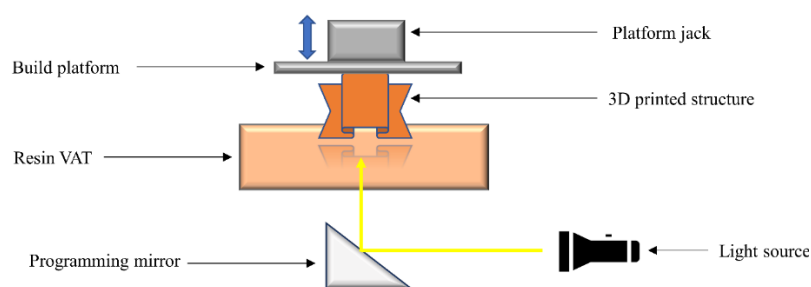
Figure 15. Schematic representation of stereolithography (SLA) [47]

SLA technology offers significant advantage in the form of high resolution for the printed articles. Additionally, since the monomers and precursors are in a liquid state, there is no need to heat the monomer feed. However, the technology is constrained by the limited availability of photopolymers. When using SLA for 3D-printing, it's important to take into account the cytotoxicity and irritation potential of the resins and unreacted monomers present in the printed articles [176].

2.5.2. Digital light processing

Digital light processing (DLP) 3D-printing is a form of vat photopolymerization technology that also uses light to initiate a local polymerization reaction. In DLP technology, it is common to combine liquid resins that contain vinyl, acrylate or epoxide groups with an appropriate photoinitiator and light absorber. Unlike SLA, the liquid resin is irradiated layer-by-layer based on the desired design of the printed object. As each layer solidifies, the printed object takes a specified shape during photopolymerization (Figure 16). After DLP 3D-printing, the cured material is removed from the building platform and the rest of the resin is retrieved from the vat [128,135].
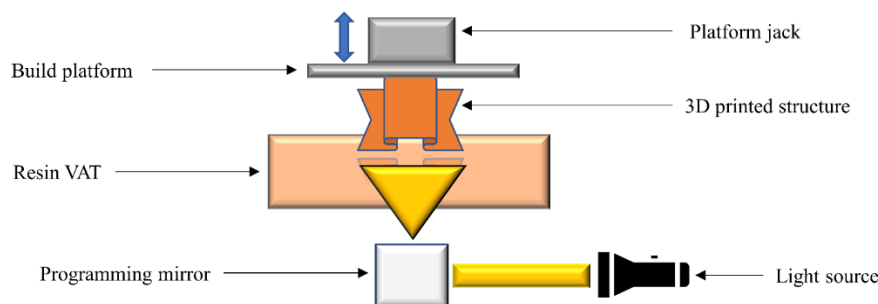
Figure 16. Schematic representation of DLP 3D-printing [47].

DLP 3D-printing offers the advantage of producing high-resolution objects quickly as it can cure the whole layer of material at the same time. However, similar to SLA technology, the availability of photopolymerizable monomers limits the DLP's potential.

2.5.3. Liquid crystal display

Liquid crystal display (LCD) 3D-printing is another vat photopolymerization method that utilizes a liquid crystal display unit to perform imaging functions. When an electric field is applied, the liquid crystal molecules undergo rearrangements that selectively block the transmission of light over certain regions (as depicted in Figure 17). The computerized decoding system translates the design of the 3D-printed object, which triggers a response in the LCD

imaging unit. Liquid crystal technology can achieve very high printing resolutions using advanced translation techniques. However, despite its potential, some molecular rearrangements may become trapped or permanently fixed under the continuous influence of an electric field, resulting in poor resolution and the passage of light through the LCD screen [47,177–179].
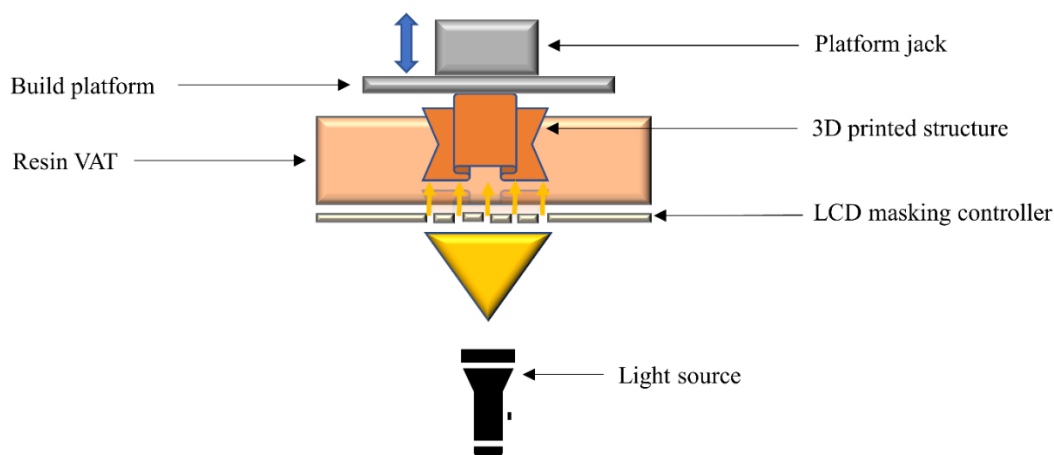
Figure 17. Schematic representation of Liquid Crystal Display (LCD) 3D-printing [47].

2.5.4. Continuous liquid interface 3D-printing

In 2015, the Continuous Liquid Interface Printing (CLIP) technology was introduced, enabling the continuous photopolymerization printing of monolithic and photopolymeric structures without layers [180]. This technology employs an oxygen-permeable chamber that creates an oxygen layer at the interface, which inhibits the radical induced polymerization reaction. The oxygen layer can also quench the excited state of photoinitiators and react with free radicals to form peroxides in the polymerizing vat [181]. Consequently, unreacted monomers are left at the interface among the oxygen film and the building platform, resulting in the rapid printing of polymer resins without the need to slice 3D-designs or use the typical layer-by-layer methodology. CLIP technology can produce printed objects at very high speeds, with a cycle of production ending in a few minutes and a product resolution better than 100 μm [180,182,183]. However, this technology is limited to curing systems that are quenched by oxygen, such as photocurable (meth)acrylate-based monomers. Figure 18 illustrates this process.
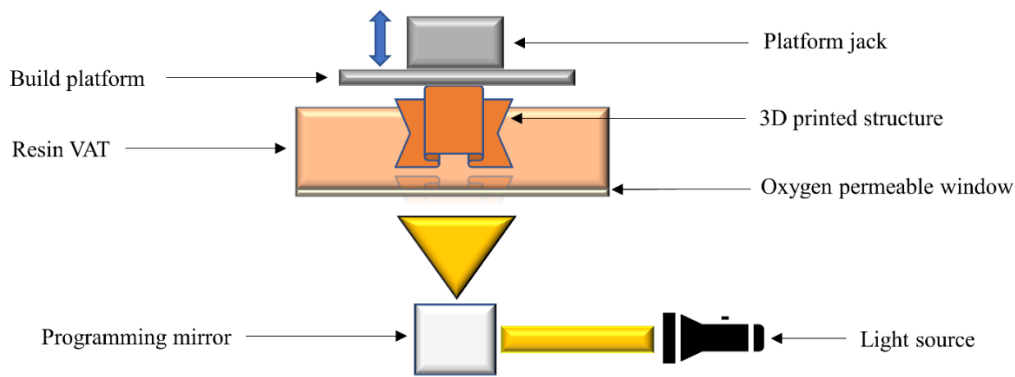
Figure 18. Schematic representation of continuous liquid interface printing (CLIP) [47,180].

2.5.5. Hot lithography

The hot lithography process differs from conventional vat photopolymerization technology in that, it utilizes an additional heating element to control the printing process temperature in vat photopolymerization. Unlike conventional processes, which maintain room temperature during printing and are limited to print the resin up to a certain viscosity, the higher temperature in hot lithography reduces the resin viscosity and increases the reactivity of monomers that cannot fully polymerize at ambient temperatures (Figure 19) [47,184–186]. The photocurable resins are still cured using a SLA or DLP projector, but the monomer conversion rate is higher due to the increased temperature [47,186]. This technology has a great potential to expand the range of resins suitable for vat photopolymerization.
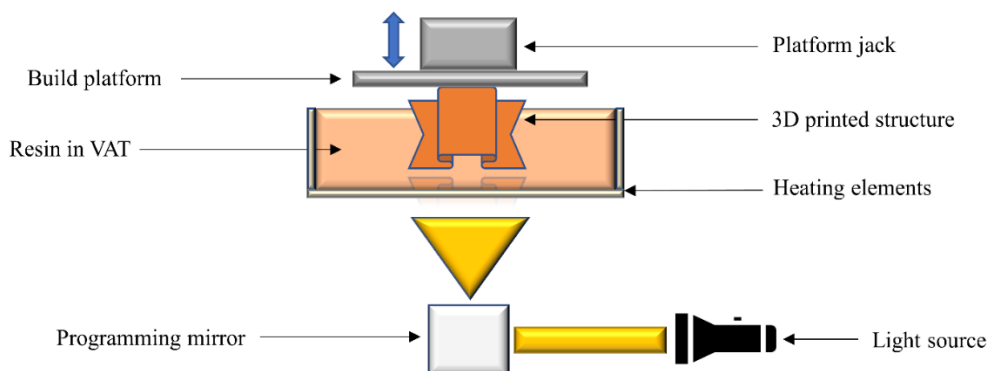
Figure 19. Schematic representation of hot lithography 3D-printing [47].

2.5.6. Two photon absorption 3D-printing

Two photon absorption (TPA) 3D-printing is a type of vat photopolymerization that utilizes an extremely compact laser beam as the illumination source. The illumination generated by the laser beam is of extremely high-power density, with a range of 10^{13} W/μm^2, and is focused on

a tiny volume, lesser than a cubic wavelength λ^3 [187]. This results in the nonlinear absorption of photons, known as two photon absorption, which allows realization of an exceptional spatial resolution, in the nanometer range, far beyond the limits of optical diffraction [47,188].

To maximize the benefits of non-linear absorption, an infrared irradiation source is used to facilitate deep penetration of laser light into the bulk of the material, reducing absorption power losses. When compared to lithography, where light exposure is linear, the material response is also limited to the first order. However, with TPA, the response can be of the second or multiple orders, due to two photon or multi-photon absorption, respectively (as shown in Figure 20) [47].
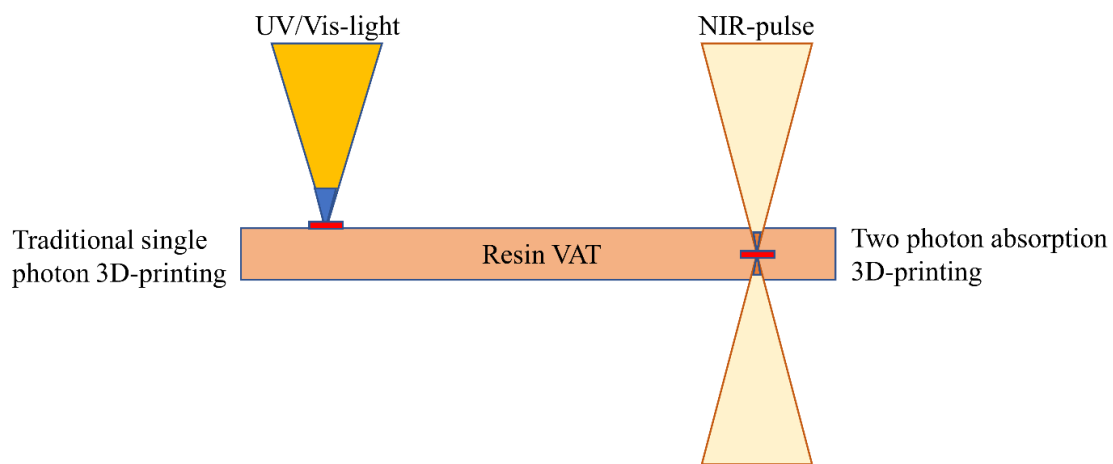
Figure 20. Absorption of UV light takes place on the surface of a photosensitive resin, limiting its application to the creation of flat structures through one-photon absorption. NIR light is directed towards the bulk of the photocurable resin and utilized for 3D-structuring through TPA [47,189].

The precision of spatial distribution in square light intensity is much higher compared to linear light intensity [188]. This results in a reduction of the volume of interaction between light and matter, which leads to an improvement in photo-printing resolution. When a photoinitiator absorbs two photons in the near-infrared range (NIR), it receives a similar amount of energy as it would from the absorption of a single photon in a photocurable formulation. Therefore, when resins are used in two photon polymerization, the spatially distributed photoinitiated radicals obey the square law of light intensity function [47].

The presence of radical scavengers such as dissolved oxygen in the resin formulations sustain radicals in regions of higher light intensity, which leads to the attainment of a polymerization threshold. The light intensity corresponding to this threshold can be tuned using printing parameters including target unit volume (voxels), illumination time and illumination intensity.

TPA 3D-printing can achieve printing resolutions that are much lower than the defined diffraction limit [47,190–195]. By adjusting 3D-printing parameters, voxels with a size of up to 100 nm can be 3D-printed [188,196,197].

The utilization of TPA 3D-printing allows for the creation of nanostructures that are unattainable with alternative techniques. The high energy output of laser illumination during TPA 3D-printing triggers numerous reactive species in the resins, necessitating a proper approach for the efficient 3D-printing of nanostructures (Table 3).

Table 3. Overview of selected printing strategies using two photon absorption polymerization. Reused with permission [47].

	Processing strategy	Application area	Resolution achieved	Reference
TPA photo-polymerization	Radical quencher	Microstructures	100 nm	[198]
	Activation beam	Microdevices	40 nm	[199]
	Scanning speed manipulation	Micromachines	25 nm	[200]
	Self-smoothing	Micro-optics	20 nm	[201]

2.5.7. Volumetric 3D-printing

In volumetric 3D-printing, multiple sliced images are projected onto a rotating resin chamber at particular angles using DLP technology based on computer-aided designs [202,203]. By combining exposed irradiation, radical species are activated above a certain threshold, resulting in the rapid polymerization of a centimeter-scale object within seconds. Oxygen inhibition prevents the photopolymerization of the resin by a single illuminated ray, but the superposition of irradiation activates the radical species in a great concentration.

By manipulating the light intensity and the duration of exposure, it is possible to regulate the degree of polymerization for each resin. Resins with higher viscosities (up to 90 Pa.s) can be used for this type of printing [202]. Conventional polymers offering good flexibility and an elastic modulus less than 10 KPa for distinct applications such as tissue engineering and bio-imprinting are quite difficult to realize during layer-by-layer printing techniques. Such curing processes are greatly influenced by the auxiliary and gravitational forces that often cause pre-mature failures and delayering of the printed structures. Volumetric 3D-printing resolves these issues by avoiding the principles of layered formation, and can develop the cured architectures

up to a resolution of 80 μm, along with a very high building speed in contrast to typical vat photopolymerization 3D-printing processes. The main categories of volumetric 3D-printing process involve

- Xolography [42]
- Computer axial lithography (CAL) [47]
- Holographic light patterning [204]
- Tomographic printing [203,205]

However, these types of methodologies are still in the development phases, with the exception of xolographic and tomographic printers which are now commercially available, but are still limited to the formation of single material structures.

On the other hand, solution mask liquid lithography (SMaLL) represents a volumetric 3D-printing technology that has exhibited a great prospective to form excellent resolution single material and multi-material 3D-structures. The process utilizes collimated UV-Vis light being irradiated upon an optically dense polymer precursor resin containing monomers, photoinitiators, sensitizes and photochromes. Special interest is being created on account of application of photochromes to employ photobleaching with the capability of initiating the photosensitizers and curing the resin deep inside, and hence significantly increase the speed of building. Reversible absorption properties of the photochromic dyes are employed to locally initiate and stop the photoreactions under different wavelengths during the 3D-printing process [163]. The individual capabilities and comparison of vat photopolymerization technologies are presented in Table 4.

Table 4. Summarized features of all vat photopolymerization process are presented in the table. Reused with permission [47].

	Suitable materials	Resolution	Building speed	Benefits	Limitations	Reference
SLA	Acrylate, methacrylate, epoxy, vinyl monomers	5 - 50 μm	0.25 mm/min	High resolution and accuracy	Limited availability of photopolymers, toxicity of monomers	[8,49,144, 206–211]
DLP	Acrylate, methacrylate, epoxy, vinyl monomers	5 - 50 μm	0.4-2.5 mm/min	High resolution and accuracy, lower cost and higher printing speed compared to SLA	Limited availability of photopolymers, toxicity of monomers	[144,207, 210]

LCD	Acrylate, methacrylate, epoxy, vinyl monomers	< 50 µm	10 mm/min	High resolution and accuracy, lower cost	Limited availability of photopolymers, toxicity of monomers	[80,178,179,212]
CLIP	Acrylate, methacrylate, vinyl monomers, epoxies	<100 µm	8-16 mm/min	High printing speed	Anisotropy of printed structures	[180,183]
TPA	Acrylate, methacrylate, vinyl monomers, epoxies	<100 nm	0.08-33 mm³/min	Excellent resolution	Expensive, time consuming, requires tedious control strategies	[213,214]
Volumetric 3D-printing	Acrylate, methacrylate, vinyl monomers, epoxies	Up to 80 µm	10 mm/min	Fast printing speed.	High viscosity resin (>10 Pa.s) required. Expensive technology, laborious resin formulation strategies, limited monomer absorption and good reactivity of monomers is essential.	[42,202,205,215]
SMaLL	Acrylate, methacrylate, vinyl monomers, epoxies	Up to 100 µm	8.33 mm/min	High depth of curing, no rotating parts needed, fast photopolymerization	Additional photochromes and sensitizer required. Reaction strategies to be developed before printing.	[163]

2.6. Bio-based monomers for photopolymerization 3D-printing

Leading 3D-printing technologies that rely on material extrusion and powder bed fusion can employ biopolymers like polylactic acid (PLA) and thermoplastic starch (TPS) [216,217]. However, vat photopolymerization has a more limited range of materials available due to its reliance on liquid photocurable polymers [91]. Typically, photopolymer resins accessible in the market for 3D-printing are derived from fossil resources and primarily rely on epoxides or acrylates which unfortunately have a substantial carbon footprint [218,219].

The scarcity of eco-friendly photopolymers poses a significant obstacle to the widespread adoption of 3D-printing. To tackle this issue, the scientific community has been working on creating sustainable alternatives to the state-of-the-art photopolymer resins that could decrease their environmental impact. The creation of vat photopolymerization materials that are

biobased, biodegradable and recyclable can play a crucial role in facilitating the shift towards a circular economy [220].

The vast range of resins used in vat photopolymerization are sourced from fossil fuels. However, in order to promote a circular economy, it is essential to develop bio-based resins for 3D-printing. To achieve this, common methods for incorporating photocuring functionality into naturally derived oligomers include the unsaturated chemical groups epoxidation, as well as the conversion of epoxy-acid and hydroxyl groups into meth-(acrylates) via reactions with methacrylic acid, glycidyl methacrylate and methacrylic anhydride respectively. Although the outputs of the research on the development of bio-based resin components have improved in the past few years, the real content for bio-based in the resulting resins is hardly reported.

Vegetable oils are frequently used as a source for bio-based resins, with the C=C bonds in the fatty acids being chemically modified through the use of acrylates [221], epoxides [222] and methacrylates [223], enabling the development of a thermoset polymer network through UV curing. One of the earliest examples of this approach from 2016, involved the use of modified soybean oil in stereolithography to create shape memory scaffold materials [224].

Over the years, there has been a growing number of reports on the use of soybean oil in vat photopolymerization. For example, epoxidized soybean oil acrylate (ESOA) has been utilized in Direct Laser Writing (DLW) to create microporous woodpile structures without the need for a photoinitiator [225]. Similarly, Guit et al. synthesized ESOA and the methacrylic counterpart (ESOMA) using a green solvent-free approach and used them, along with commercial bio-based diluents to produce a library of bio-based resins with a bio-content of 74-83%. These resins were then applied in DLP 3D-printing along with commercial diluents and demonstrated excellent layer fusion and mechanical performance comparable to their commercial counterparts [226].

Before this development, only commercial resin components were used to formulate resins with biobased content ranging from 34-67% [227,228]. In addition, epoxidized sucrose soyate, another soybean oil-based compound, was (meth)acrylated and mixed with commercial monomers and applied in vat photopolymerization, resulting in polymers that were competitive with their commercial references in terms of T_g [229].

Moreover, another study presented a blend of commercial acrylate compounds with up to 30 wt.% urethane epoxidized soybean oil, which was employed as dual-curing resin in stereolithography (SLA) to fabricate an interpenetrating network [230]. Other vegetable oils

such as modified castor oil [223], linseed oil [222] and cardanol oil [231] may also be used in vat photopolymerization since they could offer a great potential in UV curable networks formation.

Lignin has been identified as a potential biological source for photopolymers, as reported by Sutton et al. [232]. In their study, lignin was functionalized with methacrylates and incorporated into a commercial resin at levels of up to 15 wt%. The resulting polymer exhibited decreased stiffness and increased ductility as the lignin content increased. Other derivatives of lignin, such as vanillin, eugenol and guaiacol, have also been utilized in SLA [233]. Vanillin was initially methacrylated and then mixed with glycerol dimethacrylate in a 1:1 ratio to create a photopolymer resin with a bio-based content of 35%. Despite the relatively low bio-based content, the resulting 3D-printed product exhibited a high T_g corresponding to 153 °C and a Young's modulus equal to 4900 MPa. The incorporation of guaiacol and eugenol in SLA resins led to the formation of polymers having mechanical properties comparable to those of commercial SLA resins [234].

Miao et al. also demonstrated the successful formulation and DLP 3D-printing of resins having excellent mechanical properties using functionalized itaconic and succinic acids with glycidyl methacrylate, resulting in BHMP3 and BHMP2 respectively [235]. While both polymers had low ductility, they exhibited high tensile moduli of 4480 MPa and 1563 MPa respectively, with BHMP3 having a higher glass transition temperature T_g of 183 °C compared to BHMP2's T_g of 147 °C. Additionally, both resins demonstrated excellent printability by DLP, resulting in well-defined models with outstanding layer adhesion.

Another study by Cosola et al. used acrylated γ-cyclodextrin (Ac-γ-CD) as a bio-based compound for DLP 3D-printing. They mixed around 30% of this oligosaccharide, sourced from starch, with monofunctional methacrylated poly(ethylene glycol) (PEG) as reactive diluent to formulate resins [236].

Bio-based resins have also been used for biomedical applications, such as tissue engineering. Unsaturated polyesters, prepared by polycondensation of multiple bioacids with glycols, were applied in SLA and demonstrated good cell viability [237]. Furthermore, hydrogels resembling liver tissue were successfully 3D-printed using methacrylated gelatin as the building-block [238,239]. Terpenes derived from linalool monomers and limonen pre-polymers [240], polymyrcene in combination with β-myrene diluents [241], were applied to form printed porous structures having high ductility by implementing the thiol-ene chemistry.

In addition, methacrylated dervatives of starch [242], chitosan [243,244] and carboxymethyl cellulose [245] have been employed to print hydrogels, with excellent compatibility in biological system. Methacrylated silk fibroin was also applied in DLP 3D-printing to develop scaffolds that could mimic organ structures with a great biocompatibility [246]. These bio-based resins are derived from biomass, which could be used for specific purposes, including meditational or human consumption. Recently Simpson et al. synthesized photopolymer resins using McDonald's waste cooking oils [221]. Fatty acids from these consumed oils were acrylated, followed by 3D-printing of the resulting polymer precursor resin, demonstrating decent quality with slight over-exposure as presented in Figure 21.
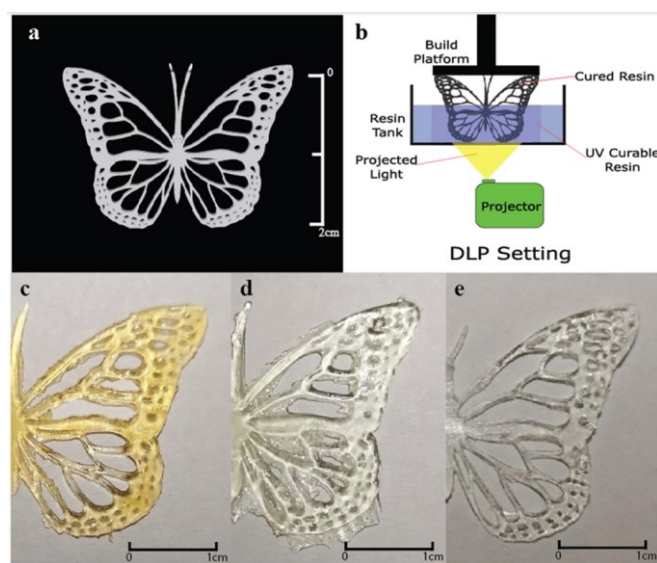
Figure 21. a) Digital model of a butterfly in 3D. b) Printing scheme of DLP 3D-printing technology. c) Butterfly 3D-printed using acrylated waste cooking oil sourced from McDonald's. d) & e) Butterfly 3D-printed from epoxidized soybean oil acrylate and commercial resin (MiiCraft) for visual comparison. Images have been reproduced with permission from the American Chemical Society and are subject to copyright laws, © 2020 [221].

2.7. Covalent adaptable networks (CANs)

Over the past few years, there has been a shift in the way we classify polymers based on their properties due to the emergence of new materials. Traditionally, polymers were categorized as either thermosets or thermoplastics, based on their distinct characteristics. Thermosetting resins are known for becoming hard and insoluble when exposed to heat, forming strong and irreversible three-dimensional networks held together by covalent bonds. In contrast, thermoplastics are composed of linear polymer chains bonded via non-covalent intermolecular forces, allowing them to be reshaped and recycled. However, by incorporating exchangeable,

reversible, or adaptable covalent bonds into the polymer matrix, the differences between these two categories of polymers become less distinct [247]. This is where the term "dynamic" comes in, referring to the reversible covalent bonds that can swiftly attain thermodynamic equilibrium under response to an external stimuli [248].

The response of covalent adaptable networks (CANs) to a particular type of stimuli, i.e. light or heat, is dependent on the nature of the dynamic chemical bonds and the rate of these exchange reactions within the network. The activation of these exchange reaction induces a macroscopic material flow and encountered stresses are relaxed [249,250]. On the other hand, partial reversibility due to side reactions is a limitation of these networks, which restricts thermoreversible cross-linking reactions up to a certain extent [58]. Bowman and Kloxin contributed to the classification of CANs into two distinct types, based on the mechanism by which their dynamic structure is achieved. One type involves kinetic bond exchange, while the other type involves reversible depolymerization through equilibrium shifts [60]. Winne et al. differentiate between two types of molecular network rearrangements (MNRs) in the context of rearrangement reactions occurring within a macromolecular matrix [251]. Single step molecular network rearrangements and multiple step molecular network rearrangements.

In the case of the concerted pathway (Figure 22), the formation of a new network connection and the interruption of the old network connection happen simultaneously, without the formation of an intermediate ordered transition state. The cross-linking density of polymer networks undergoing concerted reorientations remains consistent since all network topologies have an equal number of cross-links [251,252].
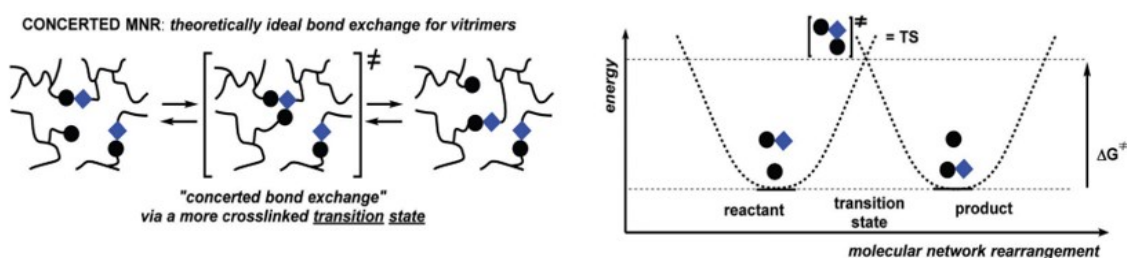
Figure 22. Depiction of the energy profiles and concerted molecular network rearrangements (MNRs) occurring within covalent networks [251].

Polyionic polymer networks with *N*-alkylated triazolium iodide groups as cross-links [253] and polythioether networks containing sulfonium sulfonate ion pair as alkylating cross-linkers [254] are examples of systems that exhibit single (concerted) pathways. The reaction mechanisms for both of these examples are depicted in the Figure 23.

1) Montarnal and Dockenmuller, 2015

2) Winne and Du Prez, 2017
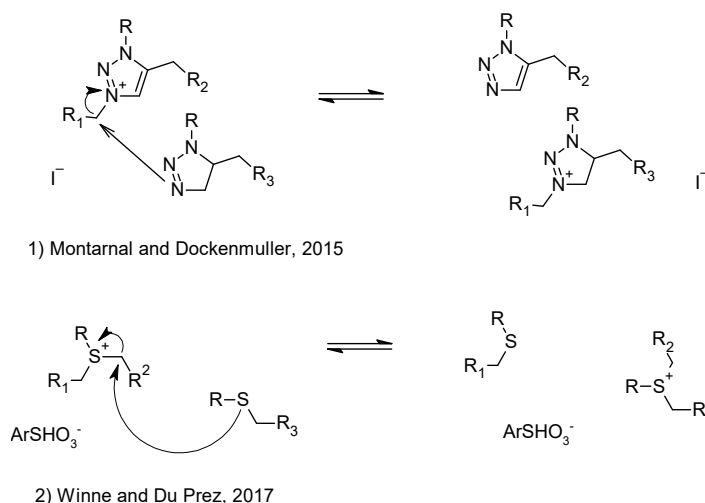
Figure 23. Illustration of potentially concerted (single) molecular network rearrangement (MNR)-based networks [251,255–257].

The non-concerted or stepwise reaction pathway is different from the concerted molecular network rearrangement (MNR) pathway in a way that it involves a bond formation step followed by a bond cleavage stage, as shown in Figure 24. An associative MNR pathway takes place through an exchange-based or addition/elimination mechanism. In this pathway, the former associations of two polymer chains are reorganized, causing a new covalent network bond formation. This is then followed by an elimination step that disintegrates another network bond [251]. This refers to the process of modifying the chain and crosslink configuration of a chemically identical product by attacking specific functionalities along the backbone using a reactant that is attached to it [251,258].
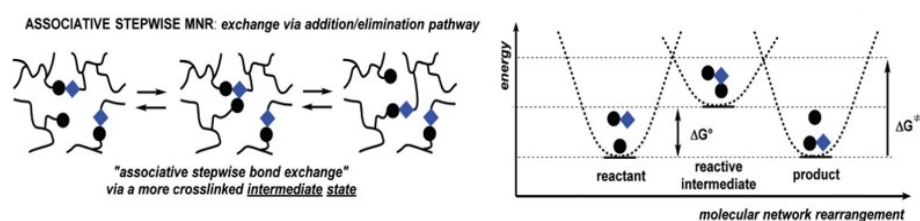
Figure 24. Demonstration of the energetic profiles and rearrangements occurring in the associative molecular networks present in dynamic covalent networks [251].

During the exchange reaction process, a temporary increase in cross-linking density in the reactive intermediate state is observed. Hence, the whole reaction rate relies on the proximity of the cross-links that will be interchanged [251]. This type of reaction can be observed in several situations including:

- The Diels-Alder (DA) cycloaddition reaction [259]

- Dynamic covalent exchanges in amines and β-ketoesters derived enaminone groups [260]

- Photo-triggered radical addition-fragmentation reactions leading to the plasticity and stress relaxation [251,261]

- Dynamic exchange of thioesters with free thiols under influence of a photobase for switching among the dynamic and non-dynamic states [262]

- Thermally induced exchange reactions in hydroxy-functional polystyrenes with siloxane crosslinkers [263]

- Accelerated exchange of ester linkages between hydroxyl moieties in an epoxy-based polyester resin by (Lewis)-acid or base catalysts [264]

Figure 25, presents a few examples of such reaction systems.
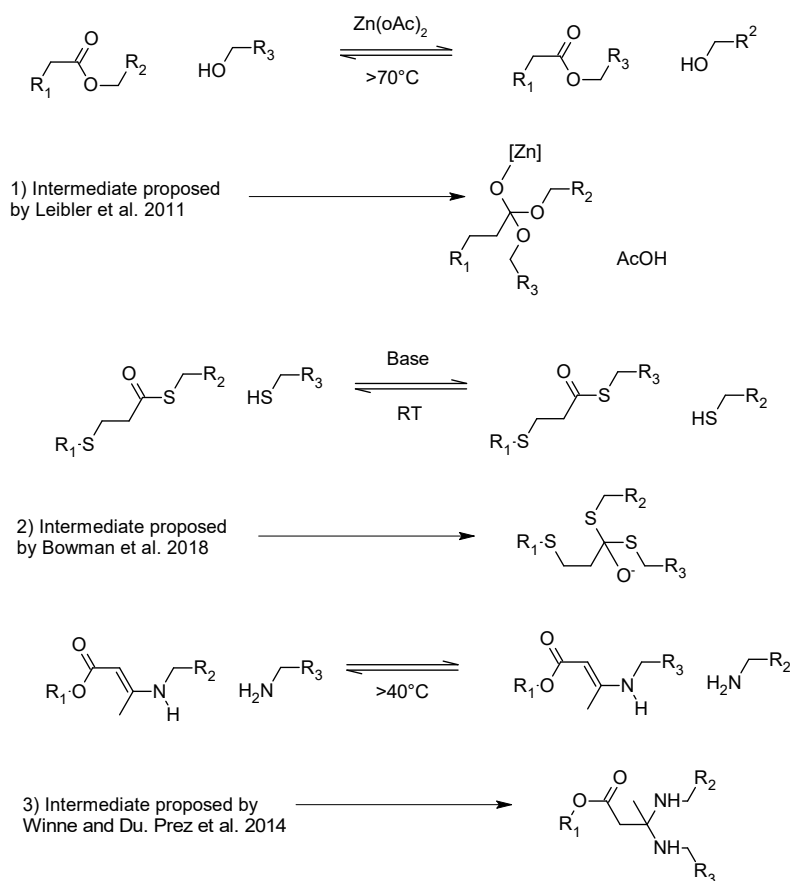
Figure 25. Illustration of some associative non-concerted (stepwise) molecular network rearrangement following dynamic covalent networks [251,257,262,264].

On the other hand, the dissociative method operates through a mechanism of either elimination/addition or reversible addition. This involves a change in the equilibrium between the groups of reactants and a linkage structure of the adduct, resulting in the fragmentation of a

chain segment into two newly formed network ends. As shown in Figure 26, an intermediate state is formed that is temporarily de-crosslinked, resulting in the creation of reactive chain ends with higher energy [251]. However, there is no polymer chain segment association since the polymer chain can disintegrate on its own. In a subsequent step, crosslinking can be re-established by interactions with other polymer chains [251,265].
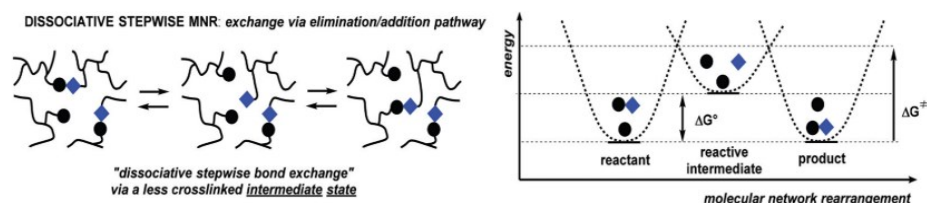
Figure 26. Demonstration of dissociative MNR following dynamic covalent bonds along with the energy profiles [251].

The dissociative CAN (dissociative NMR) pathway includes various examples such as the hetero Diels-Alder reactions with cyclopentadienyl-functionalized (C_p) and dithioester networks [266], reversible Diels–Alder reaction between dienes (furanes) and highly reactive dienophiles (acrylate-type) [267], and reactions among the reversible bonds of hindered (secondary) amines and isocyanates, which serve as a dissociative stepwise MNR process for polymers with dynamic urea networks [268]. Figure 27 depicts some of these reactions.
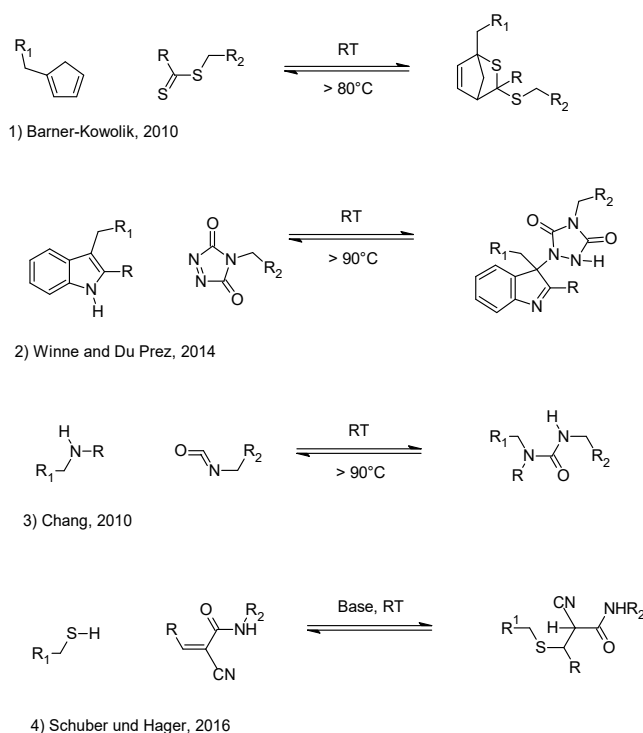
Figure 27. Demonstrations of dynamic covalent networks utilizing dissociative stepwise MNR chemistry.

However, both associative and dissociative mechanisms are unable to fulfil the ideal condition with respect to their connectivity and topology variations. According to the findings, the dissociative pathway exhibits a decrease in overall connectivity when subjected to heat and thermal external stimuli, while the associative pathway shows an increase in overall connectivity when heated. This is because heating can shift the equilibrium towards the endothermic side [251].

In 2011, the Leibler's group introduced vitrimers as a new class of materials that belong to the covalent adaptable networks (CANs) family [264]. Vitrimers are composed of covalently bonded chains that can alter their topology through associative exchange reactions, under an external thermal stimuli [252]. Consequently, the network exhibits thermal malleability. At higher temperatures, the viscosity of the material is primarily governed by associative chemical exchange reactions while maintaining a persistent number of chemical bonds and the corresponding crosslinks density. As a result, the viscosity decreases following the Arrhenius law, which is typical feature of inorganic silica-based materials [269].

This behavior is distinct from thermosetting polymers and dissociative CANs, which follow the Williams-Landel-Ferry (WLF) model for thermoplastic polymer melts [252]. The name vitrimers originates from the gradual Arrhenius-like viscosity change that occurs near the glass transition temperature (T_g), which is typical of glass-like materials such as silica and some other inorganic compounds [270,271].

The exchange reactions within the network result in a second transition temperature, and when the time scale of these reactions becomes shorter than the time scale of material deformation, the network can rearrange its topology [252]. At this point, a transition from a viscoelastic solid to a viscoelastic liquid occurs at a temperature known as the topology-freezing transition temperature, or T_v. Typically, T_v is determined when the material's viscosity reaches 10^{12} Pa.s, as stated by Leibler et al. [264]. There are several methods available to determine this transition, which will be described in the following section.

In general, there are two pathways that can be used to explain the transition dynamics that occur within a vitrimer. In both pathways, the vitrification temperature (T_v) is located at different regions [252,272]. The first scenario (Figure 28a) involves a vitrimer with a glass transition temperature (T_g) lower than the T_v. Within the temperature range encompassed by these two transition points, the vitrimer undergoes a change from a solid-state exhibiting glass-like

characteristics to a state resembling that of a rubbery or viscoelastic solid, and demonstrates a typical elastomeric behavior [252,272].
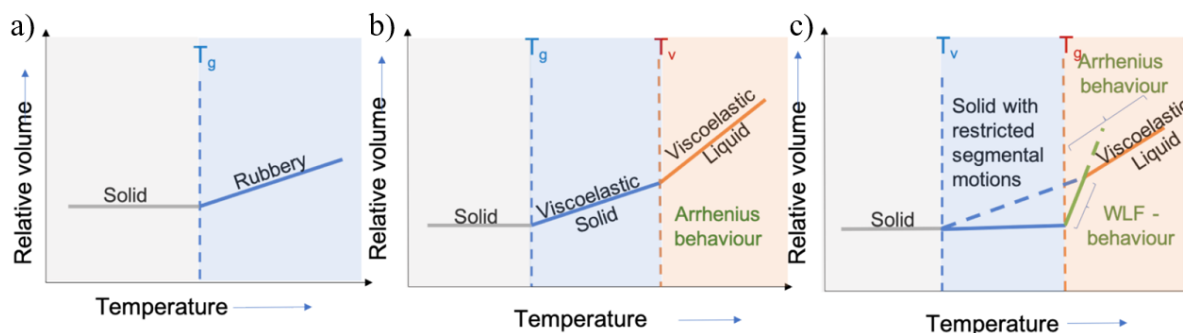
Figure 28. Phase transitions in thermosets and covalent adaptable networks. Reused with permission [272].

In this region, the exchange reaction occurs at a slow pace, causing the network structure to remain fixed. Heating the vitrimers accelerate the exchange reactions, which become significantly fast at temperatures above the T_v. Due to these exchange reactions, the elastomer behaves like a viscoelastic fluid, and its flow is primarily determined by the kinetics of bond exchange (Figure 28b). A characteristic Arrhenius behavior is represented by the viscosity change of the vitrimer and the applied temperature [252,272].

The second scenario (Figure 28c) involves a vitrimer with a T_v lower than the network's T_g. Before achieving the glass transition, the networks mobility is limited on account of the frozen segmental motions associated with T_g, which prevents exchange reactions from occurring. As the temperature increases and approaches the T_g, the segmental motion is initiated along with the activation of exchange reactions. The overall kinetics of network rearrangement are governed by diffusion and the reorientations of topology is driven by the segmental movements, resulting in a WLF viscosity response (Figure 28c) [252,272].

As the system experiences sustained heating, it eventually reaches a specific stage where it transitions from a regime governed by diffusion, to one controlled by the exchange reactions, and obeys the Arrhenius law. The inherent stiffness of the monomers, the concentration of exchangeable bonds and functional groups, the degree of cross-linking, the kinetics of exchange reactions can all significantly impact both of the transition regions [252].

2.7.1. Transesterification based vitrimers

Transesterification is a commonly known chemical reaction, also known as alcoholysis, which involves the substitution of alcohol in an ester with another alcohol, resembling the process of

hydrolysis but employing alcohol instead of water [273,274]. As an output of the transesterification reaction, the carboxylic acid ester groups are exchanged between the reacting species. Such reactions can be catalyzed by potent acids and bases, as well as enzymes such as lipases and it finds numerous applications both in laboratory and industrial scale [273,274].

Alcoholysis has been well known for its vital role in the production of PET (polyethylene terephthalate), wherein it facilitates the transesterification of dimethyl terephthalate with ethylene glycol [275,276]. Furthermore, subjecting methyl acrylate to transesterification with various alcohols, acrylic acid derivatives are synthesized, which is also a well patented industrial process [277,278]. Transesterification is applied as a fundamental reaction in the conversion of vegetable oils, where triglycerides react with alcohols to generate blends of fatty acids also known as biodiesel [273,279–281]. All these processes are catalyzed by either a strong acid or a base in the reaction systems.

The base catalyzed transesterification reactions involve the nucleophilic attack of the alkoxide conjugate base on the carbonyl ester groups, followed by the detachment of the leaving groups to form the exchanged ester functional chains. The released alkoxide groups further attack the carbonyl esters in the vicinity leading to a highly reactive system (Figure 29).
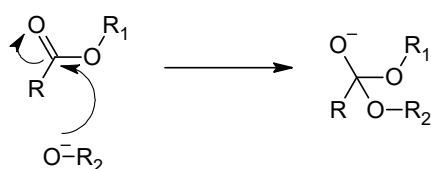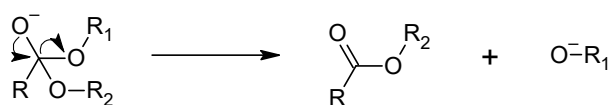
Figure 29. Transesterification reaction mechanism in the presence of a base catalyst and temperature. R, R_1 and R_2 represent the polymer chain segments [279].

On the other hand transesterification reactions can also be catalyzed via acidic catalysts which activate the carbonyl ester moieties by enhancing the electrophilicity through polarization, which could further come in contact with adjacent hydroxy moieties through coordination bonds causing the alkoxide/alcohol equilibrium to shift towards a more nucleophilic alkoxide form (Figure 30) [282]. A tetrahedral transition state is formed by a subsequent combination

with the hydroxy group generating a newly formed ester bond through proton transfer followed by the departure of leaving group and deprotonation [281] (Figure 30).

Protonation of carbonyl through acid, activation for nucleophilic attack
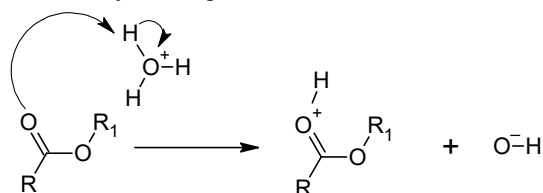
Nucleophilic attack on carbonyl
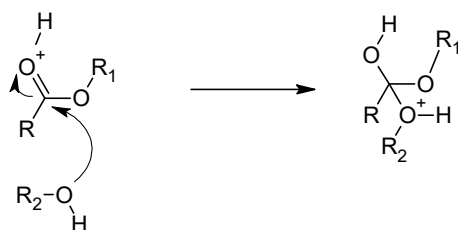
Transfer of proton
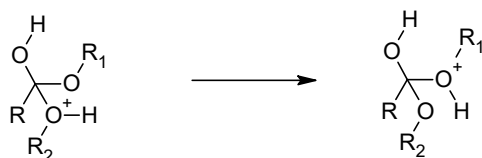
Leaving group removal
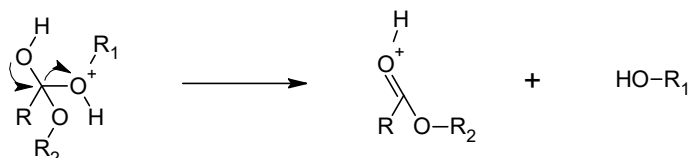
Deprotonation
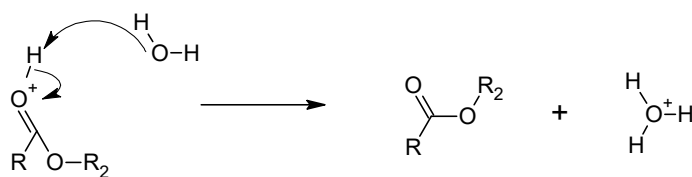
Figure 30. General transesterification reaction in the presence of temperature and acidic catalyst. R, R_1 and R_2 denote the alkyl chains [279].

Commonly employed classes of catalysts for transesterification reactions involve Brønsted acids [283,284], organo-metallic complexes [269,282,285], or organic bases [286].

In 2011, Leibler et al. introduced vitrimers exploiting a transesterification-based resin for the first time, that was derived from the traditional and well established chemistry of epoxies [264].

In the presence of Zn(OAc)$_2$, they mixed a blend of dicarboxylic and tricarboxylic acids, with DGEBA, resulting in the formation of an insoluble network [264]. This network could flow and relieve stresses at high temperatures. The stress-relaxation procedure took numerous hours at 150 °C, with the corresponding network's activation energy of 80 kJ.mol^{-1}.K^{-1}. The topological freezing temperature (T$_v$) was as low as 53 °C for a network containing 10 molar percentage of the catalyst. The network's reprocessability was successfully showcased by the authors through the grinding process, in which the material was converted into tiny fragments and subsequently utilizing injection molding technique. Interestingly, the pristine mechanical attributes were completely recovered. Furthermore they also examined a resin system, based on a blend of anhydride (glutaric anhydride) and epoxy (DGEBA) [264], along with Zn(acac)$_2$ as catalyst. The compression molding technique was effectively used to reprocess this system, demonstrating similar activation energies to those of the epoxy/acid system [264].

Subsequent to this pioneering work, many researchers have been inspired to realize novel concepts and utilize transesterification-based CANs. Epoxy resins based on transesterification are highly attractive for various purposes such as coatings, adhesives, electronics, composites and light-emitting diodes. To extend the pertinance of transesterification-based epoxies, numerous efforts have been made for integrating them in innovative materials. Consequently, advancements have been made in the development of materials such as epoxy-silica nanocomposites, healable bio-epoxies with high glass transition temperatures (T$_g$) derived from eugenol or vanillin-guaiacol, as well as commercial elastomers. The most significant advantage of transesterification lies in its ability to generate commercially admissible and straightforward chemical compounds, which makes it simple to implement [287].

The choice of catalyst for transesterification is generally limited and mostly based up on the organic nitrogen-based bases or organometallic complexes [287]. In principal, the catalysts should fulfil a number of criteria to qualify for the further applications including high solubility, compatibility with the polymer network matrix, excellent thermal stability, convenient availability and reasonable cost of the materials.

Different types of organometallic complexes have been introduced, and they have been studied in various networks as potential transesterification catalysts [288–290]. Liu et al. examined networks containing different dibutyltin salts, and demonstrated the importance of the catalyst structure and concentration through compression strength studies and stress-relaxation measurements [288]. Stannous octoate [Sn(Oct)$_2$] was also reported as a catalyst in a vitrimeric

network based on polylactide with diisocyanate crosslinks, exhibiting discrete topological rearrangements [291].

However, the most commonly used organometallic complexes as transesterification catalysts contain ionic centered zinc salts, including zinc acetate [$Zn(OAc)_2$] and zinc acetylacetonate [$Zn(acac)_2$] [269,292–296]. The transesterification mechanism in the presence of zinc catalysts involves three main steps, [289,297] which are summarized as follows:

- The coordination bonds guide the reacting species and brings them together.
- The electrophilicity of the carbonyl group in esters is intensified by polarization.
- The alcohol/alkoxide equilibrium shifts towards the more nucleophilic alkoxide during the formation of β-hydroxy esters.

Additionally, titanium-containing organic compounds are able to catalyze transesterifications in epoxy/anhydride vitrimers, along with organic zinc salts [289,297].

Anther frequently encountered catalyst for transesterification reactions is the organic nitrogen base 1,5,7-triazabicyclo[4.4.0]dec-5-ene (TBD), a potent guanidine base that can elevate the nucleophilicity of alcoholic moieties through hydrogen bonding [298,299]. Its remarkable transesterification capabilities make it a favored choice in many vitrimers, such as in dynamic epoxy/acid or nitrile-butadiene rubbers [300–303].

Triphenylphosphine (TPP) is also utilized as a transesterification catalyst in epoxy-based vitrimers by facilitating the reaction across the lone pair on the phosphorous atom [250,304,305]. However, a limited number of studies have been conducted to compare the efficiency of various catalysts in the same polymer network.

Capelot et al. explored the influence of three distinct catalysts and their concentration levels, utilizing zinc acetate [$Zn(OAc)_2$], triazabicyclodecene (TBD) and triphenylphosphine (PPh$_3$) in an epoxy-based vitrimeric network (Figure 31A) [304]. The catalytic mechanisms of organic compounds differ significantly from those of metal salts, which can greatly affect activation energies.
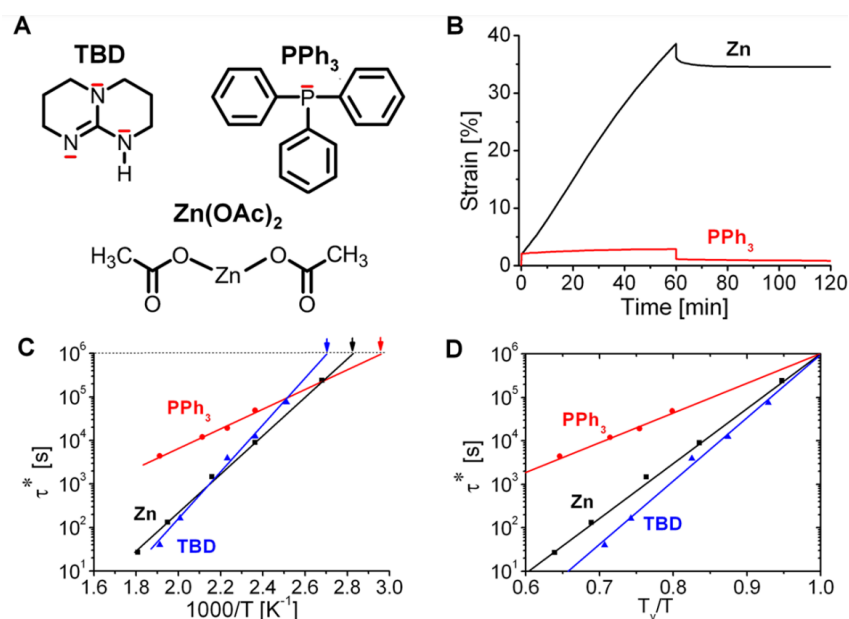
Figure 31. (A) The types of different catalyst employed in the network for comparison of performance. (B) Creep recovery tests under a stress of 0.1 MPa with sample containing 5 mol% PPh$_3$ and Zn(OAc)$_2$ carried out at 200 °C, with stress released after 60 minutes. (C) Relaxation timings for formulations containing 5 mol% of PPh$_3$, TBD and Zn(OAc)$_2$ respectively, represented via Arrhenius plots. (D) Angell fragility results of 5 mol% of PPh$_3$, TBD and Zn(OAc)$_2$ respectively, and normalized by vitrification temperature. Reused with permission [304].

The effectiveness of catalysts at specific temperatures can be determined through creep experiments as presented in Figure 31B. In general, the efficiency of catalysts for transesterification reactions (and hence the speed of exchange reactions) and the viscosity of the network are inversely proportional to each other [304].

Figure 31B also illustrates the results of elongational creep experiments conducted under identical conditions (applicated stress = 0.1 MPa, for 1 hour at 200 °C with 5 mol % catalyst) on networks containing either Zn(OAc)$_2$ or PPh$_3$. It is noteworthy that the viscoelastic behavior of the two catalysts is markedly different. Following the release of stress, the Zn(OAc)$_2$ containing sample demonstrates a remaining deformation of 35%, while the PPh$_3$ loaded sample almost entirely reaches its original position [304].

Moreover, at the same catalyst concentrations, the relaxation times τ^* for all three catalysts at various temperatures were determined using stress relaxation experiments. The variations in relaxation times with temperature followed the Arrhenius law. The catalysts: Zn(OAc)$_2$ and TBD, were determined as more efficient transesterification catalysts as they had much faster

relaxations at elevated temperatures (as exhibited in Figure 31C). The T_v were different for each catalyst, but T_g of the networks remained the same according to DSC studies. The activation energies were also notably different for each catalyst, as depicted by the "Angell fragility plot" in Figure 31D. The authors also documented that the catalyst-induced flexibility could be further exploited in adjusting the vitrimeric flow properties for various applications and operating temperatures [304].

Shi et al. employed thermo-activated transesterification to recycle 3D-printed parts [306], but the filament extrusion printing technique resulted in low resolution and inadequate surface quality. In contrast, Zhang et al. adapted the concept of DLP on photo-curable resins [296]. They utilized a photo-curable resin formulation comprising hydroxyl-functional mono- and diacrylates, a Norrish Type I photoinitiator, and $Zn(OAc)_2$ as a catalyst for bond exchange reactions, enabling the network to become thermally mendable and reprocessable. However, this approach is limited in terms of network design, as $Zn(OAc)_2$ is insoluble in most common acrylate monomers.

Bowman et al. employed TBD as a transesterification catalyst for covalent adaptable thiol-ene networks, but photocurable resins containing this catalyst are unsuitable for the adequate production of 3D-objects since TBD behaves as a radical scavenger [303] and hinders the photopolymerization. Moreover, the use of well-known transesterification catalysts such as TBD, $Zn(OAc)_2$, or triphenylphosphine can lead to thiol-Michael addition reactions, reducing the storage stability of the resins. This results in rapid gelation even in the absence of light, making it impractical to use these formulations for DLP 3D-printing [126–128].

Bates et al. conducted research on hydroxyl-functional polyesters undergoing Brønsted acid-catalyzed transesterifications in the presence of strong protic acids with varying logarithmic acid dissociation constants (pK_a) ranging from -12 (triflic acid) to 0.81 (trichloroacetic acid). They discovered a unique stress relaxation that increased as the acid catalyst's pK_a value decreased [136,283].

Rossegger et al. applied a new Brønsted acid catalyst system based on methacrylate monoester phosphate, which is available in liquid state and benefits from a high solubility in the acrylate-based systems. Furthermore, the catalyst contained methacrylate moieties which ensured its covalent bonding and integration in to the network [128]. The networks also exhibited adequate stress relaxations and a good storage stability of photocurable resins.

2.7.2. Methods for determining the bond exchange reactions in CANs

To date, three main methods have been established for determining the topological freezing temperature of a vitrimer.

Rheological measurements

One of the characteristic properties of associative CANs is their special viscoelastic behavior that can be analyzed through rheological measurements. These tests involve applying a specific torsion to the polymer sample, maintaining the deformation for a certain period of time, and then measuring the relaxation of the stress [307,308]. While the rheological method has been conventionally employed for polymer precursors, non-crosslinked melts and solutions, it has also been exploited for chemically cross-linked polymers [309]. Different rheometer geometries such as plate-plate and solid rectangular fixtures can be employed for this purpose. The assessment of the results commonly entails the application of the Maxwell model, which comprises a tandem arrangement of a spring and a dashpot, as shown in Figure 32a.
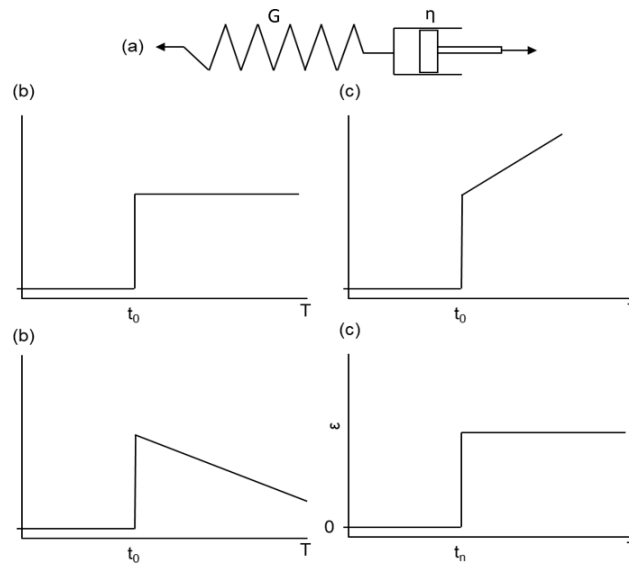
Figure 32. (a) Symbolic representation of the Maxwell model, (b) eventual deformation and the corresponding stress behavior, (c) rapid stress application and the emerging deformation behavior [307].

To evaluate the topological freezing temperature T_v, a specific procedure is employed. This involves using Eq. 8, which provides the differential equation of the Maxwell model, with η and G representing the material parameters of the elastic spring and damper, respectively.

$$\tau = \eta \frac{\delta \gamma}{\delta t} - \frac{\eta G \delta \tau}{\delta t}$$
<div align="right">Eq. 8</div>

Eq. 9 sets out the boundary condition, which states that once deformation is constant, the stress will asymptotically approach zero, with its maximum at the beginning. At the relaxation time, denoted by λ or τ, the exponent of the e-function is -1, equivalent to a mathematical number of 0.3678. This relaxation time can be exploited to determine the stress at the initial stage and a certain point during the measurement.

Applying relaxation boundary condition: $\qquad \frac{\delta\gamma}{\delta t} = 0$ $\hfill$ Eq. 9

Stress level during a relaxation test: $\qquad \tau(t) = \tau_0 e - \frac{t}{\lambda}$ $\hfill$ Eq. 10

$$\lambda = \frac{\eta}{G}$$ $\hfill$ Eq. 11

Relaxation time determination:

$$\tau = \lambda, \text{valid for } \tau = \tau_0 e^{-1} = \tau_0 \frac{1}{e} = \tau_0 * 0{,}3678$$ $\hfill$ Eq. 12

Utilizing Hooke's law in Eq. 13, the time-dependent relaxation modulus can then be calculated, corresponding to the material constant of the spring (G), at time zero. The final material constant can be calculated by dividing the viscosity of the damper by the shear modulus of the spring, as the relaxation time is defined in this manner [310]. The mathematical representation of time-dependent relaxation modulus is expressed as Eq. 13:

$$G(t) = \frac{\tau(t)}{\gamma}$$ $\hfill$ Eq. 13

To generate the master curve, each data point's time is divided by the shift factor corresponding to a specific temperature, which is calculated using Eq. 14.

Shift factor following the Arrhenius principal: $\qquad aT = e^{\left[\frac{E_A}{R}\left(\frac{1}{T} - \frac{1}{T_{Ref}}f\right)\right]}$ $\hfill$ Eq. 14

To determine the activation energy (E_A), one can plot the relaxation time at different temperatures using the Arrhenius law. This involves calculating the natural logarithm of the stress relaxation times and plotting them against 1/T or 1000/T, where T represents the absolute temperature. By examining the slope (k) of the resulting line, the activation energy can be determined. Eq. 15 to Eq. 17 illustrate the mathematical basis for this method. The general Arrhenius equation provides a rate constant, which in our scenario is the relaxation time λ. Normally, rate constants increase with temperature, but in the case of associative CANs, as temperature rises, relaxation times decrease, leading to negative activation energy values [310].

$$\lambda = A \cdot e^{\left(\frac{E_A}{RT}\right)} \qquad \text{Eq. 15}$$

A linear representation of the Arrhenius – plot can be mathematically presented as

$$\ln(\lambda) = -\frac{E_A}{R} \cdot \frac{1}{T} + \ln(A) \qquad \text{Eq. 16}$$

The activation energy can be calculated using the straight-line slope

$$k = -\frac{E_A}{R} \Rightarrow E_A = |-k \cdot R| \qquad \text{Eq. 17}$$

To determine T_v, Eq. 15 is utilized to compute the viscosity at specific measurement moment, followed by the extrapolation of viscosity values up to 10^{12} Pa.s. Subsequently, the temperature corresponding to this value represents the T_v [264,311].

Dilatometry

In this method, the sample is subjected to a constant tensile stress while its temperature is gradually increased at a constant rate and the strain of the sample is measured. As the temperature rises, the sample undergoes expansion, that eventually intensifies when transesterification reactions start to become noticeable on a macroscopic scale at a certain temperature known as the T_v. At this stage, the material can deform under stress, causing a sharp increase in elongation. Hence, the T_v is determined as the point, on which the material exhibits a non-linear response. Kaiser et al. demonstrated this distinctive behavior through dilatometry experiments (Figure 33), conducted on epoxy-acid networks containing 5 mol% of TBD catalyst at various levels of strain [305].
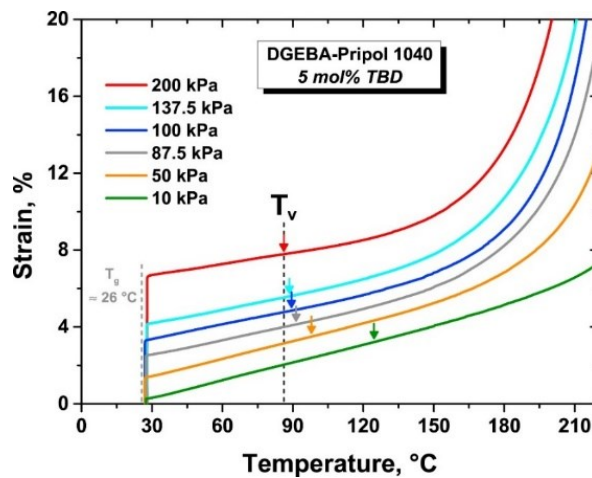
Figure 33. The elongational creep behavior of the epoxy-acid vitrimer with 5 mol% TBD as a transesterification catalyst studied under different stresses with a heating rate of 3 K/min. The arrows indicate the starting point of plastic deformation. Reused with permission [305].

As a result of the systems' softening and enhancement in the elongation, the conventional T_g of the vitrimer could also be determined [312–314]. The exact determination of T_v is based on various factors including the applied stress or heating rate. A high stress level leads to a rapid non-linear strain, while raised heating rates can cause the T_v to appear at later stages [315].

Kaiser et al. illustrated that as stress increases, the T_v of the system reaches its minimum, indicating the onset of bond exchange reactions within the polymer network. This value is determined solely by the network's chemistry and marks the beginning of reorientations. For soft epoxy-acid crosslinked systems, superposition of the entropy-driven flexible coil insertion effects on the creep are observed beyond this point, resulting in a higher T_v. This shift in T_v is less noticeable for stiffer epoxy-anhydride crosslinked networks [315,316].

Aggregation-induced emission

In 2019, Yang et al. introduced a novel technique for detecting the T_v by employing aggregation-induced-emission (AIE) luminogens. This method operates under static conditions and does not require any external force, which distinguish it from the previously discussed dynamic characterizations [272,317]. The technique involves doping the vitrimer network with AIE fluorescent molecules, and follows the operating principal that the fluorescence of these molecules undergoes a change under and beyond the T_v [272].
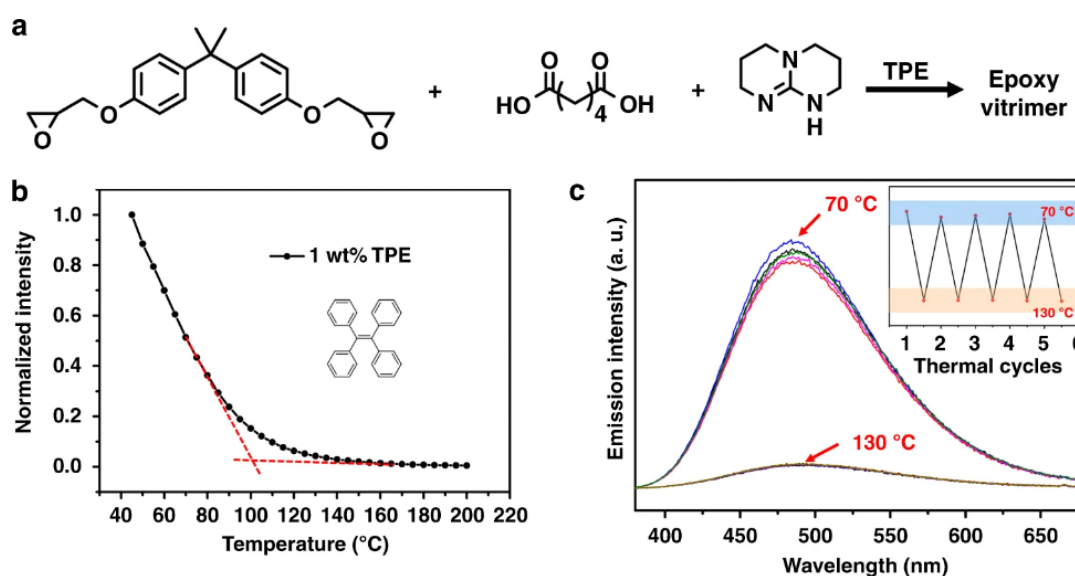
Figure 34. a) Fluorescent characteristics of the epoxy-acid vitrimers doped with tetraphenylethene (TPE). b) Fluorescence intensity measurements on epoxy-acid vitrimers containing TPE (1 wt.%) over a temperature up to 220 °C, normalized with intensities at 45 °C. c) Cyclic fluorescence spectrum of the doped vitrimer at 70 °C and 130 °C over a number of temperature switches [317].

AIE luminogens are fluorescent organic substances that emit light when intramolecular motion is restricted, causing absorbed energy to dissipate through radiation (Figure 34). In vitrimers, AIE luminogens allow for considerable molecular reorientations within the network at T_V [318].

3. Structure-property relationships in thiol-acrylate vitrimers

The section presents data and findings that were published in the journal "Polymer" under the title "Thiol–acrylate based vitrimers: From their structure–property relationship to the additive manufacturing of self-healable soft active devices," Volume 231, Issue 124110, in August 2021. The majority of the subsequent text, tables and figures were extracted from the aforementioned publication [135].

3.1. Materials and methods

3.1.1. Resin formulations development

The resin formulations were created by combining HP1A (50 mol%), DG2A (25 mol%), and 25 mol% of one of the thiols from HXDT, EGMA, EGMP, PTTMP, DPTHMP and PCLMT (Figure 35). In this manner, a total of six resin formulations were prepared with each thiol, while keeping the acrylate constant. The resin formulations were mixed on a magnetic stirrer at room temperature for 1 hour.
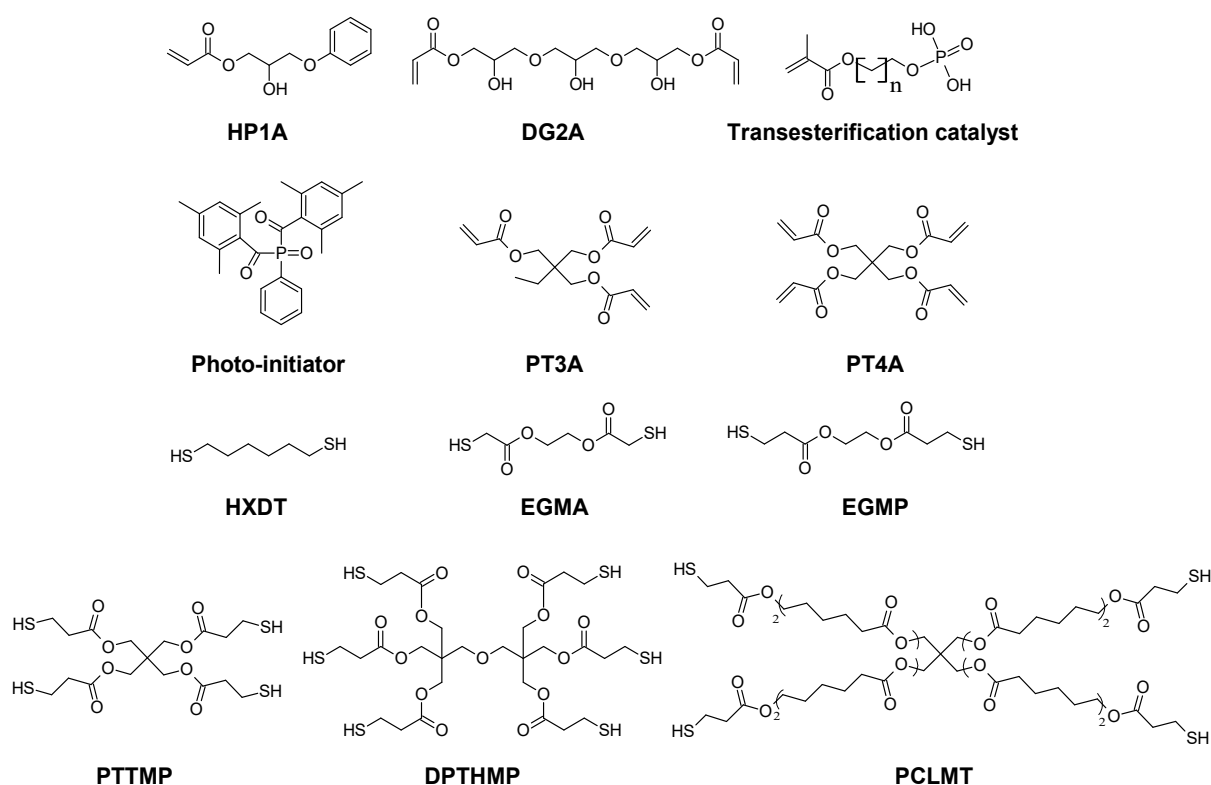
Figure 35. Chemical structure of functional acrylates and thiols, along with transesterification catalysts (Miramer A99) and photoinitiator (BAPO) [135].

For developing formulations with multi-functional acrylates, PT3A (50 mol%) and PT4A (50 mol%) were combined with DG2A (25 mol%) and thiol EGMA (25 mol%). Additionally, 2 wt.% of phenylbis(2,4,6-trimethylbenzoyl) phosphine oxide (BAPO) as a photoinitiator was added to each formulation along with 0.05 wt.% of Sudan II as a photoabsorber, and 10 wt.% of Miramer A99 as a transesterification catalyst. Each formulation was mixed for 1 hour on a magnetic stirrer at room temperature. The addition of the photoabsorber helped to achieve high-resolution printing and prevented over-curing of the resins in the vat. All of the formulations were made in light-protected glass vials, and the compositions can be found in Table 5.

Table 5. Summary of resin formulation used for development of structure-property relationships in thiol-acrylate vitrimers. All resin formulations contained 2 wt.% BAPO, 10 wt.% Miramer A99 and 0.05 wt.% Sudan II.

Resin formulation	1st Acrylate (mol%)	2nd Acrylate (mol%)	Thiol (mol%)	Stoichiometric ratio (thiol:acrylate)
HXDT-HP1A	HP1A (50%)	DG2A (25%)	HXDT (25%)	1:2
EGMA-HP1A	HP1A (50%)	DG2A (25%)	EGMA (25%)	1:2
EGMP-HP1A	HP1A (50%)	DG2A (25%)	EGMP (25%)	1:2
PCLMT-HP1A	HP1A (50%)	DG2A (25%)	PCLMT (25%)	1:1
PTTMP-HP1A	HP1A (50%)	DG2A (25%)	PTTMP (25%)	1:1
DPTHMP-HP1A	HP1A (50%)	DG2A (25%)	DPTHMP (25%)	1.5:1
EGMA-PT3A	PT3A (50%)	DG2A (25%)	EGMA (25%)	1:4
EGMA-PT4A	PT4A (50%)	DG2A (25%)	EGMA (25%)	1:5

3.1.2. DLP 3D-printing of resin formulations

An Anycubic Photon S printer (China) with a 405 nm LED source was utilized to perform DLP 3D-printing experiments. The exposure time for the first layer was 20 seconds, while the remaining layers were exposed for 15 seconds, determined by the monomer conversions derived from FTIR experiments. Each DLP printed layer had a thickness of 50 μm, with both building and retracting speeds set to 2 mm.s^{-1}.

3.1.3. Network properties and photopolymerization kinetics

The reaction progress of the photopolymerization process was analyzed using a Vertex 70 FTIR spectrometer (Bruker). For sample preparation, 1.2 µL of each resin formulation was drop-cast between two CaF_2 slides and illuminated using a LED lamp (zgood® wireless) having a power density of 3.3 mW.cm^{-2} and the illumination wavelength between 420 – 450 nm. The spectra of each formulation were taken between 4000 cm^{-1} and 700 cm^{-1} at a resolution of 4 cm^{-1}. The irradiation and curing steps were followed stepwise until maximum conversion was observed. Bond conversions at each irradiation interval were estimated using normalized peak areas of characteristic acrylate and thiol peaks at 1635 cm^{-1} and 2570 cm^{-1} respectively, by employing OPUS software.

The FTIR spectra of the cured and thermally treated samples (after 180 °C and 4 hours), were measured with the Vertex 70 FTIR spectrometer equipped with a diamond attenuated total reflection (ATR) unit. Circular disks with a diameter of 10 mm and a thickness of 0.4 mm were DLP 3D-printed and FTIR-ATR spectra were taken between 4000 cm^{-1} and 700 cm^{-1}.

3.1.4. Stress relaxation measurements

DLP 3D-printed circular disks with a diameter of 10 mm and a thickness of 1 mm were used for the stress relaxation measurements at 180 °C employing a Physica MCR-501 rheometer from Anton Paar (Austria) under a parallel plate configuration. Prior to the initiation of measurements, all cured samples were equilibrated at the measurement temperature with a constant force of 20 N for an interval of 20 minutes. Afterwards, a strain of 3% was applied on the samples and the stress was measured over the period of time.

3.1.5. Tensile testing

The tensile strength of the materials was determined with the help of DLP 3D-printed rectangular samples having dimension 30 x 10 x 1.5 mm (*l x w x h*). Zwick-Roell Z1.0 static materials testing equipment was utilized to determine the tensile strength of the materials at a crosshead elongation rate of 250 mm.min^{-1}. Five samples were tested and an arithmetic average was obtained for a cumulative result.

3.1.6. Viscosity measurements

Viscosity measurements of the liquid resins were performed using a modular compact rheometer (MCR 102) having a CP60-0.5/TI cone (1.982° opening angle and 49.97 mm diameter). A share rate from 0.1 to 300 s^{-1} was employed on 1 mL of the liquid resin at room temperature (25 °C).

3.1.7. Characterization of network properties

To determine the networks' crosslinking degree, the gel content of the materials was determined using dichloromethane. Circular 3D-printed disc (10 mm x 1 mm) were immersed in the solvent for a period of 48 hours at 20 °C. The samples were subsequently removed and the surface was dried with a tissue paper. The samples were then placed in the oven at 40 °C until all the solvent evaporated and a consistent weight of the samples was achieved. The gel content was determined from the ratio of the initial mass of the sample (m_{ini}) to the final dried mass of the sample (m_{dr}). For each formulation, five samples were tested and an arithmetic average of the samples was obtained.

To determine the printing resolution of the material, microscopic pictures of printed test structures were obtained using an Olympus BX 51 optical microscope, equipped with a Color View Illu digital camera.

3.2. Results and discussion

This chapter addresses the investigation of the structure-property relationships of thiol-acrylate based vitrimers for the 3D-printing of soft active devices with customizable thermo-mechanical properties. Special attention is given to the cure kinetics of the formulations, which is critical for the fabrication of personalized soft active devices using the DLP technology (Figure 36).
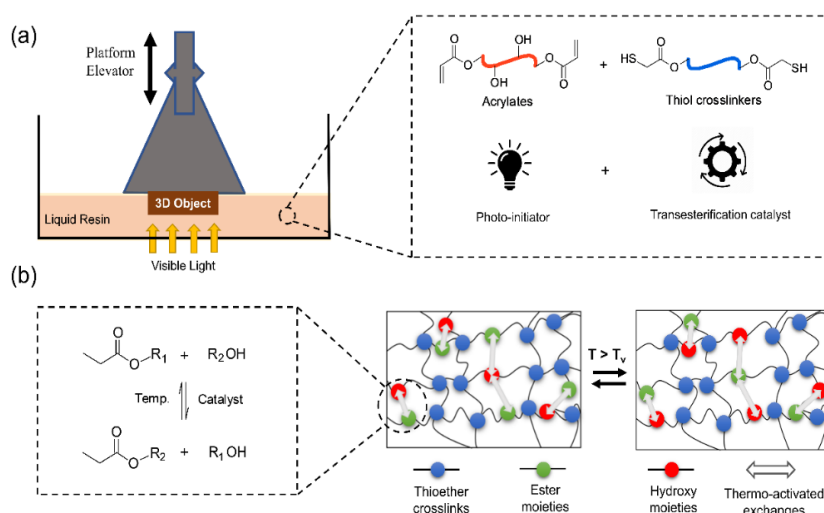
Figure 36. (a) DLP 3D-printing technology's schematic diagram and the general structure of the resin components used for the thiol-acrylate vitrimers are depicted. (b) Illustrative representation of the dynamic network, which can undergo thermo-activated ($T > T_v$), catalyzed transesterifications between the hydroxyl and ester moieties present in the thiol-acrylate vitrimers [135].

The study systematically explores the impact of the molecular structure of the acrylates and the thiol crosslinkers, including the stoichiometric functionality and quantity of hydroxy (–OH) and ester (-C=O) groups, on the bond exchange kinetics, thermal and mechanical properties of the related dynamic photopolymers. By correlating the molecular structure with the mechanical properties of the vitrimer networks, a better understanding of the relationship between network architecture and thermo-mechanical performance is achieved.

3.2.1 Effect of thiol cross-linker on photopolymerization kinetics and characteristics of thiol-acrylate vitrimers

In the initial study, thiol-acrylate based vitrimers were created by using various bi-functional thiols with differing numbers of ester moieties, while maintaining a constant concentration and ratio of –OH functional acrylate monomers (HP1A and DG2A). The chosen thiol crosslinkers were the aliphatic 1,6-hexane dithiol (HXDT), which contained no ester moiety, and two mercapto-ester thiols including ethylene glycol bis-mercaptoacetate (EGMA) and ethylene glycol bis-3-mercaptopropionate (EGMP). The photo-curing kinetics of the resin formulations was analyzed by monitoring the consumption of the characteristic stretching band of the thiol (S-H) bond at 2570 cm^{-1} and the wagging bands from the C=C group at 1635 cm^{-1} as a function of the illumination time. Figure 37 represent an exemplary FTIR spectrum of one of the resin formulations before and after full curing under LED visible light lamp.
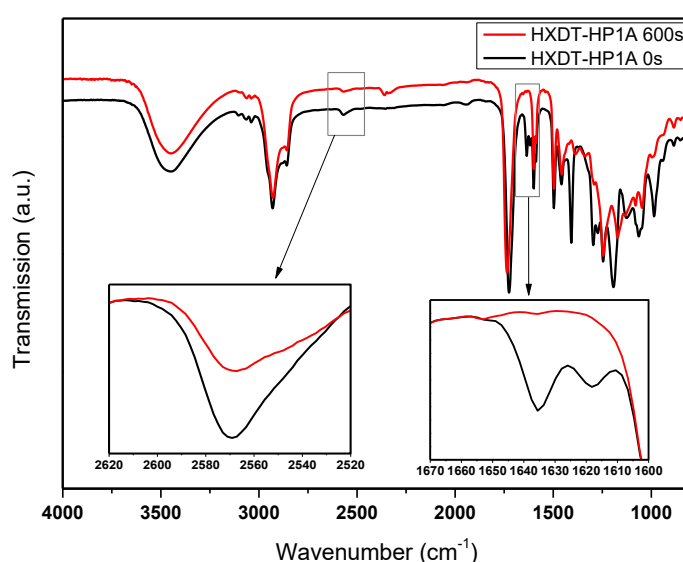
Figure 37. FTIR spectrum of the uncured (0 s) and fully cured (600 s) HXDT-HP1A resin formulation under visible light illumination. Inset plots represent the focused and zoomed regions of thiol (2570 cm^{-1}) and acrylate (1635 cm^{-1}) absorption peaks [135].

In all three resin formulations, a higher final conversion of the acrylate groups (95% - 97%) was observed in contrast to the conversion of the thiol groups (48% - 55%) (Figure 38a). This is due to the fact that the photocuring of thiol-acrylate resins follows a mixed-mode photopolymerization mechanism, where the acrylates participate in both chain-growth (homo-polymerization) and step-growth polymerization reactions [319].
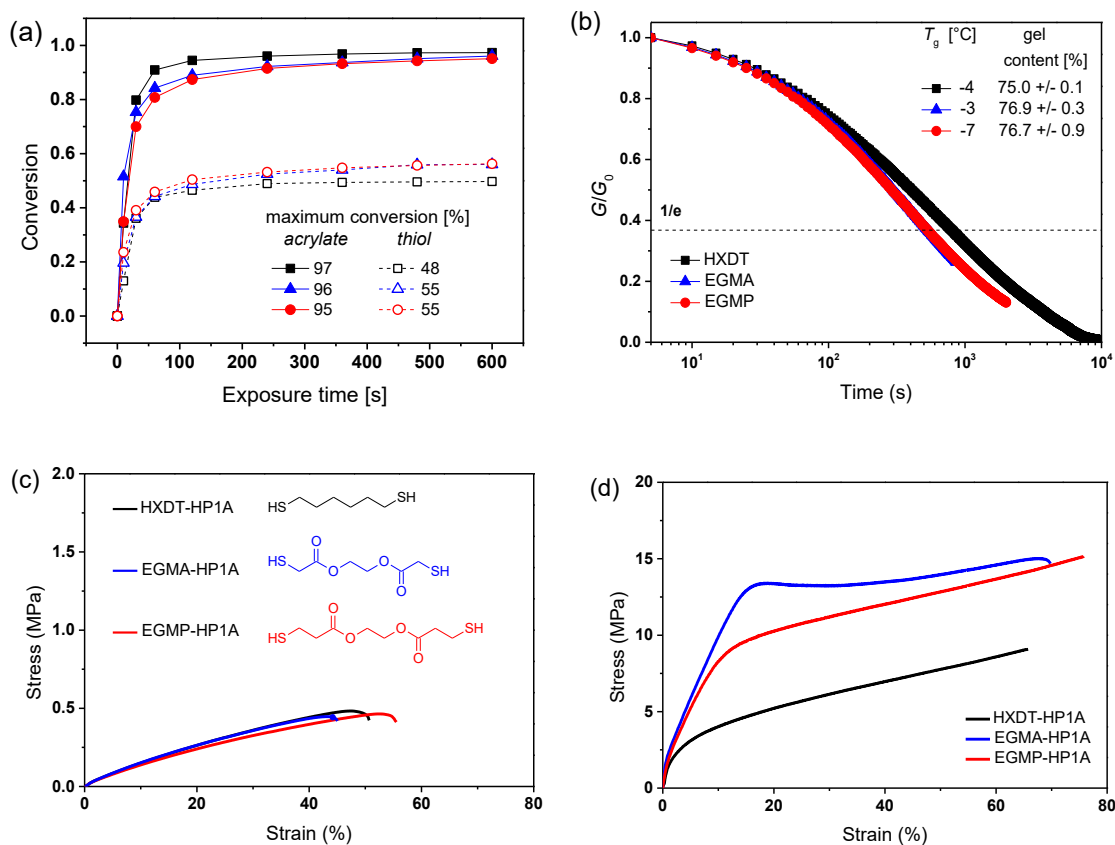
Figure 38. (a) Cure kinetics and final monomer conversions of acrylate groups at 1635 cm^{-1} (represented by solid symbols) and thiol groups at 2570 cm^{-1} (represented by hollow symbols) as a function of light exposure. Bi-functional thiols such as HXDT-HP1A (represented by black squares), EGMA-HP1A (represented by blue triangles), and EGMP-HP1A (represented by red circles) were utilized as thiol crosslinkers. (b) The stress relaxation curves of thiol-acrylate vitrimers normalized (G/G$_o$) and measured at 180 °C. The inset table displays the glass transition temperature (T$_g$) and gel content of the corresponding networks. The stress-strain behavior of thiol-acrylate vitrimers containing various bi-functional thiols (c) before and (d) after undergoing thermal annealing at 180 °C for 4 hours [135].

Chain-growth polymerization results into a sharp rise of molecular weight, while the step-growth polymerization process leads to the generation of lower molecular weight segments and prolongs the network gelation, reduces the shrinkage stresses and forms a more homogenous

network [23,122,123,320,321]. It is also important to note that the thiols can also act as chain-transfer agents during the chain-growth polymerization of the acrylates, which can also move the network gel point towards higher reaction conversions. Typically, the homo-polymerization rate of acrylates in thiol-acrylate reactions is 1.5 times greater than the thiol group's hydrogen abstraction rate [322].

While comparing the curing kinetics of a number of di-functional thiols, we observed that in the presence of the aliphatic thiol (HXDT), the thiol-acrylate network is formed having a faster acrylate conversion and lower final thiol conversion (HXDT-HP1A) in contrast to EGMA, as mercapto-acetic ester counterpart. The presence of ester moieties in EGMA, impacts the reactivity of -SH bonds and enhances the ability to undergo hydrogen abstraction reactions [23].

Moreover, the replacement of EGMA with EGMP did not lead to a considerable deviation in the curing kinetics and the ultimate monomer conversion of the thiol-acrylate vitrimers. It's also worth noting here that in these di-functional thiol-based networks, the majority of the crosslinking was achieved by the homopolymerization of the bi-functional acrylates (i.e. DG2A). This is also due to the fact that bi-functional thiols act as chain extenders and are known to increase the molecular weight among crosslinks [323,324].

The gel content of the networks was determined by immersing cured test specimens in dichloromethane for 48 hours and subsequently measuring the residual weights of the dried samples. All three thiol-acrylate networks exhibited a gel content ranging from 75.0% to 76.9%, indicating a comparable crosslink density. The incomplete conversion of the reacting species, specially the thiols, results in a lower gel content of the network, leading to the extraction of unreacted monomers during swelling. These residual thiols acted as lubricants and together with the flexible thioether bonds formed by the thiol-ene reaction, imparted significant mobility into the networks, resulting in a T_g between -4°C and -7°C (Figure 38b).

As a next step, circular discs with a 10 mm diameter and a thickness of 1 mm were 3D-printed for determining the characteristic stress relaxation and the effect of ester groups on exchange kinetics in dynamic photopolymers. The stress relaxation tests were conducted at 180 °C and the resulting curves are shown in Figure 38b. The characteristic time for stress relaxation in vitrimers was determined when the normalized modulus ($G_{(t)}/G_0$) reached 37% of its initial value [128,136]. For EGMA-HP1A and EGMP-HP1A, it was reached within 535 s and 530 s respectively, while HXDT-HP1A experienced a slower stress relaxation rate and it took 765 s until the ($G_{(t)}/G_0$) reached 37%. Despite similar crosslink density and the T_g of all three

networks, the slower relaxation rate in HXDT-HP1A can be attributed to the absence of ester groups in its building block of the network. The availability of functional groups such as -OH and ester groups is crucial for bond exchange reactions relying on transesterification, and a lower concentration of these groups leads to a slower exchange rate [2].

In addition to the networks' stress relaxation, the influence of ester moieties on the mechanical properties of the thiol-acrylate vitrimers was investigated. DLP 3D-printed test specimens were subjected to uniaxial tensile testing. All three networks exhibited a tensile strength below 0.5 MPa (Figure 38c). After thermal annealing at 180 °C for 4 h prior to the tensile test, all three networks exhibited a significant increase in both tensile strength and ultimate elongation (Figure 38d). Interestingly, the increase was more prominent in case of EGMA-HP1A and EGMP-HP1A (15 MPa), in comparison to HXDT-HP1A having and a tensile strength of 9 MPa.

Typically, the enhanced toughness of the network is due to the thermo-activated topological rearrangement and the related decrease in shrinkage stress. Prior research has demonstrated that thermal treatment can also enhance hydrogen bonding, leading to increased tensile properties [325,326]. The superior performance of EGMA-HP1A and EGMP-HP1A is likely due to their higher number of ester groups, which accelerates stress relaxation kinetics and intensifies hydrogen bonding with the network's -OH groups.

In order to increase the crosslinking points in thiol-acrylate vitrimers, multi-functional thiols were introduced in place of di-functional thiols, including two tetra-functional thiols (PTTMP and PCLMT) having a variable bond-spacer length and ester moieties as well as a hexa-functional 3-mercaptopropionate (DPTHMP). Here, the molar ratio of acrylate monomers HP1A and DG2A was kept constant within the formulations.

The results from the FTIR kinetics studies demonstrate that the increase in thiol functionality leads to a decrease in thiol and acrylate bond conversions (Figure 39a). This outcome is typical of radical-mediated thiol-ene reactions, in which the photopolymerization kinetics is governed by the diffusion limitation of reactive monomers. An increase in thiol functionality causes the gel point conversion to occur at an earlier stage in conversion, resulting in a reduction of the polymerization rate due to diffusional restrictions [323]. The utilization of oligomeric thiols with lengthy and flexible spacers resulted in higher conversions since the oligomeric radicals can primarily approach one another via segmental diffusion or propagation [2]. As the reaction

progresses and crosslink density increases, the propagation reactions' movement of radical sites becomes much quicker compared to the segmental diffusion.
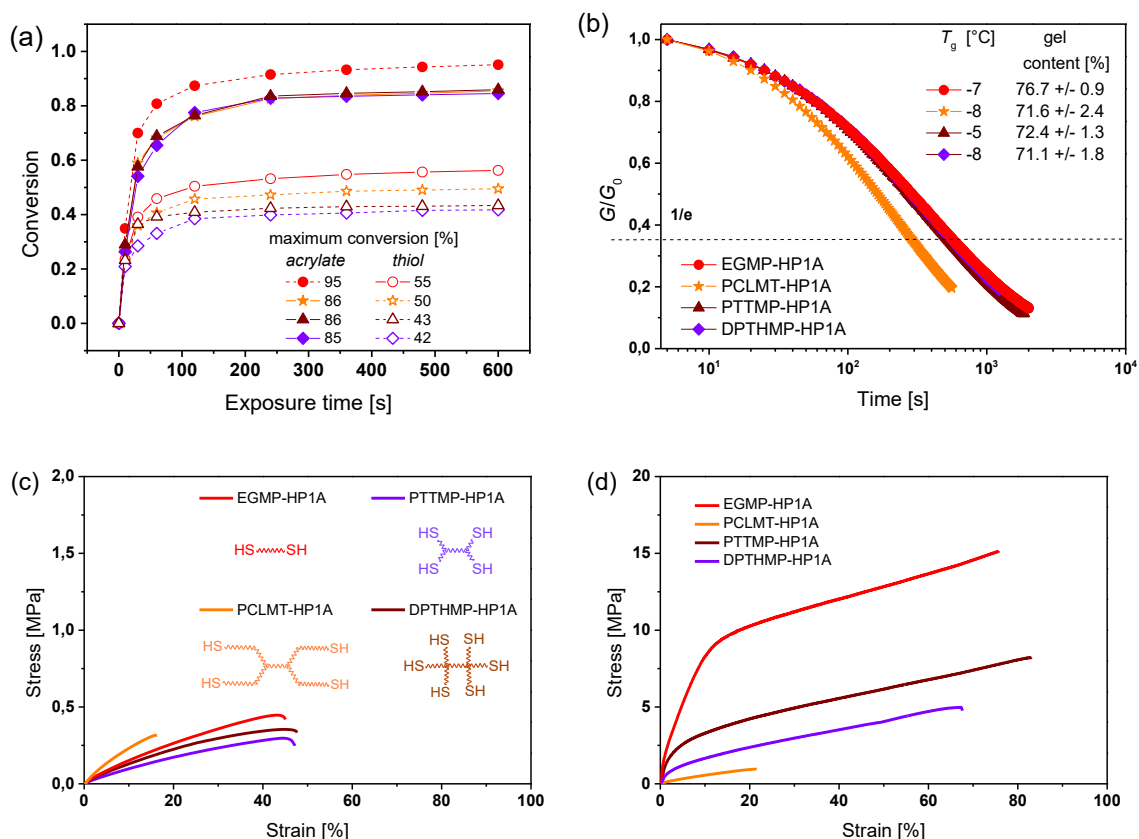
Figure 39. (a) FTIR results presenting the photo-curing kinetics and final monomer conversions of acrylates at 1635 cm^{-1} (indicated by filled symbols) and thiol groups at 2570 cm^{-1} (hollow symbols) as a function of light exposure time. Multi-functional thiols, including EGMP (red circles), PCLMT (orange stars), PTTMP (brown triangles), and DPTHMP (violet diamonds), were used as thiol crosslinkers. (b) The stress relaxation curves of thiol-acrylate vitrimers obtained at 180 °C and normalized as G/G_o are shown. Inset table provides the T_g and gel content of the respective networks. Stress-strain curves of thiol-acrylate vitrimers containing various multi-functional thiols measured (c) before and (d) after thermal annealing for 4 hours at 180 °C [135].

The formulation PCLMT-HP1A yielded higher thiol conversions (50%) compared to PTTMP-HP1A (43%) due to the polycaprolactone-based spacers between thiol groups, which significantly increased the crosslinker's flexibility. The conversion of the thiol groups in DPTHMP-HP1A (42%) was lower than formulations containing tetra-functional and bi-functional thiol due to the excess stochiometric ratio of thiol moieties with respect to the bonded acrylates (1.5:1). The higher viscosity of DPTHMP-HP1A formulation also contributed to the

diffusion limitations in the system, causing slightly lower conversion of acrylate and thiol groups. Regarding the mobility of the network, the rise in thiol functionality did not had a noteworthy impact on the T_g of the crosslinked networks. The T_g only slightly decreased from -5°C (for EGMP-HP1A) to -8°C (for DPTHMP-HP1A) (Figure 39b). The gel contents obtained with the multi-functional thiols resulted in lower monomer conversion compared to EGMP-HP1A and ranged between 71.1% and 72.4% [135].

EGMP, PTTMP and DPTHMP had an equimolar ratio between ester and thiol functional groups. The stress relaxation kinetics of these networks were similar, and the relaxation times were between 490 - 515 s (Figure 39b) [135]. In contrast, PCLMT comprised of a molar ratio of ester to thiol groups of 3:1, resulting in networks with more active ester groups. This caused faster relaxation kinetics and reduced the characteristic relaxation time to almost half (270 s), in contrast to the other thiols under investigation. These findings are consistent with the stress relaxation data presented in Figure 39b, which demonstrates the significance of the number of functional ester groups in the bond exchange kinetics of dynamic thiol-acrylate photopolymers.

Although increasing the functionality of the thiols could not enhance the mechanical properties of the thiol-acrylate vitrimers at room temperature. The multi-functional thiol-based formulations suffered from a lower breakage stress of 0.5 MPa with a corresponding ultimate elongation ranging from 18 to 55% (Figure 39c). PTTMP-HP1A and DPTHMP-HP1A networks improved in toughness after thermal annealing for 4 hours at 180 °C, although not to the extent of EMGA-HP1A [135].

Conversely, PCLMT-HP1A had a fast transesterification exchange rate but poor tensile properties that were not significantly improved even by subsequent thermal annealing at 180 °C (Figure 39d). These outcomes may be attributed to the plasticization of the networks, which becomes a dominant mechanism at higher concentrations of non-reacted thiols [135,327].

3.2.2. Influence of acrylate cross-linker on photopolymerization kinetics and characteristics of thiol-acrylate vitrimers

In order to investigate the effect of acrylate monomers on the thermo-mechanical properties and stress relaxation kinetics of thiol-acrylate vitrimers, the functionality of the acrylate monomers was varied. As described earlier, the functionality of the thiols was found to have no significant effect on the T_g and stress relaxation kinetics of the vitrimers. Therefore, in the subsequent step, HP1A was replaced by tri-functional PT3A and tetra-functional PT4A, which do not contain any -OH moieties in their chemical structure. This resulted in EGMA-PT3A and

EGMA-PT4A photopolymer networks, having a lower number of free hydroxy moieties but a higher crosslink density than the HP1A counterparts. EGMA was chosen as the thiol crosslinker in these resin formulations, and its content was kept constant [135].
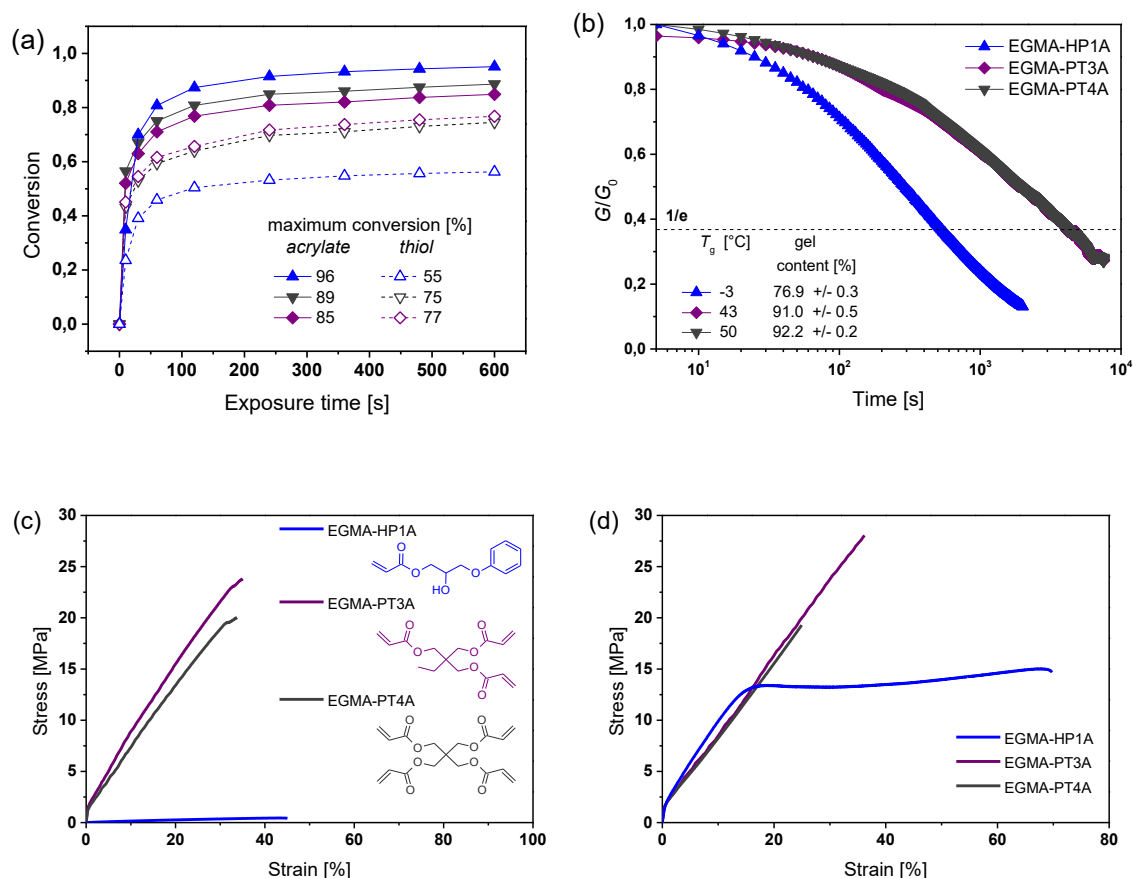
Figure 40. (a) FTIR experiments providing photopolymerization kinetics and final monomer conversions of acrylates at 1635 cm^{-1} (filled symbols) and thiol groups at 2570 cm^{-1} (hollow symbols), with respect to light exposure duration. The concentration of DG2A (25 mol%) was held constant, while additional acrylate monomers of different functionality were used: EGMA-HP1A (blue upward triangles), EGMA-PT3A (purple diamonds), and EGMA-PT4A (dark grey downward triangles). (b) The stress relaxation curves of thiol-acrylate vitrimers, measured at 180 °C, and normalized as G(t)/G$_o$. Inset table presents the corresponding network's glass transition temperature (T$_g$) and gel content. The stress-strain curves of the thiol-acrylate vitrimers containing acrylate monomers with varying functionality were obtained (c) prior to and (d) after a thermal annealing at 180 °C for 4 hours [135].

The analysis of FTIR results exploited that the initial reaction rates of both acrylates and thiols improved with growing functionality of the acrylate, as they consisted of a greater number of unsaturated bonds per monomer available for the crosslinking (Figure 40a). This was reflected

in a higher acrylate conversion for EGMA-PT3A and EGMA-PT4A (both above 50%), compared to EGMA-HP1A (35%), after 10 seconds of light exposure. The improved kinetics observed in chain-growth reactions induced by radical mechanisms caused a quicker onset of gelation and an increase in crosslink density. This increase in crosslink density was evident through a significant rise in both T_g (from -3 to 50 °C) and gel content (from 76.7 to 92.2%) for EGMA-PT3A and EGMA-PT4A. However, the associated restrictions over diffusion, slowed down the reaction and decreased the final monomer conversion. This was demonstrated by the decline in final acrylate conversions and reduced the yield of acrylate homo-polymerization.

On the other hand, the increase in the final thiol conversions from 55% (in EGMA-HP1A) to 77% (in EGMA-PT4A) was mainly due to a lower stoichiometric ratio of thiols to acrylate (1:2 and 1:5 in EGMA-HP1A and EGMA-PT4A respectively) functional groups (Figure 40a). This resulted in a higher number of thiol groups reacting with the surplus acrylate moieties present in the EGMA-PT3A and EGMA-PT4A formulations [328].

Furthermore, with the increase in acrylate conversion and functionality, the pace of acrylate homo-polymerization decreased, while the step-growth reaction between thiol and acrylate groups took precedence as the primary mechanism. Moreover, the exchange kinetics of transesterification was notably hampered due to the higher crosslink density and the reduced number of -OH groups (as illustrated in Figure 40b).
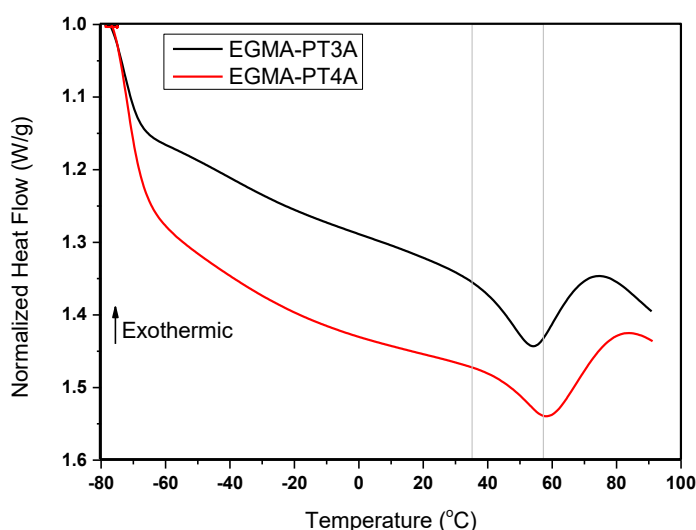
Figure 41. Normalized heat flow curves of numerous thiol-acrylate monomers with EGMA. The glass transition temperature was obtained by estimating the middle point between the tangent lines from the onset and transition-end regions [135].

During stress relaxation experiments EGMA-HP1A required only 530 s to relax 67% of its initial applied stress, while the relaxation times for EGMA-PT3A and EGMA-PT4A networks were 10 times higher in magnitude corresponding to 4825 s and 4350 s, respectively. Additionally, EGMA-PT3A and EGMA-PT4A exhibited significantly high stiffness compared to the EGMA-HP1A due to their higher crosslink density and lower number of –OH groups, as also indicated by their DSC curves in Figure 41.

This resulted in an ultimate elongation of only 12% and 19% with a tensile strength of 24 MPa and 20 MPa, respectively (Figure 40c). The impact of all these factors was also evident in the tensile properties of the thermally annealed samples (4 hours and 180 °C), which only showed minor improvement. Specifically, the tensile strength of EGMA-PT3A increased from 24 to 28 MPa, while that of EGMA-PT4A remained almost the same (Figure 40d). These findings suggest that the mechanical properties of thiol-acrylate vitrimers are influenced by multiple parameters, including network crosslinking density, residual un-reacted monomers, and the characteristic structure of the monomers, including the number of ester and –OH groups that undergo thermally induced transesterification exchange reactions.

3.2.3. Influence of thermal annealing on the thiol-acrylate vitrimers

Previous research has shown that subjecting thiol-acrylate vitrimers to a prolonged treatment at 180 °C does not only result in rearrangements in their topology but also in the creation of supplementary hydrogen bonds and crosslinking [128,325]. This results in a stiffer network and a reduced number of free –OH groups, which slows down the stress relaxation process, but also significantly improves the mechanical properties, including tensile strength and elongation. Similar findings were also reported by Zhang et al., who have investigated the properties of pristine acrylate vitrimers prior to and after thermal treatment [296].

In order to investigate the impact of thermal annealing on the intermolecular interactions, two resin formulations, namely EGMA-HP1A and EGMA-PT3A, were chosen and disc-shaped samples were 3D-printed (10 mm x 0.4 mm) and subjected to a thermal annealing at 180 °C for 4 hours under air without any applied force. A comparison of the ATR FTIR spectra of the annealed and non-annealed samples was made (Figure 42 and Figure 43) to assess any changes in the intermolecular interactions.
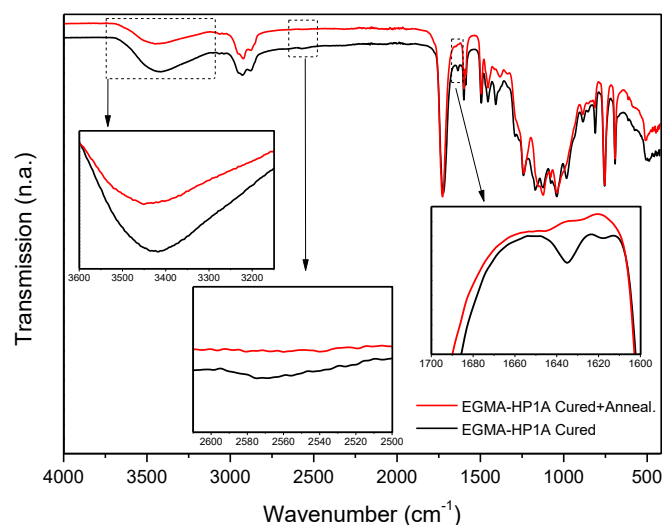
Figure 42. ATR FTIR spectra of EGMA-HP1A prior to and after thermal treatment (180 °C for 4 h) [135]. Inset rectangles present zoomed -OH group region, -SH group region and -C=C- group regions.

The results showed a slight increase in the conversion of thiols (2520 cm^{-1}) and acrylates (1635 cm^{-1}) during thermal annealing, but a significant decrease in the peaks related to hydroxy group (-OH) between 3200-3600 cm^{-1}, which indicates the formation of hydrogen bonds. This increase in the extent of hydrogen bonding also explains the significant increase in the elongation and stress at break values of EGMA-HP1A, as shown in Figure 42.
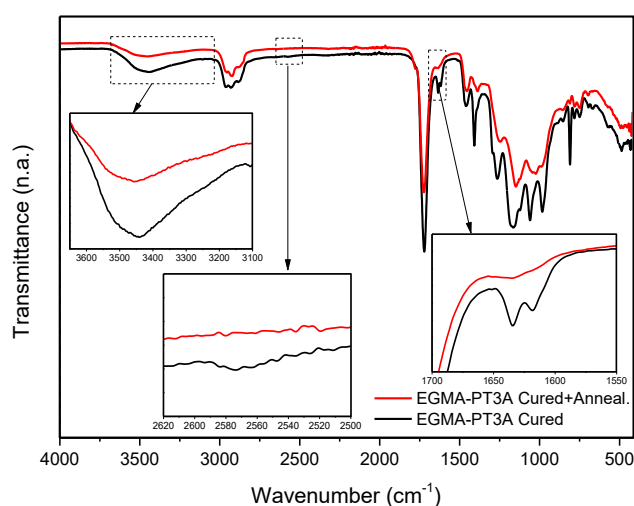
Figure 43. ATR FTIR spectra of EGMA-PT3A prior to and after thermal treatment (180 °C for 4 h) [135]. Inset rectangles present zoomed -OH group region, -SH group region and -C=C- group regions.

Furthermore, the rise in gel content, which is more noticeable in the EGMA-HP1A network that is more pliable (increasing from 76.9% to 89.1%), compared to the stiffer EGMA-PT3A system (increasing from 91.0% to 96.1%), supports the hypothesis of the change in crosslink density. This change in crosslinking density can occur due to a higher quantity of un-reacted thiols present in the EGMA-HP1A network, which are susceptible to form disulfide links in the presence of oxygen. Despite disulfides being a promising chemistry for the development of vitrimer networks [296,326,329–331], the results of stress relaxation experiments (Figure 44), exhibit that the newly added crosslinks are not dynamic in nature and slow down the stress relaxation kinetics of thiol-acrylate networks.

The effect of thermal annealing is even more noticeable in case of EGMA-HP1A, which undergoes a significant increase in the gel content. This is because of the further creation of permanent bonds that reduce the mobility of the network, as evidenced by the rise in T_g from -3 °C to 21 °C (Figure 44). EGMA-PT3A exhibited a comparable behavior with a rise in T_g from 43 °C to 55 °C. The decreased mobility, coupled with a reduction in available free hydroxy groups on account of additional hydrogen bonding, causes slower exchange kinetics and less effective stress relaxation. Specifically, for EGMA-HP1A, the time required to relax 67% of the initial stress increased from 530 s to 1,810 s after thermal annealing, while for EGMA-PT3A, it increased from 4,825 s to 10,900 s (Figure 44). Particularly important to highlight here is that overall ranking of the networks does not vary after thermal treatment.
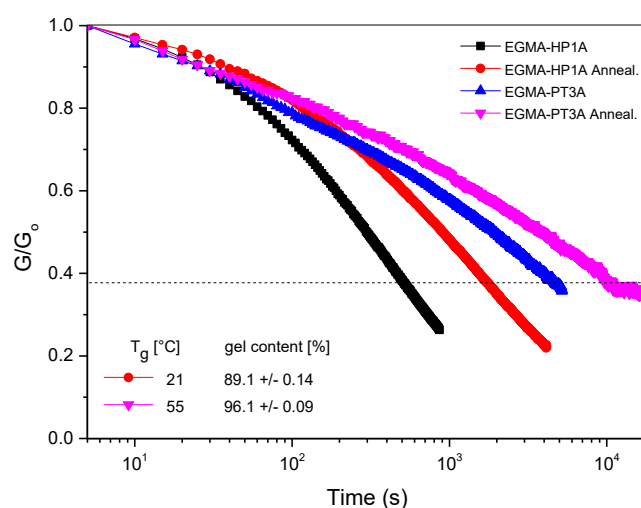
Figure 44. Stress relaxation kinetics of thiol-acrylate vitrimers with thermal annealing and without annealing measured at 180 °C (4 hours). Inset table indicates the gel content and glass transition temperature (T_g) of the thermally annealed networks [135].

3.2.4. 3D-Printing resolution of thiol-acrylate vitrimers

EGMA-PT3A's low viscosity (measured at a shear rate between 0.1 and 300 s^{-1}, resulting in 330 mPa·s), fast curing speed and satisfactory storage stability enabled the DLP 3D-printing of objects, as illustrated in Figure 45a, b, and c, with structure sizes up to 200 μm. Additional 3D-objects produced with EGMA-PT3A using DLP 3D-printing are presented in Figure 45d. To evaluate the healing performance, the test specimens were also printed using EGMA-PT3A with DLP 3D-printing.
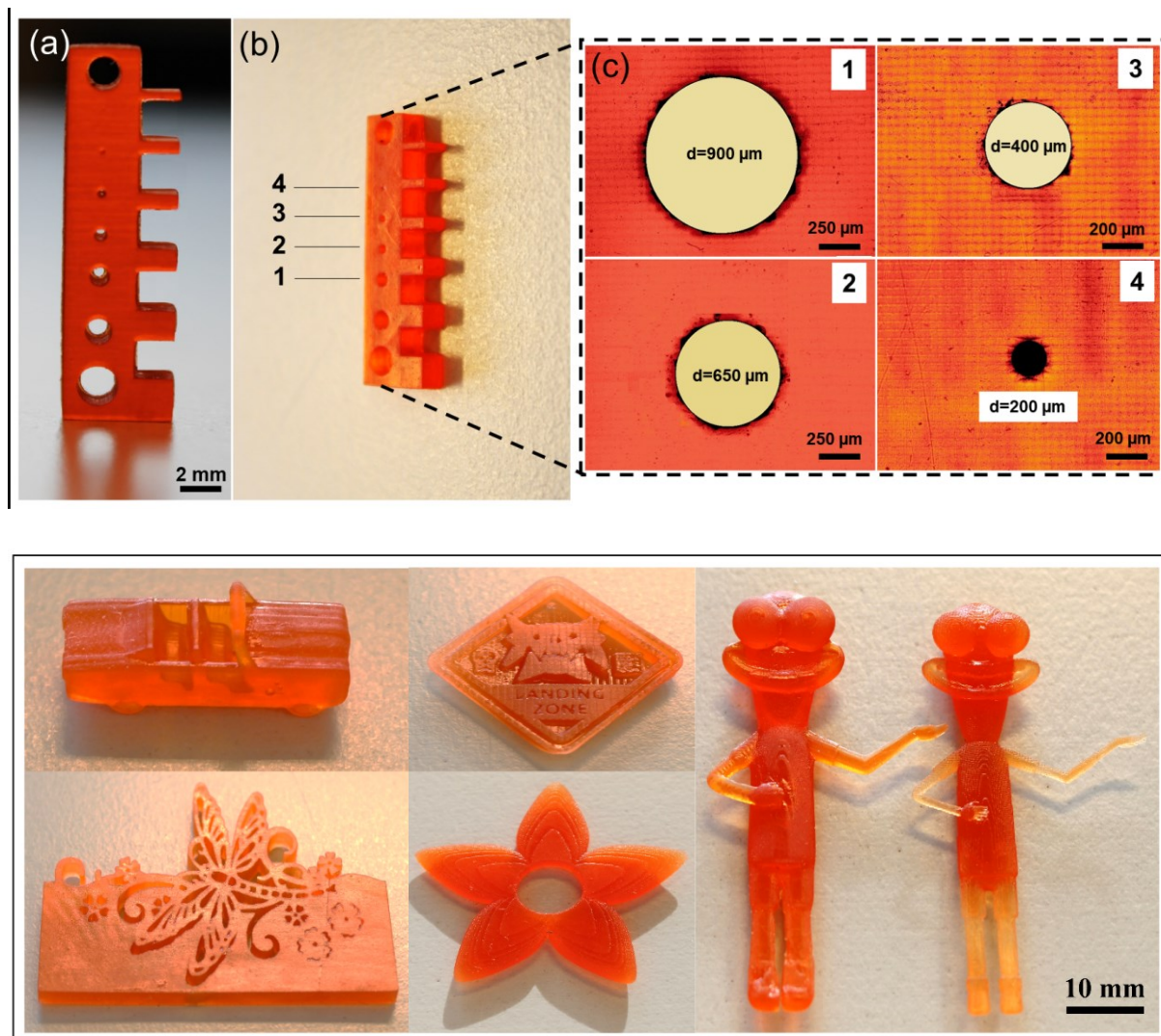
Figure 45. (a,b) Comb structures with a range of circular wholes to determine the resolution of DLP 3D-printing with EGMA-PT3A resin. (c) Observation of cavities under the optical microscope for determination of printing resolution. (d) Complex structures to show the applicability of developed resin in further applications [135].

3.2.5. DLP 3D-printing of active devices and thermal healing

EGMA-PT3A and EGMA-PT4A are the thiol-acrylate vitrimers that had a T_g above room temperature. Out of the two, EGMA-PT3A was selected to print a soft active device as it had a better tensile strength. To conduct the thermal actuation experimentations, a spring actuator measuring 15 mm in diameter and 50 mm in length was 3D-printed using DLP technology (refer to Figure 46a). In the programming step, a weight, which was twice as heavy as the actuator, was attached to the spring and the device was heated to 65 °C (refer to Figure 46b).
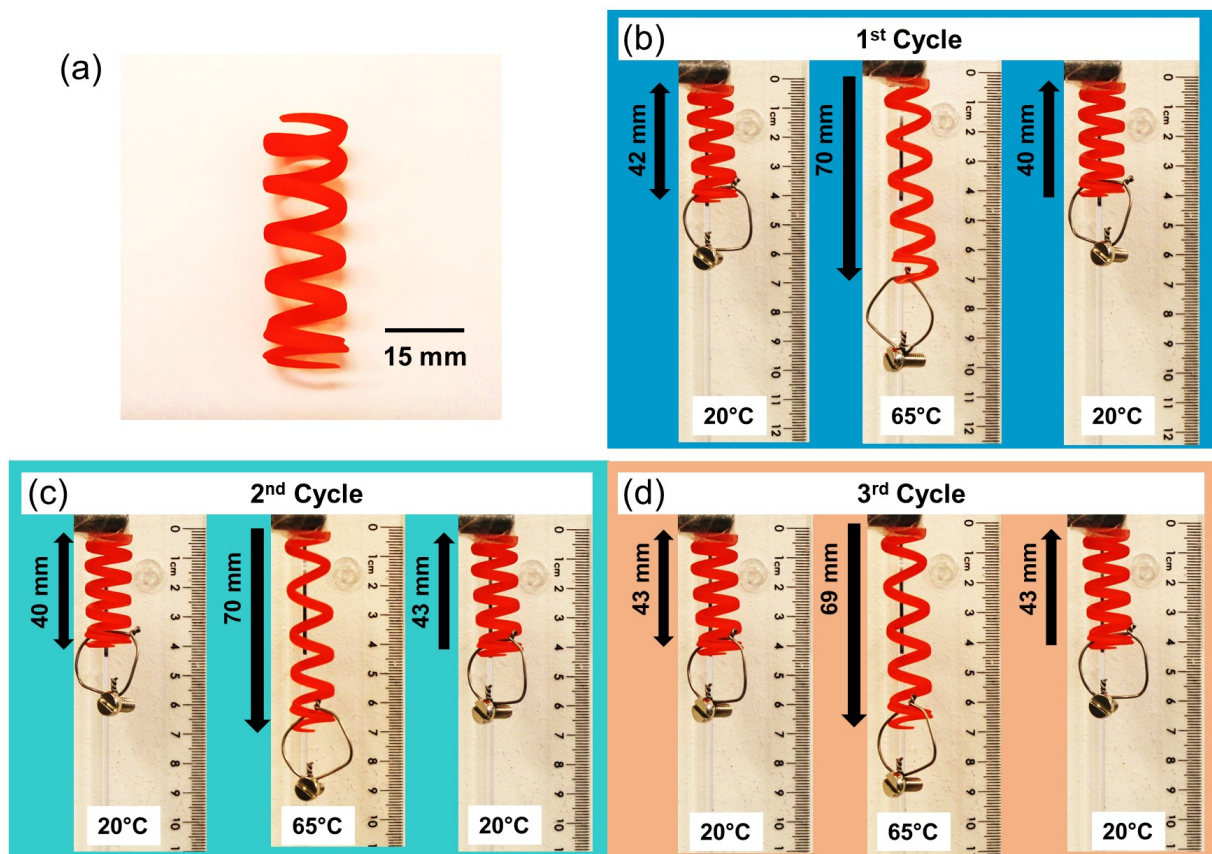
Figure 46. (a) Spring actuator fabricated by DLP 3D-printing of resin EGMA-PT3A. (b) Attaching a weight (2.9 g) to the actuator (1.5 g), leading to a deformation of the spring, when heated till 65 °C. Retraction back of spring to its original shape by cooling the actuator to 20 °C and with ability to carry the weight upward. Repeated transitions of the spring by switching the temperature: (c) second actuation cycle (d) third actuation cycle showing a full recovery of the original shape of the spring [135].

As a result of the actuator softening above its T_g (43 °C) and a corresponding decrease in its elastic modulus, the spring was able to stretch to an elongation of approximately 70%. Although the tensile tests indicated that EGMA-PT3A had limited stretchability (ultimate elongation of 36%), the helical shape of the 3D-printed actuator allowed for larger deformations. When the

actuator was cooled down to 20 °C, the spring was able to lift the attached weight and return almost to its original position within 60 seconds (Figure 46b) because of the increase in elastic modulus below the T_g. This experiment was repeated several times, and the original helical shape was completely recovered each time (Figure 46c and Figure 46d).

During the programming step of a subsequent experiment, the actuator was intentionally stretched beyond 80% of its initial length, causing the spring to break (as shown in Figure 47a). One advantage of vitrimers is their ability to flow and reshape when heated above T_v, making it possible to use thermal healing to repair damage of 3D-printed objects. Despite the fact that the EGMA-PT3A network had a slow exchange rate due to its higher crosslink density and low number of hydroxy groups, the viscoelastic reflow was still effective in thermally healing the broken spring when heated at 180 °C for 4 hours (as presented in Figure 47a). The thermally healed spring was successfully reprogrammed and could lift the same weight and underwent multiple performance cycles.
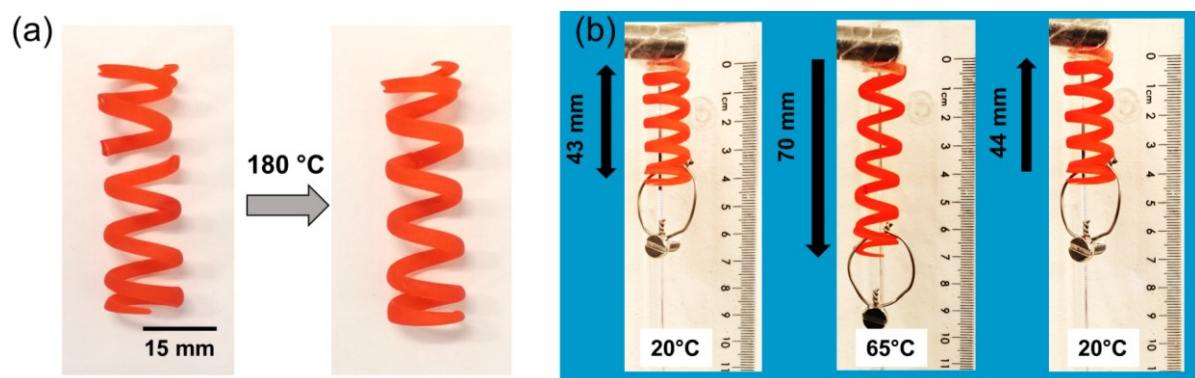
Figure 47. (a) Thermal healing of DLP 3D-printed spring actuator at 180 °C for 4 hours. (b) Performance of the healed spring actuator during programming and recovery of permanent shape [135].

To analytically determine the effectiveness of the healing process, the tensile strength of DLP 3D-printed test specimens was measured before and after thermal annealing. For this purpose, circular-shaped samples with a hole in the center and a circular-shaped counterpart were printed, which was inserted into the hole during the repair process (Figure 48a). The samples were then thermally annealed at 180 °C for 4 hours and compared to a defect-free control bar to assess the tensile properties. It was found that the healing process was highly effective, as the original elongation was fully restored and the tensile strength of the healed test specimen was even slightly higher than that of the control sample (Figure 48b).
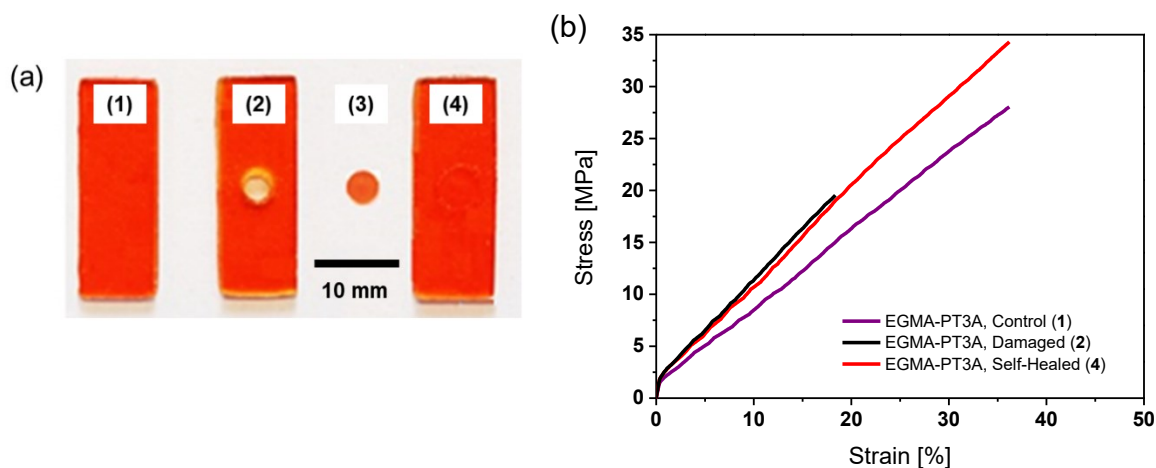
Figure 48. (a) Images of the DLP 3D-printed test specimen obtained from EGMA-PT3A: (1) defect-free control sample, (2) damaged sample with circular-shaped cavity in the center, (3) circular shaped counterpart for thermal healing and (4) healed test specimen after fitting the circular shaped counterpart in the hole and subsequent thermal treatment at 180 °C for 4 hours. (b) Stress-strain properties of the control, damaged and thermally healed (180 °C for 4 hours) samples [135].

3.3. Conclusions

The research study extensively investigated a range of thiols and acrylate monomers to determine their suitability for use in DLP 3D-printing of vitrimeric thiol-acrylate networks. By systematically assorting the monomers' structures, ester moieties and monomer functionalities, comprehensive correlations between their properties and the photo-reactivity, thermo-mechanical characteristics and network adaptability of DLP 3D-printed vitrimers were established. It was found that the number of ester moieties does not only enhance the curing kinetics but also boosts the stress relaxation rate of thiol-acrylate vitrimers, leading to an improved performance of the dynamic network after thermal annealing for 4 hours at 180 °C. On the other hand, increasing the functionality of thiols or acrylate monomers slowed down the network curing process on account of the diffusion restrictions in the mixed mode photopolymerization. Although the thiol functionality had a negligible impact on the T_g of the investigated networks (-5 °C to -8 °C), replacing the mono-functional acrylate by the tetra-functional acrylate significantly increased the T_g from -7°C to 50°C. While higher T_g networks exhibited a moderate stress relaxation kinetics, healing experiments demonstrated that the original properties of DLP 3D-printed test specimens can be fully restored by thermally treating the EGMA-PT3A networks for 4 hours at 180 °C. Leveraging the excellent resolution of the

DLP 3D-printed specimens (successfully replicating a structural size of 400 μm), soft actuators were subsequently printed having the capability of repeatedly lifting an object weighing twice as much as the actuator itself. By thermally exposing the actuator above its T_g (43 °C), the spring actuator endured up to 70% elongation and could revert to its original shape upon lateral cooling below the T_g. Furthermore, the actuator retained its functionality even after damage and thermally induced healing (180 °C).

4. Development of multi-material 3D-printed networks using dual-vat 3D-printing

This section presents the data and findings that were exploited for the development of multi-material DLP 3D-printed thiol-click vitrimers. The resin formulations described in the previous chapter of the thesis [135] were further exploited in a novel processing methodology as multi-material DLP 3D-printing. The development led to novel applications in soft robotics, where shape memory and thermal healing were integrated as additional features in multi-material DLP 3D-printed structures.

4.1. Materials and methods

4.1.1 Development of resin formulations

The resin formulations used for the development of multi-materials were taken from the previously published article [135] and discussed in the thesis in section 3.3.1. Two formulations with varying T_g and stiffnesses were used for the printing of soft and hard domains and are shown in Table 6. Both of the formulations contained 10 wt.% Miramer A99, 2 wt.% BAPO, and 0.05 wt.% pigment (Sudan II for EGMA-PT3A, while Eriochrome Blue-Black and Mordant Blue for EGMA-HP1A).

Table 6. Resin formulations used for the DLP 3D-printing of multi-material dynamic structures.

Formulation ID	Acrylate 1 (wt.%)	Acrylate 2 (wt.%)	Thiol (wt.%)	Thiol:Acrylate
EGMA-HP1A	HP1A (50%)	GD2A (25%)	EGMA (25%)	1:2
EGMA-PT3A	PT3A (50%)	GD2A (25%)	EGMA (25%)	1:4

4.1.2. Dual-vat DLP 3D-printing

A prototype from Way2Production (Austria), equipped with a visible light illumination system (405 nm), two different resin vats and an intermittent cleaning station was applied. To DLP 3D-print test specimens, the bottom layer was exposed for 15 seconds, followed by the subsequent layers illuminated for 10 seconds. Both resin vats were assigned the same illumination settings and after curing of one layer in the vat, the platform was raised up to 70 mm height and automatically cleaned on a cleaning station, consisting of a sponge foam (dimensions: 170 mm x 110 mm x 50 mm, L x W x H) for resin removal and printed structure's surface scrubbing, prior to the 3D-printing with the second resin vat. The multi-material 3D-printing was carried

out at room temperature, with a layer thickness of 100 μm using a rising and retracting speed of 5 mm/s.

4.1.3. Network evolution with multi-material 3D-priting

To determine the network evolution in multi-material 3D-printer, FTIR spectrums of the uncured resins and 3D-printed samples were measured with the Vertex 70 FTIR spectrometer equipped with a diamond attenuated total reflection (ATR) unit. Circular disks having a diameter of 10 mm and a thickness of 0.4 mm were DLP 3D-printed and FTIR-ATR spectrums were taken between 4000 cm^{-1} and 800 cm^{-1}. Bond conversions were estimated using normalized peak areas of characteristic acrylate and thiol peaks at 1635 cm^{-1} and 2570 cm^{-1} respectively, by using OPUS software.

4.1.4. Shape memory and thermal healing

Shape memory and thermal healing experiments were performed on a range of 3D-printed structures. Initial experiments were performed on a honey comb structure (29 mm x 25 mm x 4 mm), consisting of inner domains of EGMA-HP1A, with top and bottom regions formed using EGMA-PT3A resin formulation. Honey comb was compressed along y-axis at -10 °C along with a deformation force and kept deformed for 20 minutes to obtain the programmed shape. Subsequent heating of the specimens till room temperature led to the recovery of structure in 60 seconds.

The second step involved the experimentation of a cubical architecture (10 mm x 10 mm x 10 mm) evolved one-half from the EGMA-HP1A resin and the second-half using EGMA-PT3A resin formulation. The soft part of the structure was deformed and cooled up to -10 °C for 20 minutes in a freezer. The programmed structure was later on allowed to return back to its original position by exposing to room temperature without any mechanical force. For the permanent deformation, the cubical structure was deformed and placed in an oven at 180 °C for 4 hours to obtained the 2nd programmed shape.

A separate cube structure was intentionally broken from one corner and reformed into a triangle, and pressed between two metal clamps. The new geometry in the clamped state was placed in an oven at 180 °C for 4 hours resulting into thermal healing of the structure and fixed the new shape of the material.

Finally, shape memory experiments were also carried out on a multi-material gripper, consisting of inner soft teeth (EGMA-HP1A) and outer stiffer periphery (EGMA-PT3A) with an overall

(outer) diameter of 42 mm. The gripper was heated above 50 °C to become soft and malleable above T$_g$, and a compressed shape (26 mm) was programmed followed by a cooling to room temperature. The gripper was laterally heated using a heat gun and the original shape was recovered within 30 seconds. Thermal healing experiments were also performed on the same multi-material gripper, and was cut at an angle of 45 °C using a sharp knife from one end. The damaged samples were brought together and a proper contact of the damaged surfaces was ensured. Subsequently, the damaged samples were pressed between 2 glass plates and heated in an oven at 180 °C for 4 hours under a weight of 800 grams.

4.2. Results and discussion

4.2.1. Network development using dual-vat DLP 3D-printing

For dual-vat DLP 3D-printing, EGMA-PT3A and EGMA-HP1A resin formulations were selected from the previous studies (Chapter 3), as these resin formulations offered a great potential to form multi-materials with widely different stiffnesses, thermal and mechanical properties. A dual-vat DLP 3D-printer (Figure 49) with moving vats and an intermittent cleaning station was used for the printing of the multi-material functional devices.
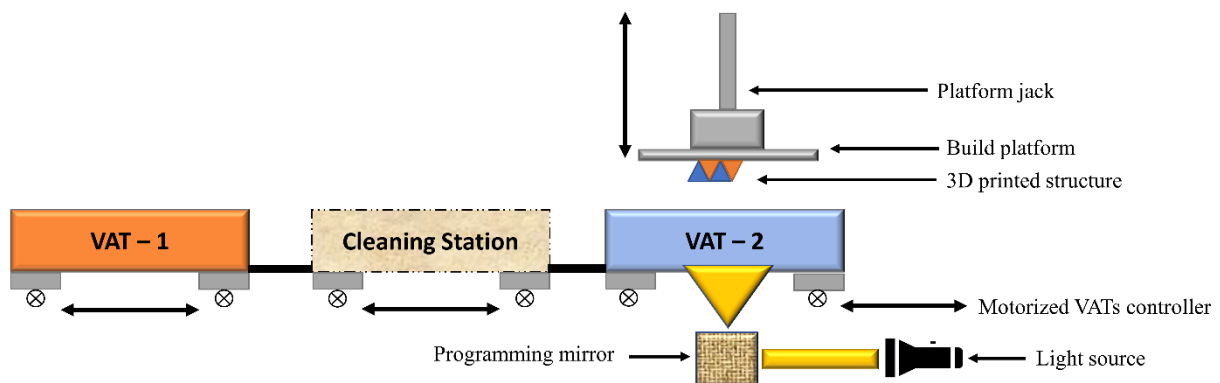
Figure 49. Dual-vat DLP 3D-printer, with mobile vats controlled by a motorized controller. A single light source was programmed and linked to each vat, and the vats were illuminated according to the adjusted settings. During vat exchange a cleaning station containing a foamy soft sponge was utilized to clean the printed materials attached to the platform, before moving to next vat.

After curing of the defined material layer on the platform, the platform raised automatically to a safe distance (z-axis: 70 mm above zero-point) and the corresponding vat was exchanged with the cleaning station. At the cleaning stage, a sponge was fitted having 50 mm height and the platform was adjusted to retract into the sponge until it penetrated to a depth of 10 mm, and

made a good surface contact by gently pressing the sponge foam's top-surface, and subsequently shearing 25 mm in the left and 25 mm in the right directions, while being in the pressed condition. This step ensured a good cleaning of the printed specimens as well as the building platform by rubbing the platform and the printed article's surface with the cleaning foam. After each printing activity, the sponge was washed with isopropanol solvent and replaced with a new sponge after every 2 printing jobs. After the cleaning, the platform was raised up again to a height of 70 mm, and the next resin vat was slid into the printing position. The whole process was continued until the required number of layers and the multi-material design was fully printed.

Furthermore, the curing times were adjusted based on the IR kinetics results predetermined in the section 3.2.1, and discussed earlier. To analyze the bond conversion of the resin formulations after DLP 3D-printing, ATR-FTIR measurements were performed with the uncured resins and the cured samples. In both resin formulations, the acrylate bonds (1635 cm^{-1}) reached a higher conversion corresponding to 96% for EGMA-HP1A and 86% for EGMA-PT3A (Figure 50 and Figure 51). While the -SH bonds reached a final conversion of 56% and 67% in the resin formulations respectively. The higher conversion of acrylates in both cases is confirmed by the mixed mode reaction mechanism of acrylates, which are involved in the homo-polymerization reactions, as well as the chain transfer reactions with the thiol groups, leading to the step-growth polymerization.
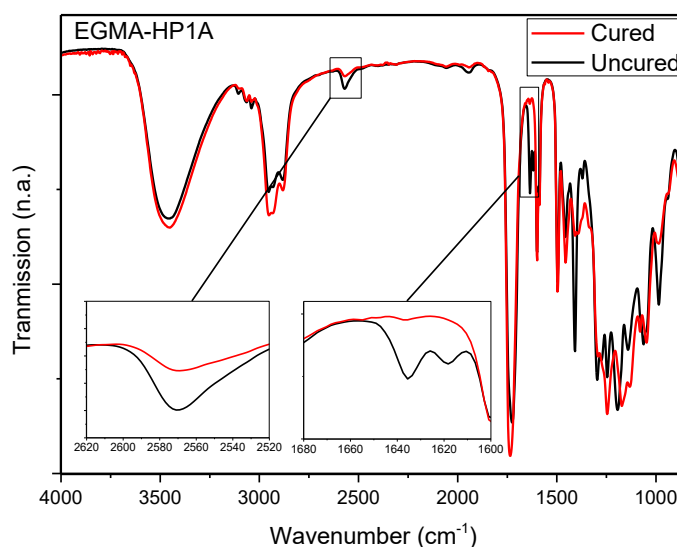
Figure 50. FTIR-ATR spectra of EGMA-HP1A resin formulation before curing and after curing in the multi-material 3D-printer.

As the functionality of acrylate is increased from mono-functional moieties to tri-functional moieties, the molar ratio of the thiol moieties per acrylate moiety is also reduced i.e. 1:2 in EGMA-HP1A and 1:4 in EGMA-PT3A, leading to a better participation of thiol bonds in the overall network formation as described earlier in chapter 3. Hence a higher conversion of thiol groups is achieved in EGMA-PT3A (67%) then EGMA-HP1A (56%), also reducing the overall conversion of acrylate moieties up to 86%, which are now more pronouncedly engaged in step-growth polymerization reactions.
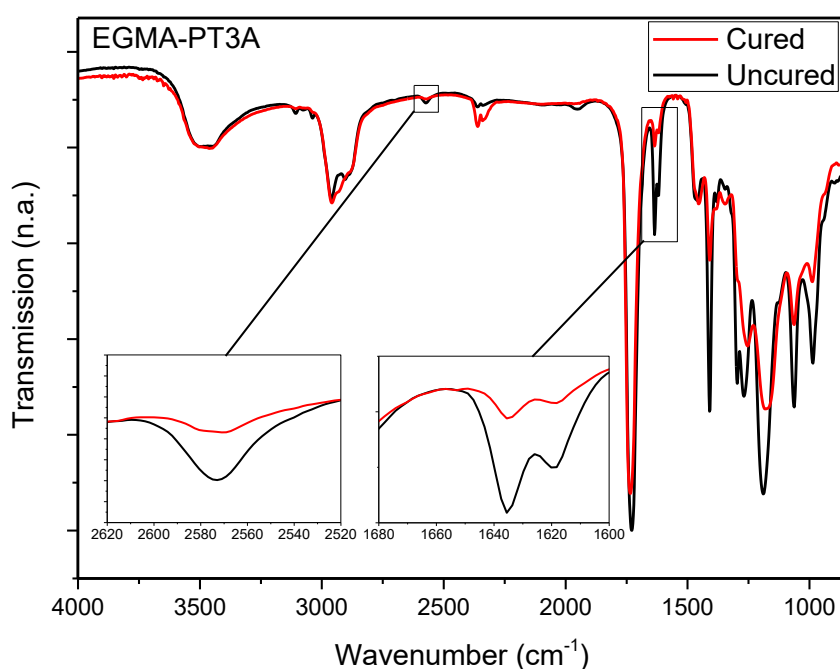
Figure 51. FTIR-ATR spectra of EGMA-PT3A resin formulation before curing and after curing in the multi-material 3D-printer.

4.2.2. 3D-printing of multi-material prototypes

To take advantage of the multi-material setup and exploit the material properties, circular structures (diameter of 30 mm and thickness of 2 mm) were initially 3D-printed with single resin formulations (EGMA-PT3A and EGMA-HP1A) separately. The differences in the network's properties in terms of glass transition temperatures (43 °C for EGMA-PT3A and -3 °C for EGMA-HP1A) and mechanical properties, were demonstrated in a hydraulic press in which both circles were pressed under a piston and bench assembly. Being the stiffer network EGMA-PT3A, could not bear a noticeable deformational strain and broke quickly under compression (Figure 52).
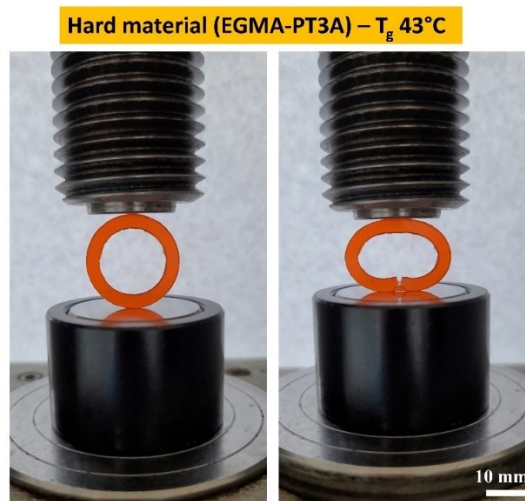
Figure 52. Single circle specimen prepared from DLP 3D-printing of EGMA-PT3A and compressed in a hydraulic press to undergo deformation tests.

On the other hand, EGMA-HP1A networks which were previously characterized with high flexibility, could endure significant deformation under the same hydraulic compression arrangement. Figure 53 presents the single circle EGMA-HP1A specimen, undergoing deformations. The sample was flexible enough to undergo a full compression before damaging, which provided concrete support to our hypothesis and both resin materials were combined in the subsequent multi-material 3D-printing.
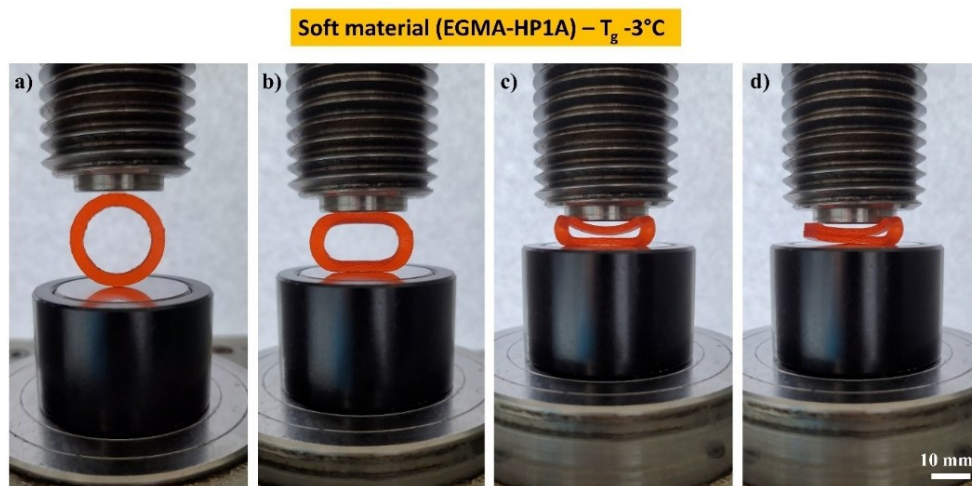
Figure 53. Single circle specimen prepared from DLP 3D-printing of EGMA-HP1A, and compressed in a hydraulic press to undergo deformation tests. Sequence of events during compression testing is presented from left to right.

As a next step, a double wheel structure was designed (Figure 54), having an inner supporting circle of 20 mm diameter (thickness = 2 mm). The main idea was to provide structural integrity

with the inner circle, printed using the stiffer EGMA-PT3A formulation. While the outer circle with connecting arcs (d = 42 mm, w = 2 mm) was printed with the soft EGMA-HP1A. Such an arrangement could mimic the functional traits of an automobile wheel, where inner parts provide structural strength while the outer parts act as soft and damage resilient segments providing adequate compression, shock absorption and abrasion resistance.
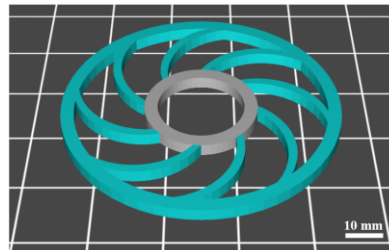
Figure 54. Model design of double-wheel structure containing an inner ring made from the hard material, and the outer ring and connecting arcs of the flexible network.

DLP 3D-printing of resin formulations was subsequently carried out with the dual-vat 3D-printer, and the multi-material wheel was fabricated (Figure 55). Physical compression experiments were performed under the same arrangement in a hydraulic press and it was observed that the soft domains (EGMA-HP1A) had an exceptional compression ability without any damage, and multiple compression and retraction cycles could be undertaken by the wheel (Figure 55). However, the hard-inner ring (EGMA-PT3A) remained intact and maintained its structural features without presenting any deformation.
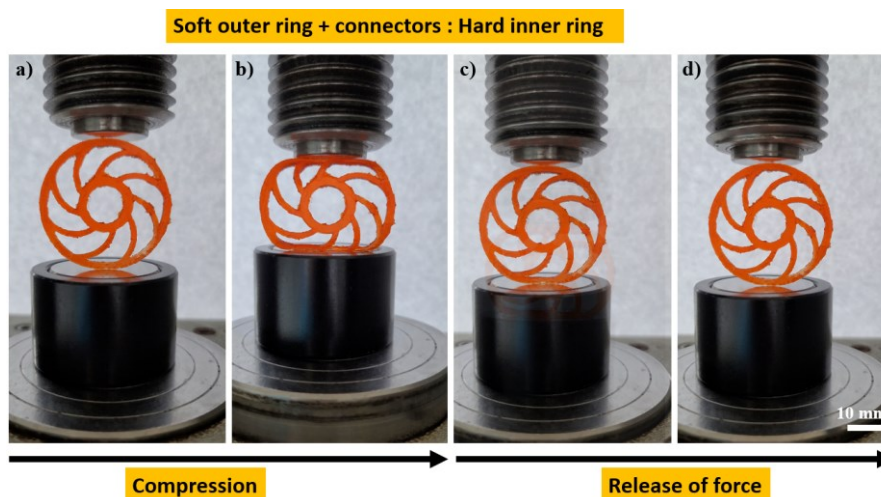
Figure 55. Circular wheel specimen prepared from the DLP 3D-printing of EGMA-HP1A (soft outer part) and EGMA-PT3A (hard inner part) compressed in a hydraulic press to undergo deformation tests. (a,b) Sequence of events during physical compression testing. (c,d) Sequence of events during retraction, by release of force.

To demonstrate the printing of more complex multi-material objects, shape memory experiments were performed on a DLP 3D-printed honey comb structure. The outer parts of the honey comb were printed with the stiff formulation to provide support and integrity, while the inner structure was printed with the flexible network. Figure 56 presents the three-dimensional geometry of the multi-material honeycomb.
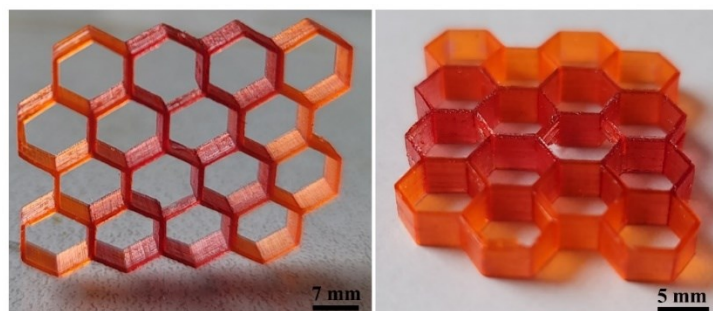
Figure 56. Multi-material DLP 3D-printed honeycomb structure using EGMA-PT3A (outer stiff regions), and EGMA-HP1A (inner soft regions).

The programming of the as-printed structure was carried out by applying compression along the y-axis and fixing the compressed structure in a deep freezer at -10 °C for 20 minutes. The programmed shape was subsequently exposed to room temperature which led to the recovery of the as-printed shape in 60 seconds (Figure 57).
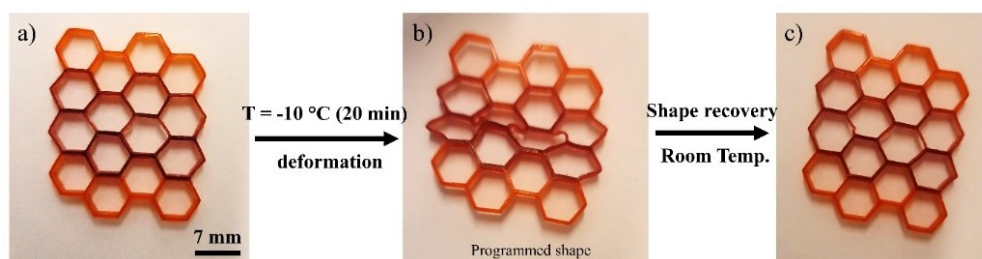
Figure 57. (a) As-printed DLP 3D-printed honeycomb structure with outer regions of EGMA-PT3A and inner regions of EGMA-HP1A. (b) Programmed shape of the honeycomb structure obtained after compression for 20 min at -10 °C. (c) Recovery of the as-printed shape by heating the honeycomb structure to room temperature.

Additionally, a cubical structure was multi-material DLP 3D-printed using both resin formulations (Figure 58a). The first programmed shape was obtained after localized deformation of the soft regions for 20 minutes at -10 °C. The original structure was recovered at room temperature (Figure 58b and c). Furthermore, the developed dynamic thiol-acrylate networks were formerly characterized by an efficient transesterification-based material reflow at 180 °C (Chapter 3). To take the advantage of malleability of the dynamic photopolymers, the

cubical structure was deformed from one side and placed in an oven at 180 °C for 4 hours, leading to a permanent deformation of the cubical structure (programmed shape – 2, Figure 58d).
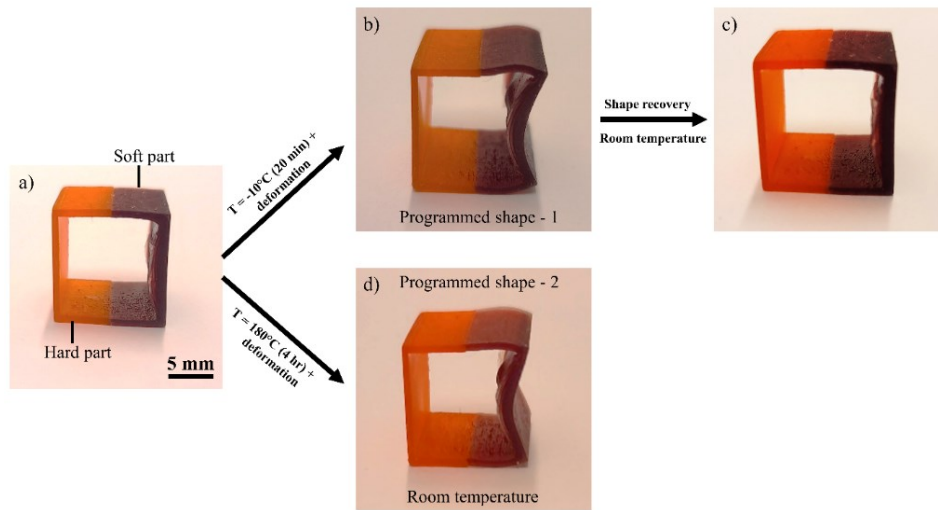
Figure 58. (a) Multi-material DLP 3D-printed cube using EGMA-PT3A and EGMA-HP1A resin formulations. (b) Programmed shape – 1 obtained by compressing the soft part of the cube and placing it in the freezer for 20 minutes at -10 °C. (c) Original shape recovery by heating the programmed shape to room temperature. (d) Permanent deformed shape – 2 obtained by compressing the soft regions and placing the object in the oven (under deformation) at 180 °C for 4 hours.

Advancing from the proof of concept studies, a multi-material gripper model (Figure 59) was printed with inner teeth of the softer material (EGMA-HP1A) and outer periphery of the stiff network (EGMA-PT3A). The concept was inspired by the basic design of human body parts i.e. hands which are a combination of hard bones, covered by hundreds of muscles, soft tissues and skin for gripping and compliance.
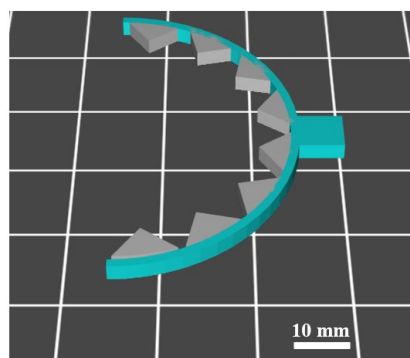
Figure 59. Model design of a gripper structure containing inner teeth of the soft material and the outer periphery of the stiff network.

In addition to the multi-material properties, the shape memory performance was used to grip and release objects. Due to the glass transition temperature of 43 °C for EGMA-PT3A, the structural programming and reshaping could be carried out above room temperature. Figure 60a, presents the structural features of 3D-printed multi-material gripper composed of EGMA-PT3A and EGMA-HP1A. The original width (x-axis dimension) of the gripper was 42 mm (Figure 60b) and it was possible to reshape the gripper by compression at 50 °C up to 26 mm without any damage. The gripper was removed from heat in the compressed shape and the network was fixed in the programmed shape at room temperature (Figure 60c).
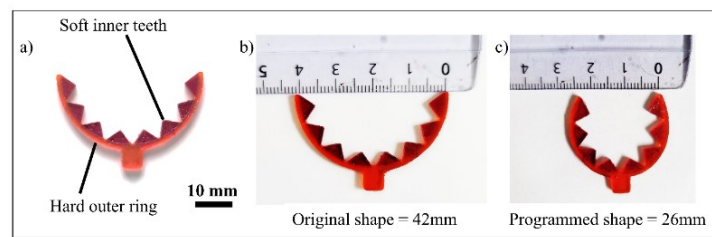
Figure 60. (a) Structural features of the DLP 3D-printed gripper with inner parts of the EGMA-HP1A and outer part from EGMA-PT3A resin. (b) Original dimensions of the 3D-printed gripper. (c) Programmed shape of the gripper.

To examine the gripping abilities, natural object that require a special care during pick-up and release stage was chosen, i.e. a strawberry, which could be easily damaged when pressed or crushed hardly. In the programmed shape (Figure 61b) of the gripper, the strawberry was lifted and held at room temperature without any damage (Figure 61c and d). Furthermore, by increasing the temperature above the stiff network's T_g with a heat gun, led to the shape recovery and subsequent release of the strawberry (Figure 61e and f)
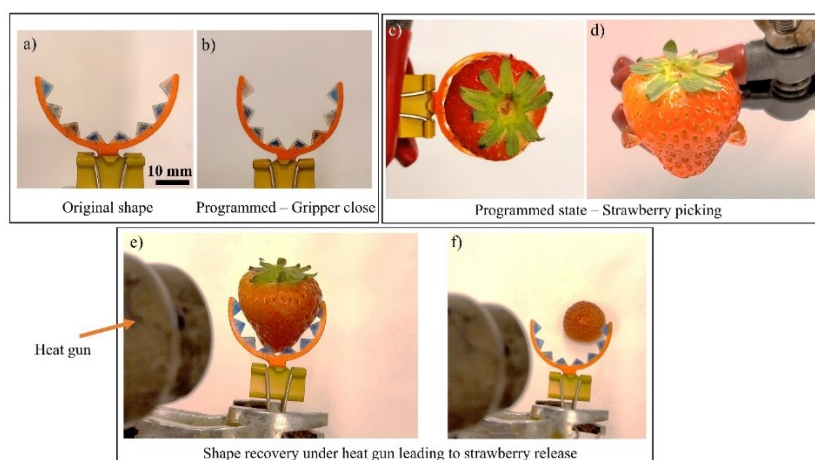
Figure 61. (a) Original shape of 3D-printed multi-material gripper with inner teeth of soft resin formulation (EGMA-HP1A) and outer domains of hard material (EGMA-PT3A). (b)

Programmed shape of gripper above T_g and fixed at room temperature. (c,d) Top and front view of the multi-material gripper carrying a strawberry. (e) Gradual heating of the gripper under a head gun and partial shape recovery of the gripper. (f) Full shape recovery of the gripper and release of strawberry.

4.2.3. Thermal healing of 3D-printed multi-material structures

Vitrimers possess the exceptional abilities to thermally reflow at sufficiently high temperature ($T > T_v$) and can rearrange their network topology. As previously discussed in section (3.2), the abundance of hydroxy and ester moieties in EGMA-HP1A and EGMA-PT3A, along with an efficient phosphate ester catalyst (Miramer A99) resulted in fast transesterification and stress relaxations up to 37% (1/e) of initial applied stresses in a time span of 9 minutes and 80 minutes at 180 °C, respectively.

To examine the thermal healing abilities in multi-material structures, the damage was initially induced in the hard domains of the cubical structure intentionally. The cube was then turned into a triangle and clamped between two metal clips. The clamped structure was placed in the oven at 180 °C for 4 hours and allowed to restructure under vitrimeric reflow Figure 62.
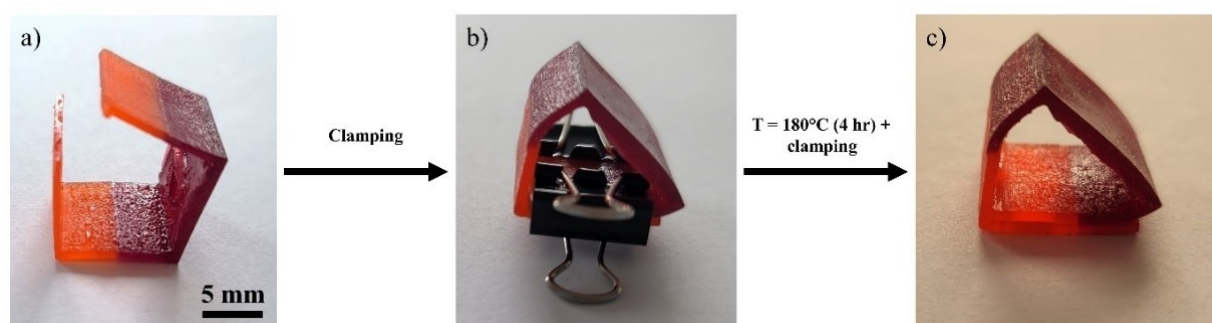
Figure 62. (a) Multi-material cube structure damaged at one corner. (b) Reshaped triangular structure clamped between two metal clips and heated in an oven at 180 °C for 4 hours. (c) Reshaped structure of the cube after 4 hours of thermal treatment.

Keeping in view these outcomes, the multi-material gripper was also cut using a sharp blade to induce damage in both soft and hard domains (Figure 63). The damaged sections were bought together to join physically, and were placed in between two glass plates. The glass plates were further pressed under 2 weights of 400 g each and placed in an oven at 180 °C for 4 hours (Figure 63).
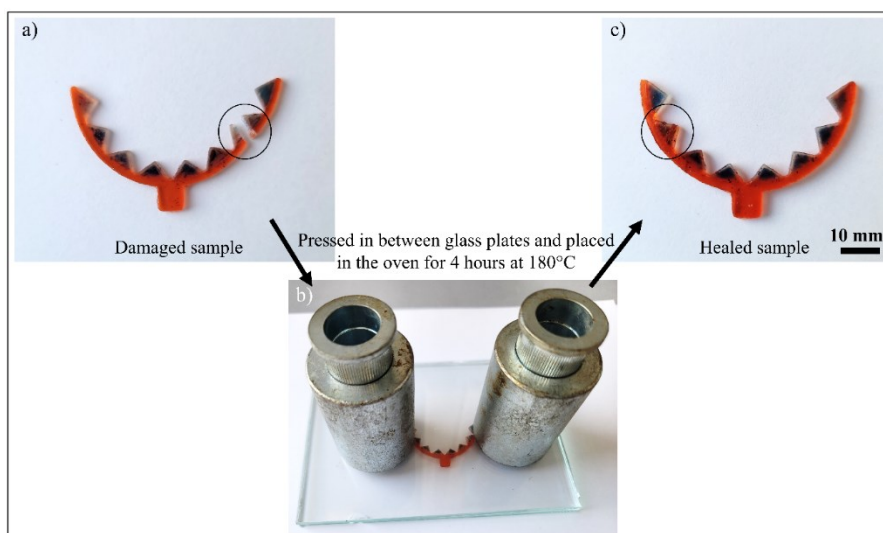
Figure 63. (a) Damaged multi-material 3D-printed gripper. (b) Joining the damaged gripper sections and pressing between glass plates and 800 g weight (180 °C for 4 hours). (c) Thermally healed multi-material gripper.

Thanks to the efficient transesterification reactions, the damaged section was fully healed after thermal treatment (Figure 64). To demonstrate the regained integrity and shape memory traits, gripping experiments were carried out with the thermally healed gripper. It was possible to achieve the same deformation (26 mm) and programming shape as of the original multi-material gripper (Figure 64). Furthermore, the healed gripper was also able to carry the weight of strawberry and lift it in the programmed conditions (Figure 64). The strawberry was subsequently released by applying temperature via heat gun, governed by the shape recovery of gripper.
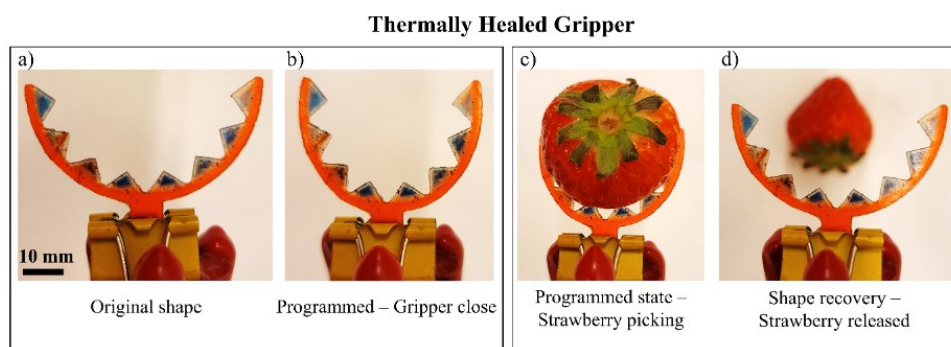
Figure 64. (a) Original dimensions of the thermally healed gripper. (b) Programmed shape of the multi-material gripper obtained by heating above 50 °C along with compression, followed by cooling to room temperature. (c) Strawberry picking by multi-material gripper in the programmed state. (d) Shape recovery of the healed multi-material gripper under temperature, leading to the release of strawberry.

4.3. Conclusions

In this research, the application of structure-property relationships in thiol acrylate vitrimers, led to the advanced fabrication of multi-material actuators using dual-vat DLP 3D-printing. Double wheel structures with internal hard domains (EGMA-PT3A) for structural integrity and the outer soft periphery (EGMA-HP1A) for shock absorbing and resilience were fabricated, which underwent multiple compression and retraction cycles. A range of multi-material structures including a honeycomb and cubical design were DLP 3D-printed and exhibited exceptional shape memory properties and structural re-orientations in localized regions. Furthermore, a multi-material gripper was fabricated, whose shape memory properties enabled carrying and releasing of dedicated soft objects like strawberries. The outer domains of the multi-material gripper were printed with EGMA-PT3A, which had a T_g of 43 °C and provided the shape transitions above room temperature, whilst the gripper contained soft inner teeth made from EGMA-HP1A (T_g amounted to -3 °C), which ensured a delicate gripping of the strawberries. The programming of the outer periphery of gripper above T_g led to the compression and gripping of the delicate objects, which were subsequently released, as the temperature was raised above glass transition resulting in the retraction of the grippers. The dynamic transesterification exchange reactions in the thiol-acrylate vitrimers were further exploited to thermally heal damages in the multi-material structures. During thermal treatment (180 °C for 4 hours), the multi-material cubical structure as well as the gripper could undertake macroscopic reflow leading to the damage healing. Healed multi-material gripper could further undergo multiple compression and retraction cycles with analogous gripping and releasing of strawberries, as of the original one.

5. Using photolatent catalysts for dynamic thiol-click vitrimers processable by dual-wavelength 3D-printing

This section presents data and findings that were published in the journal "RSC: Polymer" with the title "The effect of photolatent catalysts on the exchange kinetics of dual-wavelength 3D printable and photopatternable thiol-click vitrimers", in May 2023. The majority of the subsequent text, tables, and figures were extracted from the aforementioned publication [332]. Part of the experimental work including IR and UV-Vis spectroscopy, TGA and shape memory experiments were carried out by Elisabeth Rossegger.

5.1. Materials and methods

5.1.1. Development of resin formulations and DLP 3D-printing

Thiol-acrylate formulations were prepared by adding 50 mol% HP1A, 25 mol% DG2A, and 25 mol% TM3MP, along with 2 wt.% BAPO as photoinitiator. Each photoacid generator was dissolved separately in propylene carbonate (50 wt.%) at 50 °C using a magnetic stirrer at 500 rpm. 1.5 mol% of the photoacid generator (relative to the –OH groups within the resin formulation) was then added to the thiol-acrylate resin formulation and homogenized with a magnetic stirrer at 20 °C. In the printing experiments, Sudan II was added as a dye (0.05 wt%.) to the formulations to improve the resolution of the 3D-printed objects.

A prototype from Way2Production (Austria), equipped with two LED light sources (405 nm and 365 nm), was used for DLP 3D-printing. To prepare test specimens for stress relaxation experiments, the bottom layer was exposed to 405 nm light (4 mW.cm^{-2}) for 8 s and the subsequent layers illuminated at 405 nm for 6 s. The samples were post UV irradiated with a mercury emitter (Omnicure S1000, Lumen Dynamics, Canada) to activate the latent transesterification catalyst. The UV light intensity during activation of the samples was measured using an integrating radiometer (Powerpuck II, EIT Instrument Markets, United States) and was found to be 20 mW.cm^{-2} with wavelengths (λ) in the range of 250 to 470 nm.

Dual-wavelength DLP 3D-printed structures with spatial catalyst activation during printing were prepared, by exposing the bottom layers again to 405 nm light (with 8 mW.cm^{-2}) for 8 s, while subsequent layers were illuminated at 405 nm for 6 s. Meanwhile the catalyst in the desired layers during the printing process were also activated by irradiation at 365 nm (8 mW.cm^{-2}) for 10 s.

5.1.2. Fourier-transform infrared spectroscopy

The Vertex 70 FTIR spectrometer (Bruker, United States) was used to determine the cure kinetics of the resins. 16 scans were accumulated in transmission mode across the range of 4000 cm^{-1} to 700 cm^{-1}, with a resolution of 4 cm^{-1}. The absorption peak areas were then calculated using OPUS software. For sample preparation, 1.5 µL of each formulation was drop-casted between two CaF$_2$ discs, and a zgood® wireless LED curing lamp was used to initiate the curing process, with a power density of 3.3 mW.cm^{-2} (λ = 420–450 nm). The bond conversion rates were then calculated using the OPUS software, based on the normalized intensity of absorption bands from acrylate -C=C (1635 cm^{-1}) and thiol -SH (2570 cm^{-1}).

5.1.3. UV/Vis light spectroscopy

A UV/VIS Spectrophotometer Cary 50 Conc (Varian Inc.) was used to conduct ultraviolet-visible spectrophotometry (UV/Vis). The absorption characteristics of all photoacid generators were measured in the range of 200 to 420 nm after being dissolved in acetonitrile (1 mol%).

5.1.4. Network properties evaluation

A Mettler Toledo (United States) TGA thermogravimetric analyzer was used to perform Thermogravimetric Analysis (TGA) under N$_2$ atmosphere. The samples were heated from 30 ° to 900 °C at a heating rate of 10 °C.min^{-1}.

The cured networks were analyzed using a Mettler-Toledo DSC 821e instrument (United States) to conduct Differential Scanning Calorimetry (DSC) measurements. The heating rate was set at 10 K.min^{-1}, and the samples were heated from -25 °C to 120 °C in a nitrogen atmosphere with a nitrogen flow of 20 mL.min^{-1}. Middle point of the heat flow from the second DSC heating cycle was exploited to determine the glass transition temperature (T$_g$) of the samples.

5.1.5. Stress relaxation and rheological measurements

The MCR 102 rheometer (Anton Paar, Austria) was used to perform stress relaxation analysis at various temperatures (140 °C, 160 °C, 170 °C, and 180 °C) on 10 mm diameter and 1mm thick samples, that were DLP 3D-printed. Prior to the measurements, the samples were equilibrated at the desired test temperature for 20 min at 20 N force in the rheometer. Following the equilibration step, a 3% step strain was applied and the stress decrease was recorded over time. Stress relaxation times were evaluated when the stress reached 37% of its initial value.

In order to obtain the viscosity of the formulations, a modular compact rheometer MCR 102 from Anton Paar (Austria) was utilized with a CP60-0.5/TI cone (49.97 mm diameter and 1.982° opening angle). Each measurement was conducted at 20 °C and the shear rate ranged between 0.1 and 300 s^{-1} using 1 mL of liquid resin formulation.

5.1.6. Shape memory experiments

Dual-wavelength DLP 3D-printed test specimens, including a rectangular shaped film, an open cube, a spring with a height of 60 mm and diameter of 25 mm, and a hand built up by a lattice structure, were utilized in shape memory experiments. The 3D-objects' specific regions were illuminated with 365 nm light to activate the photocatalyst, while other parts of the printed structures were exposed to 405 nm light. Erasing the thermal history was achieved by heating the samples to 160 °C for an hour. To set the initial shape, the samples were heated to 160 °C, deformed using external force, and maintained at 160 °C for two hours. The samples were then cooled to room temperature, and the external force was removed. Heating the printed test specimens at 45 °C, which was above the network's T_g (3 °C), facilitated selective shape recovery of the regions printed at 405 nm, which had no photo-induced activation of the transesterification catalyst.

5.2. Results and discussions

The introduction of a photolatent transesterification allows for a localized control of bond exchange reactions in dynamic photopolymers. Additionally, by using photo-reactive resin formulations, they can be conveniently processed by vat-based 3D-printing processes through local curing by light illumination [49]. To achieve this, the photolatent catalyst must meet various requirements, such as good dissolution in the resin formulation, good thermal stability above T_v, optical transparency to visible light irradiation for preventing premature activation during the photopolymerization process, and the efficient release of catalyzing species that accelerates bond exchange reactions.

Former research works have shown that onium salts satisfy these necessities and ensure the selective generation of strong Brønsted acids, that can proficiently catalyze transesterifications exchange reactions in thiol-acrylate vitrimers [137]. Among these salts, triarylsulfonium salts show special promises due to their low reduction potential for oxidizing photolytically generated radicals [333]. Unlike conventional acid-catalyzed transesterifications which could be easily controlled via pK_a of the acids, the application of photolatent acids more complex due to the factors affecting the formation of the catalyzing species, including the quantum yields

and absorption properties, which ultimately impact the photochemistry of the reacting components [283].

In this study, the performance of several triphenylsulfonium salts with different chemical structures was examined to study the catalytic activity of photoacid generators in dynamic thiol-click vitrimers in detail. When exposed to direct UV light, the triphenylsulfonium salts undergo heterolytic bond rupture of the sulfur-carbon bond, resulting in the formation of reactive carbocations (C^+) [334,335]. These cations can further react with monomers or solvents to create potent Brønsted acids, whose acidity is affected by the counter anion's chemical composition and properties. The acidity of the released acid is determined by the nucleophilicity and size of the anion, while the photochemistry of the triphenylsulfonium salt, including its absorption characteristics, molar extinction coefficients and quantum yields is governed by the cation's structure.

5.2.1. Impact of photolatent catalyst's counter anion

Initially, it was assessed how the counter anion affects the stress relaxation of a thiol-acrylate vitrimer, comprising of 50 mol% HP1A, 25 mol% DG2A, 25 mol% TM3MP, and 2 wt.% BAPO as a photoinitiator that absorbs in the long wavelength region (Figure 65). Following 405 nm light irradiation, a photopolymer network with a T_g of 3 °C was obtained, providing abundant hydroxy and ester moieties for consequential transesterification that can be activated by heat.
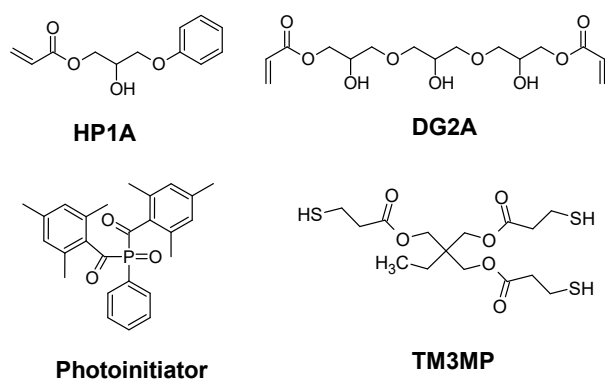
Figure 65. Components of the resin formulations, employed for the exploitation of the impact of photolatent acids [332].

To compare the performance of different photoacid catalysts, they were dissolved in propylene carbonate and added at a constant content of 1.5 mol% (relative to the free hydroxy groups in the network) to the monomers. Specifically, SpeedCure 992, which is a blend of triphenylsulphonium hexafluorophosphate and its bis-functional derivative, was compared to

SpeedCure 976s, which is its hexafluoroantimonate counterpart (Figure 66a). As the absorption properties of onium salts are largely controlled by the organic cation, both derivatives have a similar UV-Vis absorption spectrum (Figure 66b). They exhibit absorption peaks at 231 nm, 285 nm and 325 nm, and are transparent in the visible light region. Additionally, a triflate counterpart (4-phenylthiophenyl)-diphenylsulfonium trifluoromethane sulfonate (PDS-triflate) was used, which lacks bis-functional groups and therefore only has two absorption maxima at 234 nm and 300 nm. However, it is presumed that its photochemistry is analogous to the other two sulfonium salts.

It is important to use onium salts with anions that are not highly nucleophilic and do not coordinate in cationic polymerization or curing of epoxides to prevent termination reactions caused by the combination of anion and cation. Previous research has demonstrated that the curing kinetics and molar mass of corresponding polymer systems decreases as the nucleophilicity of the anions increases, with the order being $SbF_6^- > PF_6^- > CF_3SO_3^-$ [336,337]. Simultaneously, the generated Brønsted acid's acidity grows in the identical sequence, which is expected to have a direct impact on the transesterification rate.
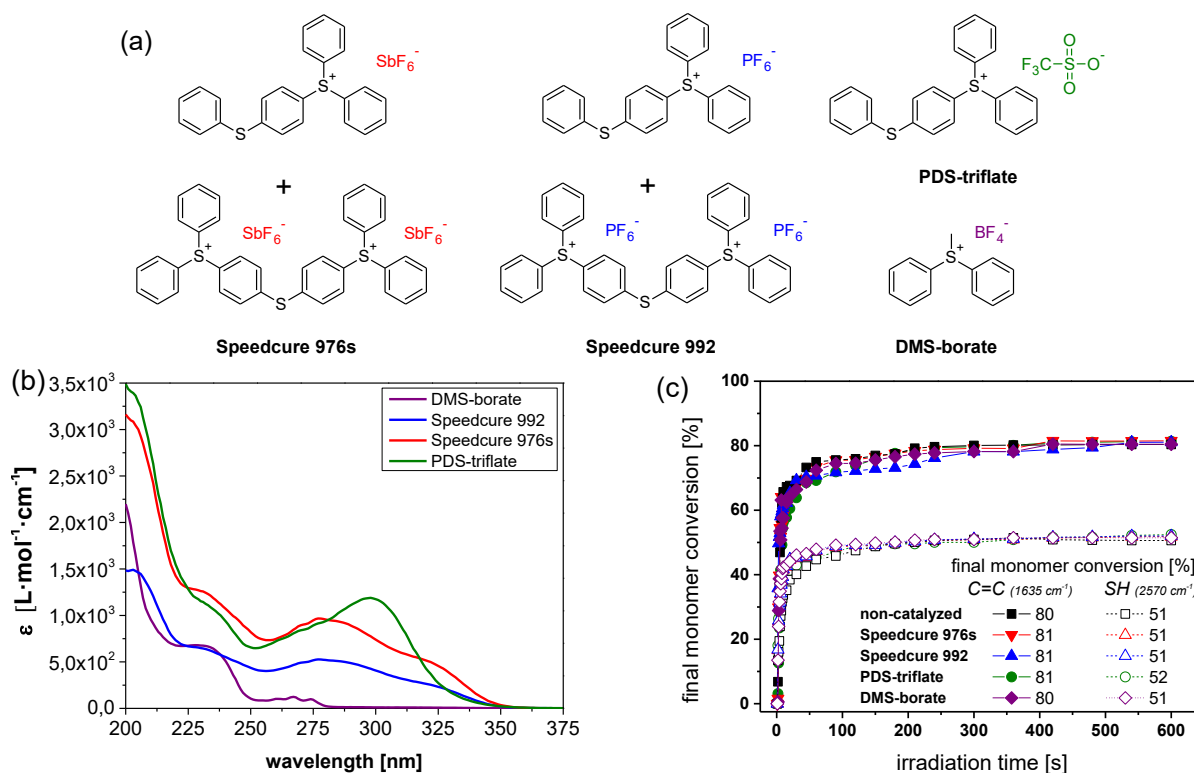
Figure 66. (a) Chemical structures of the photolatent acid generators. (b) UV-Vis spectra of triphenylsulfonium salts having various anions. (c) FTIR curing kinetics of the non-catalyzed and catalyzed formulations. The normalized areas of acrylate (1635 cm^{-1}) and thiol (2570 cm^{-1}) were determined and plotted versus time [332].

Since the photoacid generators being studied were only sensitive to short UV wavelengths (< 350 nm), they did not interfere with the visible light-triggered curing of the thiol-acrylate system. The curing studies also indicated that all catalyzed and non-catalyzed thiol-acrylate formulations had a similar rate of curing and identical ultimate conversions, as seen in Figure 66c. The ultimate conversion of acrylates (80-81%) was notably higher than that of the thiols (51-52%), because acrylates can also undergo homopolymerization via a chain-growth mechanism in addition to the step growth reaction between thiols and acrylates [338]. The depletion of the characteristic FTIR absorption bands of acrylate (1635 cm^{-1}) and thiol groups (2570 cm^{-1}) in the PDS-triflate catalyzed resin formulation is also shown in Figure 67.
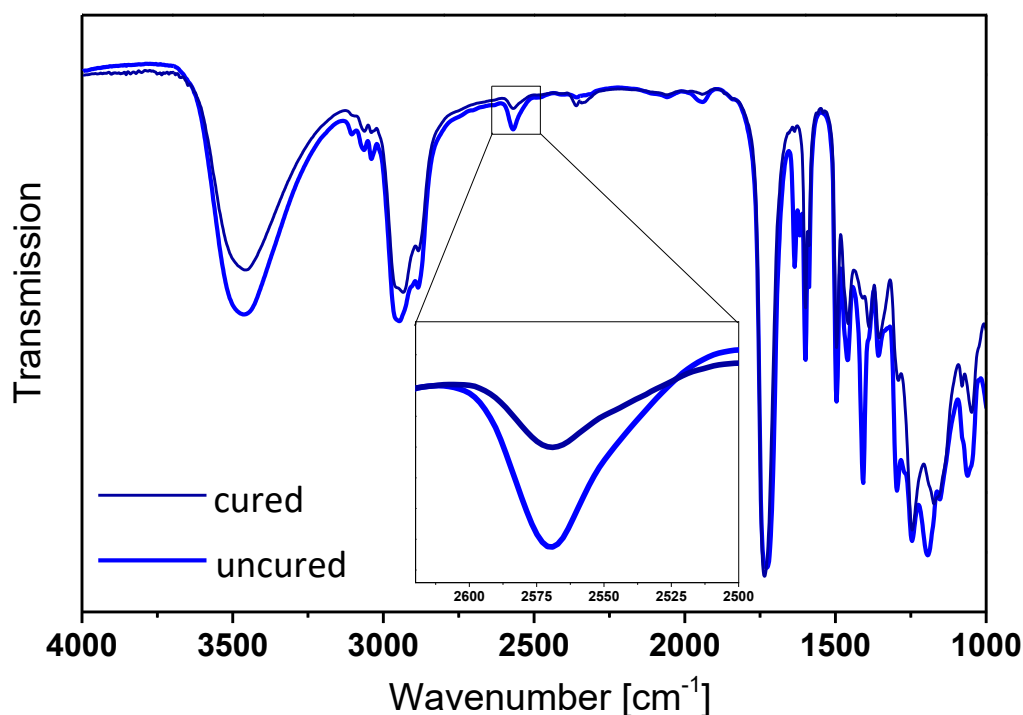
Figure 67. FTIR spectrum of the PDS-triflate catalyzed thiol-acrylate resin formulation, without light illumination (uncured) and 600s visible light illumination (cured). The inset zoom-in curve shows the difference in the thiol peak area (2570 cm^{-1}) [332].

In addition, thermogravimetric analysis was performed to analyze the thermal stability of the studied photolatent transesterification catalysts and the results indicate that the photolatent catalysts did not affect the thermal stability of the photopolymer networks, which remained stable well above 180 °C (Figure 68).
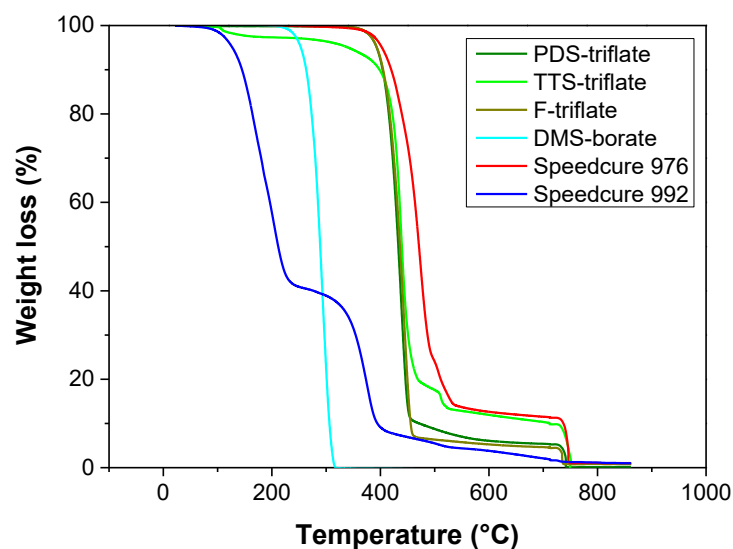
Figure 68. Thermogravimetric studies indicating the mass loss over the range of temperature, for various latent catalyst systems being integrated in thiol-acrylate networks [332].

Furthermore, experiments were conducted to determine the stress relaxation kinetics of cured photopolymers. DLP 3D-printing was used to form circular discs which were subsequently employed in a rheometer for stress relaxation measurements. The activation of the circular discs was carried out under a mercury UV lamp and the stress relaxation kinetics of activated and non-activated samples was measured at 180 °C.
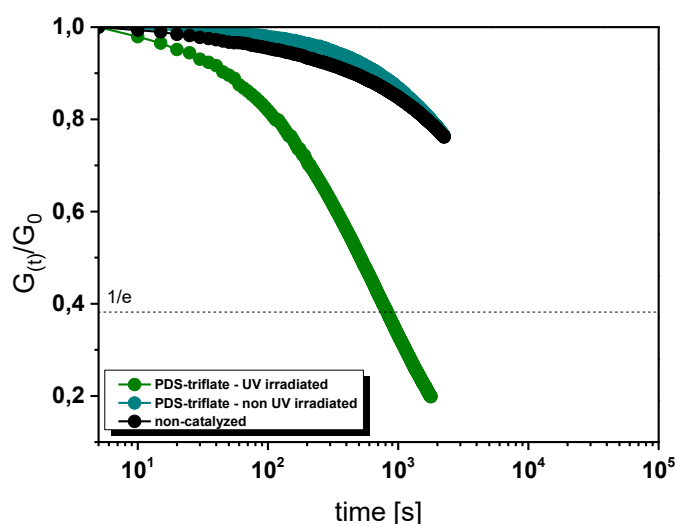
Figure 69. Normalized stress relaxation of a catalyzed (PDF-triflate) and non-catalyzed thiol-acrylate network obtained at 180 °C. For comparison of catalytic activity, non-UV activated results are also presented [332].

Only a low stress relaxation was measured in the absence of the photolatent catalysts, which was due to the thermal relaxation of volumetric shrinkage stresses that arose during network curing [128]. However, the catalyzed networks exhibited similar behavior before UV exposure, indicating that the catalyzing species was not prematurely released during the photo-curing process. Figure 69 presents the stress relaxation of the PDS-triflate catalyzed thiol-acrylate network.

The results of the stress relaxation studies demonstrate that all three photolatent catalysts are capable of catalyzing bond exchanges after irradiation and activation under UV light, although at varying rates (as shown in Figure 70a). It is worth noting that the rate of stress relaxation, which corresponds to the rate of bond exchange reactions, appears to increase as the acidity of the "super acid" released decreases: $HSbF_6 < HPF_6 < HCF_3SO_3$. However, it is important to mention that HCF_3SO_3 do not decompose near room temperature, unlike $HSbF_6$ and HPF_6, which exhibit low thermal stability and begin to degrade at 25 °C and 40 °C, respectively [339–342]. Thermolysis of the acids yields HF, which has a remarkably lower pK_a value (3.18) compared to HCF_3SO_3 (-14.27) [343,344]. As stress relaxation experiments were conducted at temperatures ranging from 140 °C to 180 °C, it is assumed that most of the "super acids" released during the process were converted into the less acidic HF.

The higher reactivity of HPF_6 in comparison to $HSbF_6$ may be due to the size of their respective counter anions. Besides acidity, the counter anion's size also affects the rate of migration of the liberated acid. A study on positive tone photoresists showed that using a photoacid generator with a larger counter anion size resulted in improved resolution of the micropatterns due to the slower migration of the released acid [345]. Given the limited spectral sensitivity, it is anticipated that the surface of the printed disc is where Brønsted acids are predominantly released, after which they migrate within the bulk to create a more uniform distribution of the photochemically formed catalyst. Hence, the faster migration of HPF_6, relative to the larger $HSbF_6$, may account for the superior stress relaxation, seen in the samples that employed hexafluorophosphate salt as the photolatent acid.

To validate the significance of the counter anion size and migration characteristics in the stress relaxation kinetics, additional measurements using diphenyl(methyl)sulfonium tetrafluoroborate (DMS-borate) were conducted. DMS borate has a counter anion (BF_4^-) with the least nucleophilicity but smallest size among the four photolatent acids studied (Figure 70a).
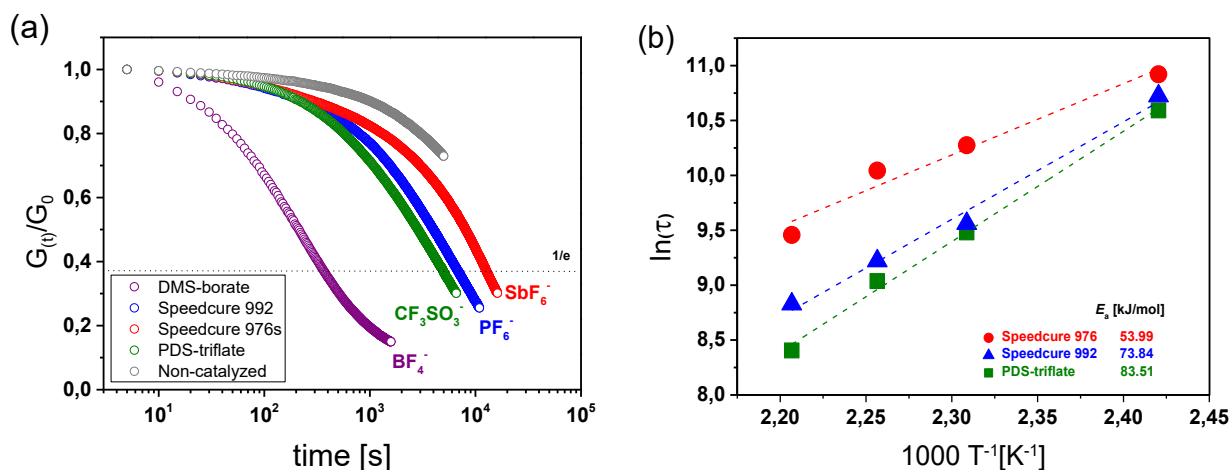
Figure 70. (a) Normalized relaxation modulus measured at 180 °C for a range of catalyst systems integrated in thiol-acrylate networks. (b) Arrhenius plots for the vitrimeric systems catalyzed by Speedcure 972, Speedcure 976 and PDS-triflate over a range of range [332].

The acid (HBF$_4$) that is released is highly mobile but has lower acidity compared to HPF$_6$ and HSbF$_6$. However, it offers a limited thermal stability up to 130 °C [346,347]. We also noticed that the chemistry of DMS-borate cannot be simply compared to the other three onium salts under investigation, due to differences in the cation's absorption characteristics. It only has a UV absorption in the shorter wavelength region of UV light and therefore, we anticipate a lower quantum yield under the given irradiation conditions.
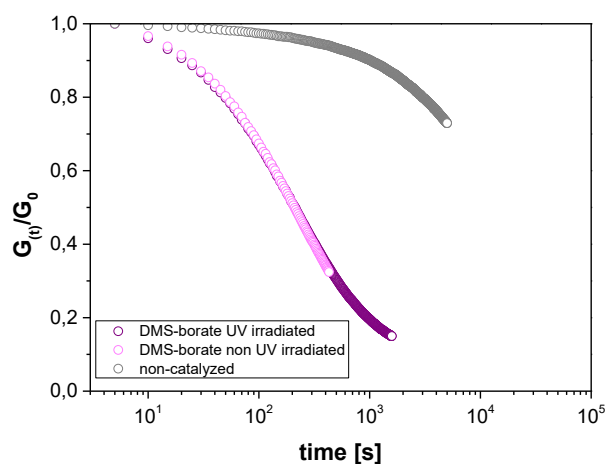
Figure 71. Normalized relaxation modulus of non-catalyzed and DMS-borate catalytic system in the thiol-acrylate photopolymer networks with and without UV-light activation [332].

In spite of its unsuitable absorption properties with reduced acidity compared to the liberated Brønsted acid, DMS-borate proves to be the most efficient catalyst in the current study (Figure

101

70a). However, it is evident from the comparison of the relaxation curves before and after UV illumination that the catalyst has been already activated thermally (Figure 71), as the exchange kinetics are similar.

The conventional acid catalysts utilized in vitrimers differ from photolatent systems in their impact on transesterification efficiency. The findings of current study, indicate that the catalytic performance of photolatent systems is predominantly influenced by the migration kinetics and thermal stability of the catalyst, while the released Brønsted acid's acidity has a minor effect. Consequently, by altering the counter anion of the photoacid generator, we could manipulate the relaxation time by more than twice of the magnitude (Figure 70a).

To find out the activation energy (E_a) of the catalyzed bond exchange reactions, temperature-dependent relaxation kinetics was studied, as the bond exchange rate in vitrimers is directly linked to stress relaxation [348].

In networks that undergo associative bond exchange reactions, the characteristic relaxation time (τ^*) has a temperature dependence described by an Arrhenius-type equation: $\tau^* = \tau_0$ exp (E_a/RT), where E_a represents the activation energy of the exchange reaction, R is the universal gas constant, and τ_0 is a characteristic time [250,264]. To determine τ^*, the normalized relaxation modulus ($G_{(t)}/G_0$) needed to reach 37% (1/e) of the original stress is measured, by implementing the Maxwell Model. The resulting τ^* values are then plotted versus (T^{-1}) on a semilogarithmic scale, while the activation energy (E_a) of the catalyzed reorientation reactions is calculated by determining the slope ($m=E_a/R$) of the data-fitted straight line, as shown in Figure 70b [136]. The linear trend observed for the irradiated thiol-acrylate networks confirms the Arrhenius-type temperature dependence and the vitrimeric nature of the networks, irrespective of the photoacid generator used [304,349]. Although the networks had similar ultimate bond conversions and network characteristics, their E_a values varied significantly.

The networks showed activation energy (E_a) values ranging from 73.84 to 53.99 kJ/mol with networks containing PDS-triflate, Speedcure 992, or Speedcure 976 (Figure 70b). Comparable E_a values (42.4 to 64.5 kJ/mol) were obtained with organophosphate catalysts with pK_a values ranging from 1.29 to 2.11 within the same thiol-acrylate networks [128,136]. These results illustrate the high adaptability of photolatent catalysts in vitrimeric networks by boosting the dynamic bond reorientation reactions. Furthermore, depending on their migration behavior, pK_a (acidity), thermal response and stability, they can appropriately facilitate the regulation of exchange kinetics.

5.2.2. Impact of counter cation in photolatent catalyst over vitrimeric properties

As a next step, the role of the cation of photolatent catalysts was studied in depth by using triphenylsulfonium triflates with different substituted groups on the phenyl rings (Figure 72a). The UV-Vis spectra of the investigated photolatent catalysts are shown in Figure 72b, indicating how the cation's structure affects its absorption properties. Compared to the unsubstituted triphenylsulfonium cation (F-triflate), having an absorption maxima at 235 nm, the substituted derivatives have an extended absorption window towards longer wavelengths [350]. These findings also align with the work of Dektar and Hacker, illustrating that the triphenylsulfonium salts' absorption coefficients rise with side group modifications, leading to a shift in the absorption maxima towards longer wavelengths [333]. Specially, PDS-triflate exhibits the highest red shifted maximum at 300 nm which was reported by Dektar and Hacker as a result of the resonance stabilization of 4-phenylthio moieties capable of donating electrons.
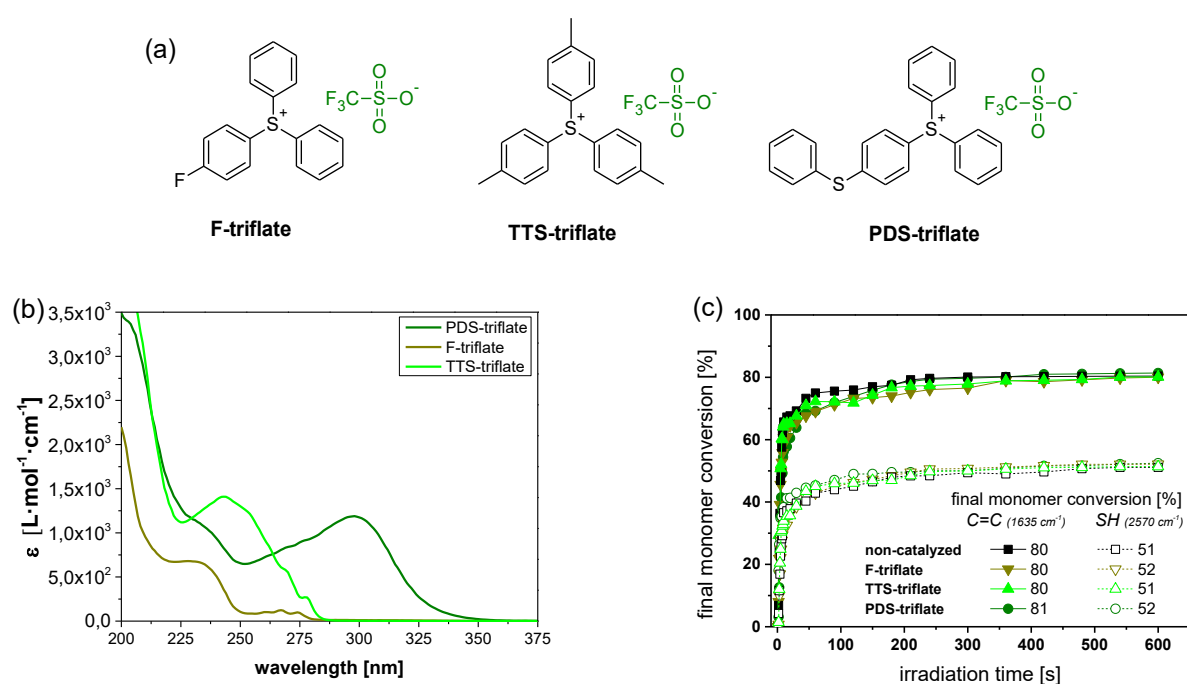
Figure 72. (a) Structures of the photolatent acids with varying cations. (b) UV-Vis spectra of triphenylsulfonium salts substituted with varying cations. (c) FTIR curing kinetics of non-catalyzed, F-triflate, TTS-triflate and PDS-triflate system over the illumination period. Bond conversions were obtained by integrating normalized absorption peak areas for acrylate (1635 cm^{-1}) and thiol groups (2570 cm^{-1}) [332].

The rate of acid formation is influenced by the substituents in addition to the absorption properties. Although the mono-fluoro (F-triflate) substituted and tris-tolyl (TTS-triflate)

substituted salts are observed to have a similar rate of acid formation compared to the unsubstituted triphenylsulfonium salt, the 4-phenylthio substituted derivatives, such as PDS-triflate, exhibit a notably faster reaction rate. This is explained by the dissimilarities in the photodissociation of triphenylsulfonium salts. The photodissociation of 4-phenylthio modified salts occurs via their triplet form, while the mono-substituted and pristine triphenylsulfonium salt dissociates through the singlet form [333].The triphenylsulfonium triflates that are being studied have been introduced as photolatent catalysts in the same thiol-acrylate resin formulation and according to FTIR experiments (Figure 72c), they do not impact the curing kinetics of the radical polymerization reaction, induced by the visible light. In fact, the curing rate and final monomer conversions are similar to those of the thiol-acrylate resin that does not contain a catalyst.

However, when exposed to UV light, an HCF_3SO_3 is released by all three triphenylsulfonium salts at varying rates, which also affects the stress relaxation kinetics of the photopolymerized thiol-acrylate networks. Networks containing TTS-triflate and F-triflate have slower stress relaxation rates at 180 °C, with 63% of the initial stress being relaxed in 196 and 153 minutes, respectively. On the other hand, the stress relaxation rate is significantly faster with PDS-triflate, having only 79 minutes required for relaxing 63% of the initial stress Figure 73a.
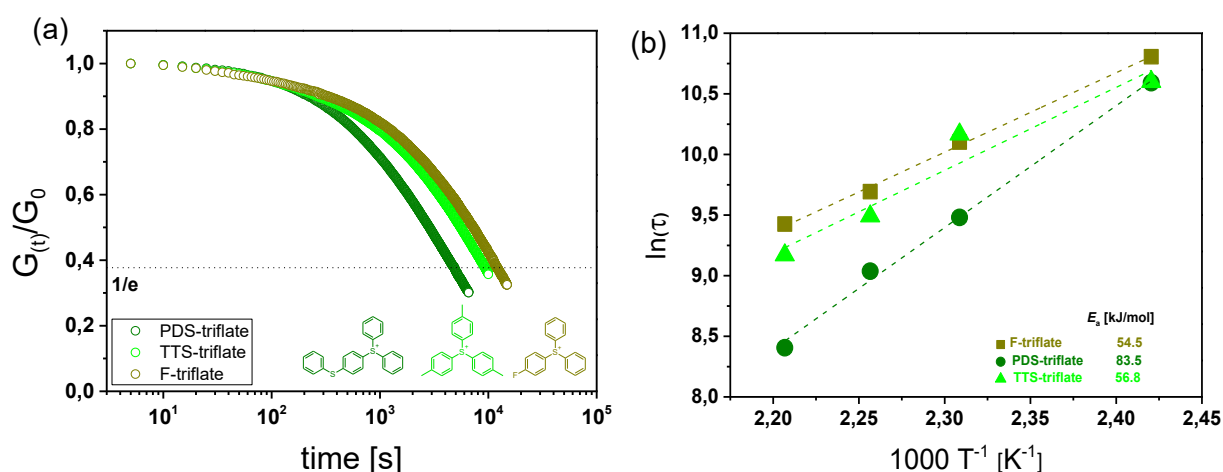
Figure 73. (a) Stress relaxation of thiol-acrylate vitrimers containing triphenylsulfonium salts with different cations. All samples were illuminated with UV light (20 mW.cm^{-2}) for 10 s using a mercury emitter lamp (λ = 200 – 550 nm). (b) Arrhenius plot obtained from the relaxation times of PDS-triflate, TTS-triflate and F-triflate at varying temperatures [332].

The findings demonstrate a strong correlation between the rate of acid formation of the photolatent catalysts and the exchange reactions, which occur more rapidly with a higher acid

content. This aligns with earlier research on vitrimers that rely on transesterification as the acid-catalyzed exchange rate also increased with a larger quantity of catalyst [128,351].

5.2.3. Dual wavelength DLP 3D-printing of soft devices

The PDS-triflate catalyst was utilized for 3D-printing experiments due to its exceptional performance in catalyzed thermally-induced transesterification in the thiol-acrylate networks being examined. DMS-borate was found to have a higher reactivity, but its limited thermal stability resulted in the undesirable release of the catalyst, making it inappropriate for the precise and local regulation of exchange reactions in DLP 3D-printed objects. Given the significance of stability and viscosity in 3D-printing, the viscosity of the resin was measured with a shear rate ranging between 1 to 300 s^{-1}, and was found to be 1078 mPa.s, which is in a typical range for DLP 3D-printing.

To produce flexible active devices with shape memory properties that could be controlled locally, the dual wavelength 3D-printer was utilized equipped with 405 nm and 365 nm light sources (Figure 74a). The thiol-acrylate material was selectively photopolymerized layer-by-layer using visible light irradiation at 405 nm, avoiding initiating the PDS-triflate catalyst prematurely. On the other hand, when printed with UV light (365 nm), the photopolymer underwent radical curing of thiol-acrylate network and the catalyst's activation at the same time.

To illustrate the experimental applicability of photo-latent catalytic systems, shape memory experiments and the topological reorientations were exploited and presented in Figure 74. Initially, a simple flower shaped test specimen was DLP 3D-printed with UV-light only as shown in Figure 74b (i). During the programming stage, the flower was exposed to a temperature of 160 °C for 2 hours, that exceeded the network's T_v, and was simultaneously deformed by the application of an external force leading to the first programmed shape in Figure 74b (ii). The flower was further subjected to programming above the T_g and deformed into a closed flower, followed by cooling to room temperature and removal of force, that fixed the second shape Figure 74b (iii). The closed specimen was reheated above the T_g, leading to the recovery of the first shape of the flower.
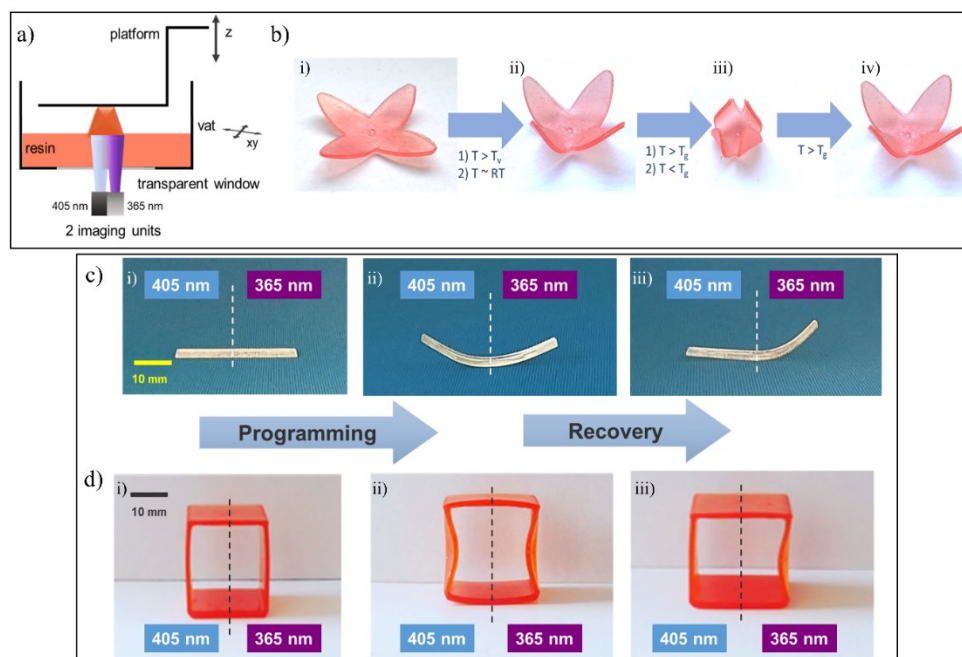
Figure 74. (a) Schematic diagram of dual-wavelength DLP 3D-printing equipment. (b) DLP 3D-printed flower using UV-light only, curing thiol-acrylate network as well as catalyst activation. The printed structure (i) was heated above T_v and cooled below T_g to fix the temporary shape (ii), which was further programmed above T_g and cooled to room temperature to fix shape (iii). Shape recovery (iv) was obtained after heating the programmed structure above T_g. (c,d) Rectangular bars and square cubes printed one half with UV light and the other half with visible light (i), Deformation of both sides above T_v for 2 hours for programming and cooling to room temperature to fix the programmed shape (ii), and shape recovery of 405 nm illuminated domains by raising temperature above T_g (iii) [332].

Furthermore, to exploit the localized topological control, a rectangular bar and a cubical structure were DLP 3D-printed with left-half of the material cured using visible light and the right-half of the material illuminated with UV-light (Figure 74c, Figure 74d). Both specimens were programmed above the material's T_v (160 °C for 2 hours under deformation), and cooled afterwards to room temperature with the removal of force, fixing the shape, as show in Figure 74c (ii) and Figure 74d (ii), respectively. The specimens were then heated to a temperature of 45 °C (above the network's T_g) leading to the recovery of the local regions printed with 405 nm (visible light) within 40 minutes, on account of the retractions of the stretched polymer entanglements to a favorable entropic state. On the other hand, regions printed and exposed to UV-light (365 nm) preserved their programmed shape on account of topological reorientations caused by the activated catalysts as shown in Figure 74c (iii) and Figure 74d (iii).

106
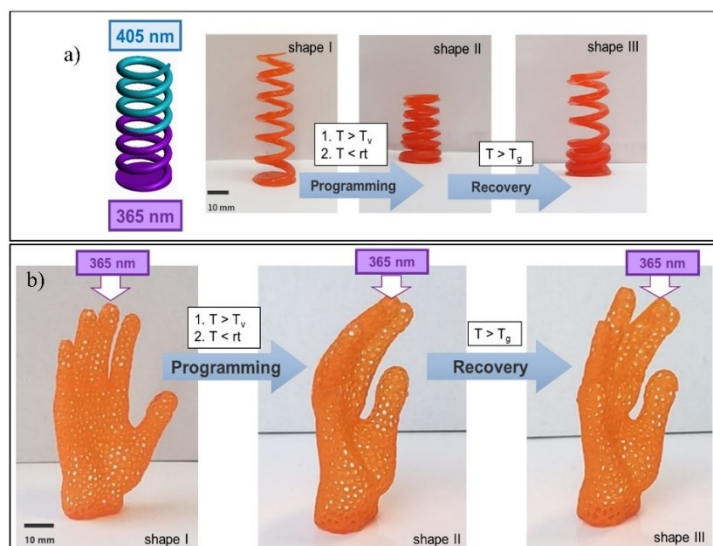
Figure 75. (a) DLP 3D-printed spring structure half (lower) printed with UV-light and the other half (upper) with visible light. Shape I shows the as-printed structure, which was programmed above T_v and cooled below room temperature to obtain shape II. Subsequently heating it above T_g returns the shape III. (b) DLP 3D-printed hand with only middle finger irradiated with UV light (shape 1). Subsequent programming of shape 1 above T_v and cooling below room temperature fixes shape II. Heating of shape II above T_g recovers all 4 four fingers except the middle finger that underwent topological rearrangements (shape III) [332].

As a further step, a structure in the shape of a spring and a hand (Figure 75) was printed to showcase the potential for creating intricate 3D-objects with locally controlled shape memory properties. The spring and fingers of the hand were printed using two different wavelengths in a very specific way, such that one half of the spring was cured using UV light and the other one with visible light, while in case of hand, only the middle finger was printed with 365 nm, while the other four fingers were printed with 405 nm.

During the programming stage, the fingers were bent and only the middle finger underwent topological rearrangements at a temperature of 160 °C. As a result, during the subsequent shape recovery process at 45 °C, the middle finger remained in its bent shape, while the other fingers returned to their original positions. This demonstrates that the use of photolatent catalysts in combination with dual wavelength DLP 3D-printing is a promising approach for personalized fabrication of complex soft active devices.

5.3. Conclusions

A comprehensive investigation was conducted to assess the effectiveness of specific photolatent catalysts in promoting localized activation of topological rearrangements in thermo-activated

vitrimers. Triphenylsulfonium salts were employed for this purpose, as they are transparent in the visible (405 nm) light range and release potent Brønsted acids upon exposure to ultraviolet (365 nm) light. However, the utilization of photolatent acids in catalyzing transesterifications in vitrimers is considerably more intricate compared to conventional protic acids. This complexity arises due to the influence of the counter anion's type, which defines the acidity of the released acid and the cation's structure, which affects the absorption characteristics and quantum yields of the released acid on the formation of the catalyzing species. In the context of thiol-acrylate vitrimers, it was observed that the rate of bond exchange reactions did not increase with the counter-anion's size or with the acidity of the liberated acid. This can be attributed to the relatively low thermal stability of the released Brønsted acids (SbF_6 and HPF_6), which readily convert to HF upon heat exposure, as well as the enhanced mobility of acids possessing smaller anions. In comparison, stress relaxation results indicated a positive correlation between the bond exchange rate and the quantum yield of the respective triphenylsulfonium triflates. Furthermore, the investigation involved triphenylsulfonium salts with a limited absorption range in the UV region only. As a result, curing of thiol-acrylate photopolymers using visible light was successfully achieved, excluding the premature generation of acid. Additionally, the presence of the photolatent catalyst did not affect the curing process. This breakthrough allowed for spatial activation of the catalyst in three-dimensional objects during dual-wavelength 3D-printing, using two distinct light wavelengths (i.e. 365 nm and 405 nm). Owing to the suitable absorption properties and rapid relaxation kinetics, PDS-triflate was used as photolatent catalyst in 3D-printing experiments. By programming the objects above the network's T_v, complex 3D-structures could be locally moved, endorsing the catalyst's spatial activation during the 3D-printing process.

6. Dynamic thiol-acrylate networks using bio-derived building blocks

This section presents the data and findings that were published in the journal "Polymer" with the title "Vat Photopolymerization 3D-Printing of Dynamic Thiol-Acrylate Photopolymers Using Bio-Derived Building Blocks", Volume 14, Issue 5377, in December 2022. The majority of the subsequent text, tables, and figures were extracted from the aforementioned publication [352]. Synthesis of the AELO monomer was carried out by Bernhard Sölle.

6.1. Materials and methods

6.1.1 Synthesis of monomers

Acrylated epoxidized linseed oil (AELO) was obtained by combining epoxidized linseed oil (100.05 g), butylated hydroxytoluene (0.33 g) and acrylic acid (23.076 g, 0.32 mol) in a round-bottom flask. The mixture was stirred for 20 min at 60 °C before triphenylphosphine (8.12 g, 0.037 mol) was added and the stirring continued for another hour. More acrylic acid (22.055 g, 0.306 mol) was then added and the mixture was stirred overnight at the same temperature. After cooling, the resulting mixture was dissolved in ethyl acetate (100 mL), and excess acrylic acid was removed through multiple washings with sodium bicarbonate and brine. The remaining organic layer was dried and the solvent was evaporated under vacuum. The final AELO product was a yellowish liquid having an estimated acrylate functionality of 3.2. The composition of the product was analyzed through ^{1}H-NMR spectroscopy [352].

^{1}H-NMR (400MHz, CDCl$_3$): δ [ppm] = 6.52 – 6.32 (m, H$_a$); 6.25 – 6.01 (m, H$_b$); 5.94 – 5.77 (m, H$_c$); 3.20 – 2.84 (m, H$_d$, H$_e$); 2.38 – 2.20 (s, H$_f$).

6.1.2. Development of resin formulations and 3D-printing

The resin formulations consisted of 70 wt.% AELO, mixed with 8 wt.% bis(2-methacryloyloxy)ethyl phosphate (DMEP) as transesterification catalyst, 2 wt.% BAPO as photoinitiator and 0.05 wt.% Sudan II. The liquid resin was mixed for 30 min in an ultrasonic bath at 40 °C. After dissolution of all components, 20 wt.% of the thiol crosslinker was added in the resin formulations at room temperature. Two different thiol crosslinkers, ethylene bis(3-mercaptopropionate) (EGMP) and trimethylolpropane tri(3-mercaptopropionate) (TMP3MP), were employed to study the impact of crosslinking degree on the photocured networks. The detailed compositions of resin formulations are summarized in Table 7, and the chemical structures are presented in Figure 76.
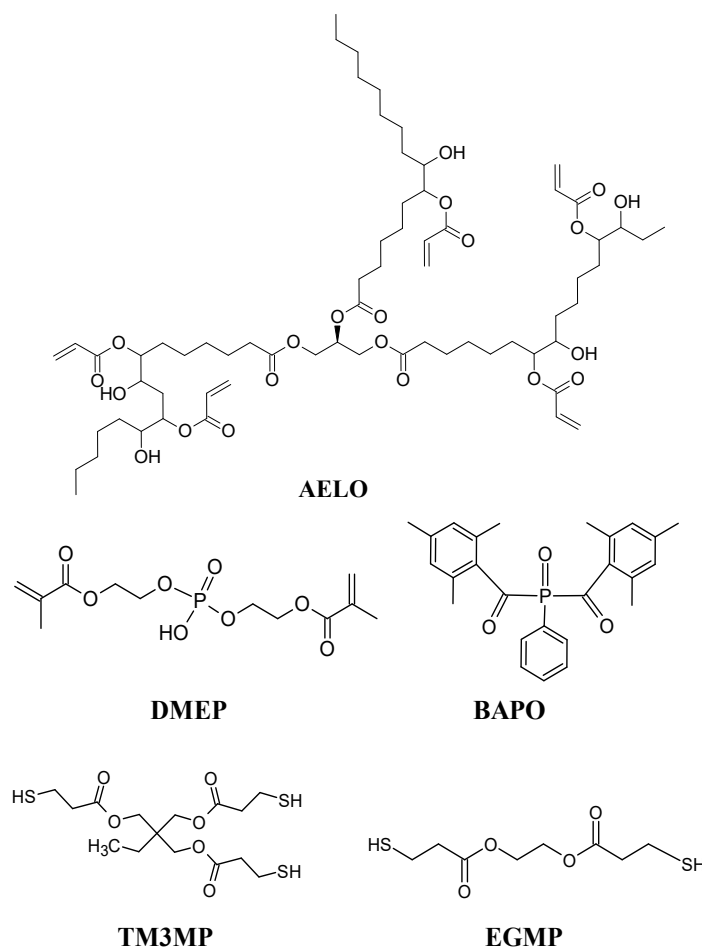
Figure 76. Chemical structure of AELO (acrylate component), DMEP (transesterification catalyst), EGMP and TM3MP (thiol crosslinker), and BAPO (photoinitiator) [352].

Table 7. Composition of resin formulations containing AELO and thiol crosslinkers. All resins consisted of 2 wt.% BAPO, 8 wt.% DMEP, and 0.05 wt.% Sudan II [352].

Resin formulation	AELO (wt.%)	Thiol (wt.%)
AELO-EGMP	AELO (70%)	EGMP (20%)
AELO-TMP3MP	AELO (70%)	TMP3MP (20%)

For DLP 3D-printing of resin formulations, an Anycubic Photon zero printer was used, which was equipped with a build-in light source operating at 405 nm. The overall light exposure was controlled using bottom and normal exposure settings with a corresponding duration of 90 s and 70 s, based on the optimal monomer conversions estimated from the FTIR spectroscopy. The layer thickness was 50 µm and the rising and retracting speed of the building platform were set to 2 mm.s^{-1}.

6.1.3. Fourier-transform infrared spectroscopy

Fourier transform infrared radiation (FT-IR) spectroscopy was carried out using a Vertex 70 spectrometer (Bruker, USA) using transmission mode. 16 scans were measured from 4000 to 700 cm^{-1}, along with a resolution of 4 cm^{-1}.

Sample preparation followed drop-casting the liquid resins (1.2 µL) between two CaF$_2$ slides. Curing studies were performed by illuminating the casted resin with a LED lamp (zgood® wireless), which had a power density of 3.3 mW.cm^{-2} (illumination wavelength = 420 – 450 nm). Using OPUS software, the exposure dose was correlated with the normalized peak areas of acrylate (1635 cm^{-1}) and thiol (2570 cm^{-1}) groups to estimate the reaction conversions. The normalization of these peaks was achieved by following the unaltered C=O peak (1750 cm^{-1}) during the curing process.

For measuring the FT-IR spectra of thermally post-treated materials, a reflection diamond attenuated total reflection (ATR) accessory (Platinum ATR) was employed, and the measurements were performed in the range of 4000 to 700 cm^{-1}.

6.1.4. Evaluation of network properties

Glass transition temperature (T$_g$) of the 3D-printed resins was determined with the help of a differential scanning calorimeter. The heating rate of the measurements was set to 20 K.min^{-1} and the cycles were run between -50 °C to 200 °C und nitrogen atmosphere. The T$_g$ of the material was determined using the midpoint results of the second heating cycle.

For determination of the gel content of cured networks, circular discs (10 mm x 1 mm) were immersed in dichloromethane for 48 hours. The samples were removed and the surface was dried with a tissue paper, followed by weighing the samples (m$_{ini}$). Subsequently, the samples were placed in the oven at 40 °C for 24 hours, until a constant weight of the sample was achieved. The final weight of the dried samples was measured (m$_{end}$) and the ratio of the weights (m$_{end}$/m$_{ini}$) was calculated, which corresponded with the gel content of the network.

To analyze the resolution of the DLP 3D-printing process with the formulated bio-derived resins, an optical microscope (Olympus BX 51, Tokyo, Japan) with an integrate software Color View IIIu digital camera was utilized.

6.1.5. Stress relaxation and rheological measurements

The resins' viscosities were measured with a compact modular rheometer (MCR 102 Anton Paar, Austria) provided with a CP60-0.5/TI cone having an opening angle of 1.982° and a

diameter of 49.97 mm. 1.2 mL of each liquid resin was used during the measurements at 30 °C, with a shear rate between 0.1 to 300 s^{-1}.

A second rheometer set-up (Anton Paar Physica MCR-501, Austria) was used to measure the stress relaxation of the disc samples (10mm x 1mm) under selected temperatures between 140 and 180 °C. Samples were equilibrated at a force of 20 N, 20 minutes prior to the start of measurement recording. At a fixed temperature, 3% strain was employed on the disc samples in a parallel plate arrangement and the descending stress was determined over time.

6.1.6. Thermal healing and shape memory

By employing the resin formulation AELO-EGMP, thermal healing experiments were conducted on DLP 3D-printed rectangular bars (l = 30 mm, w = 10 mm, h = 1.5 mm) with a central cavity (d = 5 mm). Additionally, circular cavities (5 x 1.5 mm) and control samples without cavities (l = 30 mm, w = 10 mm, h = 1.5 mm) were printed. The samples were thermally treated at 180 °C for 4 hours in the oven to test the effectiveness of the healing after the circular discs was inserted into the cavities of the rectangular bars. The Zwick Roell Z1.0 static material testing apparatus (Ulm, Germany) was used to conduct tensile tests on rectangular bars with cavities, healed samples and control samples at a cross-head speed of 250 mm per minute.

The shape memory experiments were carried out on DLP 3D-printed grippers having the dimensions of 50 mm x 1 mm (diameter x thickness). Prior to experimentation, the grippers were thermally treated at 180 °C for 2 hours. The first shape of the material was fixed by heating the gripper at 180 °C for 2 hours. For the second shape, the gripper was cooled to room temperature and reshaped, followed by freezing the structure in the deep freezer at -20 °C. By exposing the gripper to 30 °C, the first shape was regained within 30 seconds. The permanent structure of the printed gripper was bought back by reheating the gripper for 2 hours at 180 °C.

6.2. Results and discussion

6.2.1. Photopolymerization of dynamic thiol-acrylate networks

The focus of this research was the exploration of an acrylated linseed oil (AELO) as a building block for 3D-printable thiol-click networks, which additionally contained dynamic hydroxy ester bonds. To activate transesterification reactions in the photopolymer network, an organic phosphate ester catalyst (DMEP) was added and the cure kinetics, stress relaxation, and mechanical properties were analyzed versus network composition. The chemical compositions of the resin mixtures are presented in Table 7. DLP 3D-printing of the resin formulations was carried out and the whole methodology is presented in Figure 77.
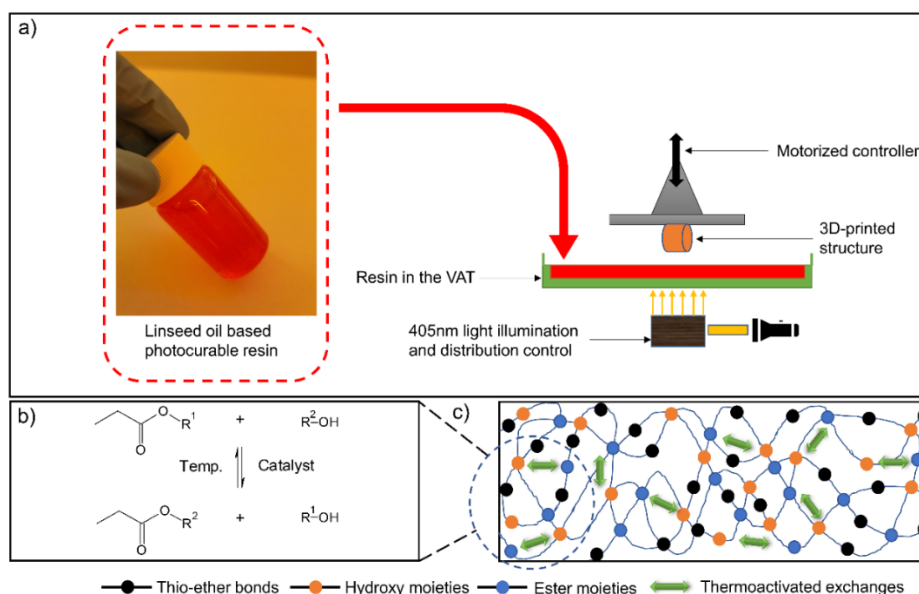
Figure 77. (a) Photograph of the bio-derived resin formulation used for 3D-printing and the schematic representation of the DLP 3D-printing process. (b) Conceptual demonstration of hydroxy-ester exchange reactions activated via thermal treatment in the presence of a catalyst. (c) Schematic illustration of the transesterification exchange reactions in a cured polymer network [352].

The synthesis of the acrylated epoxidized linseed oil was performed by a nucleophilic ring-opening reaction of a fully bio-based epoxidized linseed oil via acrylic acid, in accordance with the literature [353]. The monomer was synthesized in high yields using a one-pot method, which was verified by analyzing ^{1}H NMR spectra in deuterated chloroform (Figure 78 and Figure 79).
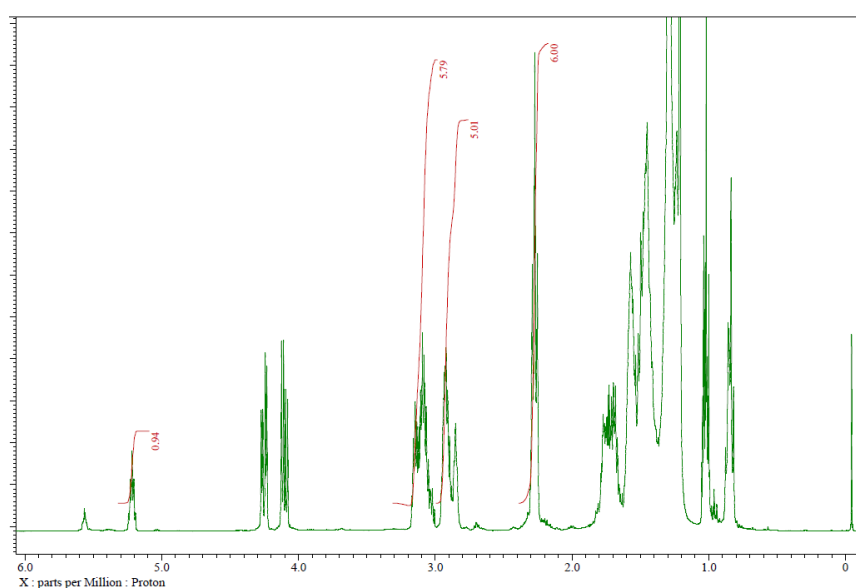
Figure 78. ^{1}H NMR spectrum of epoxidized linseed oil (ELO) in deuterated chloroform [352].
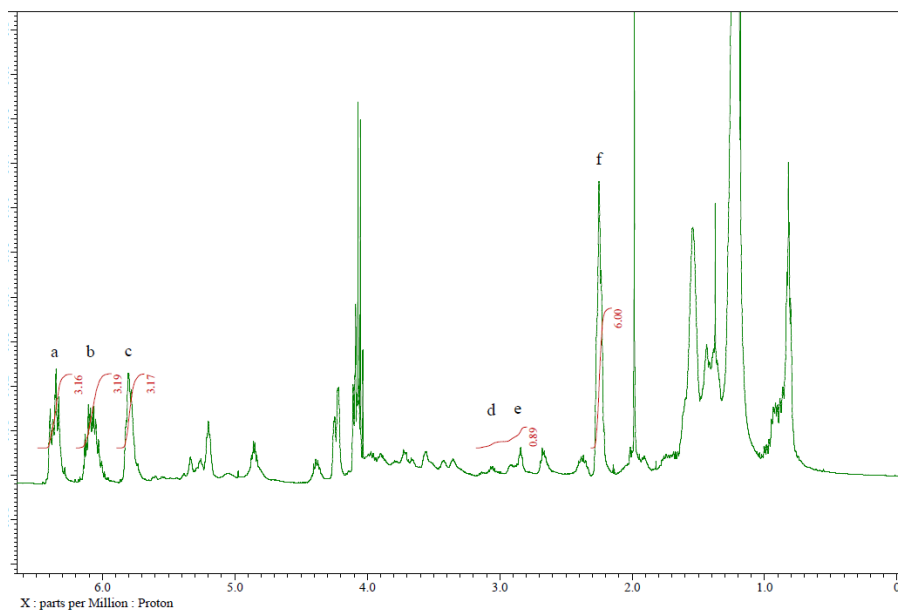
Figure 79. ^{1}H NMR spectrum of acrylated epoxidized linseed oil (AELO) in deuterated chloroform [352].

The three CH$_2$ groups (H$_f$) attached to the ester carbonyl at the α-position were assigned to the signal at 2.3 ppm, which was also utilized as a reference for quantifying the introduced acrylates at 5.85, 6.15, and 6.4 ppm. By setting the integral value of H$_f$ to 6, the integrals of H$_{a-c}$ were directly used to determine the average acrylate functionality per triglyceride molecule. In addition, the reduction in epoxide functionality (3.0 ppm) from 5 to 0.4 per triglyceride molecule confirmed a successful reaction. NMR results also revealed that 90% of the epoxide moieties participated in the ring-opening process. The calculated acrylate functionality was 3.2. On the other hand, the functionality of residual epoxide groups was estimated to be 0.45. The results suggest that a part of the epoxide groups was engaged in hydrolysis or other side reactions as the stochiometric consumption of epoxy monomers was more than the generated acrylate. As the resulting acrylate functionality of 3.2 was deemed sufficiently high for the targeted photopolymerization reaction, further optimization of synthesis protocol was not performed.

Two types of thiols with different functionalities, the trifunctional thiol TMP3MP and the difunctional thiol EGMP, were used to prepare AELO-thiol resins. The curing of these resins was achieved under visible light exposure using BAPO as a radical photoinitiator. The curing kinetics were followed by measuring the decrease in intensity of the characteristic S-H stretching band at 2570 cm^{-1} and the C=C wagging band at 1635 cm^{-1} as a function of exposure dose (Figure 80).
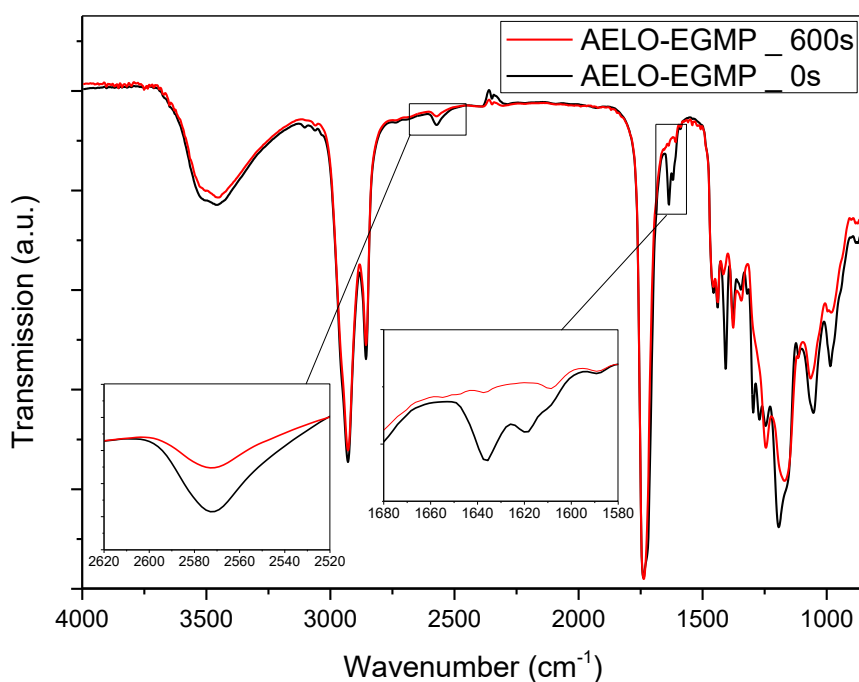
Figure 80. FTIR spectrum of the uncured AELO-EGMP resin (0 s) and the cured AELO-EGMP resin (600 s). The acrylate and thiol groups consumption can be observed at 1635 cm^{-1} and 2570 cm^{-1} [352].

The acrylate conversion in both resins was notably superior (87% and 97%) than the thiol conversions, which only reached 46% and 48% for AELO-TMP3MP and AELO-EGMP, respectively (Figure 81a and Figure 81b). This is due to the involvement of the acrylate groups in homopolymerization and thiol-ene addition reactions [47,128,135].

Although chain-growth polymerization reactions achieve high molecular weights quickly, step growth polymerization tends to produce lower molecular weight components, resulting in a delayed gelation, more uniform networks and reduced shrinkage stress [47,123,128,135,323]. In general, the conversion of acrylate is typically 1.5 times higher than the thiol conversion in such reactions [123,322], which accounts for the higher acrylate conversions in thiol-acrylate click-reactions.

The conversion of the thiol groups decreased with increasing thiol functionality (Figure 81a and Figure 81b), due to the diffusional restrictions of the reactive monomers. As the thiol functionality increased, gel point was shifted to lower conversion and the polymerization rate slowed down due to the diffusional constraints. Notably, both cases recorded almost similar reaction kinetics during the first 70 seconds of illumination and acrylate conversion exceeded

70% in both cases. Additionally, the trifunctional thiol acted as a crosslinker while the difunctional thiol acted as a chain extender, increasing the molecular weight among adjoining crosslinks [135,323,324], which was also verified by the sol-gel experiments. The networks that were formed using the difunctional thiol (EGMP) had a gel content of 71.5% ± 1.9%, while the networks formed with the trifunctional thiol (TMP3MP) comprised a gel fraction of 77.7% ± 2.3% (Figure 81b). The reason for the higher gel content in the AELO-TMP3MP system can be attributed to the increased crosslink density resulting from the higher functionality of the thiol used. Typically, incomplete monomer conversion, especially with thiol crosslinkers, can result in low gel content, which may be related to the extraction of thiol crosslinkers from the networks during swelling.
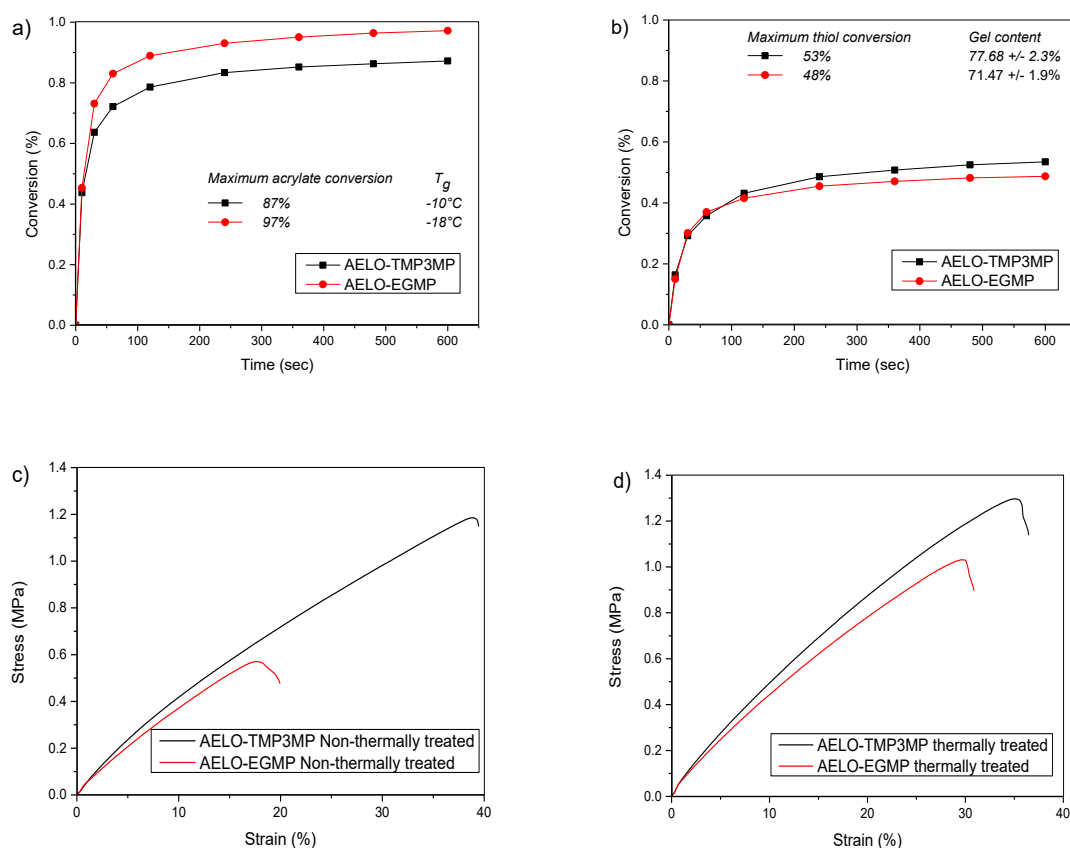
Figure 81. (a) Acrylate conversions in AELO-TMP3MP and AELO-EGMP resin formulations determined using FTIR along with the networks' T_g. (b) Thiol conversions in AELO-TMP3MP and AELO-EGMP resin formulations determined using FTIR and networks' gel fractions. (c) Stress-strain curves of AELO-TMP3MP and AELO-EGMP networks. (d) Stress-strain curves of thermally annealed (180 °C, 4 h) AELO-TMP3MP and AELO-EGMP networks [352].

6.2.2. Network characteristics of dynamic thiol-acrylate photopolymers

To further characterize the mechanical strength, samples for uniaxial tensile tests were prepared using DLP 3D-printing. The networks were relatively soft at room temperature, resulting in a lower tensile strength of 1.18 MPa and 0.58 MPa for the TMP3MP and EGMP based formulations, respectively. AELO-EGMP had an ultimate elongation that was lower than the value observed in AELO-TMP3MP (as shown in Figure 81c). However, by subjecting the 3D-printed tensile specimens to thermal annealing at 180 °C for 4 hours, both networks' mechanical properties and Young's moduli were improved (Figure 81d). The tensile strength and ultimate elongation of both networks were altered, with a maximum strain of 31% for AELO-EGMP and 36.5% for AELO-TMP3MP, and a tensile strength of 1.04 MPa for AELO-EGMP and 1.3 MPa for AELO-TMP3MP, respectively. The increase is related to thermally induced rearrangements along with the reduction of shrinkage stress. Earlier studies have shown that subjecting the material to thermal treatment results in the formation of hydrogen bonds, leading to a boost in its tensile properties [135,324,325]. Additionally, the analysis of ATR spectra of the treated samples indicated a decrease in the -OH groups region (3300-3600 cm^{-1}), indicating the formation of hydrogen bonds (Figure 82).
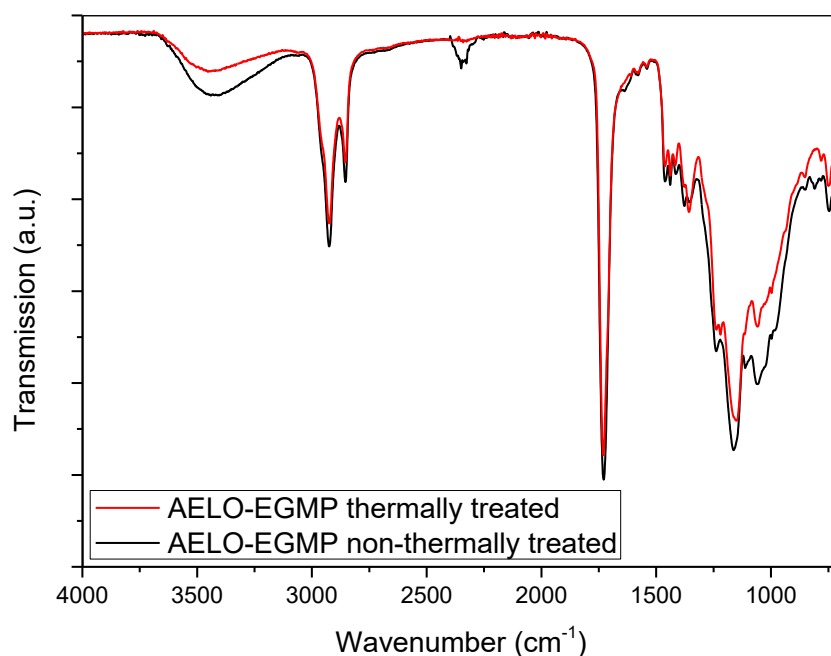
Figure 82. ATR FTIR spectra of AELO-EGMP prior to and after thermal post-treatment (4 hours at 180 °C) showing the decrease of the IR band related to -OH groups (3300-3600 cm^{-1}) [352].

117

AELO-EGMP and AELO-TMP3MP exhibited a T_g of -18 °C and -10 °C respectively, and the DSC plot of the formulations are provided in Figure 83.
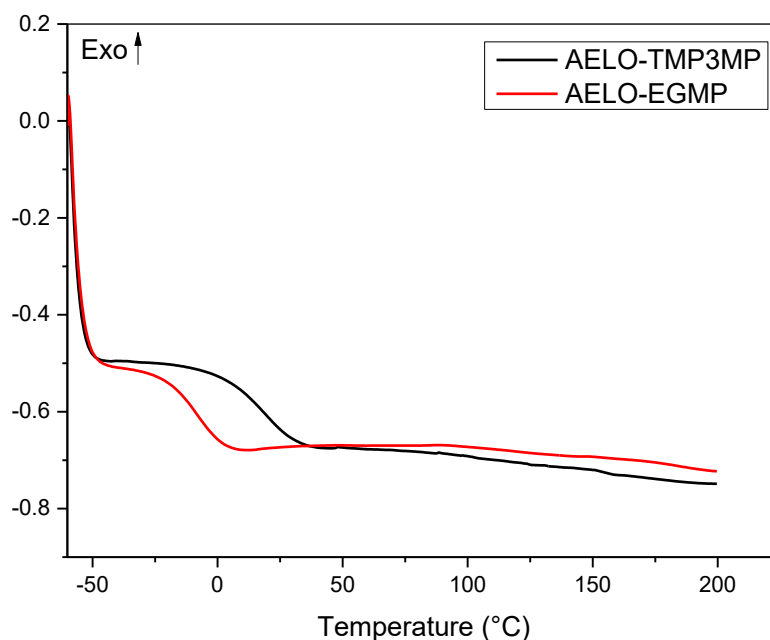
Figure 83. DSC results of the cured AELO-EGMP and AELO-TMP3MP resin formulations (T_g was estimated from the midpoint exploitation) [352].

Stress relaxation experiments were carried out between 140 °C and 180 °C were used to characterize the kinetics of thermo-activated bond exchange reactions. DLP 3D-printed specimens with a diameter of 10 mm (thickness of 1 mm) were used and the impact of thiol crosslinker on the exchange kinetics was evaluated.

Figure 84a illustrates the time-dependent behavior of the stress relaxation modulus at 180 °C for three different networks: AELO-TMP3MP, AELO-EGMP, and AELO-EGMP without a transesterification catalyst. The addition of DMEP as a transesterification catalyst induces stress relaxation in the networks, although the rates of relaxation differs among the networks. Additionally, the thiol-acrylate networks exhibit some stress relaxation even in the absence of the catalyst, but the rate of relaxation is significantly slower (Figure 84a). This relaxation is attributable to the thermal release of volumetric shrinkage stresses [128,354].
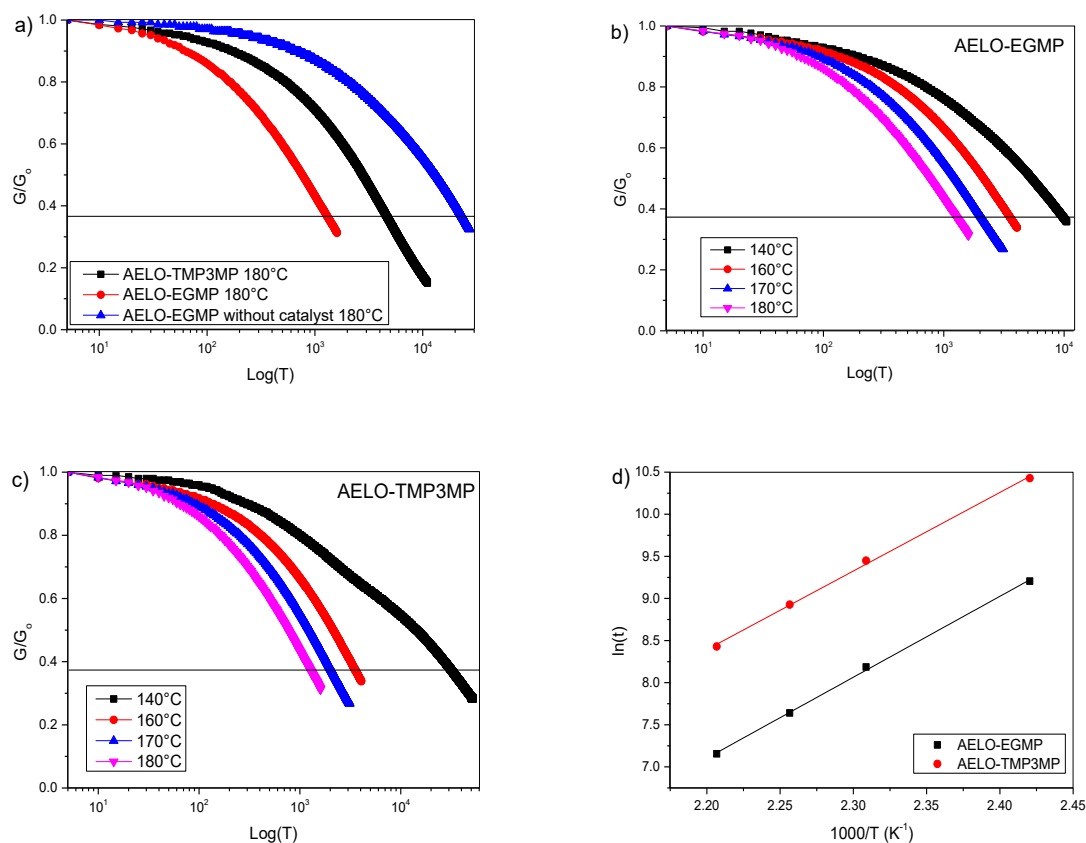
Figure 84. (a) Normalized relaxation modulus for AELO-EGMP, AELO-TMP3MP and AELO-EGMP without catalyst measured at 180 °C. (b) Normalized relaxation modulus for catalyzed AELO-EGMP at different applied temperatures (140 °C to 180 °C) over time. (c) Normalized relaxation modulus for catalyzed AELO- TMP3MP at different applied temperatures (140 °C to 180 °C) over time. (d) Arrhenius plot for AELO-EGMP and AELO-TMP3MP verifying the linear dependence [352].

The faster relaxation rate of catalyzed AELO-EGMP (22 min) in comparison to catalyzed AELO-TMP3MP (77 min) can be attributed to the higher degree of crosslinking in AELO-TMP3MP, despite both networks having a similar number of -OH and ester groups. Additionally, both networks exhibit temperature dependence in stress relaxation, with an increase in bond exchange rate as temperature increases (Figure 84b and Figure 84c). Figure 84d shows a semilogarithmic plot of τ^* versus $1/T$, which confirms the linear Arrhenius type temperature dependence and vitrimeric nature of the photopolymers [355]. The slope ($m=E_a/R$) of the linear trend obtained from both networks was used to determine their respective activation energies (E_a), which were found to be 77.58 kJ.mol^{-1}.K^{-1} for AELO-EGMP and 79.88 kJ.mol^{-1}.K^{-1} in case of AELP-TMP3MP networks.

6.2.3. Thermal healing and thermally triggered shape memory

Due to the lower viscosity of the AELO-EGMP resin (2.1 Pa.s at a shear rate between 0.1 - 300 s^{-1}), as compared to the AELO-TM3MP resin (11.9 Pa.s at the same shear rate range), is was further used the printed objects using DLP 3D-printing technology. To assess the printing resolution, a comb-shaped structure with holes of varying sizes was 3D-printed (as depicted in Figure 85a). The resolution was found to be as high as 250 µm (Figure 85b).
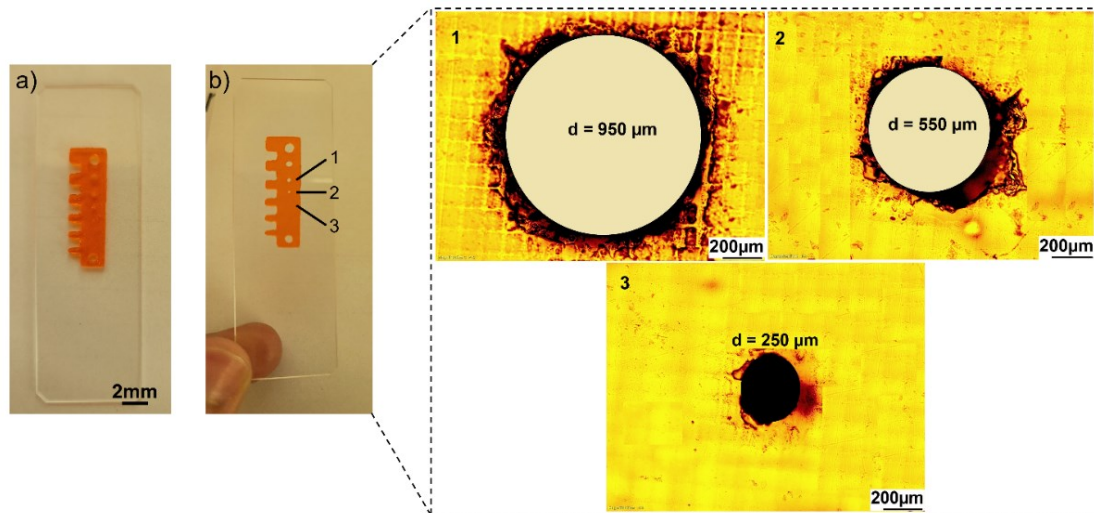
Figure 85. (a) DLP 3D-printing resolution tests with the resin AELO-EGMP by employing a comb structure. (b) Circular cavities inspection with naked eye followed by zoomed images under the optical microscope with 1, 2 and 3 presenting the circular holes in the comb [352].

The AELO-EGMP photopolymer, containing dynamic thiol-acrylate networks, offered the unique characteristic of triple shape memory and the capability to undergo controlled and macroscopic deformation upon heating and programming beyond its two transition temperatures, T_v and T_g. To demonstrate this, a DLP 3D-printed and thermally annealed flower was subjected to an external deformation force and heated above its transition temperature (T_v) at 180 °C, as shown in Figure 86a and Figure 86b. This temperature was selected based on rheological experiments that revealed fast stress relaxation at this temperature (Figure 84b). The first temporary shape was then fixed by cooling the specimen to 30 °C, which was above the T_g of the material, enabling the programming of a second shape. Subsequently, the second temporary shape was fixed by applying a deformation force and cooling the sample below T_g to -20 °C. The flower structures were able to sequentially recover the different shapes under thermal stimulus without any force application (Figure 86a and Figure 86b). The first temporary shape had a recovery time of 30 seconds, demonstrating the potential application of partly bio-based thiol-acrylate resins in biomedical and soft robotic systems.
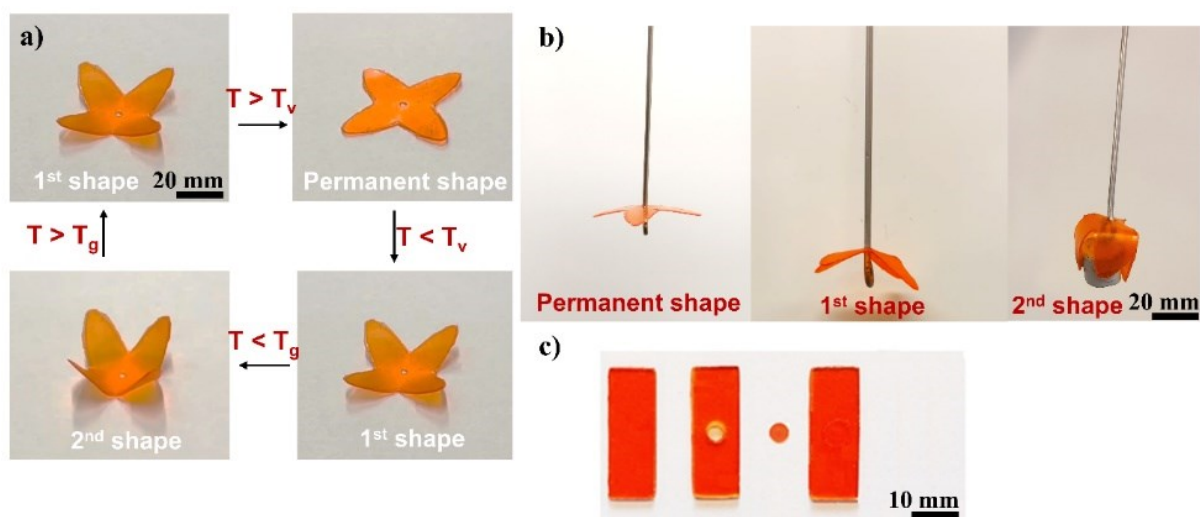
Figure 86. (a) Shape memory experiments of a DLP 3D-printed flower gripper using AELO-EGMP. The first shape of the material was fixed by heating it at 180 °C followed by cooling to room temperature, permanent shape represents the as-printed structure of the gripper. The second shape of the gripper was programmed using T_g and the structures were able to recover the shapes by subsequent increase of the temperature. (b) Application of the flower gripper to grab and release soft rubber objects. (c) AELO-EGMP based control, damage, disc and thermally healed samples (sequence from left to right) by putting the disc into the hole of the printed par and thermally annealing the assembly for 4 hours at 180 °C.

The thermal healing and repair properties of the AELO-EGMP photopolymer were also investigated in a subsequent stage. To achieve this, rectangular samples were 3D-printed using DLP technology, with one set containing a circular cavity in the center (referred to as the "damage" sample), and the other set being defect-free and used as the control (Figure 86c). A disc was also 3D-printed to fit perfectly inside the cavity of the defect sample. The sample was then subjected to thermal healing and welding by being placed in an oven at 180 °C for 4 hours and resulted in excellent mendability after thermal treatment (as shown in Figure 86c).

Tensile testing was carried out on the healed samples and it was observed that their stress-strain behavior was almost identical to those of the defect-free control samples, indicating a high healing efficiency of the dynamic AELO-EGMP photopolymer network (Figure 87).
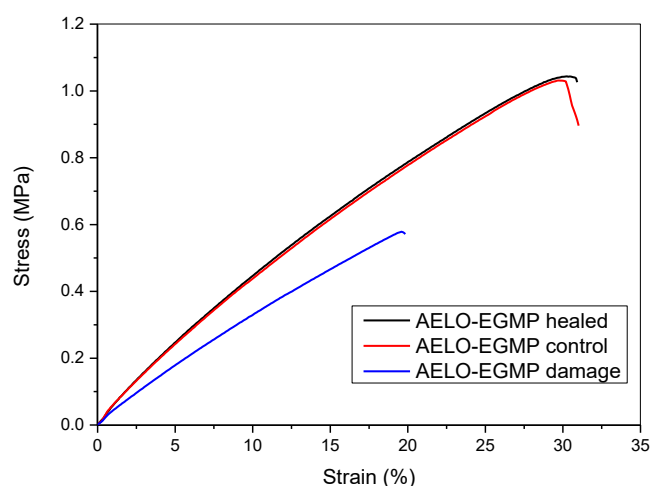
Figure 87. Stress-strain curves of the AELO-EGMP-based damage, control and healed sample [352].

6.3. Conclusions

In this study, a bio-based acrylated linseed oil was synthesized and directly utilized as a building block to form dynamic thiol-acrylate photopolymers, as it also contained sufficient ester and hydroxy moieties which underwent thermo-activated transesterification reactions. The relationship between the structure and properties of these networks using two different thiols, each having a different functionality, was studied. Both thiols enabled adequate curing kinetics resulting in evolution of thiol-acrylate networks under visible light. The bi-functional thiol resulted in a lower crosslinked photopolymer with a glass transition temperature of -18 °C, whereas the tri-functional thiol counterpart had a T_g of -10 °C. Due to its lower viscosity, AELO-EGMP was utilized in subsequent 3D-printing experiments and objects with a structure size of 550 μm were successfully fabricated. The abundance of ester and hydroxy moieties in AELO-EGMP formulations, when combined with an organic phosphate ester catalyst, underwent efficient transesterification exchange reactions at sufficiently high temperatures (>140 °C). This macroscopic reflow was further employed for reshaping and damage healing of the printed specimens. After thermal treatment at 180 °C for 4 hours, healed materials exhibited almost complete recovery of the tensile properties. Additionally, the 3D-printed structures demonstrated triple-shape memory, allowing them to transition between two different programmed shapes by utilizing the glass transition state and topological freezing temperature of the dynamic thiol-acrylate networks. This presents a great potential of such dynamic networks in soft robotic industry.

7. Development of fully bio-based, 3D-printable dynamic networks

This section presents the data and findings that were exploited for the development of fully bio-based vitrimers processable via DLP 3D-printing. Synthesis of the monomers and catalysts, and stress relaxation experiments were performed by Bernhard Sölle. Various photocurable resin formulations were developed and successfully processed by DLP 3D-printing. Photocuring kinetics, network crosslinking, thermal and mechanical properties and stress relaxation characteristics were studied in detail. Possible application in soft robotics was demonstrated exploiting triple shape memory and thermal healing as novel features.

7.1. Materials and methods

7.1.1 Synthesis of resins and catalysts

Synthesis of acrylated epoxidized linseed oil (AELO)

Acrylated epoxidized linseed oil (AELO) was synthesized following the same synthesis procedure as mentioned in section 6.1.1.

Synthesis of eugenol ester phosphate (EUGP)

Eugenol ester phosphate (EUGP) was synthesized by reaction of phosphorus oxychloride across eugenol following a synthesis procedure described in literature [356,357]. For this purpose, toluene and phosphorus oxychloride ($POCl_3$) were mixed in a 250 mL three necked round bottomed flask equipped with a reflux condenser and a thermometer. Sideward, eugenol and triethylamine (Et_3N) were added in a dropping funnel. Subsequently, the eugenol mixture was allowed to gradually drop in to the $POCl_3$ solution under vigorous stirring for 4 hours. The insoluble salts formed at the bottom were filtered-out and the reaction mixture was placed in a two necked round bottomed flask, where steam from an external steam generator was bubbled into the mixture for 25 minutes. The phases were separated and the organic layer was mixed with ethyl acetate. The organic layer was dried over sodium sulfate and the solvent was removed using a rotary evaporator. The overall synthesis scheme is presented in Figure 88.
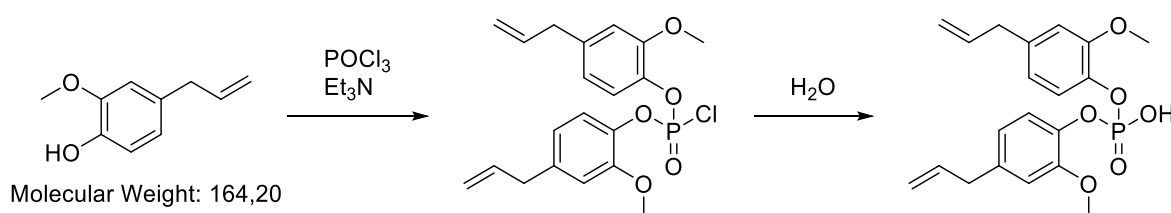
Figure 88. Reaction scheme for the synthesis of transesterification catalyst EUGP.

The final product was a yellowish oily liquid. The composition of the product was analyzed through ^{1}H-NMR, ^{13}C-NMR and ^{31}P-NMR spectroscopy, with the resulting peaks falling within specific ranges of chemical shift values.

^{1}H NMR (400 MHz, CDCl$_3$): δ [ppm] = 7.30-7.23 (m, 1H); 6.79 (s, 1H); 6.76-6.70 (m, 1H); 6.01-5.84 (m, 1H); 5.14-5.03 (m, 2H); 3.84 (s, 3H); 3.4-3.3 (m, 2H).

^{13}C NMR (400 MHz, CDCl$_3$): δ [ppm] = 150.6; 139.3; 137.6; 136.9; 121.5; 120.7; 116.4; 113.4; 56.0; 40.1

^{31}P NMR (400MHz, CDCl$_3$): -2.71

Synthesis of citronellol ester phosphate (CitrP)

Citronellol ester phosphate (CitrP) was synthesized by the reaction of phosphorus oxychloride across citronellol following a synthesis procedure described in literature [356,357]. To achieve the product, toluene and phosphorus oxychloride (POCl$_3$) were placed in a 250 mL three necked round bottomed flask equipped with a reflux condenser and a thermometer. Separately, citronellol and triethylamine (Et$_3$N) were mixed in a dropping funnel. Afterwards, the mixture of citronellol was slowly dropped within a period of 4 hours in to the POCl$_3$ solution under continuous stirring. The formed insoluble salt was subsequently filtered-off. The reaction mixture was then placed in a two necked round bottomed flask and steam from an external steam generator was bubbled into the mixture for 30 minutes. The phases were separated and then the organic layer was dried over sodium sulfate followed by the solvent removal on a rotary evaporator. The synthesis reaction is presented in Figure 89.
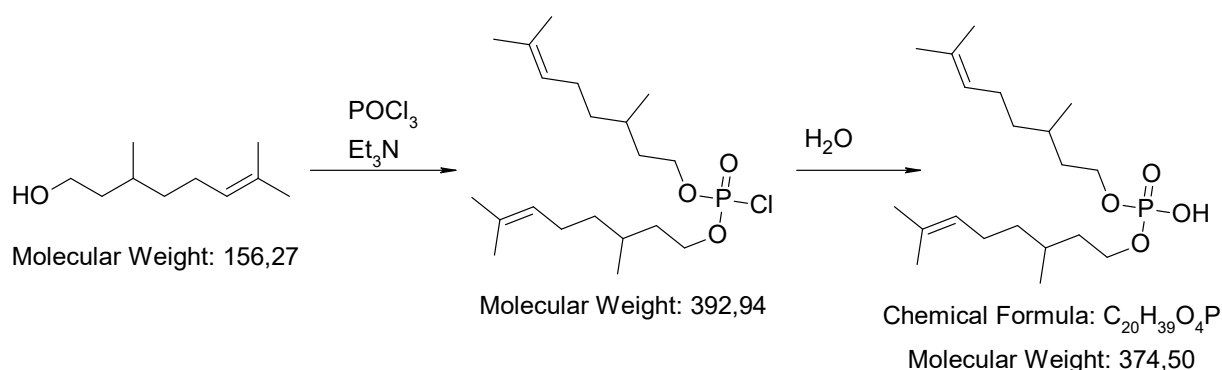
Figure 89. Reaction scheme for the synthesis of transesterification catalyst CitrP.

A yellowish oily liquid was obtained as an end product. The success of the synthesis procedure was analyzed by composition of the product, which was analyzed using ^{1}H-NMR spectroscopy.

^{1}H NMR (400MHz, CDCl$_3$): δ [ppm] = 5.07-4.98 (m, 1H); 4.26-3.94 (m, 2H); 2.03-1.83 (m, 2H); 1.80-1.22 (m, 10H); 1.21-1.05 (m, 1H); 0.93-0.78 (m, 3H).

Synthesis of acrylated eugenol (AEUG)

Acrylated eugenol (AEUG) was synthesized by reacting eugenol with acrylolchloride (Figure 90). 60 mL of dry stabilized tetrahydrofuran (THF) was added in a three necked round bottomed flask. Afterwards, eugenol and Et$_3$N were added and the mixture was stirred for 10 minutes. Sidewise, acryloyl chloride was diluted with 10 mL dry THF and added dropwise over a time period of 30 minutes into the prepared eugenol mixture. The mixture was stirred at room temperature for 5 hours. Afterwards, the precipitated salt was filtered out and the solvent was evaporated.
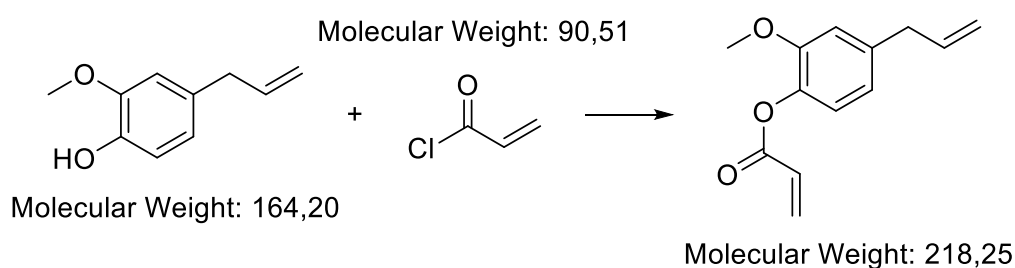
Figure 90. Reaction scheme for synthesis of reactive diluent AEUG

The success of the synthesis procedure was analyzed by composition of the product, which was analyzed using ^{1}H-NMR spectroscopy.

^{1}H NMR (300 MHz, CDCl$_3$): δ [ppm] = 6.98 (d, J=8.16Hz, 1H); 6.84-6.71 (m, 2H); 6.61 (dd, J=17.34 Hz, 1H); 6.3 (dd, J=17.34 Hz, 1H); 6.03-5.85 (m, 2H); 5.16-5.01 (m, 2H); 3.77 (s, 3H); 3.37 (d, J=6.64 Hz, 2H).

7.1.2. Preparation of resin formulations and DLP 3D-printing

The resin formulations contained acrylated epoxidized linseed oil (AELO), mixed with acrylate eugenol (AEUG) serving as a reactive diluent. Additionally, two different transesterification catalysts were used, namely eugenol ester phosphate (EUGP) and citronellol ester phosphate (CitrP), along with BAPO as a photoinitiator (2 wt.%) and Karmin (0.02 wt.%) as a natural pigment. A variety of resin formulations with varying ratio between AELO and AEUG were prepared and are exhibited in Table 8.

Table 8. Composition of resin formulations based on AELO and AEUG. All resins consisted of 2 wt.% BAPO and 0.02 wt.% Karmin. R represent the reference samples without catalyst.

Resin formulation	AELO (wt.%)	AEUG (wt.%)	Catalyst (wt.%)
EUGP_A25:E75	AELO (25%)	AEUG (75%)	EUGP (4.5%)
EUGP_A50:E50	AELO (50%)	AEUG (50%)	EUGP (4.5%)
EUGP_A75:E25	AELO (75%)	AEUG (25%)	EUGP (4.5%)
CitrP_A25:E75	AELO (25%)	AEUG (75%)	CitrP (4.5%)
CitrP_A50:E50	AELO (50%)	AEUG (50%)	CitrP (4.5%)
CitrP_A75:E25	AELO (75%)	AEUG (25%)	CitrP (4.5%)
R_A25:E75	AELO (25%)	AEUG (75%)	-
R_A50:E50	AELO (50%)	AEUG (50%)	-
R_A75:E25	AELO (75%)	AEUG (25%)	-

All the liquid resin formulations were mixed for 30 minutes in light protected glass vials using an ultrasonic bath at 30 °C, followed by mixing on a magnetic stirrer for another 60 minutes at 30 °C and 500 rpm.

3D-printing of the resin samples was carried out using a Photon Mono printer (Anycubic, China), provided with a visible light illumination source of 420 nm. The exposure times for bottom layer and subsequent normal layers were set on the basis of FTIR kinetics and corresponded to 35 seconds and 25 seconds, respectively. The rising and retracting speeds of the printing platform were set to 1 mm.s^{-1} with a rising height of 6 mm.

7.1.3. Fourier-transform infrared spectroscopy

To monitor the progress of the light-induced curing reaction, Fourier transform infrared radiation (FTIR) spectroscopy was performed using a Vertex 70 spectrometer (Bruker, USA). The transmission mode was used and 16 scans were measured from 4000 to 700 cm^{-1}, with a resolution of 4 cm^{-1}. Liquid resins (1.2 µL) were spin-cast on silicon wafers. Kinetics studies were carried out by illuminating the casted resins under a visible light LED Control 5S lamp (Opsytec Dr. Groebel, Germany) with a power density of 3.8 mW.cm^{-2}. The irradiation was carried out under inert conditions. The normalized peak areas of the acrylates' C=C bonds at 1635 cm^{-1} were calculated using OPUS software to estimate the reaction conversions. The C=O

peak (1750 cm^{-1}) was used as reference. To measure the FT-IR spectra of thermally post-treated materials, a reflection diamond attenuated total reflection (ATR) accessory (Platinum ATR) was utilized and transmission spectrum measurements were recorded in the range of 4000^{-1} to 700 cm^{-1}.

7.1.4. Characterization of network properties

A Mettler Toledo (United States) TGA thermogravimetric analyzer was used to perform Thermogravimetric Analysis (TGA) under N$_2$ atmosphere. The samples were heated from 30 ° to 500 °C at a heating rate of 10 °C.min^{-1}.

Dynamic mechanical analysis of the 3D-printed samples (20 mm x 4 mm x 1.5 mm, l x w x h) was performed to determine the glass transition temperature (T$_g$) and storage modulus of the cured resins. For this purpose, a DMA/SDTA861e (Mettler-Toledo GmbH, Switzerland) with a heating rate of 10 K.min^{-1} was used. The measurement runs were recorded between -50 °C and 150 °C using a frequency of 1 Hz and maximum amplitude of 3 μm in tensile mode.

To determine the gel content of the cured networks, circular disks (10 mm x 1 mm) were immersed in dichloromethane for 48 hours. After removing the samples and drying the surface with a tissue paper, the samples were weighed (m$_{sw}$) and then placed in an oven at 40 °C for 24 hours until a constant weight was achieved (m$_{dry}$). The gel content of the network was calculated as the ratio of the two weights (m$_{dry}$/m$_{sw}$).

The resolution of the DLP 3D-printed samples was analyzed by an optical microscope (Olympus BX 51, Tokyo, Japan) equipped with an integrated software Color View IIIu digital camera (Soft Imaging System, Münster, Germany).

7.1.5. Stress relaxation and rheological measurements

The viscosity of the resins was assessed using a compact modular rheometer (MCR 102 Anton Paar, Austria) with a CP60-0.5/TI cone that had a diameter of 49.97 mm and an opening angle of 1.982°. The measurements were conducted at 30 °C with a shear rate ranging from 0.1 to 300 s^{-1}, and 1.2 mL of each liquid resin was used.

To measure the stress relaxation of the DLP 3D-printed circular disc samples (10mm x 1mm), another rheometer device (Anton Paar Physica MCR-501, Austria) was employed. The measurements were taken at temperatures between 140 °C and 200 °C. Before the start of the recording, the samples were equilibrated at a force of 20 N for 20 minutes at the measurement temperatures. At a fixed temperature, the disc samples were subjected to a 3% strain in a parallel

plate configuration and the decreasing stress was recorded over time. Stress relaxation time was determined when the descending stress reached 37% of its initial value.

7.1.6. Thermal healing and shape memory

Using the resin formulation EUGP_A50:E50, experiments were conducted on DLP 3D-printed rectangular bars (30 mm x 10 mm x 0.5 mm, l x w x h). A small scratch was introduced on the top surface using a sharp blade at room temperature and the scratch was characterized by optical microscopy. The damaged sample was clamped and pressed between two glass slides with end-metallic clips, followed by thermal treatment for 4 hours at 180 °C in an oven. The healing of the samples was determined optically by examining the thermally treated samples under the microscope.

Shape memory experiments were performed on rectangular bar samples that were 3D-printed and had dimensions of 70 mm in length, 10 mm in width and 1 mm in thickness. The first shape of the material was fixed by heating up the stripes at 180 °C for 2 hours along with a deformation, followed by cooling to 20 °C. For the second shape, the strips were further reshaped at 70 °C in an oven and cooled down to 20 °C. The first shape was regained within 60 seconds by exposing the gripper again to 70 °C.

To further exploit the shape memory concept, a honey comb structure was DLP 3D-printed in dimensions of 25 mm x 29 mm x 2 mm (l x w x h). Specimens were thermally treated for 2 hours at 180 °C by applying compression along the x-axis, followed by cooling to 20 °C. The second shape of the honey comb was programmed by heating it further in the oven at 70 °C and applying compression along the y-axis, and cooling down to 20 °C. Shape recovery of the second programmed structure was achieved by heating the specimen at 70 °C, leading to the recovery of first shape without applying any external force.

7.2. Results and discussion

7.2.1. Network curing and DLP 3D-printing of resin formulations

To reduce the carbon foot print of the photocurable vitrimers, biologically abundant raw materials were exploited as starting materials to synthesize novel acrylic monomers and transesterification catalysts. To achieve this target, fully bio-based epoxidized linseed oil was employed as a starting material and modified to acrylated epoxidized linseed oil as described in the aforementioned sections (Chapter 6). In addition to that, eugenol acrylate was synthesized as a reactive diluent to support the network formation and reduce the viscosity of the photocurable resin formulations. As previously deliberated in chapter 6, the acrylated linseed

oil resin formulations benefited from the abundance of hydroxy and ester moieties that could undergo efficient dynamic transesterification by employing an appropriate catalyst at elevated temperatures. Although mineral phosphates are commonly employed as heterogeneous catalysts for transesterification reactions in solution [358,359], the stress relaxation data of previous work provided clear evidence that organic alternatives are capable of effectively catalyzing transesterification within cured polymer networks. The mono and diesters of phosphoric acid possess free -OH groups and can act as potent Brønsted acids, enabling them to catalyze transesterification reactions [360].

To further discover the salient features of these phosphate esters in photocurable resin formulations and decrease the reliance on fossil-fuel derived chemicals, two new bio-sourced catalysts were synthesized by reacting phosphorous oxychloride across eugenol and citronellol. The synthesized catalysts presented a bio-based alternative to conventional transesterification catalysts. Furthermore, the presence of vinyl monomers ensured the efficient integration of the catalysts in the photopolymers during network evolution (Figure 91).
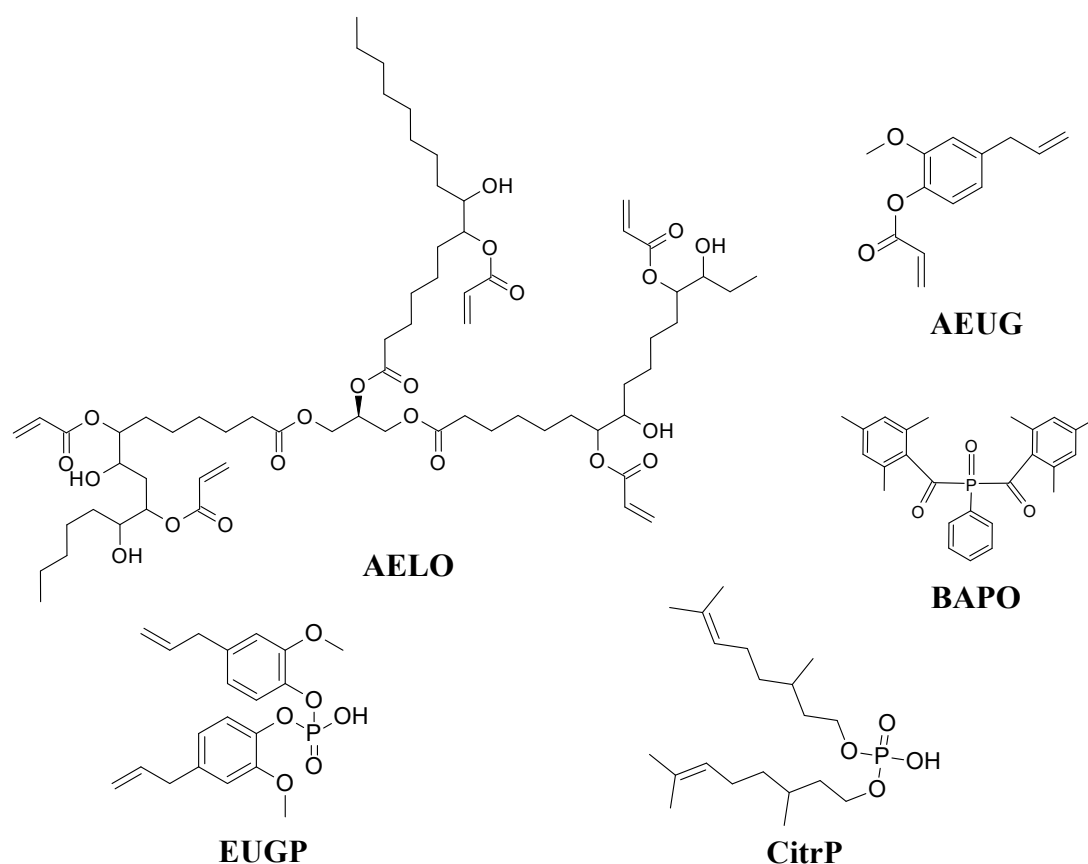
Figure 91. Chemical structures of the components used for the bio-based resin formulations under investigation.

Following a free radical chain-growth reaction of the acrylate groups, the resin formulations were cured under visible light exposure using BAPO as a radical photoinitiator. The curing kinetics was monitored by following the intensity of the characteristic C=C wagging bands at 1635 cm^{-1} as a function of the exposure dose (Figure 92b and c).
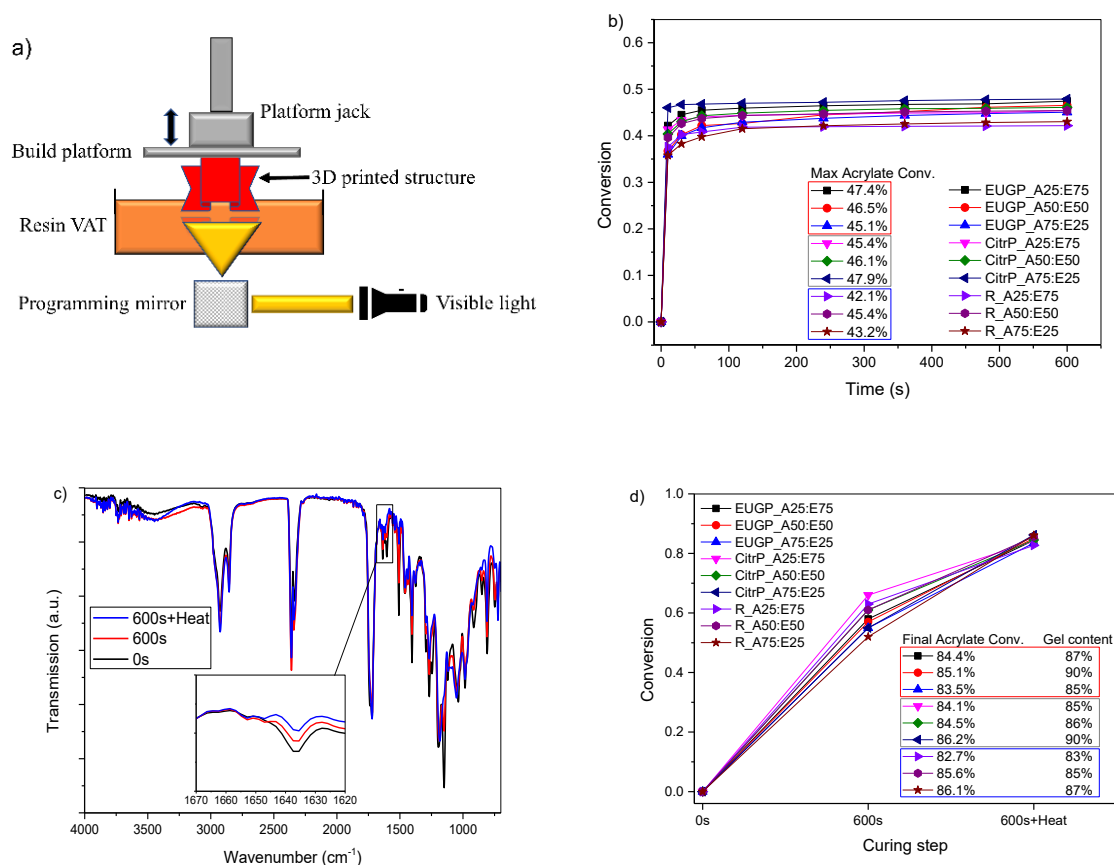
Figure 92. (a) Schematic presentation of DLP 3D-printing setup. (b) FTIR kinetics of resin formulations as a function of composition versus exposure time. Reaction conversions were obtained by integrating the area of the C=C peak at 1635 cm^{-1} using OPUS software. Inset tables represent the maximum acrylate conversion achieved after 600 s. (c) ATR spectra of EUGP_A50:E50: uncured (0 s), illuminated (600 s) under visible light prior to and after thermal post-treatment (180 °C for 20 mins). The inset plot presents the zoom-in image of the C=C peak. (d) C=C bond conversions of resin formulations as a function of composition over 600 s illumination and after 20 minutes thermal post-treatment at 180 °C. Inset tables represent the maximum acrylate conversions and gel contents of the cured networks achieved after thermal treatments.

The acrylate conversion in both catalyzed resin formulations was in the range of 45 – 47%, which was considerably lower in comparison to a typical thiol-acrylate formulation (Figure 92b) [135,352]. Both catalyzed resin formulations predominately consisted of plenty of acrylates and vinyl bonds which follow the chain-growth addition polymerization under visible light irradiation. The radicals formed during photoinitiation and cleavage of BAPO, activate the unsaturated C=C bonds in the resin formulations and propagate abruptly with the vicinity monomers and result into rapid gelation of the network. Furthermore, the fast addition reaction governed by acrylate moieties results in a diffusion limited regime, where the unreacted monomers are trapped by the poor mobility of the system [361]. This was also confirmed by the FTIR kinetics, when the resin formulations reached around 40% conversions during the initial 20 seconds of illuminations (Figure 92b). In addition, all resin formulations contained abundance of vinyl groups being contributed by the reactive diluent AEUG, transesterification catalysts EUGP and CitrP, which are well known for their poor reaction kinetics in radical-mediated chain-growth reactions.

The presence of carbonyl groups in acrylates enhances the reactivity of the unsaturated C=C bonds and hence the acrylates will mainly participate in the chain-growth reaction in the resins under investigation. These results are also in accordance with the study of Hoyle et al., who report that in an acrylate-vinyl reaction system, the acrylate monomers reached up to 80% conversion during photoirradiation, while vinyl monomers hardly reached 10% bond conversion under the same irradiation conditions.

Furthermore, it is also well documented that the vinyl groups show much less reactivity and remain as pendant side group [361–365]. On the other hand, the acrylates' dominated addition polymerization results in cured networks typically possessing heterogenous set of properties and develop stiffer materials than thiol-ene counterparts [23,135,321,321].

In addition, the reference formulations without containing any transesterification catalyst, did not exhibited better reaction conversions and also suffered from lower bond conversions ranging from 42 to 45% for all the resin combinations (Figure 92b).

To overcome the low reaction conversion of the monomers, the resin formulations were thermally treated at 180 °C for 20 minutes after photo-illumination. Samples were cured in the form of circular discs (d = 10 mm, h = 0.4 mm) and ATR FTIR spectra of the thermally post-cured samples revealed that the samples reached up to 81% bond conversions after 20 minutes of post-treatment (Figure 92c). For analytical demonstration purpose, silicon wafers were

casted with the resin formulations and IR spectra were recorded prior to and after 600 s of visible light irradiation (Figure 92d). The coated silicon wafers were then subjected to a thermal treatment in an oven at 180 °C for 20 minutes followed by the measurement of FTIR spectrum. The C=C bond conversions of all the resin formulations ranged between 82 – 86% after thermal treatment (Figure 92d).

To further evaluate the network evolution, the gel content of the thermally post-treated samples was measured by immersing the samples in DCM for 48 hours. All the cured samples presented gel contents ranging between 82 to 90%, which confirms the high final bond conversions of the thermally cured samples observed in FTIR studies.

7.2.2. Stress relaxation kinetics of the networks

To evaluate the catalytic activity of the synthesized phosphate ester compounds within the resin formulations, temperature-dependent stress relaxation properties were studied. Samples were DLP 3D-printed with each resin formulation and the normalized storage modulus was monitored. The resin formulations containing EUGP were measured within a temperature range of 160 °C and 200 °C. Although the networks were physically quite stiff, the bond exchange reactions were efficiently catalyzed and the initial stress could be relaxed to 37% within a period of 33 minutes at 200 °C and 140 minutes at 160 °C (Figure 93a). As a characteristic property of vitrimers, the bond exchange reactions became faster with the increasing application temperature and hence a temperature dependent relaxation behavior was recorded and presented in (Figure 93a and Figure 93b).

Figure 93b, exhibits the relaxation times plotted against the measurement temperature (1/T) in a semilogarithmic manner, resulting in a linear trend for all the measurement temperatures (between 160 °C and 200°C), and confirms the vitrimeric nature of the networks by proving the Arrhenius dependent response with an activation energy of 62.04 KJ.mol^{-1} [252,366].

Along with EUGP, the stress relaxations for CitrP catalyzed system and non-catalyzed reference system were determined at 180 °C. The acrylate based photocured networks are known to exhibit some thermal relaxations at high enough temperatures, even in the absence of any transesterification catalyst, due to the release of volumetric shrinkage stresses incorporated during network formation [128,355]. These relaxations could be released during stress relaxation measurements but were insufficient to relax up to 37% level at an appropriate rate (Figure 93c). The dynamic transesterification reactions were only initiated at high temperatures

in the presence of suitable catalysts, as presented in Figure 93c by EUGP and CitrP at the same measurement temperature (180 °C).
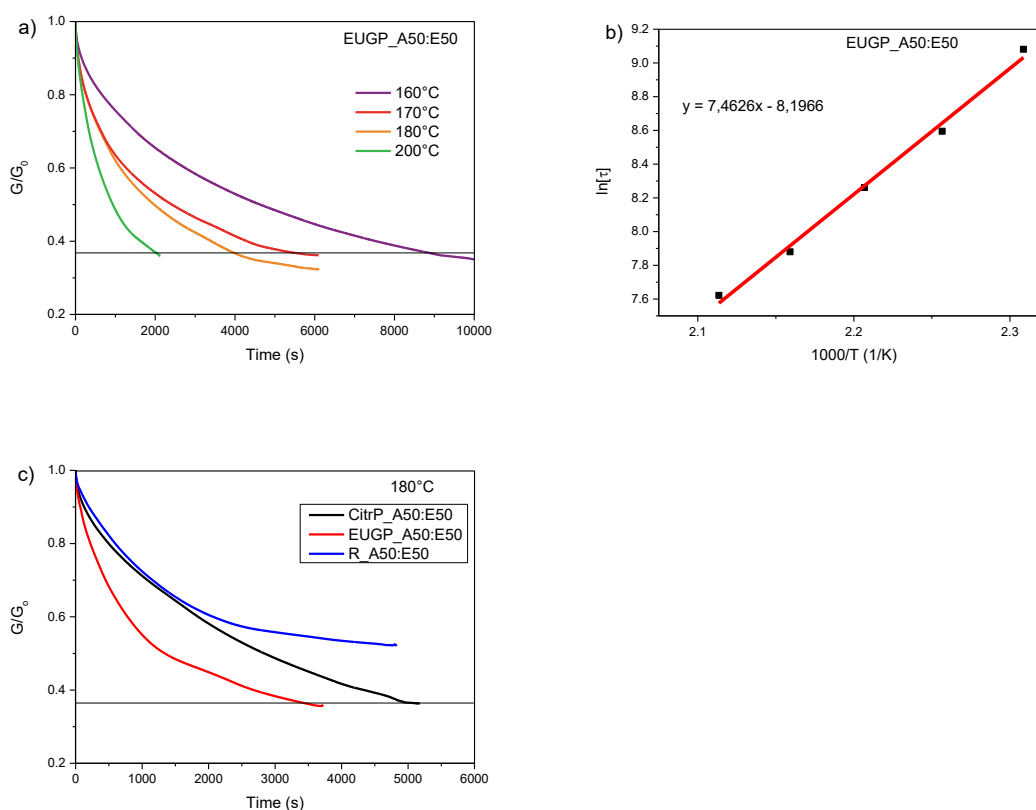
Figure 93. (a) Normalized stress relaxation plot of samples developed using EUGP_A50:E50, as a function of temperature. (b) Arrhenius plot of the EUGP_A50:E50, confirming the linear temperature dependent behavior. (c) Normalized stress relaxation results of CitrP_A50:E50 and R_A50:E50 based samples in contrast to EUGP_A50:E50 measured at 180°C.

Additionally, the slower stress relaxation behavior in CitrP catalyzed network at 180 °C leading to 37% relaxation after 80 minutes, in contrast to EUGP (37% relaxation at 180 °C in 63 minutes), presented EUGP as the most suitable catalyst with capability to induce fast dynamic reactions. These fast transesterification reactions in EUGP could be contributed by the existence of electrophilic benzyl groups coupled with the phosphate moieties, which can increase the acidity of phosphate ester catalysts, and hence can increase the transesterification efficiency, in contrast to CitrP which involves aliphatic chained segments.

Additionally, the thermal stability of the network was evaluated by performing TGA studies, which revealed that the formulations remained stable until 180 °C, after which a gradual mass loss was observed, which could be contributed by the presence of free unreacted monomers

[367]. Although the sharp mass loss observed after 300 °C (Figure 94) represented the high stability of the networks.
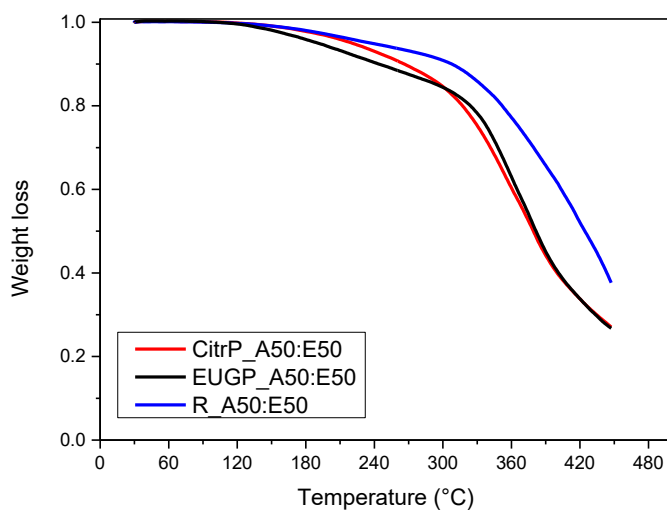
Figure 94. TGA plot of CitrP and EUGP catalyzed formulation in comparison with the reference formulation.

7.2.3. Network characteristics

Dynamic mechanical analysis of the DLP 3D-printed samples was performed to characterize the thermomechanical behavior of the networks. As EUGP catalyzed resin formulations offered the fastest relaxation kinetics, DMA characterization and further studies were performed on EUGP-based formulations. The broad tan delta peaks measured for all monomer combinations confirmed the heterogenous nature of the cured networks (Figure 95). The EUGP resin formulation containing 25% AELO had the tan delta peak at 59 °C with a storage modulus of 645 MPa at 25 °C, in comparison to the 50% AELO formulation, that exhibited a tan delta peak maximum at 68 °C with a corresponding storage modulus of 884 MPa at room temperature (Figure 95). For the resin formulation containing 75% AELO, we observed a higher degree of heterogeneity with a very broad tan delta peak. The tan delta peak presented a wide plateau between 55.9 – 80.1 °C, with a storage modulus of 858 MPa at 25 °C, which was slightly lower than the 50% AELO formulation (Figure 95). The increase in the network's T_g and storage modulus, while switching from 25% AELO to 50% AELO composition correlates well with the fact that acrylate-based networks form typically stiffer and heterogenous networks, and the stiffness increases with the increasing acrylate content, as they are the active components in the chain-growth reactions. Likewise, 75% AELO formulation presented a very broad glass

transition region till 80.1 °C but a slightly lower storage modulus than 50% AELO composition, could be contributed by the localized regions of varying crosslinking density, evolved due to the diffusion constrained photopolymerization.
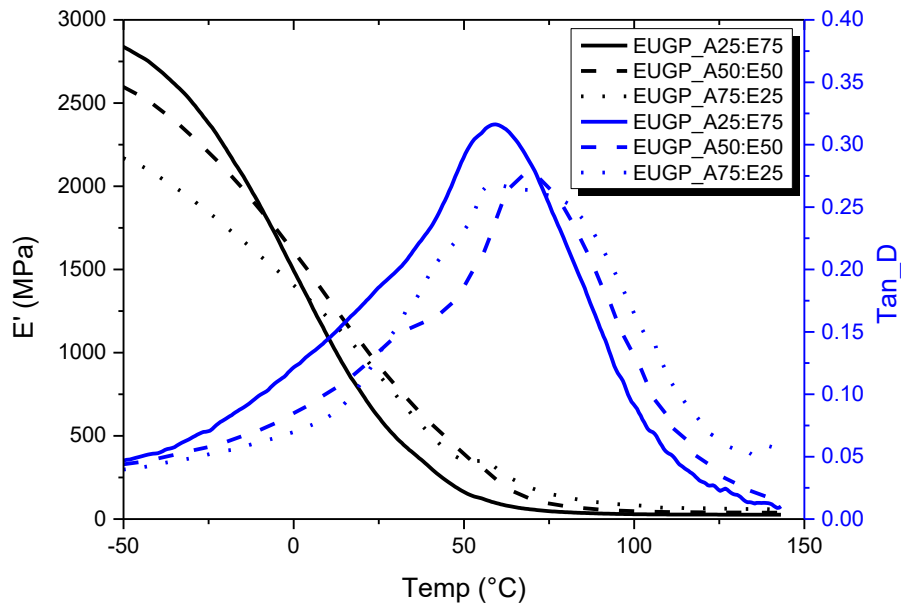
Figure 95. Tan delta and storage modulus curves of EUGP catalyzed resin formulations as a function of the chemical composition obtained between -50 °C and 150 °C.

Furthermore, the viscosities of the A50:E50 resin formulations, containing EUGP, CitrP and without catalyst were also determined at 30 °C and the results showed that the reference formulation had a viscosity of 804 mPa.s (shear rate ranging from 0.1 to 300 s^{-1}), in contrast to the resin formulations containing EUGP and CitrP having viscosities of 880 mPa.s and 864 mPa.s respectively, under the same measurement conditions. The addition of catalysts in the formulation slightly increased the viscosity but the deviation was not large enough to impact the printability of materials. Hence, EUGP being the superior performance catalyst was exploited for further processing.

7.2.4. Shape memory and thermal healing

As discussed in the previous sections, one advantage of vitrimers is their ability to show macroscopic reflow at sufficiently high temperatures (above T_v) making them suitable for special applications such as damage healing and structural reorientations. Among the studied bio-based resins, EUGP_A50:E50 was selected for further DLP 3D-printed specimens' development along with shape memory and thermal healing experiments.

Initially, bar structures with a length of 70 mm, a width of 10 mm and a thickness of 1 mm were DLP 3D-printed (Figure 96a) The fully cured samples were heated at 180 °C for 2 hours and the first shape was programmed. The sample was removed subsequently from the oven and cooled down to room temperature. After cooling, the sample was reheated and reshaped into a bent hook structure at 70 °C which was above the T_g of the material. Removing the specimen form heat in deformed condition and cooling to room temperature fixed the second shape (Figure 96a). Heating the samples above 70 °C returned the specimen to the first programmed shape, and subsequently reheating the sample at 180 °C for 4 hours under deformation, returned the permanent shape of the material (Figure 96a).

In addition, the application of a hook structure (Figure 96b) for lifting and releasing a circular ring was also realized with the help of shape memory experiments, where the second programmed shape could release the gripped O-ring under application of temperature and the return to its first programmed shape without any external deformation force (Figure 96b).
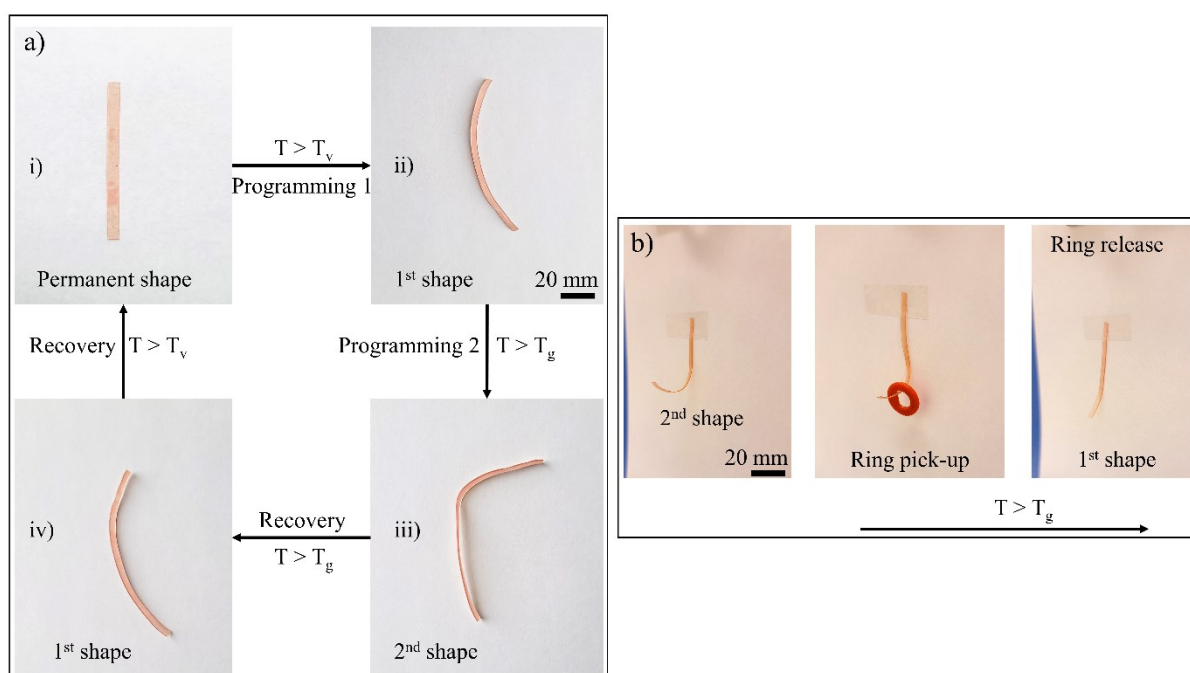
Figure 96. (a) (i) Permanent shape of a DLP 3D-printed bar for shape memory experiments using EUGP_A50:E50 formulation. (ii) Heating the specimen and bending it at 180 °C for 2 hours, cooling down to room temperature and fixing the first shape. (iii) Heating of sample and bending further at 70 °C for 10 minutes and subsequently cooling down to room temperature with force removal giving the second shape. (iv) Recovery of first shape by heating the second programmed shape at 70 °C for 60 seconds. (b) Application of second programmed shape for lifting an O-ring and releasing it under application of heat via shape recovery.

To further exploit the shape memory features, a complex honey comb structure (25 mm x 29 mm x 2 mm) as shown in Figure 97a was DLP 3D-printed. As the first programming stage, the honey comb was compressed along its x-axis at 180 °C for 4 hours, following by cooling down to room temperature and removal of the force, fixing shape 1 (Figure 97b). For the next programming stage, the shape 1 was heated to 70 °C and compressed along y-axis. Subsequent cooling of the specimen to room temperature fixed the programmed shape 2 (Figure 97c). The recovery of shape 1 was achieved, by heating the sample again at 70 °C for 60 seconds (Figure 97c).
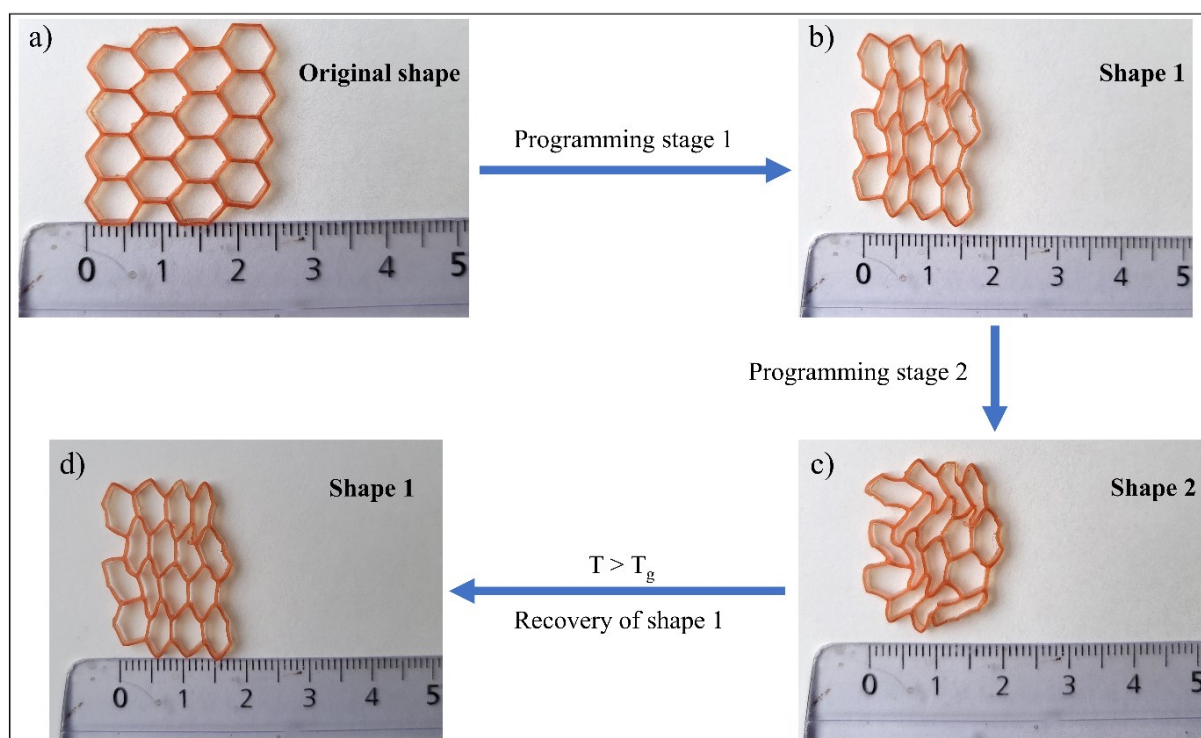
Figure 97. (a) Permanent shape of a DLP 3D-printed honey comb's structure using EUGP catalyzed A50:E50 resin. (b) Programmed shape at 180 °C, followed by cooling to room temperature. (c) Shape 2, programmed by heating sample to 70 °C and cooling down after programming. (d) Recovery of shape 1 by heating shape 2 above T_g.

In addition to shape memory, thermal healing and macroscopic reflow of the material was also visually evaluated during mending of a scratch inserted in a DLP 3D-printed rectangular bar (30 mm x 10 mm x 0.5 mm) (Figure 98a). For the healing, the scratched sample was pressed between two glass slides and clamped from both ends using a metal clip.
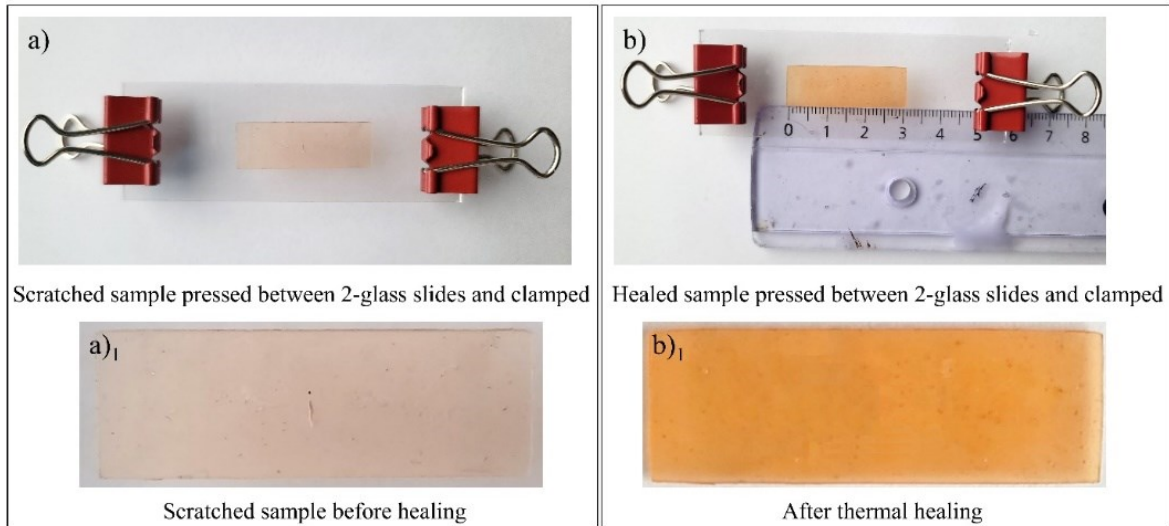
Figure 98. (a) DLP 3D-printed sample marked with a scratch at the center, in which (a)$_1$ presents the sample's zoomed-in image with scratch marked in the center. (b) Sample thermally healed at 180 °C in clamped condition between two glass slides, (b)$_1$ represents the zoomed-in optical image of the after treated sample.

To investigate the thermal healing process, optical micrographs were taken from the damaged and thermally healed samples and the length of the scratch was measured prior to and after the thermal treatment. The initial scratch was 1221 µm in length (Figure 99a).
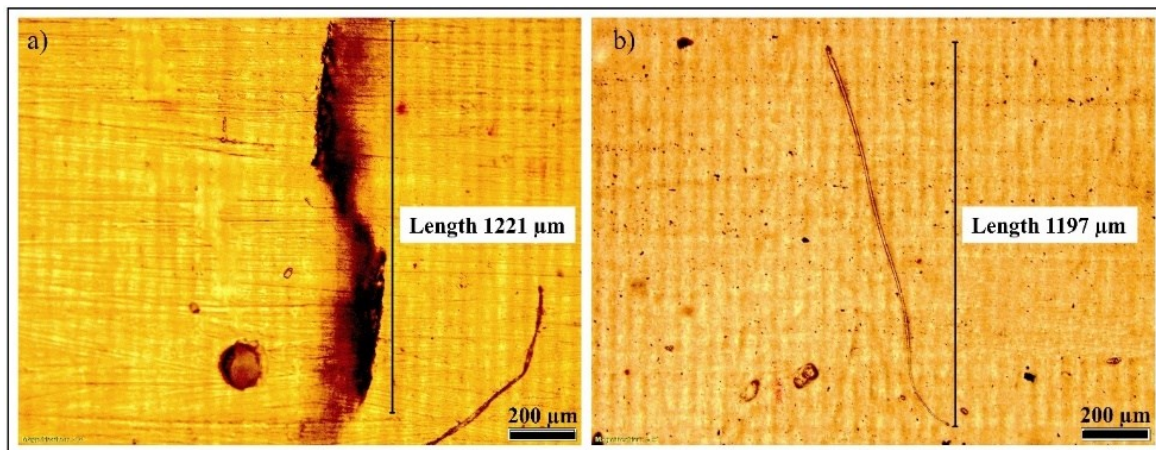
Figure 99. (a) Microscopic images of the top surface of the DLP 3D-printed rectangular sample using EUGP_A50:E50 resin formulation and marked with a scratch at the center. Scratch length was measured by the analytical software integrated with the microscope. (b) Microscopic image of the scratched specimen after thermal treatment at 180 °C for 4 hours.

After thermal treatment at 180 °C (4 hours), only a small scratch mark of almost the same length (1197 µm) was observed on the surface at the same location (Figure 99b). The microscopic

138

experiments also proved the excellent transesterification induced thermal reflow of the network, efficiently healing the damaged area.One of the distinguishing features of the DLP 3D-printing technology is its excellent material resolution and surface finishing in contrast to other additive manufacturing technologies. To test the resolution of the bio-based resin formulations, a comb structure with circular cavities of different sizes was DLP 3D-printed (Figure 100a). The sizes of the cavities were analyzed under optical microscope and images of the minimum achievable holes are presented in Figure 100b. EUGP_A50:E50 exhibited a good 3D-printability and enabled the development of structural patterns up to 461 µm, after which the material started to lose resolution. Furthermore, the teeth of the resolution test comb were designed in a descending size order and the smallest teeth corresponded to a width of 500 µm (and length of 3 mm) which was magnificently translated during DLP 3D-printing, and also highlights the high-resolution printing potential using bio-based resin formulations.
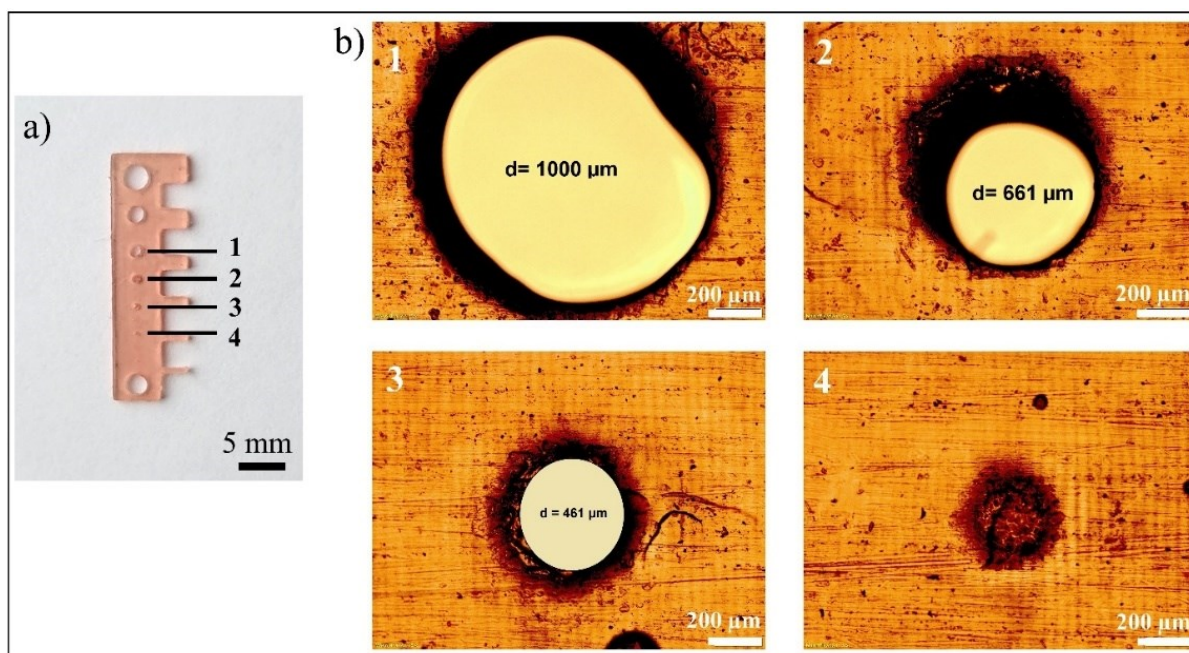
Figure 100. (a) DLP 3D-printed comb structure for the resolution testing using EUGP_A50:E50 resin formulation. (b) Microscopic pictures of the corresponding circular cavities 1,2,3 and 4.

7.3. Conclusion

The research work involved the synthesis of monomers for DLP 3D-printing, that could be easily derived from bio-renewable resources and exhibited a great independency from fossil fuels. The idea of developing fully bio-based networks was realized by synthesizing eugenol acrylate and acrylated linseed oil. To further increase the functionality of the final materials and take advantage of the ester and hydroxy moieties in the resin formulations, two different

phosphate ester catalysts derived from biologically abundant eugenol and citronellol were synthesized. The synthesized organic phosphate ester catalysts acted as Brønsted acids and were well soluble in the resin formulations. Various combinations of resin formulations and catalyst monomers were developed and compared with the non-catalyzed reference systems. All the resin formulations exhibited fast curing kinetics but the final conversions were controlled by the diffusion dominated regime, as the network evolution followed the chain-growth polymerization mechanism and resin formulations provided abundance of acrylate and vinyl groups, which typically suffer from low reactivity and fast gelation. Thermal post-treatment of the networks was carried out to increase the final monomer conversions. Highly crosslinked networks with glass transition temperatures ranging between 59 °C and 80 °C were obtained. Furthermore, stress relaxation experiments also revealed a rapid stress relaxation of the networks governed by the thermo-induced transesterification reactions, but the better performance of EUGP catalyzed system in contrast to CitrP and reference resin convinced for continuation of further 3D-printing works with EUGP catalyzed resin formulations. Thanks to the vitrimeric nature of the networks, which was proved by the Arrhenius nature of thermal response, shape memory programming steps could be carried out using vitrification temperature in addition to the network's glass transition temperature. As a result, 3D-printed structures revealed a full shape recovery when exposed to the temperatures above transition states, leading to the carrying and releasing of real-life objects. Furthermore, thermal healing experiments exhibited an excellent reflow and healing of the marked scratch monitored under the microscope. High printing resolution (up to 461 µm) of bio-sourced resin formulation, coupled with the additional functionalities and dynamic nature of the networks resulted in efficient crosslinking and functional materials development with great applicability in soft-robotics.

8. Conclusions and outlook

The current thesis covers a range of strategies for the development of stimuli responsive materials processable via vat photopolymerization DLP 3D-printing. The integration of suitable catalysts in the developed photoreactive resin formulations did not only result in a stimuli responsive behavior, but also resulted in a thermal reflow and reprocessing of the materials above their topological freezing temperature (T_v) of otherwise non-reprocessable and covalently crosslinked polymer networks.

As an initial aspect, the salient features of thiol-acrylate click chemistry were employed to design DLP 3D-printable resins with dynamic covalent bonds. A vast variety of thiols and acrylates along with a phosphate ester acting as transesterification catalyst were systematically combined and curing kinetics, thermo-mechanical properties and temperature-dependent bond exchange kinetics were studied in detail. All dynamic photopolymers exhibited fast curing and good printability with a T_g ranging from -7 ° to 50 °C. In addition, the presence of hydroxy and ester moieties in the designed resins led to fast transesterifications at sufficiently high temperatures, which rendered the network healable above T_v. Along with acting as catalyst for transesterifications, the organic phosphate served as stabilizer for the thiol-acrylate resins, which benefited from a high storage stability. The fast cure rate, high shelf life together with the high printing resolution (feature sizes of 400 μm could be printed) enabled the fabrication of 3D-actuators using the DLP 3D-printing technology. The actuators did not only exhibit excellent shape memory and thermally induced contraction-expansion features, but also offered a great thermal heal-ability for repairing damages, which were inflected into the soft active devices.

Advancing from single material printing of healable soft actuators, dual-vat DLP 3D-printing was employed using the developed resins' library, to realize sophisticated actuators consisting of soft and hard material domains during one printing process. Such an approach enables to take advantage of different material features deployed at localized areas and allowed the development of multi-material prototypes in the form of a circular wheel. The inner structural support was photopolymerized with EGMA-PT3A having a T_g of 43 °C, while the outer wheel part along with the interconnecting linkages were printed with EGMA-HP1A resin having a T_g of -3 °C. The multi-material wheel structures acted as shock absorbers, due to the flexibility of the soft outer material, and the material could undergo various cycles of deformation and retraction without any physical damage. Moreover, multi-material semi-circular grippers consisting of a stiff outer housing from EGMA-PT3A and soft internal teeth from EGMA-

HP1A were manufactured by dual-vat 3D-printing. The grippers were easily programmed above room temperature using the T_g of EGMA-PT3A for shape memory, while the inner material remained soft and efficiently gripped strawberries without any damage. Subsequent heating of the gripper resulted in a release of gripped strawberries by shape recovery. Along with shape memory properties, the dynamic thiol-acrylate photopolymers were also characterized with good stress relaxation kinetics. Thus, damaged grippers were healed at elevated temperature using the macroscopic flow induced by catalyzed transesterification reactions. The healed gripper exhibited a performance and gripping which was comparable to the pristine material and gives evidence of the high healing efficiency of the developed photopolymers.

To locally control the bond exchange reactions, latent transesterification catalysts were used in a further work on dynamic thiol-acrylate networks and employing a dual wavelength 3D-printer, equipped with two different light sources: UV (365 nm) and visible (405 nm) light. To ensure a sequence dependent orthogonality between the curing and activation reaction, triphenylsulfonium salts were applied as photolatent acids, which could be selectively activated under UV (365 nm) light and released strong Brønsted acids. The photolatent catalysts were transparent in the visible (405 nm) light region, which allowed a visible light induced curing of the thiol-acrylate resin without premature activation of the catalyst. However, research revealed that the bond exchange rate did not increase proportionally with the acidity of liberated acid or the counter-anion's size as the use of photolatent catalysts is more complex compared to classical Brønsted acids. This is attributed to the relatively low thermal stability of the produced Brønsted acids ($HSbF_6$ and HPF_6), which readily convert to HF at elevated temperatures, as well as the quicker migration of acids with smaller anions. Conversely, stress relaxation experiments demonstrated a strong correlation between the bond exchange rate, the quantum yield and the rate of acid formation in corresponding triphenylsulfonium triflates. PDS-triflate was determined to be the fastest and most stable photolatent acid, which was also employed in DLP 3D-printing of actuators with spatially illuminated and activated catalyst regions. This enabled the fabrication of materials, with localized variation in properties. Whilst T_g based shape memory could be realized in the whole actuators, T_v based transitions were only activated and observed in the catalyzed (UV-irradiated) domains of the actuators, which led to the formation of spatially controlled actuation systems.

To mitigate or at least reduce the environmental impact of the photocurable resin systems, efforts were also made to develop greener alternatives that could be reasonably 3D-printed and

contain dynamic covalent bonds. This was realized by chemically converting a fully bio-based epoxidized linseed oil to an acrylated epoxidized linseed oil by ring-opening polymerization reaction of the epoxy groups. To reduce the viscosity of the developed monomers and taking advantage of the thiol-acrylate click chemistry, a relatively small quantity of different thiol crosslinkers was added. Subsequently, two different dynamic thiol-acrylate photopolymers having a T_g of -18 °C and -10 °C were prepared. The resins did not only contain more than 65 wt% bio-derived building units, but also underwent efficient stress relaxations via thermally activated transesterification. Soft actuators with triple shape memory were successfully DLP 3D-printed, which were thermally healable (180 °C for 4 hours).

To further improve the share of bio-based building blocks in dynamic photopolymers, naturally abundant monomer such as eugenol and citronellol were equipped with functional acrylate and phosphate groups. The synthesized acrylates monomers were used as reactive diluents and combined with acrylated epoxidized linseed oil. Following the idea of a complete bio-based model resin system, eugenol phosphate and citronellol phosphate also provided a greener alternative to conventional transesterification catalysts, and acted as Brønsted acids at elevated temperatures. The curing studies revealed fast reaction kinetics of the acrylate resin systems, but diffusion-controlled reaction regime was observed in all resins on account of the chain-growth polymerization reaction. Thermal post-curing resulted in fully cured networks with great stability at room temperature, and a T_g in the range of 59 °C to 80 °C. The good printing resolution, low viscosity and excellent stress relaxation kinetics facilitated the printing of soft active devices with triple shape memory properties employing T_g and T_v. Moreover, efficient catalyst activity and abundance of free hydroxy and ester moieties resulted in a thermal reflow and efficient healing of cracks and damages inserted in the DLP 3D-printed photopolymers.

The combination of these additive manufacturing methods and advanced resin formulations presents a compelling alternative to traditional polymers and their processing. These approaches demonstrate network adaptability and allow for thermal reflow by incorporating an effective catalyst and carefully designing the network structure. The thesis does not only offer a comprehensive understanding of the various structure-property relationship of the chemical constituents that govern the final material but also gives proof of concepts of future applications of the developed materials in functional soft robotic devices and their potential use. Furthermore, the thesis aligns with the universal pursuit of developing more environmentally friendly and reprocessable materials. It addresses the need to reduce our environmental impact and tackle global issues, while also providing innovative material solutions and technologies

that are stimuli responsive, are cost-effective, and yield superior final material performance compared to conventional processing methods.

Additionally, to fully unlock the potential of these materials and integrate them into technical applications, future research must prioritize exploring the combination of various stimuli, investigating novel bond exchange mechanisms, equipment's costs, efficiency, and addressing environmental considerations. Furthermore, another aspect of manufacturing and upscaling of bio-based resin formulations should be stressed in the future, to implement the technologies on a broader and greener scale.

9. References

1. Davidson, R.S. *Exploring the science, technology and applications of U.V. and E.B. curing;* SITA Technology: London, 1999, ISBN 0947798412.
2. Andrzejewska, E. Photopolymerization kinetics of multifunctional monomers. *Progress in Polymer Science* **2001**, *26*, 605–665, doi:10.1016/S0079-6700(01)00004-1.
3. Scranton, A.B.; Bowman, C.N.; Peiffer, R.W. *Photopolymerization*: *Fundamentals and applications / Alec B. Scranton, editor, Christopher N. Bowman, editor, Robert W. Peiffer, editor;* American Chemical Society: Washington, DC, 1997, ISBN 9780841235205.
4. Arnost Reiser. *Photoreactive Polymers: The Science and Technology of Resists;* John Wiley & Sons, New York, 1989: New York, NY, 1989, ISBN 9780471855507.
5. L. F. Thompson, C. Grant Willson, M. J. Bowden. *Introduction to Microlithography: Theory, Materials, and Processing;* The Society: American Chemical Society, 1983, ISBN 9780841207752.
6. *Processes in Photoreactive Polymers;* Krongauz, V.V.; Trifunac, A.D., Eds.; Springer: New York, NY, 2013, ISBN 9781461517672.
7. Liu, Y.; Pharr, M.; Salvatore, G.A. Lab-on-Skin: A Review of Flexible and Stretchable Electronics for Wearable Health Monitoring. *ACS Nano* **2017**, *11*, 9614–9635, doi:10.1021/acsnano.7b04898.
8. Wallin, T.J.; Pikul, J.H.; Bodkhe, S.; Peele, B.N.; Mac Murray, B.C.; Therriault, D.; McEnerney, B.W.; Dillon, R.P.; Giannelis, E.P.; Shepherd, R.F. Click chemistry stereolithography for soft robots that self-heal. *J. Mater. Chem. B* **2017**, *5*, 6249–6255, doi:10.1039/c7tb01605k.
9. Peiffer, R.W. Applications of Photopolymer Technology. *ACS Symposium Series*; American Chemical Society: Washington, DC, 1997; pp 1–14, ISBN 0097-6156.
10. Kenichiro Nakamura. *Photopolymers: Photoresist Materials, Processes, and Applications;* CRC Press: New York, NY, 2014, ISBN 978-1-4665-1728-8.
11. Ryspayeva, A.; Zhakeyev, A.; Desmulliez, M.P.Y.; Marques-Hueso, J. Multimaterial 3D Printing Technique for Electronic Circuitry Using Photopolymer and Selective Metallization. *Adv. Eng. Mater.* **2022**, *24*, 2201243, doi:10.1002/adem.202201243.
12. Trout, T.J.; Schmieg, J.J.; Gambogi, W.J.; Weber, A.M. Optical Photopolymers: Design and Applications. *Adv. Mater.* **1998**, *10*, 1219–1224, doi:10.1002/(SICI)1521-4095(199810)10:15<1219:AID-ADMA1219>3.0.CO;2-D.
13. Stansbury, J.W. Curing dental resins and composites by photopolymerization. *J. Esthet. Dent.* **2000**, *12*, 300–308, doi:10.1111/j.1708-8240.2000.tb00239.x.
14. Andjela, L.; Abdurahmanovich, V.M.; Vladimirovna, S.N.; Mikhailovna, G.I.; Yurievich, D.D.; Alekseevna, M.Y. A review on Vat Photopolymerization 3D-printing processes for dental application. *Dent. Mater.* **2022**, *38*, e284-e296, doi:10.1016/j.dental.2022.09.005.
15. Nguyen, A.K.; Narayan, R.J. Two-photon polymerization for biological applications. *Materials Today* **2017**, *20*, 314–322, doi:10.1016/j.mattod.2017.06.004.
16. Bens, A.; Seitz, H.; Bermes, G.; Emons, M.; Pansky, A.; Roitzheim, B.; Tobiasch, E.; Tille, C. Non-toxic flexible photopolymers for medical stereolithography technology. *RPJ* **2007**, *13*, 38–47, doi:10.1108/13552540710719208.
17. Ni, X.; Ye, J.; Dong, C. Kinetics studies of methyl methacrylate photopolymerization initiated by titanium dioxide semiconductor nanoparticles. *Journal of Photochemistry and Photobiology A: Chemistry* **2006**, *181*, 19–27, doi:10.1016/j.jphotochem.2005.10.021.

18. Gao, S.; Tang, G.; Hua, D.; Xiong, R.; Han, J.; Jiang, S.; Zhang, Q.; Huang, C. Stimuli-responsive bio-based polymeric systems and their applications. *J. Mater. Chem. B* **2019**, *7*, 709–729, doi:10.1039/c8tb02491j.

19. Jochum, F.D.; Theato, P. Temperature- and light-responsive smart polymer materials. *Chem. Soc. Rev.* **2013**, *42*, 7468–7483, doi:10.1039/c2cs35191a.

20. Roth, P.J.; Lowe, A.B. Stimulus-responsive polymers. *Polym. Chem.* **2017**, *8*, 10–11, doi:10.1039/C6PY90169G.

21. Roy, D.; Cambre, J.N.; Sumerlin, B.S. Future perspectives and recent advances in stimuli-responsive materials. *Progress in Polymer Science* **2010**, *35*, 278–301, doi:10.1016/j.progpolymsci.2009.10.008.

22. Theato, P.; Sumerlin, B.S.; O'Reilly, R.K.; Epps, T.H. Stimuli responsive materials. *Chem. Soc. Rev.* **2013**, *42*, 7055–7056, doi:10.1039/c3cs90057f.

23. Hoyle, C.E.; Lee, T.Y.; Roper, T. Thiol-enes: Chemistry of the past with promise for the future. *J. Polym. Sci. A Polym. Chem.* **2004**, *42*, 5301–5338, doi:10.1002/pola.20366.

24. Crivello, J.V. The discovery and development of onium salt cationic photoinitiators. *J. Polym. Sci. A Polym. Chem.* **1999**, *37*, 4241–4254, doi:10.1002/(SICI)1099-0518(19991201)37:23<4241:AID-POLA1>3.0.CO;2-R.

25. Klessinger, M.; Michl, J. *Excited states and photochemistry of organic molecules;* VCH: New York, Cambridge, 1995, ISBN 1560815884.

26. Wardle, B. *Principles and Applications of Photochemistry*, 1st ed.; John Wiley & Sons, Incorporated: Newark, 2010, ISBN 9780470710135.

27. Schnabel, W. *Polymers and light*: *Fundamentals and technical applications / W. Schnabel;* Wiley-VCH; Chichester : John Wiley [distributor]: Weinheim, 2007, ISBN 9783527318667.

28. Balzani, V.; Ceroni, P.; Juris, A. *Photochemistry and photophysics*: *Concepts, research, applications / Vincenzo Balzani, Paola Ceroni, and Alberto Juris;* Wiley-VCH Verlag GmbH & Co. KGaA: Weinheim, Germany, 2014, ISBN 9783527671052.

29. Evans, R.C.; Douglas, P.; Burrows, H. *Applied photochemistry;* Springer: Dordrecht, 2013, ISBN 978-90-481-3829-6.

30. Gilbert, A. *Photochemistry. Vol. 31;* Royal Society of Chemistry: Cambridge, 2000, ISBN 978-0-85404-425-2.

31. Clayden, J., Greeves, N., Warren, S., & Wothers, P. Organic Chemistry. *The American Naturalist* **2001**, *40*, 1990–1992, doi:10.1086/278635.

32. Bredas, J.-L. Mind the gap! *Mater. Horiz.* **2014**, *1*, 17–19, doi:10.1039/C3MH00098B.

33. Montalti, M.; Credi, A.; Prodi, L.; Gandolfi, M.T.; Michl, J.; Balzani, V. *Handbook of photochemistry*, Third edition; CRC/Taylor & Francis: Boca Raton, 2020, ISBN 9780367577902.

34. Persico, M.; Granucci, G. *Photochemistry*: *A modern theoretical perspective / Maurizio Persico, Giovanni Granucci;* Springer: Cham, Switzerland, 2018, ISBN 9783319899725.

35. Allen, N.S.; Gilbert, A. *Photochemistry*: *A review of the literature published between July 1995 and June 1996 / senior reporter, A. Gilbert ; reporters, N.S. Allen [and others];* Royal Society of Chemistry: London, 1997, ISBN 9781847554772.

36. Evans, R.C.; Douglas, P.; Burrows, H. *Applied photochemistry;* Springer: Dordrecht, 2013, ISBN 9789048138296.

37. Fomina, N.; Sankaranarayanan, J.; Almutairi, A. Photochemical mechanisms of light-triggered release from nanocarriers. *Adv. Drug Deliv. Rev.* **2012**, *64*, 1005–1020, doi:10.1016/j.addr.2012.02.006.

38. Pape, M. Industrial applications of photochemistry. *Pure and Applied Chemistry* **1975**, *41*, 535–558, doi:10.1351/pac197541040535.

39. Chatani, S.; Kloxin, C.J.; Bowman, C.N. The power of light in polymer science: photochemical processes to manipulate polymer formation, structure, and properties. *Polym. Chem.* **2014**, *5*, 2187–2201, doi:10.1039/C3PY01334K.

40. Sampson, K.L.; Deore, B.; Go, A.; Nayak, M.A.; Orth, A.; Gallerneault, M.; Malenfant, P.R.L.; Paquet, C. Multimaterial Vat Polymerization Additive Manufacturing. *ACS Appl. Polym. Mater.* **2021**, *3*, 4304–4324, doi:10.1021/acsapm.1c00262.

41. Andreu, A.; Su, P.-C.; Kim, J.-H.; Ng, C.S.; Kim, S.; Kim, I.; Lee, J.; Noh, J.; Subramanian, A.S.; Yoon, Y.-J. 4D printing materials for vat photopolymerization. *Additive Manufacturing* **2021**, *44*, 102024, doi:10.1016/j.addma.2021.102024.

42. Regehly, M.; Garmshausen, Y.; Reuter, M.; König, N.F.; Israel, E.; Kelly, D.P.; Chou, C.-Y.; Koch, K.; Asfari, B.; Hecht, S. Xolography for linear volumetric 3D printing. *Nature* **2020**, *588*, 620–624, doi:10.1038/s41586-020-3029-7.

43. Cabane, E.; Zhang, X.; Langowska, K.; Palivan, C.G.; Meier, W. Stimuli-Responsive Polymers and Their Applications in Nanomedicine. *Biointerphases* **2012**, *7*, 9, doi:10.1007/s13758-011-0009-3.

44. Fouassier, J.P.; Rabek, J.F. *Radiation curing in polymer science and technology;* Elsevier Applied Science: London, 1993, ISBN 1851669396.

45. Chan, B.P. Biomedical Applications of Photochemistry. *Tissue Engineering Part B: Reviews* **2010**, *16*, 509–522, doi:10.1089/ten.teb.2009.0797.

46. Woehrle, D.; Tausch, M.W.; Stohrer, W.-D. *Photochemie*: *Konzepte, Methoden, Experimente*, Online-Ausg; John Wiley & Sons: Hoboken, 2012, ISBN 9783527661077.

47. Shaukat, U.; Rossegger, E.; Schlögl, S. A Review of Multi-Material 3D Printing of Functional Materials via Vat Photopolymerization. *Polymers* **2022**, *14*, 2449, doi:10.3390/polym14122449.

48. Jasinski, F.; Zetterlund, P.B.; Braun, A.M.; Chemtob, A. Photopolymerization in dispersed systems. *Progress in Polymer Science* **2018**, *84*, 47–88, doi:10.1016/j.progpolymsci.2018.06.006.

49. Ligon, S.C.; Liska, R.; Stampfl, J.; Gurr, M.; Mülhaupt, R. Polymers for 3D Printing and Customized Additive Manufacturing. *Chem. Rev.* **2017**, *117*, 10212–10290, doi:10.1021/acs.chemrev.7b00074.

50. Wayner, D.D.M.; Clark, K.B.; Rauk, A.; Yu, D.; Armstrong, D.A. C−H Bond Dissociation Energies of Alkyl Amines: Radical Structures and Stabilization Energies. *J. Am. Chem. Soc.* **1997**, *119*, 8925–8932, doi:10.1021/ja971365v.

51. Yagci, Y.; Jockusch, S.; Turro, N.J. Photoinitiated Polymerization: Advances, Challenges, and Opportunities. *Macromolecules* **2010**, *43*, 6245–6260, doi:10.1021/ma1007545.

52. Sumiyoshi, T.; Schnabel, W. On the reactivity of phosphonyl radicals towards olefinic compounds. *Makromol. Chem.* **1985**, *186*, 1811–1823, doi:10.1002/macp.1985.021860910.

53. Mondschein, R.J.; Kanitkar, A.; Williams, C.B.; Verbridge, S.S.; Long, T.E. Polymer structure-property requirements for stereolithographic 3D printing of soft tissue engineering scaffolds. *Biomaterials* **2017**, *140*, 170–188, doi:10.1016/j.biomaterials.2017.06.005.

54. Montalti, M.; Murov, S.L. *Handbook of photochemistry*, 3rd ed.; CRC/Taylor & Francis: Boca Raton, 2006, ISBN 9780429115387.

55. Mäntele, W.; Deniz, E. UV–VIS absorption spectroscopy: Lambert-Beer reloaded. *Spectrochimica Acta Part A: Molecular and Biomolecular Spectroscopy* **2017**, *173*, 965–968, doi:10.1016/j.saa.2016.09.037.

56. Davidson, R.S. The Chemistry of Excited Complexes: a Survey of Reactions. In *Advances in Physical Organic Chemistry*; Gold, V., Bethell, D., Eds.; Academic Press, 1983; pp 1–130, ISBN 0065-3160.

57. Hutchison, J.; Lambert, M.C.; Ledwith, A. Rôle of semi-pinacol radicals in the benzophenone-photoinitiated polymerization of methyl methacrylate. *Polymer* **1973**, *14*, 250–254, doi:10.1016/0032-3861(73)90084-0.

58. Norman S. Allen. Photoinitiators for UV and visible curing of coatings: Mechanisms and properties **1996**, *100*, 101–107, doi:10.1016/S1010-6030(96)04426-7.

59. Bagheri, A.; Jin, J. Photopolymerization in 3D Printing. *ACS Appl. Polym. Mater.* **2019**, *1*, 593–611, doi:10.1021/acsapm.8b00165.

60. Jing Zhang, Frédéric Dumur, Pu Xiao, Bernadette Graff, David Bardelang, Didier Gigmes, Jean Pierre Fouassier, Jacques Lalevée. Structure Design of Naphthalimide Derivatives: Toward Versatile Photoinitiators for Near-UV/Visible LEDs, 3D Printing, and Water-Soluble Photoinitiating Systems **2015**, *7*, 2054–2063, doi:10.1021/acs.macromol.5b00201.

61. Wu, G.-H.; Hsu, S. Review: Polymeric-Based 3D Printing for Tissue Engineering. *J. Med. Biol. Eng.* **2015**, *35*, 285–292, doi:10.1007/s40846-015-0038-3.

62. Cullen, A.T.; Price, A.D. Digital light processing for the fabrication of 3D intrinsically conductive polymer structures. *Synthetic Metals* **2018**, *235*, 34–41, doi:10.1016/j.synthmet.2017.11.003.

63. Gou, M.; Qu, X.; Zhu, W.; Xiang, M.; Yang, J.; Zhang, K.; Wei, Y.; Chen, S. Bio-inspired detoxification using 3D-printed hydrogel nanocomposites. *Nat Commun* **2014**, *5*, 3774, doi:10.1038/ncomms4774.

64. Schafer, K.J.; Hales, J.M.; Balu, M.; Belfield, K.D.; van Stryland, E.W.; Hagan, D.J. Two-photon absorption cross-sections of common photoinitiators. *Journal of Photochemistry and Photobiology A: Chemistry* **2004**, *162*, 497–502, doi:10.1016/S1010-6030(03)00394-0.

65. Cullen, A.T.; Price, A.D. Digital light processing for the fabrication of 3D intrinsically conductive polymer structures. *Synthetic Metals* **2018**, *235*, 34–41, doi:10.1016/j.synthmet.2017.11.003.

66. Dilla, R.A.; M Motta, C.M.; Snyder, S.R.; Wilson, J.A.; Wesdemiotis, C.; Becker, M.L. Synthesis and 3D Printing of PEG-Poly(propylene fumarate) Diblock and Triblock Copolymer Hydrogels. *ACS Macro Lett.* **2018**, *7*, 1254–1260, doi:10.1021/acsmacrolett.8b00720.

67. Huang, T.Q.; Qu, X.; Liu, J.; Chen, S. 3D printing of biomimetic microstructures for cancer cell migration. *Biomed Microdevices* **2014**, *16*, 127–132, doi:10.1007/s10544-013-9812-6.

68. Gauvin, R.; Chen, Y.-C.; Lee, J.W.; Soman, P.; Zorlutuna, P.; Nichol, J.W.; Bae, H.; Chen, S.; Khademhosseini, A. Microfabrication of complex porous tissue engineering scaffolds using 3D projection stereolithography. *Biomaterials* **2012**, *33*, 3824–3834, doi:10.1016/j.biomaterials.2012.01.048.

69. Mann, B.K.; Gobin, A.S.; Tsai, A.T.; Schmedlen, R.H.; West, J.L. Smooth muscle cell growth in photopolymerized hydrogels with cell adhesive and proteolytically degradable domains: synthetic ECM analogs for tissue engineering. *Biomaterials* **2001**, *22*, 3045–3051, doi:10.1016/S0142-9612(01)00051-5.

70. Wu, G.-H.; Hsu, S. Review: Polymeric-Based 3D Printing for Tissue Engineering. *J. Med. Biol. Eng.* **2015**, *35*, 285–292, doi:10.1007/s40846-015-0038-3.

71. Ravve, A. *Light-associated reactions of synthetic polymers;* Springer: New York, 2006, ISBN 9780387364148.

72. Lin, H.; Zhang, D.; Alexander, P.G.; Yang, G.; Tan, J.; Cheng, A.W.-M.; Tuan, R.S. Application of visible light-based projection stereolithography for live cell-scaffold fabrication with designed architecture. *Biomaterials* **2013**, *34*, 331–339, doi:10.1016/j.biomaterials.2012.09.048.

73. Dilla, R.A.; M Motta, C.M.; Snyder, S.R.; Wilson, J.A.; Wesdemiotis, C.; Becker, M.L. Synthesis and 3D Printing of PEG-Poly(propylene fumarate) Diblock and Triblock Copolymer Hydrogels. *ACS Macro Lett.* **2018**, *7*, 1254–1260, doi:10.1021/acsmacrolett.8b00720.

74. Jauk, S.; Liska, R. Photoinitiators with Functional Groups, 8. *Macromol. Rapid Commun.* **2005**, *26*, 1687–1692, doi:10.1002/marc.200500507.

75. Park, H.K.; Shin, M.; Kim, B.; Park, J.W.; Lee, H. A visible light-curable yet visible wavelength-transparent resin for stereolithography 3D printing. *NPG Asia Mater* **2018**, *10*, 82–89, doi:10.1038/s41427-018-0021-x.

76. Warner, J.; Soman, P.; Zhu, W.; Tom, M.; Chen, S. Design and 3D Printing of Hydrogel Scaffolds with Fractal Geometries. *ACS Biomater. Sci. Eng.* **2016**, *2*, 1763–1770, doi:10.1021/acsbiomaterials.6b00140.

77. Huang, Z.; Gu, Y.; Liu, X.; Zhang, L.; Cheng, Z.; Zhu, X. Metal-Free Atom Transfer Radical Polymerization of Methyl Methacrylate with ppm Level of Organic Photocatalyst. *Macromol. Rapid Commun.* **2017**, *38*, doi:10.1002/marc.201600461.

78. Al Mousawi, A.; Dumur, F.; Garra, P.; Toufaily, J.; Hamieh, T.; Graff, B.; Gigmes, D.; Fouassier, J.P.; Lalevée, J. Carbazole Scaffold Based Photoinitiator/Photoredox Catalysts: Toward New High Performance Photoinitiating Systems and Application in LED Projector 3D Printing Resins. *Macromolecules* **2017**, *50*, 2747–2758, doi:10.1021/acs.macromol.7b00210.

79. Khorasani, M.; Ghasemi, A.; Rolfe, B.; Gibson, I. Additive manufacturing a powerful tool for the aerospace industry. *RPJ* **2022**, *28*, 87–100, doi:10.1108/RPJ-01-2021-0009.

80. Zhang, F.; Zhu, L.; Li, Z.; Wang, S.; Shi, J.; Tang, W.; Li, N.; Yang, J. The recent development of vat photopolymerization: A review. *Additive Manufacturing* **2021**, *48*, 102423, doi:10.1016/j.addma.2021.102423.

81. Gülcan, O.; Günaydın, K.; Tamer, A. The State of the Art of Material Jetting-A Critical Review. *Polymers* **2021**, *13*, 2829, doi:10.3390/polym13162829.

82. Crivello, J.V.; Bulut, U. Dual photo- and thermally initiated cationic polymerization of epoxy monomers. *J. Polym. Sci. A Polym. Chem.* **2006**, *44*, 6750–6764, doi:10.1002/pola.21791.

83. Michaudel, Q.; Kottisch, V.; Fors, B.P. Cationic Polymerization: From Photoinitiation to Photocontrol. *Angew. Chem. Int. Ed Engl.* **2017**, *56*, 9670–9679, doi:10.1002/anie.201701425.

84. Tee, Y.L.; Tran, P.; Leary, M.; Pille, P.; Brandt, M. 3D Printing of polymer composites with material jetting: Mechanical and fractographic analysis. *Additive Manufacturing* **2020**, *36*, 101558, doi:10.1016/j.addma.2020.101558.

85. Shahrubudin, N.; Lee, T.C.; Ramlan, R. An Overview on 3D Printing Technology: Technological, Materials, and Applications. *Procedia Manufacturing* **2019**, *35*, 1286–1296, doi:10.1016/j.promfg.2019.06.089.

86. McKeen, L.W. *The effect of UV light and weather on plastics and elastomers*, Fourth edition; William Andrew: Norwich, 2019, ISBN 9780128172711.

87. Hasirci, V.; Huri, P.Y.; Tanir, T.E.; Eke, G.; Hasirci, N. Polymer Fundamentals: Polymer Synthesis. In *Comprehensive biomaterials II,* [Second edition]; Ducheyne, P., Grainger, D.W., Healy, K.E., Hutmacher, D.W., Kirkpatrick, C.J., Eds.; Elsevier: Amsterdam, Netherlands, 2017; pp 478–506, ISBN 9780081006924.

88. Tulig, T.J.; Tirrell, M. Molecular theory of the Trommsdorff effect. *Macromolecules* **1981**, *14*, 1501–1511, doi:10.1021/ma50006a070.

89. Tulig, T.J.; Tirrell, M. On the onset of the Trommsdorff effect. *Macromolecules* **1982**, *15*, 459–463, doi:10.1021/ma00230a050.

90. Mishra, M.K.; Yagci, Y. *Handbook of radical vinyl polymerization;* Marcel Dekker: New York, 1998, ISBN 0824794648.

91. Ligon-Auer, S.C.; Schwentenwein, M.; Gorsche, C.; Stampfl, J.; Liska, R. Toughening of photo-curable polymer networks: a review. *Polym. Chem.* **2016**, *7*, 257–286, doi:10.1039/C5PY01631B.

92. Tanzi, M.C.; Farè, S.; Candiani, G. *Foundations of biomaterials engineering;* Elsevier: Amsterdam, 2019, ISBN 9780128094594.

93. Patrick Glöckner. *Radiation curing*: *Coatings and printing inks ; technical basics, applications and trouble shooting;* Vincentz Network: Hannover, 2008, ISBN 3866309074.

94. Colombani, D. Chain-growth control in free radical polymerization. *Progress in Polymer Science* **1997**, *22*, 1649–1720, doi:10.1016/S0079-6700(97)00022-1.

95. Cowie, J.; Arrighi, V. *Polymers*: *Chemistry and Physics of Modern Materials, Third Edition*, 3rd ed.; CRC Press: Boca Raton, Florida, 2007, ISBN 9780429125546.

96. Odian, G.G. *Principles of polymerization*, 4th ed.; Wiley: New York, Chichester, 2004, ISBN 0471274003.

97. Young, R.J.; Lovell, P.A. *Introduction to Polymers, 3rd Edition;* CRC Press, 2017, ISBN 9781439894156.

98. Flory, P.J. *Principles of Polymer Chemistry;* Cornell University Press: S.l., 1953 (1969), ISBN 0801401348.

99. Braun, D. *Polymer synthesis*: *Theory and practice fundamentals, methods, experiments*, Fifth edition; Springer: Heidelberg, New York, 2013, ISBN 9783642289798.

100. Bamford, C.H.; Jenkins, A.D.; Symons, M.C.R.; Townsend, M.G. Trapped radicals in heterogeneous vinyl polymerization. *J. Polym. Sci.* **1959**, *34*, 181–198, doi:10.1002/pol.1959.1203412716.

101. Saleh, T.A. *Polymer hybrid materials and nanocomposites*: *Fundamentals and applications / Tawfik Abdo Saleh;* William Andrew: Norwich, 2019, ISBN 9780128132951.

102. Stille, J.K. Step-growth polymerization. *J. Chem. Educ.* **1981**, *58*, 862, doi:10.1021/ed058p862.

103. Zaneldin, E.; Ahmed, W.; Mansour, A.; Hassan, A.E. Dimensional Stability of 3D Printed Objects Made from Plastic Waste Using FDM: Potential Construction Applications. *Buildings* **2021**, *11*, 516, doi:10.3390/buildings11110516.

104. Arefin, A.M.E.; Khatri, N.R.; Kulkarni, N.; Egan, P.F. Polymer 3D Printing Review: Materials, Process, and Design Strategies for Medical Applications. *Polymers* **2021**, *13*, doi:10.3390/polym13091499.

105. Steyrer, B.; Neubauer, P.; Liska, R.; Stampfl, J. Visible Light Photoinitiator for 3D-Printing of Tough Methacrylate Resins. *Materials (Basel)* **2017**, *10*, doi:10.3390/ma10121445.

106. Decker, C.; Nguyen Thi Viet, T.; Pham Thi, H. Photoinitiated cationic polymerization of epoxides. *Polym. Int.* **2001**, *50*, 986–997, doi:10.1002/pi.730.

107. Sangermano, M.; Rodriguez, D.; Gonzalez, M.C.; Laurenti, E.; Yagci, Y. Visible Light Induced Cationic Polymerization of Epoxides by Using Multiwalled Carbon Nanotubes. *Macromol. Rapid Commun.* **2018**, *39*, e1800250, doi:10.1002/marc.201800250.

108. Crivello, J.V.; Lam, J.H.W. Photoinitiated cationic polymerization with triarylsulfonium salts. *J. Polym. Sci. A Polym. Chem.* **1996**, *34*, 3231–3253, doi:10.1002/pola.1996.873.

109. Crivello, J.V.; Lam, J.H.W. Complex triarylsulfonium salt photoinitiators. I. The identification, characterization, and syntheses of a new class of triarylsulfonium salt photoinitiators. *J. Polym. Sci. Polym. Chem. Ed.* **1980**, *18*, 2677–2695, doi:10.1002/pol.1980.170180825.

110. Al Mousawi, A.; Garra, P.; Schmitt, M.; Toufaily, J.; Hamieh, T.; Graff, B.; Fouassier, J.P.; Dumur, F.; Lalevée, J. 3-Hydroxyflavone and N -Phenylglycine in High Performance Photoinitiating Systems for 3D Printing and Photocomposites Synthesis. *Macromolecules* **2018**, *51*, 4633–4641, doi:10.1021/acs.macromol.8b00979.

111. Al Mousawi, A.; Dumur, F.; Garra, P.; Toufaily, J.; Hamieh, T.; Goubard, F.; Bui, T.-T.; Graff, B.; Gigmes, D.; Pierre Fouassier, J.; et al. Azahelicenes as visible light photoinitiators for cationic and radical polymerization: Preparation of photoluminescent polymers and use in high performance LED projector 3D printing resins. *J. Polym. Sci. A Polym. Chem.* **2017**, *55*, 1189–1199, doi:10.1002/pola.28476.

112. Zhang, J.; Dumur, F.; Xiao, P.; Graff, B.; Gigmes, D.; Pierre Fouassier, J.; Lalevée, J. Aminothiazonaphthalic anhydride derivatives as photoinitiators for violet/blue LED-Induced cationic and radical photopolymerizations and 3D-Printing resins. *J. Polym. Sci. A Polym. Chem.* **2016**, *54*, 1189–1196, doi:10.1002/pola.27958.

113. Al Mousawi, A.; Lara, D.M.; Noirbent, G.; Dumur, F.; Toufaily, J.; Hamieh, T.; Bui, T.-T.; Goubard, F.; Graff, B.; Gigmes, D.; et al. Carbazole Derivatives with Thermally Activated Delayed Fluorescence Property as Photoinitiators/Photoredox Catalysts for LED 3D Printing Technology. *Macromolecules* **2017**, *50*, 4913–4926, doi:10.1021/acs.macromol.7b01114.

114. Steinmann B., Wolf J.-P., Schulthess A., Hunziker M. Photosensitive Compositions.

115. Steinmann, B.; Schulthess, A. Liquid Radiation-Curable Composition, Especially for Stereolithography.

116. Al Mousawi, A.; Poriel, C.; Dumur, F.; Toufaily, J.; Hamieh, T.; Fouassier, J.P.; Lalevée, J. Zinc Tetraphenylporphyrin as High Performance Visible Light Photoinitiator of Cationic Photosensitive Resins for LED Projector 3D Printing Applications. *Macromolecules* **2017**, *50*, 746–753, doi:10.1021/acs.macromol.6b02596.

117. Crivello, J.V.; Liu, S. Photoinitiated cationic polymerization of epoxy alcohol monomers. *J. Polym. Sci. A Polym. Chem.* **2000**, *38*, 389–401, doi:10.1002/(SICI)1099-0518(20000201)38:3<389:AID-POLA1>3.0.CO;2-G.

118. Weems, A.C.; Pérez-Madrigal, M.M.; Arno, M.C.; Dove, A.P. 3D Printing for the Clinic: Examining Contemporary Polymeric Biomaterials and Their Clinical Utility. *Biomacromolecules* **2020**, *21*, 1037–1059, doi:10.1021/acs.biomac.9b01539.

119. Fan, D.; Staufer, U.; Accardo, A. Engineered 3D Polymer and Hydrogel Microenvironments for Cell Culture Applications. *Bioengineering (Basel)* **2019**, *6*, doi:10.3390/bioengineering6040113.

120. Carothers, W.H. Polymers and polyfunctionality. *Trans. Faraday Soc.* **1936**, *32*, 39, doi:10.1039/tf9363200039.

121. Kolb, H.C.; Finn, M.G.; Sharpless, K.B. Click Chemistry: Diverse Chemical Function from a Few Good Reactions. *Angew. Chem. Int. Ed.* **2001**, *40*, 2004–2021, doi:10.1002/1521-3773(20010601)40:11<2004:AID-ANIE2004>3.0.CO;2-5.

122. Kade, M.J.; Burke, D.J.; Hawker, C.J. The power of thiol-ene chemistry. *J. Polym. Sci. A Polym. Chem.* **2010**, *48*, 743–750, doi:10.1002/pola.23824.

123. Hoyle, C.E.; Bowman, C.N. Thiol-ene click chemistry. *Angew. Chem. Int. Ed.* **2010**, *49*, 1540–1573, doi:10.1002/anie.200903924.

124. Weerakoon-Ratnayake, K.M.; O'Neil, C.E.; Uba, F.I.; Soper, S.A. Thermoplastic nanofluidic devices for biomedical applications. *Lab Chip* **2017**, *17*, 362–381, doi:10.1039/c6lc01173j.

125. Sycks, D.G.; Wu, T.; Park, H.S.; Gall, K. Tough, stable spiroacetal thiol-ene resin for 3D printing. *J. Appl. Polym. Sci.* **2018**, *135*, 46259, doi:10.1002/app.46259.

126. Rohit, K.R.; Ujwaldev, S.M.; Krishnan, K.K.; Anilkumar, G. Recent Developments and Perspectives in the Zinc-Catalysed Michael Addition. *Asian J. Org. Chem.* **2018**, *7*, 85–102, doi:10.1002/ajoc.201700491.

127. Nair, D.P.; Podgórski, M.; Chatani, S.; Gong, T.; Xi, W.; Fenoli, C.R.; Bowman, C.N. The Thiol-Michael Addition Click Reaction: A Powerful and Widely Used Tool in Materials Chemistry. *Chem. Mater.* **2014**, *26*, 724–744, doi:10.1021/cm402180t.

128. Rossegger, E.; Höller, R.; Reisinger, D.; Strasser, J.; Fleisch, M.; Griesser, T.; Schlögl, S. Digital light processing 3D printing with thiol–acrylate vitrimers. *Polym. Chem.* **2021**, *12*, 639–644, doi:10.1039/D0PY01520B.

129. Husár, B.; Ligon, S.C.; Wutzel, H.; Hoffmann, H.; Liska, R. The formulator's guide to anti-oxygen inhibition additives. *Progress in Organic Coatings* **2014**, *77*, 1789–1798, doi:10.1016/j.porgcoat.2014.06.005.

130. McNair, O.D.; Janisse, A.P.; Krzeminski, D.E.; Brent, D.E.; Gould, T.E.; Rawlins, J.W.; Savin, D.A. Impact properties of thiol-ene networks. *ACS Appl. Mater. Interfaces* **2013**, *5*, 11004–11013, doi:10.1021/am403238g.

131. Senyurt, A.F.; Wei, H.; Phillips, B.; Cole, M.; Nazarenko, S.; Hoyle, C.E.; Piland, S.G.; Gould, T.E. Physical and Mechanical Properties of Photopolymerized Thiol−Ene/Acrylates. *Macromolecules* **2006**, *39*, 6315–6317, doi:10.1021/ma060507f.

132. Senyurt, A.F.; Hoyle, C.E.; Wei, H.; Piland, S.G.; Gould, T.E. Thermal and Mechanical Properties of Cross-Linked Photopolymers Based on Multifunctional Thiol−Urethane Ene Monomers. *Macromolecules* **2007**, *40*, 3174–3182, doi:10.1021/ma0626463.

133. Oesterreicher, A.; Wiener, J.; Roth, M.; Moser, A.; Gmeiner, R.; Edler, M.; Pinter, G.; Griesser, T. Tough and degradable photopolymers derived from alkyne monomers for 3D printing of biomedical materials. *Polym. Chem.* **2016**, *7*, 5169–5180, doi:10.1039/C6PY01132B.

134. Oesterreicher, A.; Moser, A.; Edler, M.; Griesser, H.; Schlögl, S.; Pichelmayer, M.; Griesser, T. Investigating Photocurable Thiol-Yne Resins for Biomedical Materials. *Macromol. Mater. Eng.* **2017**, *302*, 1600450, doi:10.1002/mame.201600450.

135. Shaukat, U.; Rossegger, E.; Schlögl, S. Thiol–acrylate based vitrimers: From their structure–property relationship to the additive manufacturing of self-healable soft active devices. *Polymer* **2021**, *231*, 124110, doi:10.1016/j.polymer.2021.124110.

136. Moazzen, K.; Rossegger, E.; Alabiso, W.; Shaukat, U.; Schlögl, S. Role of Organic Phosphates and Phosphonates in Catalyzing Dynamic Exchange Reactions in Thiol-Click Vitrimers. *Macromol. Chem. Phys.* **2021**, *222*, 2100072, doi:10.1002/macp.202100072.

137. Rossegger, E.; Moazzen, K.; Fleisch, M.; Schlögl, S. Locally controlling dynamic exchange reactions in 3D printed thiol-acrylate vitrimers using dual-wavelength digital light processing. *Polym. Chem.* **2021**, *12*, 3077–3083, doi:10.1039/D1PY00427A.

138. Lowe, A.B.; Hoyle, C.E.; Bowman, C.N. Thiol-yne click chemistry: A powerful and versatile methodology for materials synthesis. *J. Mater. Chem.* **2010**, *20*, 4745, doi:10.1039/b917102a.

139. Roppolo, I.; Frascella, F.; Gastaldi, M.; Castellino, M.; Ciubini, B.; Barolo, C.; Scaltrito, L.; Nicosia, C.; Zanetti, M.; Chiappone, A. Thiol–yne chemistry for 3D printing: exploiting an off-stoichiometric route for selective functionalization of 3D objects. *Polym. Chem.* **2019**, *10*, 5950–5958, doi:10.1039/C9PY00962K.

140. Yao, B.; Sun, J.; Qin, A.; Tang, B.Z. Thiol-yne click polymerization. *Chin. Sci. Bull.* **2013**, *58*, 2711–2718, doi:10.1007/s11434-013-5892-1.

141. Griffini, G.; Invernizzi, M.; Levi, M.; Natale, G.; Postiglione, G.; Turri, S. 3D-printable CFR polymer composites with dual-cure sequential IPNs. *Polymer* **2016**, *91*, 174–179, doi:10.1016/j.polymer.2016.03.048.

142. Decker, C.; Nguyen Thi Viet, T.; Decker, D.; Weber-Koehl, E. UV-radiation curing of acrylate/epoxide systems. *Polymer* **2001**, *42*, 5531–5541, doi:10.1016/S0032-3861(01)00065-9.

143. Jian, Y.; He, Y.; Sun, Y.; Yang, H.; Yang, W.; Nie, J. Thiol–epoxy/thiol–acrylate hybrid materials synthesized by photopolymerization. *J. Mater. Chem. C* **2013**, *1*, 4481, doi:10.1039/c3tc30360h.

144. Zhou, L.-Y.; Fu, J.; He, Y. A Review of 3D Printing Technologies for Soft Polymer Materials. *Adv. Funct. Mater.* **2020**, *30*, 2000187, doi:10.1002/adfm.202000187.

145. Kutz, M. *Handbook of materials selection;* Wiley: New York, Chichester, 2002, ISBN 0471359246.

146. Shafranek, R.T.; Millik, S.C.; Smith, P.T.; Lee, C.-U.; Boydston, A.J.; Nelson, A. Stimuli-responsive materials in additive manufacturing. *Progress in Polymer Science* **2019**, *93*, 36–67, doi:10.1016/j.progpolymsci.2019.03.002.

147. Jana Herzberger, Justin M. Sirrine, Christopher B. Williams, Timothy E. Long. Polymer Design for 3D Printing Elastomers: Recent Advances in Structure, Properties, and Printing **2019**, *97*, doi:10.1016/j.progpolymsci.2019.101144.

148. Brady, R.F. *Comprehensive desk reference of polymer characterization and analysis;* American Chemical Society; Oxford : Oxford University Press: Washington, D.C., 2003, ISBN 0841236658.

149. Gao, W.; Zhang, Y.; Ramanujan, D.; Ramani, K.; Chen, Y.; Williams, C.B.; Wang, C.C.; Shin, Y.C.; Zhang, S.; Zavattieri, P.D. The status, challenges, and future of additive manufacturing in engineering. *Computer-Aided Design* **2015**, *69*, 65–89, doi:10.1016/j.cad.2015.04.001.

150. Gibson, I.; Rosen, D.; Stucker, B.; Khorasani, M. *Additive Manufacturing Technologies*, 3rd ed. 2021; Springer International Publishing: Cham, 2021, ISBN 9783030561277.

151. Dixit, N.; Sharma, V.; Kumar, P. Experimental investigations into abrasive flow machining (AFM) of 3D printed ABS and PLA parts. *RPJ* **2022**, *28*, 161–174, doi:10.1108/RPJ-01-2021-0013.

152. Zhu, K.; Deng, Z.; Dai, S.; Yu, Y. Temperature-compensated constitutive model of fused filament fabrication 3D printed PLA materials with full extrusion temperatures. *RPJ* **2022**, *28*, 41–51, doi:10.1108/RPJ-04-2021-0101.

153. Yan, R.; Wang, Y.; Luo, P.; Li, Y.; Lu, X. Fused filament fabrication of continuous optic fiber reinforced polylactic acid composites. *RPJ* **2022**, *28*, 766–776, doi:10.1108/RPJ-06-2021-0145.

154. Arifvianto, B.; Wirawan, Y.B.; Salim, U.A.; Suyitno, S.; Mahardika, M. Effects of extruder temperatures and raster orientations on mechanical properties of the FFF-processed polylactic-acid (PLA) material. *RPJ* **2021**, *27*, 1761–1775, doi:10.1108/RPJ-10-2019-0270.

155. Vanaei, H.R.; Shirinbayan, M.; Vanaei, S.; Fitoussi, J.; Khelladi, S.; Tcharkhtchi, A. Multi-scale damage analysis and fatigue behavior of PLA manufactured by fused deposition modeling (FDM). *RPJ* **2021**, *27*, 371–378, doi:10.1108/RPJ-11-2019-0300.

156. Chatham, C.A.; Long, T.E.; Williams, C.B. A review of the process physics and material screening methods for polymer powder bed fusion additive manufacturing. *Progress in Polymer Science* **2019**, *93*, 68–95, doi:10.1016/j.progpolymsci.2019.03.003.

157. Singh, R.; Gupta, A.; Tripathi, O.; Srivastava, S.; Singh, B.; Awasthi, A.; Rajput, S.K.; Sonia, P.; Singhal, P.; Saxena, K.K. Powder bed fusion process in additive manufacturing: An overview. *Materials Today: Proceedings* **2020**, *26*, 3058–3070, doi:10.1016/j.matpr.2020.02.635.

158. Pagac, M.; Hajnys, J.; Ma, Q.-P.; Jancar, L.; Jansa, J.; Stefek, P.; Mesicek, J. A Review of Vat Photopolymerization Technology: Materials, Applications, Challenges, and Future Trends of 3D Printing. *Polymers* **2021**, *13*, doi:10.3390/polym13040598.

159. Zhao, W.; Wang, Z.; Zhang, J.; Wang, X.; Xu, Y.; Ding, N.; Peng, Z. Vat Photopolymerization 3D Printing of Advanced Soft Sensors and Actuators: From Architecture to Function. *Adv. Mater. Technol.* **2021**, *6*, 2001218, doi:10.1002/admt.202001218.

160. Nohut, S.; Schwentenwein, M. Vat Photopolymerization Additive Manufacturing of Functionally Graded Materials: A Review. *JMMP* **2022**, *6*, 17, doi:10.3390/jmmp6010017.

161. Salmi, M. Additive Manufacturing Processes in Medical Applications. *Materials (Basel)* **2021**, *14*, doi:10.3390/ma14010191.

162. Zhang, F.; Wei, M.; Viswanathan, V.V.; Swart, B.; Shao, Y.; Wu, G.; Zhou, C. 3D printing technologies for electrochemical energy storage. *Nano Energy* **2017**, *40*, 418–431, doi:10.1016/j.nanoen.2017.08.037.

163. Dolinski, N.D.; Page, Z.A.; Callaway, E.B.; Eisenreich, F.; Garcia, R.V.; Chavez, R.; Bothman, D.P.; Hecht, S.; Zok, F.W.; Hawker, C.J. Solution Mask Liquid Lithography (SMaLL) for One-Step, Multimaterial 3D Printing. *Adv. Mater.* **2018**, *30*, e1800364, doi:10.1002/adma.201800364.

164. Gross, B.; Lockwood, S.Y.; Spence, D.M. Recent Advances in Analytical Chemistry by 3D Printing. *Anal. Chem.* **2017**, *89*, 57–70, doi:10.1021/acs.analchem.6b04344.

165. Choi, J.-W.; MacDonald, E.; Wicker, R. Multi-material microstereolithography. Available online: https://link.springer.com/article/10.1007/s00170-009-2434-8 (accessed on 20 April 2023).

166. Choi, J.-W.; Kim, H.-C.; Wicker, R. Multi-material stereolithography. *Journal of Materials Processing Technology* **2011**, *211*, 318–328, doi:10.1016/j.jmatprotec.2010.10.003.

167. Paolini, A.; Kollmannsberger, S.; Rank, E. Additive manufacturing in construction: A review on processes, applications, and digital planning methods. *Additive Manufacturing* **2019**, *30*, 100894, doi:10.1016/j.addma.2019.100894.

168. Tan, L.J.; Zhu, W.; Zhou, K. Recent Progress on Polymer Materials for Additive Manufacturing. *Adv. Funct. Mater.* **2020**, *30*, 2003062, doi:10.1002/adfm.202003062.

169. Beaman, J.J.; Bourell, D.L.; Seepersad, C.C.; Kovar, D. Additive Manufacturing Review: Early Past to Current Practice. *Journal of Manufacturing Science and Engineering* **2020**, *142*, doi:10.1115/1.4048193.

170. Wu, H.; Fahy, W.P.; Kim, S.; Kim, H.; Zhao, N.; Pilato, L.; Kafi, A.; Bateman, S.; Koo, J.H. Recent developments in polymers/polymer nanocomposites for additive manufacturing. *Progress in Materials Science* **2020**, *111*, 100638, doi:10.1016/j.pmatsci.2020.100638.

171. Ning, F.; Cong, W.; Qiu, J.; Wei, J.; Wang, S. Additive manufacturing of carbon fiber reinforced thermoplastic composites using fused deposition modeling. *Composites Part B: Engineering* **2015**, *80*, 369–378, doi:10.1016/j.compositesb.2015.06.013.

172. Tian, X.; Liu, T.; Yang, C.; Wang, Q.; Li, D. Interface and performance of 3D printed continuous carbon fiber reinforced PLA composites. *Composites Part A: Applied Science and Manufacturing* **2016**, *88*, 198–205, doi:10.1016/j.compositesa.2016.05.032.

173. Bîrcă, A.; Gherasim, O.; Grumezescu, V.; Grumezescu, A.M. Introduction in thermoplastic and thermosetting polymers. In *Materials for biomedical engineering. Thermoset and thermoplastic polymers*; Grumezescu, A.M., Grumezescu, V., Eds.; Elsevier: Amsterdam, 2019; pp 1–28, ISBN 9780128168745.

174. Lin, C.-H.; Lin, Y.-M.; Lai, Y.-L.; Lee, S.-Y. Mechanical properties, accuracy, and cytotoxicity of UV-polymerized 3D printing resins composed of Bis-EMA, UDMA, and TEGDMA. *J. Prosthet. Dent.* **2020**, *123*, 349–354, doi:10.1016/j.prosdent.2019.05.002.

175. Schmidleithner, C.; Kalaskar, D.M. Stereolithography. In *3D printing*; Cvetković, D., Ed.; IntechOpen: London, United Kingdom, 2018, ISBN 978-1-78923-965-2.

176. Wang, X.; Jiang, M.; Zhou, Z.; Gou, J.; Hui, D. 3D printing of polymer matrix composites: A review and prospective. *Composites Part B: Engineering* **2017**, *110*, 442–458, doi:10.1016/j.compositesb.2016.11.034.

177. Masahiro, I.; Tetsuya, K.; Hiroshi, Y.; Masaru, T. Liquid Crystal Display 3D Printing.

178. Shan, W.; Chen, Y.; Hu, M.; Qin, S.; Liu, P. 4D printing of shape memory polymer via liquid crystal display (LCD) stereolithographic 3D printing. *Mater. Res. Express* **2020**, *7*, 105305, doi:10.1088/2053-1591/abbd05.

179. Quan, H.; Zhang, T.; Xu, H.; Luo, S.; Nie, J.; Zhu, X. Photo-curing 3D printing technique and its challenges. *Bioact. Mater.* **2020**, *5*, 110–115, doi:10.1016/j.bioactmat.2019.12.003.

180. Tumbleston, J.R.; Shirvanyants, D.; Ermoshkin, N.; Janusziewicz, R.; Johnson, A.R.; Kelly, D.; Chen, K.; Pinschmidt, R.; Rolland, J.P.; Ermoshkin, A.; et al. Additive manufacturing. Continuous liquid interface production of 3D objects. *Science* **2015**, *347*, 1349–1352, doi:10.1126/science.aaa2397.

181. Xu, J.; Jung, K.; Atme, A.; Shanmugam, S.; Boyer, C. A robust and versatile photoinduced living polymerization of conjugated and unconjugated monomers and its oxygen tolerance. *J. Am. Chem. Soc.* **2014**, *136*, 5508–5519, doi:10.1021/ja501745g.

182. DeSimone, J.M.; Samulski, E.T.; Ermoshkin, A.; DESIMONE, P.M. RAPID 3D CONTINUOUS PRINTING OF CASTING MOLDS FOR METALS AND OTHER MATERIALS, November 26, 2013.

183. Janusziewicz, R.; Tumbleston, J.R.; Quintanilla, A.L.; Mecham, S.J.; DeSimone, J.M. Layerless fabrication with continuous liquid interface production. *Proc. Natl. Acad. Sci. U. S. A.* **2016**, *113*, 11703–11708, doi:10.1073/pnas.1605271113.

184. Dall'Argine, C.; Hochwallner, A.; Klikovits, N.; Liska, R.; Stampf, J.; Sangermano, M. Hot-Lithography SLA-3D Printing of Epoxy Resin. *Macromol. Mater. Eng.* **2020**, *305*, 2000325, doi:10.1002/mame.202000325.

185. Pfaffinger, M. Hot Lithography - New Possibilities in Polymer 3D Printing. *LTJ* **2018**, *15*, 45–47, doi:10.1002/latj.201800024.

186. Steyrer, B.; Busetti, B.; Harakály, G.; Liska, R.; Stampfl, J. Hot Lithography vs. room temperature DLP 3D-printing of a dimethacrylate. *Additive Manufacturing* **2018**, *21*, 209–214, doi:10.1016/j.addma.2018.03.013.

187. Sun, H.-B.; Kawata, S. Two-Photon Photopolymerization and 3D Lithographic Microfabrication. In *NMR, 3D analysis, photopolymerization*; Fatkullin, N., Ed.; Springer: Berlin, London, 2004; pp 169–273, ISBN 978-3-540-20510-4.

188. Tanaka, T.; Sun, H.-B.; Kawata, S. Rapid sub-diffraction-limit laser micro/nanoprocessing in a threshold material system. *Appl. Phys. Lett.* **2002**, *80*, 312–314, doi:10.1063/1.1432450.

189. Wu, S.; Serbin, J.; Gu, M. Two-photon polymerisation for three-dimensional micro-fabrication. *Journal of Photochemistry and Photobiology A: Chemistry* **2006**, *181*, 1–11, doi:10.1016/j.jphotochem.2006.03.004.

190. Sun, H.-B.; Takada, K.; Kim, M.-S.; Lee, K.-S.; Kawata, S. Scaling laws of voxels in two-photon photopolymerization nanofabrication. *Appl. Phys. Lett.* **2003**, *83*, 1104–1106, doi:10.1063/1.1599968.

191. Sun, H.-B.; Tanaka, T.; Kawata, S. Three-dimensional focal spots related to two-photon excitation. *Appl. Phys. Lett.* **2002**, *80*, 3673–3675, doi:10.1063/1.1478128.

192. Hong-Bo Sun; Satoshi Kawata. Two-Photon Laser Precision Microfabrication and Its Applications to Micro-Nano Devices and Systems. *J. Lightwave Technol., JLT* **2003**, *21*, 624.

193. Sun, H.-B.; Maeda, M.; Takada, K.; Chon, J.W.M.; Gu, M.; Kawata, S. Experimental investigation of single voxels for laser nanofabrication via two-photon photopolymerization. *Appl. Phys. Lett.* **2003**, *83*, 819–821, doi:10.1063/1.1598293.

194. Takada, K.; Kaneko, K.; Li, Y.-D.; Kawata, S.; Chen, Q.-D.; Sun, H.-B. Temperature effects on pinpoint photopolymerization and polymerized micronanostructures. *Appl. Phys. Lett.* **2008**, *92*, 41902, doi:10.1063/1.2834365.

195. Morikawa, J.; Orie, A.; Hashimoto, T.; Juodkazis, S. Thermal and optical properties of the femtosecond-laser-structured and stress-induced birefringent regions in sapphire. *Opt. Express* **2010**, *18*, 8300–8310, doi:10.1364/OE.18.008300.

196. Takada, K.; Wu, D.; Chen, Q.-D.; Shoji, S.; Xia, H.; Kawata, S.; Sun, H.-B. Size-dependent behaviors of femtosecond laser-prototyped polymer micronanowires. *Opt. Lett.* **2009**, *34*, 566–568, doi:10.1364/ol.34.000566.

197. Wu, D.; Chen, Q.-D.; Niu, L.-G.; Jiao, J.; Xia, H.; Song, J.-F.; Sun, H.-B. 100% Fill-Factor Aspheric Microlens Arrays (AMLA) With Sub-20-nm Precision. *IEEE Photonics Technology Letters* **2009**, *21*, 1535–1537, doi:10.1109/LPT.2009.2029346.

198. Lee, K.-S.; Kim, R.H.; Yang, D.-Y.; Park, S.H. Advances in 3D nano/microfabrication using two-photon initiated polymerization. *Progress in Polymer Science* **2008**, *33*, 631–681, doi:10.1016/j.progpolymsci.2008.01.001.

199. Li, L.; Gattass, R.R.; Gershgoren, E.; Hwang, H.; Fourkas, J.T. Achieving lambda/20 resolution by one-color initiation and deactivation of polymerization. *Science* **2009**, *324*, 910–913, doi:10.1126/science.1168996.

200. Zhang, Y.-L.; Chen, Q.-D.; Xia, H.; Sun, H.-B. Designable 3D nanofabrication by femtosecond laser direct writing. *Nano Today* **2010**, *5*, 435–448, doi:10.1016/j.nantod.2010.08.007.

201. Wu, D.; Wu, S.-Z.; Niu, L.-G.; Chen, Q.-D.; Wang, R.; Song, J.-F.; Fang, H.-H.; Sun, H.-B. High numerical aperture microlens arrays of close packing. *Appl. Phys. Lett.* **2010**, *97*, 31109, doi:10.1063/1.3464979.

202. Kelly, B.E.; Bhattacharya, I.; Heidari, H.; Shusteff, M.; Spadaccini, C.M.; Taylor, H.K. Volumetric additive manufacturing via tomographic reconstruction. *Science* **2019**, *363*, 1075–1079, doi:10.1126/science.aau7114.

203. Bernal, P.N.; Delrot, P.; Loterie, D.; Li, Y.; Malda, J.; Moser, C.; Levato, R. Volumetric Bioprinting of Complex Living-Tissue Constructs within Seconds. *Adv. Mater.* **2019**, *31*, e1904209, doi:10.1002/adma.201904209.

204. Shusteff, M.; Browar, A.E.M.; Kelly, B.E.; Henriksson, J.; Weisgraber, T.H.; Panas, R.M.; Fang, N.X.; Spadaccini, C.M. One-step volumetric additive manufacturing of complex polymer structures. *Sci. Adv.* **2017**, *3*, eaao5496, doi:10.1126/sciadv.aao5496.

205. Loterie, D.; Delrot, P.; Moser, C. High-resolution tomographic volumetric additive manufacturing. *Nat. Commun.* **2020**, *11*, 852, doi:10.1038/s41467-020-14630-4.

206. Liu, G.; Zhang, X.; Chen, X.; He, Y.; Cheng, L.; Huo, M.; Yin, J.; Hao, F.; Chen, S.; Wang, P.; et al. Additive manufacturing of structural materials. *Materials Science and Engineering: R: Reports* **2021**, *145*, 100596, doi:10.1016/j.mser.2020.100596.

207. Rafiee, M.; Farahani, R.D.; Therriault, D. Multi-Material 3D and 4D Printing: A Survey. *Adv. Sci. (Weinh)* **2020**, *7*, 1902307, doi:10.1002/advs.201902307.

208. Waheed, S.; Cabot, J.M.; Macdonald, N.P.; Lewis, T.; Guijt, R.M.; Paull, B.; Breadmore, M.C. 3D printed microfluidic devices: enablers and barriers. *Lab Chip* **2016**, *16*, 1993–2013, doi:10.1039/C6LC00284F.

209. Stampfl, J.; Baudis, S.; Heller, C.; Liska, R.; Neumeister, A.; Kling, R.; Ostendorf, A.; Spitzbart, M. Photopolymers with tunable mechanical properties processed by laser-based high-resolution stereolithography. *J. Micromech. Microeng.* **2008**, *18*, 125014, doi:10.1088/0960-1317/18/12/125014.

210. Gong, H.; Bickham, B.P.; Woolley, A.T.; Nordin, G.P. Custom 3D printer and resin for 18 μm × 20 μm microfluidic flow channels. *Lab Chip* **2017**, *17*, 2899–2909, doi:10.1039/c7lc00644f.

211. Raman, R.; Bhaduri, B.; Mir, M.; Shkumatov, A.; Lee, M.K.; Popescu, G.; Kong, H.; Bashir, R. Bioprinting: High-Resolution Projection Microstereolithography for Patterning of Neovasculature (Adv. Healthcare Mater. 5/2016). *Adv. Healthcare Mater.* **2016**, *5*, 622, doi:10.1002/adhm.201670025.

212. M. Ishii, T. Kawamura, H. Yamate, M. Takabatake. Liquid crystal display 3D Printing.

213. Geng, Q.; Wang, D.; Chen, P.; Chen, S.-C. Ultrafast multi-focus 3-D nano-fabrication based on two-photon polymerization. *Nat Commun* **2019**, *10*, 2179, doi:10.1038/s41467-019-10249-2.

214. Saha, S.K.; Wang, D.; Nguyen, V.H.; Chang, Y.; Oakdale, J.S.; Chen, S.-C. Scalable submicrometer additive manufacturing. *Science* **2019**, *366*, 105–109, doi:10.1126/science.aax8760.

215. Kelly, B.; Bhattacharya, I.; Shusteff, M.; Panas, R.M.; Taylor, H.K.; Spadaccini, C.M. *Computed Axial Lithography (CAL): Toward Single Step 3D Printing of Arbitrary Geometries;* arXiv, 2017.

216. van Wijk, A.; van Wijk, I. *3d printing with biomaterials*: *Towards a sustainable and circular economy / Ad van Wijk & Iris van Wijk;* Ios Press: Amsterdam, The Netherlands, 2015, ISBN 9781614994855.

217. *3D Printing and Bio-Based Materials in Global health;* S. K. Bhatia, K. W. Ramadurai, Ed.; Springer Nature: Cham, Switzerland 2017., 2017.

218. Yang, E.; Miao, S.; Zhong, J.; Zhang, Z.; Mills, D.K.; Zhang, L.G. Bio-Based Polymers for 3D Printing of Bioscaffolds. *Polym. Rev. (Phila Pa)* **2018**, *58*, 668–687, doi:10.1080/15583724.2018.1484761.

219. Li, W.; Mille, L.S.; Robledo, J.A.; Uribe, T.; Huerta, V.; Zhang, Y.S. Recent Advances in Formulating and Processing Biomaterial Inks for Vat Polymerization-Based 3D Printing. *Adv. Healthc. Mater.* **2020**, *9*, e2000156, doi:10.1002/adhm.202000156.

220. Liu, J.; Sun, L.; Xu, W.; Wang, Q.; Yu, S.; Sun, J. Current advances and future perspectives of 3D printing natural-derived biopolymers. *Carbohydr. Polym.* **2019**, *207*, 297–316, doi:10.1016/j.carbpol.2018.11.077.

221. Wu, B.; Sufi, A.; Ghosh Biswas, R.; Hisatsune, A.; Moxley-Paquette, V.; Ning, P.; Soong, R.; Dicks, A.P.; Simpson, A.J. Direct Conversion of McDonald's Waste Cooking Oil into a Biodegradable High-Resolution 3D-Printing Resin. *ACS Sustainable Chem. Eng.* **2020**, *8*, 1171–1177, doi:10.1021/acssuschemeng.9b06281.

222. Branciforti, D.S.; Lazzaroni, S.; Milanese, C.; Castiglioni, M.; Auricchio, F.; Pasini, D.; Dondi, D. Visible light 3D printing with epoxidized vegetable oils. *Additive Manufacturing* **2019**, *25*, 317–324, doi:10.1016/j.addma.2018.11.020.

223. Liang, B.; Li, R.; Zhang, C.; Yang, Z.; Yuan, T. Synthesis and characterization of a novel tri-functional bio-based methacrylate prepolymer from castor oil and its application in UV-curable coatings. *Industrial Crops and Products* **2019**, *135*, 170–178, doi:10.1016/j.indcrop.2019.04.039.

224. Miao, S.; Zhu, W.; Castro, N.J.; Nowicki, M.; Zhou, X.; Cui, H.; Fisher, J.P.; Zhang, L.G. 4D printing smart biomedical scaffolds with novel soybean oil epoxidized acrylate. *Sci. Rep.* **2016**, *6*, 27226, doi:10.1038/srep27226.

225. Lebedevaite, M.; Ostrauskaite, J.; Skliutas, E.; Malinauskas, M. Photoinitiator Free Resins Composed of Plant-Derived Monomers for the Optical μ-3D Printing of Thermosets. *Polymers* **2019**, *11*, doi:10.3390/polym11010116.

226. Guit, J.; Tavares, M.B.; Hul, J.; Ye, C.; Loos, K.; Jager, J.; Folkersma, R.; Voet, V.S. Photopolymer Resins with Biobased Methacrylates Based on Soybean Oil for Stereolithography. *ACS Appl. Polym. Mater.* **2020**, *2*, 949–957, doi:10.1021/acsapm.9b01143.

227. Voet, V.S.D.; Strating, T.; Schnelting, G.H.M.; Dijkstra, P.; Tietema, M.; Xu, J.; Woortman, A.J.J.; Loos, K.; Jager, J.; Folkersma, R. Biobased Acrylate Photocurable Resin Formulation for Stereolithography 3D Printing. *ACS Omega* **2018**, *3*, 1403–1408, doi:10.1021/acsomega.7b01648.

228. Voet, V.S.D.; Schnelting, G.H.M.; Xu, J.; Loos, K.; Folkersma, R.; Jager, J. Stereolithographic 3D Printing with Renewable Acrylates. *J. Vis. Exp.* **2018**, doi:10.3791/58177.

229. Silbert, S.D.; Simpson, P.; Setien, R.; Holthaus, M.; La Scala, J.; Ulven, C.A.; Webster, D.C. Exploration of Bio-Based Functionalized Sucrose Ester Resins for Additive Manufacturing via Stereolithography. *ACS Appl. Polym. Mater.* **2020**, *2*, 2910–2918, doi:10.1021/acsapm.0c00417.

230. Cui, Y.; Yang, J.; Lei, D.; Su, J. 3D Printing of a Dual-Curing Resin with Cationic Curable Vegetable Oil. *Ind. Eng. Chem. Res.* **2020**, *59*, 11381–11388, doi:10.1021/acs.iecr.0c01507.

231. Hu, Y.; Shang, Q.; Bo, C.; Jia, P.; Feng, G.; Zhang, F.; Liu, C.; Zhou, Y. Synthesis and Properties of UV-Curable Polyfunctional Polyurethane Acrylate Resins from Cardanol. *ACS Omega* **2019**, *4*, 12505–12511, doi:10.1021/acsomega.9b01174.

232. Sutton, J.T.; Rajan, K.; Harper, D.P.; Chmely, S.C. Lignin-Containing Photoactive Resins for 3D Printing by Stereolithography. *ACS Appl. Mater. Interfaces* **2018**, *10*, 36456–36463, doi:10.1021/acsami.8b13031.

233. Bassett, A.W.; Honnig, A.E.; Breyta, C.M.; Dunn, I.C.; La Scala, J.J.; Stanzione, J.F. Vanillin-Based Resin for Additive Manufacturing. *ACS Sustainable Chem. Eng.* **2020**, *8*, 5626–5635, doi:10.1021/acssuschemeng.0c00159.

234. Ding, R.; Du, Y.; Goncalves, R.B.; Francis, L.F.; Reineke, T.M. Sustainable near UV-curable acrylates based on natural phenolics for stereolithography 3D printing. *Polym. Chem.* **2019**, *10*, 1067–1077, doi:10.1039/C8PY01652F.

235. Miao, J.-T.; Peng, S.; Ge, M.; Li, Y.; Zhong, J.; Weng, Z.; Wu, L.; Zheng, L. Three-Dimensional Printing Fully Biobased Heat-Resistant Photoactive Acrylates from Aliphatic Biomass. *ACS Sustainable Chem. Eng.* **2020**, *8*, 9415–9424, doi:10.1021/acssuschemeng.0c02168.

236. Cosola, A.; Conti, R.; Grützmacher, H.; Sangermano, M.; Roppolo, I.; Pirri, C.F.; Chiappone, A. Multiacrylated Cyclodextrin: A Bio-Derived Photocurable Macromer for VAT 3D Printing. *Macromol. Mater. Eng.* **2020**, *305*, 2000350, doi:10.1002/mame.202000350.

237. Gonçalves, F.A.M.M.; Costa, C.S.M.F.; Fabela, I.G.P.; Farinha, D.; Faneca, H.; Simões, P.N.; Serra, A.C.; Bártolo, P.J.; Coelho, J.F.J. 3D printing of new biobased unsaturated polyesters by microstereo-thermallithography. *Biofabrication* **2014**, *6*, 35024, doi:10.1088/1758-5082/6/3/035024.

238. Ma, X.; Qu, X.; Zhu, W.; Li, Y.-S.; Yuan, S.; Zhang, H.; Liu, J.; Wang, P.; Lai, C.S.E.; Zanella, F.; et al. Deterministically patterned biomimetic human iPSC-derived hepatic model via rapid 3D bioprinting. *Proc. Natl. Acad. Sci. U. S. A.* **2016**, *113*, 2206–2211, doi:10.1073/pnas.1524510113.

239. Krishnamoorthy, S.; Wadnap, S.; Noorani, B.; Xu, H.; Xu, C. Investigation of gelatin methacrylate working curves in dynamic optical projection stereolithography of vascular-like constructs. *European Polymer Journal* **2020**, *124*, 109487, doi:10.1016/j.eurpolymj.2020.109487.

240. Weems, A.C.; Delle Chiaie, K.R.; Worch, J.C.; Stubbs, C.J.; Dove, A.P. Terpene- and terpenoid-based polymeric resins for stereolithography 3D printing. *Polym. Chem.* **2019**, *10*, 5959–5966, doi:10.1039/C9PY00950G.

241. Weems, A.C.; Delle Chiaie, K.R.; Yee, R.; Dove, A.P. Selective Reactivity of Myrcene for Vat Photopolymerization 3D Printing and Postfabrication Surface Modification. *Biomacromolecules* **2020**, *21*, 163–170, doi:10.1021/acs.biomac.9b01125.

242. Noè, C.; Tonda-Turo, C.; Chiappone, A.; Sangermano, M.; Hakkarainen, M. Light Processable Starch Hydrogels. *Polymers* **2020**, *12*, doi:10.3390/polym12061359.

243. Seo, J.W.; Shin, S.R.; Park, Y.J.; Bae, H. Hydrogel Production Platform with Dynamic Movement Using Photo-Crosslinkable/Temperature Reversible Chitosan Polymer and Stereolithography 4D Printing Technology. *Tissue Eng. Regen. Med.* **2020**, *17*, 423–431, doi:10.1007/s13770-020-00264-6.

244. Shen, Y.; Tang, H.; Huang, X.; Hang, R.; Zhang, X.; Wang, Y.; Yao, X. DLP printing photocurable chitosan to build bio-constructs for tissue engineering. *Carbohydr. Polym.* **2020**, *235*, 115970, doi:10.1016/j.carbpol.2020.115970.

245. Melilli, G.; Carmagnola, I.; Tonda-Turo, C.; Pirri, F.; Ciardelli, G.; Sangermano, M.; Hakkarainen, M.; Chiappone, A. DLP 3D Printing Meets Lignocellulosic Biopolymers: Carboxymethyl Cellulose Inks for 3D Biocompatible Hydrogels. *Polymers* **2020**, *12*, doi:10.3390/polym12081655.

246. Kim, S.H.; Yeon, Y.K.; Lee, J.M.; Chao, J.R.; Lee, Y.J.; Seo, Y.B.; Sultan, M.T.; Lee, O.J.; Lee, J.S.; Yoon, S.-I.; et al. Precisely printable and biocompatible silk fibroin bioink for digital light processing 3D printing. *Nat. Commun.* **2018**, *9*, 1620, doi:10.1038/s41467-018-03759-y.

247. Zou, W.; Dong, J.; Luo, Y.; Zhao, Q.; Xie, T. Dynamic Covalent Polymer Networks: from Old Chemistry to Modern Day Innovations. *Adv. Mater.* **2017**, *29*, doi:10.1002/adma.201606100.

248. van Zee, N.J.; Nicolaÿ, R. Vitrimers: Permanently crosslinked polymers with dynamic network topology. *Progress in Polymer Science* **2020**, *104*, 101233, doi:10.1016/j.progpolymsci.2020.101233.

249. Hayes, W.; Greenland, B.W. *Healable polymer systems;* Royal Society of Chemistry: Cambridge, 2013, ISBN 9781849737470.

250. Liu, T.; Zhao, B.; Zhang, J. Recent development of repairable, malleable and recyclable thermosetting polymers through dynamic transesterification. *Polymer* **2020**, *194*, 122392, doi:10.1016/j.polymer.2020.122392.

251. Winne, J.M.; Leibler, L.; Du Prez, F.E. Dynamic covalent chemistry in polymer networks: a mechanistic perspective. *Polym. Chem.* **2019**, *10*, 6091–6108, doi:10.1039/C9PY01260E.

252. Denissen, W.; Winne, J.M.; Du Prez, F.E. Vitrimers: permanent organic networks with glass-like fluidity. *Chem. Sci.* **2016**, *7*, 30–38, doi:10.1039/c5sc02223a.

253. Obadia, M.M.; Mudraboyina, B.P.; Serghei, A.; Montarnal, D.; Drockenmuller, E. Reprocessing and Recycling of Highly Cross-Linked Ion-Conducting Networks through Transalkylation Exchanges of C-N Bonds. *J. Am. Chem. Soc.* **2015**, *137*, 6078–6083, doi:10.1021/jacs.5b02653.

254. Obadia, M.M.; Jourdain, A.; Cassagnau, P.; Montarnal, D.; Drockenmuller, E. Tuning the Viscosity Profile of Ionic Vitrimers Incorporating 1,2,3-Triazolium Cross-Links. *Adv. Funct. Mater.* **2017**, *27*, 1703258, doi:10.1002/adfm.201703258.

255. Montarnal, D.; Delbosc, N.; Chamignon, C.; Virolleaud, M.-A.; Luo, Y.; Hawker, C.J.; Drockenmuller, E.; Bernard, J. Highly ordered nanoporous films from supramolecular diblock copolymers with hydrogen-bonding junctions. *Angew. Chem. Int. Ed.* **2015**, *54*, 11117–11121, doi:10.1002/anie.201504838.

256. Hendriks, B.; Waelkens, J.; Winne, J.M.; Du Prez, F.E. Poly(thioether) Vitrimers via Transalkylation of Trialkylsulfonium Salts. *ACS Macro Lett.* **2017**, *6*, 930–934, doi:10.1021/acsmacrolett.7b00494.

257. Jourdain, A.; Asbai, R.; Anaya, O.; Chehimi, M.M.; Drockenmuller, E.; Montarnal, D. Rheological Properties of Covalent Adaptable Networks with 1,2,3-Triazolium Cross-Links: The Missing Link between Vitrimers and Dissociative Networks. *Macromolecules* **2020**, *53*, 1884–1900, doi:10.1021/acs.macromol.9b02204.

258. Zhang, Z.; Chen, Q.; Colby, R.H. Dynamics of associative polymers. *Soft Matter* **2018**, *14*, 2961–2977, doi:10.1039/c8sm00044a.

259. Mohamed Marref; Nathalie Mignard; C. Jegat; M. Taha; M. Belbachir; R. Meghabar. Epoxy-amine based thermoresponsive networks designed by Diels–Alder reactions. *Polymer International* **2013**.

260. Denissen, W.; Rivero, G.; Nicolaÿ, R.; Leibler, L.; Winne, J.M.; Du Prez, F.E. Vinylogous Urethane Vitrimers. *Adv. Funct. Mater.* **2015**, *25*, 2451–2457, doi:10.1002/adfm.201404553.

261. Scott, T.F.; Schneider, A.D.; Cook, W.D.; Bowman, C.N. Photoinduced plasticity in cross-linked polymers. *Science* **2005**, *308*, 1615–1617, doi:10.1126/science.1110505.

262. Worrell, B.T.; McBride, M.K.; Lyon, G.B.; Cox, L.M.; Wang, C.; Mavila, S.; Lim, C.-H.; Coley, H.M.; Musgrave, C.B.; Ding, Y.; et al. Bistable and photoswitchable states of matter. *Nat. Commun.* **2018**, *9*, 2804, doi:10.1038/s41467-018-05300-7.

263. Nishimura, Y.; Chung, J.; Muradyan, H.; Guan, Z. Silyl Ether as a Robust and Thermally Stable Dynamic Covalent Motif for Malleable Polymer Design. *J. Am. Chem. Soc.* **2017**, *139*, 14881–14884, doi:10.1021/jacs.7b08826.

264. Montarnal, D.; Capelot, M.; Tournilhac, F.; Leibler, L. Silica-like malleable materials from permanent organic networks. *Science* **2011**, *334*, 965–968, doi:10.1126/science.1212648.

265. Chakma, P.; Konkolewicz, D. Dynamic Covalent Bonds in Polymeric Materials. *Angew. Chem. Int. Ed.* **2019**, *58*, 9682–9695, doi:10.1002/anie.201813525.

266. Inglis, A.J.; Nebhani, L.; Altintas, O.; Schmidt, F.G.; Barner-Kowollik, C. Rapid Bonding/Debonding on Demand: Reversibly Cross-Linked Functional Polymers via Diels−Alder Chemistry. *Macromolecules* **2010**, *43*, 5515–5520, doi:10.1021/ma100945b.

267. Reutenauer, P.; Buhler, E.; Boul, P.J.; Candau, S.J.; Lehn, J.-M. Room temperature dynamic polymers based on Diels-Alder chemistry. *Chemistry* **2009**, *15*, 1893–1900, doi:10.1002/chem.200802145.

268. Ying, H.; Zhang, Y.; Cheng, J. Dynamic urea bond for the design of reversible and self-healing polymers. *Nat. Commun.* **2014**, *5*, 3218, doi:10.1038/ncomms4218.

269. Capelot, M.; Montarnal, D.; Tournilhac, F.; Leibler, L. Metal-catalyzed transesterification for healing and assembling of thermosets. *J. Am. Chem. Soc.* **2012**, *134*, 7664–7667, doi:10.1021/ja302894k.

270. Bottinga, Y.; Richet, P. Silicate melts: The "anomalous" pressure dependence of the viscosity. *Geochimica et Cosmochimica Acta* **1995**, *59*, 2725–2731, doi:10.1016/0016-7037(95)00168-Y.

271. Saika-Voivod, I.; Poole, P.H.; Sciortino, F. Fragile-to-strong transition and polyamorphism in the energy landscape of liquid silica. *Nature* **2001**, *412*, 514–517, doi:10.1038/35087524.

272. Krishnakumar, B.; Sanka, R.P.; Binder, W.H.; Parthasarthy, V.; Rana, S.; Karak, N. Vitrimers: Associative dynamic covalent adaptive networks in thermoset polymers. *Chemical Engineering Journal* **2020**, *385*, 123820, doi:10.1016/j.cej.2019.123820.

273. Srivastava, A.; Prasad, R. Triglycerides-based diesel fuels. *Renewable and Sustainable Energy Reviews* **2000**, *4*, 111–133, doi:10.1016/S1364-0321(99)00013-1.

274. Baskar, G.; Kalavathy, G.; Aiswarya, R.; Abarnaebenezer Selvakumari, I. Advances in bio-oil extraction from nonedible oil seeds and algal biomass. In *Advances in eco-fuels for a sustainable environment*; Azad, K., Ed.; Woodhead Publishing: Oxford, 2018; pp 187–210, ISBN 9780081027288.

275. Awaja, F.; Pavel, D. Recycling of PET. *European Polymer Journal* **2005**, *41*, 1453–1477, doi:10.1016/j.eurpolymj.2005.02.005.

276. Collins, S.; Peace, S.K.; Richards, R.W.; MacDonald, W.A.; Mills, P.; King, S.M. Transesterification in Poly(ethylene terephthalate). Molecular Weight and End Group Effects. *Macromolecules* **2000**, *33*, 2981–2988, doi:10.1021/ma991637.

277. Fritz Schlosser; Peter J. Arndt; Manfred Mueller; Lothar Janssen. Method for preparing esters of acrylic acid and methacrylic acid by transesterification.

278. Abraham Benderly; Michael R. Ryan; Donald R. Weyler. Transesterification process for production of (meth)acrylate ester monomers.

279. MEHER, L.; VIDYASAGAR, D.; NAIK, S. Technical aspects of biodiesel production by transesterification—a review. *Renewable and Sustainable Energy Reviews* **2006**, *10*, 248–268, doi:10.1016/j.rser.2004.09.002.

280. M. Canakci, J. Van Gerpen. Biodiesel production via acid catalysts **1999**, *42(5)*, 1203–1210.

281. Lotero, E.; Liu, Y.; Lopez, D.E.; Suwannakarn, K.; Bruce, D.A.; Goodwin, J.G. Synthesis of Biodiesel via Acid Catalysis. *Ind. Eng. Chem. Res.* **2005**, *44*, 5353–5363, doi:10.1021/ie049157g.

282. Demongeot, A.; Mougnier, S.J.; Okada, S.; Soulié-Ziakovic, C.; Tournilhac, F. Coordination and catalysis of Zn 2+ in epoxy-based vitrimers. *Polym. Chem.* **2016**, *7*, 4486–4493, doi:10.1039/C6PY00752J.

283. Self, J.L.; Dolinski, N.D.; Zayas, M.S.; Read de Alaniz, J.; Bates, C.M. Brønsted-Acid-Catalyzed Exchange in Polyester Dynamic Covalent Networks. *ACS Macro Lett.* **2018**, *7*, 817–821, doi:10.1021/acsmacrolett.8b00370.

284. Otera, J. Transesterification. *Chem. Rev.* **1993**, *93*, 1449–1470, doi:10.1021/cr00020a004.

285. Hayashi, M.; Obara, H.; Miwa, Y. Design and basic properties of polyester vitrimers combined with an ionomer concept. *Mol. Syst. Des. Eng.* **2021**, *6*, 234–241, doi:10.1039/D1ME00002K.

286. Newton, J.J.; Britton, R.; Friesen, C.M. Base-Catalyzed Transesterification of Thionoesters. *J. Org. Chem.* **2018**, *83*, 12784–12792, doi:10.1021/acs.joc.8b02260.

287. Alabiso, W.; Schlögl, S. The Impact of Vitrimers on the Industry of the Future: Chemistry, Properties and Sustainable Forward-Looking Applications. *Polymers* **2020**, *12*, doi:10.3390/polym12081660.

288. Liu, W.; Schmidt, D.F.; Reynaud, E. Catalyst Selection, Creep, and Stress Relaxation in High-Performance Epoxy Vitrimers. *Ind. Eng. Chem. Res.* **2017**, *56*, 2667–2672, doi:10.1021/acs.iecr.6b03829.

289. Snyder, R.L.; Fortman, D.J.; Hoe, G.X. de; Hillmyer, M.A.; Dichtel, W.R. Reprocessable Acid-Degradable Polycarbonate Vitrimers. *Macromolecules* **2018**, *51*, 389–397, doi:10.1021/acs.macromol.7b02299.

290. Wei Zhao; Zihao Feng; Zhenhua Liang; Yanfeng Lv; Fukang Xiang; Chuanyin Xiong; Chao Duan; Lei Dai; Y. Ni. Vitrimer-Cellulose Paper Composites: A New Class of Strong, Smart, Green and Sustainable Materials. *ACS Appl. Mater. Interfaces* **2019**.

291. Brutman, J.P.; Delgado, P.A.; Hillmyer, M.A. Polylactide Vitrimers. *ACS Macro Lett.* **2014**, *3*, 607–610, doi:10.1021/mz500269w.

292. A. Demongeot; R. Groote; H. Goossens; T. Hoeks; F. Tournilhac; L. Leibler. Cross-Linking of Poly(butylene terephthalate) by Reactive Extrusion Using Zn(II) Epoxy-Vitrimer Chemistry. *Macromolecules* **2017**.

293. Xu, C.; Huang, X.; Li, C.; Chen, Y.; Lin, B.; Liang, X. Design of "Zn 2+ Salt-Bondings" Cross-Linked Carboxylated Styrene Butadiene Rubber with Reprocessing and Recycling Ability via Rearrangements of Ionic Cross-Linkings. *ACS Sustainable Chem. Eng.* **2016**, *4*, 6981–6990, doi:10.1021/acssuschemeng.6b01897.

294. Jeske, R.C.; DiCiccio, A.M.; Coates, G.W. Alternating copolymerization of epoxides and cyclic anhydrides: an improved route to aliphatic polyesters. *J. Am. Chem. Soc.* **2007**, *129*, 11330–11331, doi:10.1021/ja0737568.

295. Han, J.; Liu, T.; Zhang, S.; Hao, C.; Xin, J.; Guo, B.; Zhang, J. Hyperbranched Polymer Assisted Curing and Repairing of an Epoxy Coating. *Industrial & engineering chemistry process design and development* **2019**.

296. Zhang, B.; Kowsari, K.; Serjouei, A.; Dunn, M.L.; Ge, Q. Reprocessable thermosets for sustainable three-dimensional printing. *Nat. Commun.* **2018**, *9*, 1831, doi:10.1038/s41467-018-04292-8.

297. Christophe Duquenne; Sébastien-Jun MOUGNIER; François-Genes TOURNILHAC; Ludwik Leibler. Titanium-based catalyst for vitrimer resins of expoxy/anhyride type.

298. Kiesewetter, M.K.; Scholten, M.D.; Kirn, N.; Weber, R.L.; Hedrick, J.L.; Waymouth, R.M. Cyclic guanidine organic catalysts: what is magic about triazabicyclodecene? *J. Org. Chem.* **2009**, *74*, 9490–9496, doi:10.1021/jo902369g.

299. Simón, L.; Goodman, J.M. The mechanism of TBD-catalyzed ring-opening polymerization of cyclic esters. *J. Org. Chem.* **2007**, *72*, 9656–9662, doi:10.1021/jo702088c.

300. Chen, J.-H.; An, X.-P.; Li, Y.-D.; Wang, M.; Zeng, J.-B. Reprocessible Epoxy Networks with Tunable Physical Properties: Synthesis, Stress Relaxation and Recyclability. *Chin J Polym Sci* **2018**, *36*, 641–648, doi:10.1007/s10118-018-2027-9.

301. Yang, Y.; Pei, Z.; Zhang, X.; Tao, L.; Wei, Y.; Ji, Y. Carbon nanotube–vitrimer composite for facile and efficient photo-welding of epoxy. *Chem. Sci.* **2014**, *5*, 3486–3492, doi:10.1039/C4SC00543K.

302. Kaiser, S.; Wurzer, S.; Pilz, G.; Kern, W.; Schlögl, S. Stress relaxation and thermally adaptable properties in vitrimer-like elastomers from HXNBR rubber with covalent bonds. *Soft Matter* **2019**, *15*, 6062–6072, doi:10.1039/c9sm00856j.

303. Lyon, G.B.; Cox, L.M.; Goodrich, J.T.; Baranek, A.D.; Ding, Y.; Bowman, C.N. Remoldable Thiol–Ene Vitrimers for Photopatterning and Nanoimprint Lithography. *Macromolecules* **2016**, *49*, 8905–8913, doi:10.1021/acs.macromol.6b01281.

304. Capelot, M.; Unterlass, M.M.; Tournilhac, F.; Leibler, L. Catalytic Control of the Vitrimer Glass Transition. *ACS Macro Lett.* **2012**, *1*, 789–792, doi:10.1021/mz300239f.

305. Kaiser, S.; Novak, P.; Giebler, M.; Gschwandl, M.; Novak, P.; Pilz, G.; Morak, M.; Schlögl, S. The crucial role of external force in the estimation of the topology freezing transition temperature of vitrimers by elongational creep measurements. *Polymer* **2020**, *204*, 122804, doi:10.1016/j.polymer.2020.122804.

306. Shi, Q.; Yu, K.; Kuang, X.; Mu, X.; Dunn, C.K.; Dunn, M.L.; Wang, T.; Jerry Qi, H. Recyclable 3D printing of vitrimer epoxy. *Mater. Horiz.* **2017**, *4*, 598–607, doi:10.1039/C7MH00043J.

307. Mezger, T. *The Rheology Handbook*: *For users of rotational and oscillatory rheometers;* Vincentz Network: Hannover, 2020, ISBN 9783748603702.

308. *Handbuch Kunststoff-Verbindungstechnik;* Ehrenstein, G.W., Ed.; Hanser: München, 2004, ISBN 9783446226685.

309. Rudolph, N.S.; Osswald, T.A. *Polymer rheology*: *Fundamentals and apllications;* Hanser Publishers; Hanser Publications: Munich, Cincinnati, 2015, ISBN 9781523101290.

310. *Entwicklung und Charakterisierung ausgewählter Vitrimersysteme;* Sperling C, Ed.; Montanuniversität Leoben, A., 2020.

311. Altuna, F.I.; Hoppe, C.E.; Williams, R.J. Epoxy vitrimers with a covalently bonded tertiary amine as catalyst of the transesterification reaction. *European Polymer Journal* **2019**, *113*, 297–304, doi:10.1016/j.eurpolymj.2019.01.045.

312. Bowman, C.N.; Kloxin, C.J. Covalent adaptable networks: reversible bond structures incorporated in polymer networks. *Angew. Chem. Int. Ed.* **2012**, *51*, 4272–4274, doi:10.1002/anie.201200708.

313. Sue, H.-J.; Puckett, P.M.; Bertram, J.L.; Walker, L.L. The Network Structure of Epoxy Systems and Its Relationship to Toughness and Toughenability. In *Toughening of plastics*: *Advances in modeling and experiments / Raymond A. Pearson, editor, H.-J. Sue, editor, A.F. Yee, editor*; Pearson, R.A., Sue, H.-J., Yee, A.F., Eds.; American Chemical Society; Oxford : Oxford University Press [distributir]: Washington, DC, 2000; pp 171–197, ISBN 9780841236578.

314. Jocelyne Galy, Abed Sabra, Jean-Pierre Pascault. Characterization of epoxy thermosetting systems by differential scanning calorimetry **1986**, *26*, doi:10.1002/pen.760262108.

315. J.L. Hedrick; Michael J Jurek; Iskender Yilgor; J.E. McGrath. Chemical modification of matrix Resin networks with engineering thermoplastics: 1. Phenolic hydroxyl terminated poly (aryl ether sulfone)-epoxy systems **1985**, *13*, 201–208.

316. Overcash, M.; Twomey, J.; Asmatulu, E.; Vozzola, E.; Griffing, E. Thermoset composite recycling – Driving forces, development, and evolution of new opportunities. *Journal of Composite Materials* **2018**, *52*, 1033–1043, doi:10.1177/0021998317720000.

317. Yang, Y.; Zhang, S.; Zhang, X.; Gao, L.; Wei, Y.; Ji, Y. Detecting topology freezing transition temperature of vitrimers by AIE luminogens. *Nat. Commun.* **2019**, *10*, 3165, doi:10.1038/s41467-019-11144-6.

318. Podgórski, M.; Fairbanks, B.D.; Kirkpatrick, B.E.; McBride, M.; Martinez, A.; Dobson, A.; Bongiardina, N.J.; Bowman, C.N. Toward Stimuli-Responsive Dynamic Thermosets through Continuous Development and Improvements in Covalent Adaptable Networks (CANs). *Adv. Mater.* **2020**, *32*, e1906876, doi:10.1002/adma.201906876.

319. Northrop, B.H.; Coffey, R.N. Thiol-ene click chemistry: computational and kinetic analysis of the influence of alkene functionality. *J. Am. Chem. Soc.* **2012**, *134*, 13804–13817, doi:10.1021/ja305441d.

320. Dondoni, A. The emergence of thiol-ene coupling as a click process for materials and bioorganic chemistry. *Angew. Chem. Int. Ed.* **2008**, *47*, 8995–8997, doi:10.1002/anie.200802516.

321. Hoyle, C.E.; Lowe, A.B.; Bowman, C.N. Thiol-click chemistry: a multifaceted toolbox for small molecule and polymer synthesis. *Chem. Soc. Rev.* **2010**, *39*, 1355–1387, doi:10.1039/b901979k.

322. Sahin, M.; Ayalur-Karunakaran, S.; Manhart, J.; Wolfahrt, M.; Kern, W.; Schlögl, S. Thiol-Ene versus Binary Thiol-Acrylate Chemistry: Material Properties and Network

Characteristics of Photopolymers. *Adv. Eng. Mater.* **2017**, *19*, 1600620, doi:10.1002/adem.201600620.

323. Radl, S.V.; Schipfer, C.; Kaiser, S.; Moser, A.; Kaynak, B.; Kern, W.; Schlögl, S. Photo-responsive thiol–ene networks for the design of switchable polymer patterns. *Polym. Chem.* **2017**, *8*, 1562–1572, doi:10.1039/C7PY00055C.

324. van den Berg, O.; Nguyen, L.-T.T.; Teixeira, R.F.A.; Goethals, F.; Özdilek, C.; Berghmans, S.; Du Prez, F.E. Low Modulus Dry Silicone-Gel Materials by Photoinduced Thiol–Ene Chemistry. *Macromolecules* **2014**, *47*, 1292–1300, doi:10.1021/ma402564a.

325. Wang, S.; Teng, N.; Dai, J.; Liu, J.; Cao, L.; Zhao, W.; Liu, X. Taking advantages of intramolecular hydrogen bonding to prepare mechanically robust and catalyst-free vitrimer. *Polymer* **2020**, *210*, 123004, doi:10.1016/j.polymer.2020.123004.

326. Benight, S.J.; Wang, C.; Tok, J.B.; Bao, Z. Stretchable and self-healing polymers and devices for electronic skin. *Progress in Polymer Science* **2013**, *38*, 1961–1977, doi:10.1016/j.progpolymsci.2013.08.001.

327. Li, C.; Johansson, M.; Buijsen, P.; Dijkstra, G.; Sablong, R.J.; Koning, C.E. Limonene-derived polycarbonates as biobased UV-curable (powder) coating resins. *Progress in Organic Coatings* **2021**, *151*, 106073, doi:10.1016/j.porgcoat.2020.106073.

328. Senyurt, A.F.; Wei, H.; Hoyle, C.E.; Piland, S.G.; Gould, T.E. Ternary Thiol−Ene/Acrylate Photopolymers: Effect of Acrylate Structure on Mechanical Properties. *Macromolecules* **2007**, *40*, 4901–4909, doi:10.1021/ma062534b.

329. Li, X.; Yu, R.; He, Y.; Zhang, Y.; Yang, X.; Zhao, X.; Huang, W. Self-Healing Polyurethane Elastomers Based on a Disulfide Bond by Digital Light Processing 3D Printing. *ACS Macro Lett.* **2019**, *8*, 1511–1516, doi:10.1021/acsmacrolett.9b00766.

330. Nevejans, S.; Ballard, N.; Miranda, J.I.; Reck, B.; Asua, J.M. The underlying mechanisms for self-healing of poly(disulfide)s. *Phys. Chem. Chem. Phys.* **2016**, *18*, 27577–27583, doi:10.1039/c6cp04028d.

331. Canadell, J.; Goossens, H.; Klumperman, B. Self-Healing Materials Based on Disulfide Links. *Macromolecules* **2011**, *44*, 2536–2541, doi:10.1021/ma2001492.

332. Rossegger, E.; Shaukat, U.; Moazzen, K.; Fleisch, M.; Berer, M.; Schlögl, S. The effect of photolatent catalysts on the exchange kinetics of dual-wavelength 3D printable and photopatternable thiol-click vitrimers. *Polym. Chem.* **2023**, doi:10.1039/D3PY00333G.

333. John L. Dektar; Nigel P. Hacker. Photochemistry of triarylsulfonium salts **1990**, *16*, 6004–6015.

334. Sangermano, M.; Roppolo, I.; Chiappone, A. New Horizons in Cationic Photopolymerization. *Polymers* **2018**, *10*, doi:10.3390/polym10020136.

335. Crivello, J.V.; Lam, J.H.W. Photoinitiated cationic polymerization with triarylsulfonium salts. *J. Polym. Sci. Polym. Chem. Ed.* **1979**, *17*, 977–999, doi:10.1002/pol.1979.170170405.

336. Zivic, N.; Kuroishi, P.K.; Dumur, F.; Gigmes, D.; Dove, A.P.; Sardon, H. Recent Advances and Challenges in the Design of Organic Photoacid and Photobase Generators for Polymerizations. *Angew. Chem. Int. Ed.* **2019**, *58*, 10410–10422, doi:10.1002/anie.201810118.

337. Shi, S.; Croutxé-Barghorn, C.; Allonas, X. Photoinitiating systems for cationic photopolymerization: Ongoing push toward long wavelengths and low light intensities. *Progress in Polymer Science* **2017**, *65*, 1–41, doi:10.1016/j.progpolymsci.2016.09.007.

338. Cramer, N.B.; Scott, J.P.; Bowman, C.N. Photopolymerizations of Thiol−Ene Polymers without Photoinitiators. *Macromolecules* **2002**, *35*, 5361–5365, doi:10.1021/ma0200672.

339. Chidambaram, M.; Curulla-Ferre, D.; Singh, A.P.; Anderson, B.G. Synthesis and characterization of triflic acid-functionalized mesoporous Zr-TMS catalysts: heterogenization of CF3SO3H over Zr-TMS and its catalytic activity. *Journal of Catalysis* **2003**, *220*, 442–456, doi:10.1016/S0021-9517(03)00282-3.

340. Sharma, J.P.; Yamada, K.; Sekhon, S.S. Conductivity studies of plasticized PEO–HPF6–fumed silica nanocomposite polymer electrolyte system. *Ionics* **2012**, *18*, 151–158, doi:10.1007/s11581-011-0610-y.

341. Ma, L.-P.; Dong, S.; Chen, M.; Ma, W.; Sun, D.; Gao, Y.; Ma, T.; Cheng, H.-M.; Ren, W. UV-Epoxy-Enabled Simultaneous Intact Transfer and Highly Efficient Doping for Roll-to-Roll Production of High-Performance Graphene Films. *ACS Appl. Mater. Interfaces* **2018**, *10*, 40756–40763, doi:10.1021/acsami.8b13686.

342. Rard, J.A.; Palmer, D.A.; Albright, J.G. Isopiestic Determination of the Osmotic and Activity Coefficients of Aqueous Sodium Trifluoromethanesulfonate at 298.15 K and 323.15 K, and Representation with an Extended Ion-Interaction (Pitzer) Model. *J. Chem. Eng. Data* **2003**, *48*, 158–166, doi:10.1021/je020134n.

343. Kim, G.M.; Bae, Y.H.; Jo, W.H. pH-induced micelle formation of poly(histidine-co-phenylalanine)-block-poly(ethylene glycol) in aqueous media. *Macromol. Biosci.* **2005**, *5*, 1118–1124, doi:10.1002/mabi.200500121.

344. Fosshaug, H.; Askebjer, P.; Karlsson, J.; Bajramovic, A.; Xing, K.; Eklund, R.; Walford, J.; Ekberg, M.; Hogfeldt, P.; Ùstr÷m, T. Influence of writing strategy on CD control for the spatial-light-modulator-based Sigma7300 DUV laser pattern generator. In *Advances in Resist Technology and Processing XXI.* Microlithography 2004, Santa Clara, CA, Sunday 22 February 2004; Sturtevant, J.L., Ed.; SPIE, 2004; p 879.

345. Cameron, J.F.; Ablaza, S.L.; Xu, G.; Yueh, W. Impact of photoacid generator structure on DUV resist performance. In *Advances in Resist Technology and Processing XVI.* Microlithography '99, Santa Clara, CA, Sunday 14 March 1999; Conley, W., Ed.; SPIE, 1999; p 785.

346. Doyle, M.; Choi, S.K.; Proulx, G. High-Temperature Proton Conducting Membranes Based on Perfluorinated Ionomer Membrane-Ionic Liquid Composites. *J. Electrochem. Soc.* **2000**, *147*, 34, doi:10.1149/1.1393153.

347. Baek, J.-S.; Park, J.-S.; Sekhon, S.S.; Yang, T.-H.; Shul, Y.-G.; Choi, J.-H. Preparation and Characterisation of Non-aqueous Proton-Conducting Membranes with the Low Content of Ionic Liquids. *Fuel Cells* **2010**, *10*, 762–769, doi:10.1002/fuce.200900176.

348. Yang, X.; Guo, L.; Xu, X.; Shang, S.; Liu, H. A fully bio-based epoxy vitrimer: Self-healing, triple-shape memory and reprocessing triggered by dynamic covalent bond exchange. *Materials & Design* **2020**, *186*, 108248, doi:10.1016/j.matdes.2019.108248.

349. Yu, K.; Taynton, P.; Zhang, W.; Dunn, M.L.; Qi, H.J. Influence of stoichiometry on the glass transition and bond exchange reactions in epoxy thermoset polymers. *RSC Adv* **2014**, *4*, 48682–48690, doi:10.1039/C4RA06543C.

350. Lin, Q. Advances in Resist Materials and Processing Technology XXIV. *Advances in Resist Materials and Processing Technology XXIV* **2007**, *6519*.

351. Rossegger, E.; Höller, R.; Reisinger, D.; Fleisch, M.; Strasser, J.; Wieser, V.; Griesser, T.; Schlögl, S. High resolution additive manufacturing with acrylate based vitrimers using organic phosphates as transesterification catalyst. *Polymer* **2021**, *221*, 123631, doi:10.1016/j.polymer.2021.123631.

352. Shaukat, U.; Sölle, B.; Rossegger, E.; Rana, S.; Schlögl, S. Vat Photopolymerization 3D-Printing of Dynamic Thiol-Acrylate Photopolymers Using Bio-Derived Building Blocks. *Polymers* **2022**, *14*, doi:10.3390/polym14245377.

353. Boucher, D.; Ladmiral, V.; Negrell, C.; Caussé, N.; Pébère, N. Partially acrylated linseed oil UV-cured coating containing a dihemiacetal ester for the corrosion protection of an aluminium alloy. *Progress in Organic Coatings* **2021**, *158*, 106344, doi:10.1016/j.porgcoat.2021.106344.

354. Kaiser, S.; Jandl, J.; Novak, P.; Schlögl, S. Design and characterisation of vitrimer-like elastomeric composites from HXNBR rubber. *Soft Matter* **2020**, *16*, 8577–8590, doi:10.1039/d0sm00362j.

355. Chen, J.; Jiang, S.; Gao, Y.; Sun, F. Reducing volumetric shrinkage of photopolymerizable materials using reversible disulfide-bond reactions. *J Mater Sci* **2018**, *53*, 16169–16181, doi:10.1007/s10853-018-2778-2.

356. Faye, I.; Decostanzi, M.; Ecochard, Y.; Caillol, S. Eugenol bio-based epoxy thermosets: from cloves to applied materials. *Green Chem* **2017**, *19*, 5236–5242, doi:10.1039/C7GC02322G.

357. Aitken, R.; Collett, C.; Mesher, S. Convenient Preparation of Long-Chain Dialkyl Phosphates: Synthesis of Dialkyl Phosphates. *Synthesis* **2012**, *44*, 2515–2518, doi:10.1055/s-0031-1290823.

358. Bazi, F.; El Badaoui, H.; Sokori, S.; Tamani, S.; Hamza, M.; Boulaajaj, S.; Sebti, S. Transesterification of Methylbenzoate with Alcohols Catalyzed by Natural Phosphate. *Synthetic Communications* **2006**, *36*, 1585–1592, doi:10.1080/00397910600591508.

359. Thinnakorn, K.; Tscheikuna, J. Biodiesel production via transesterification of palm olein using sodium phosphate as a heterogeneous catalyst. *Applied Catalysis A: General* **2014**, *476*, 26–33, doi:10.1016/j.apcata.2014.02.016.

360. Streitwieser Andrew; Clayton H. Heathcock; Edward M. Kosower; Penelope J. Corfield. *Introduction to organic chemistry (No. 547 STR)*, 3rd; Macmillan: New York, 1992.

361. Lee, T.Y.; Roper, T.M.; Jonsson, E.; Kudyakov, I.; Viswanathan, K.; Nason, C.; Guymon, C.; Hoyle, C. The kinetics of vinyl acrylate photopolymerization. *Polymer* **2003**, *44*, 2859–2865, doi:10.1016/S0032-3861(03)00213-1.

362. Weber, M.; Khudyakov, I.V.; Turro, N.J. Electron Spin Resonance and Laser Flash Photolysis Study of Radical Addition to Vinyl Acrylate and Related Alkenes. *J. Phys. Chem. A* **2002**, *106*, 1938–1945, doi:10.1021/jp011813s.

363. Fukuda, W.; Nakao, M.; Okumura, K.; Kakiuchi, H. Polymerizations of vinyl methacrylate and vinyl acrylate. *J. Polym. Sci. A-1 Polym. Chem.* **1972**, *10*, 237–250, doi:10.1002/pol.1972.150100121.

364. Fukuda, W.; Yamano, Y.; Tsuriya, M.; Kakiuchi, H. Mechanism of Cyclopolymerization of Vinyl Acrylate, Methacrylate, and α-Chloroacrylate. *Polym J* **1982**, *14*, 127–136, doi:10.1295/polymj.14.127.

365. Khudyakov, I.V.; Fox, W.S.; Purvis, M.B. Photopolymerization of Vinyl Acrylate Studied by PhotoDSC. *Ind. Eng. Chem. Res.* **2001**, *40*, 3092–3097, doi:10.1021/ie010082f.

366. Imbernon, L.; Norvez, S.; Leibler, L. Stress Relaxation and Self-Adhesion of Rubbers with Exchangeable Links. *Macromolecules* **2016**, *49*, 2172–2178, doi:10.1021/acs.macromol.5b02751.

367. Stanescu Paul O.; Nicoleta M. Florea; Adriana Lungu; Horia Iovu. Kinetic study on the thermal degradation of UDMA-BisGMA copolymers **2011**, *48*, 148–153.

10. List of Abbreviations

Abbreviation	Description
DLP	Digital light processing
CAN	Covalent adaptable network
SLA	Stereolithography
DA	Diels-Alder
3D	Three dimensional
DMA	Dynamic mechanical analysis
TGA	Thermogravimetric analysis
DSC	Differential scanning calorimetry
E_a	Activation energy
HP1A	2-Hydroxy-3-phenoxypropyl acrylate
GD2A	Glycerol 1,3-diglycerolate diacrylate
PT3A	Trimethylolpropane triacrylate
PT4A	Pentaerythritol tetraacrylate
EGMA	Ethylene glycol bis-mercaptoacetate
EGMP	Ethylene glycol bis(3-mercaptopropionate)
TMP3MP	Trimethylolpropane tri(3-mercaptopropionate)
DPTDMP	Dipentaerythritol hexakis(3-mercaptopropionate)
PCLMT	Polycaprolactone tetra-mercaptopropionate
HXDT	1,6 hexane dithiol
PTTMP	Pentaerythritol tetrakis(3-mercapto-propionate)
BAPO	Phenylbis(2,4,6-trimethylbenzoyl) phosphine oxide
AELO	Acrylated expoxidized linseed oil
EUGP	Eugenol ester phosphate
AEUG	Acrylated eugenol
CitrP	Citronellol phosphate
PDS-triflate	(4-phenylthiophenyl)-diphenylsulfonium trifluoromethane sulfonate
DMS-borate	Diphenyl(methyl) sulfonium tetrafluoroborate
F-triflate	(4-fluorphenyl)-diphenylsulfonium trifluormethane sulfonate
TTS-triflate	tri-p-tolylsulfonium trifluoromethane sulfonate
DMEP	bis(2-methacryloyloxy ethyl) phosphate
ELO	Epoxidized linseed oil
BHT	Butylated hydroxytoluene
PPh_3	Triphenylphosphine
AA	Acrylic acid
Et_3N	Triethylamine
$POCl_3$	phosphorus oxychloride
EA	Ethylacetate
DCM	Dichloromethane
$Zn(acac)_2$	Zinc acetylacetonate
$Zn(OAc)_2$	Zinc acetate

THF	Tetrahydrofuran
R	General gas constant
G_t	Relaxation modulus at time t
G_o	Initial modulus
τ^*	Relaxation time
τ_o	Characteristic relaxation time
et al.	*et alii*
etc.	*et cetera*
T_g	Glass transition temperature
FT-IR	Fourier-transform infrared
ATR	Attenuated total reflectance
T	Temperature
T_v	Vitrification temperature
SMaLL	Solution mask liquid lithography
TPA	Two photon absorption
HOMO	Highest occupied molecular orbital
LCD	Liquid crystal display
LED	Light emitting diode
LUMO	Lowest unoccupied molecular orbital
MNR	Molecular network rearrangements
NMR	Nuclear magnetic resonance
PI	Photoinitiator
T_g	Glass transition temperature
T_V	Vitrification temperature
TBD	1,5,7-Triazabicyclo[4.4.0]dec-5-ene
UV	Ultraviolet
UV/Vis	Ultraviolet/visible
WLF	Williams–Landel–Ferry theory
wt.%	Weight percentage

11. Appendix

Date of birth: 27. August 1992

Donawitzer Straße 04/EG/02,
8700 Leoben, Austria.

☎ +43 688 6477 5932
✉ usmanshaukat61@gmail.com

Skills

MS Office	●●●●●
Origin	●●●●○
OPUS	●●●○○
Matlab	●●●○○
TPM-5S	●●●●○

Languages

English – (C2, Fluent)
German – (B2, Fluent)
Urdu – (Fluent)
Hindi – (Fluent)
Dutch – (Basic)
French – (Basic)

Interests/Hobbys
Travelling, Book reading, Sports

Curriculum Vitae

Professional Experience

09/2020 – 06/2023	**Researcher – Polymer Competence Center Leoben, Austria.** Participation in scientific projects on development and characterization of polymers.
01/2018 – 08/2018	**Operations Engineer – Fatima Fertilizer, Pakistan.** Control of nitrogen phosphate production plant, Responsible for achieving production targets, Troubleshooting and maintenance of equipment, research and development.
09/2014 – 12/2017	**Operations Engineer – Lotte Chemicals, Pakistan.** Control of production plant (purified terephthalic acid), Troubleshooting and maintenance of equipments, research and development.
07/2014 – 09/2014	**Customer Service and Technical Marketing - Binrasheed Chemicals, Pakistan.** Manufacturing of polymer masterbatches, troubleshooting and solution-oriented consulting at customer sites, technical guidance of customers on polymer production.

Education

09/2020 – 09/2023	**PhD at the Chair of Chemistry of Polymeric Materials at Montanuniversität Leoben.**
08/2018 – 08/2020	**1. Master degree in chemical engineering.** **2. Master in materials and process engineering.** **3. Master in membranes engineering.** University of Twente (Enschede, NL), University of Montpellier (Montpellier, FR), University Paul Sabatier III Toulouse (Toulouse, FR), University of Chemistry and Technology (Prague, CZ).
09/2010 – 08/2014	**Bachelor degree in chemical engineering.** University of Engineering and Technology, Pakistan.

Publications (Peer-reviewed) journals

2023 **Manuscript under preparation**	<u>Shaukat U.</u>; Rossegger E.; Schlögl S. Multi-material 3D-printing of soft active devices using vat-photopolymerization 3D-printing of dynamic thiol-acrylate networks. **2023**.
2023 **Manuscript under preparation**	<u>Shaukat U.</u>; Sölle B.; Rossegger E.; Schlögl S. Vat photopolymerization 3D-printing of vitrimeric photopolymers using bio-derived building blocks. **2023**
2023	Rossegger E.; <u>Shaukat U.</u>; Moazzen K.; Fleisch M; Berer M.; Schlögl S. The role of photolatent catalysts on the exchange kinetics of dual-wavelength 3D printable and photopatternable thiol-click vitrimers. *RSC, Polymer Chemistry.* **2023**. doi: 10.1039/D3PY00333G
2023	Li Y.; <u>Shaukat U.</u>; Schlögl S.; Xue T.; Li J.; Nie J.; Zhu X. A pyrrole–carbazole photoinitiator for radical and cationic visible light LED photopolymerization. *Elsevier, European Polymer Journal.* **2023**, 182, 111700. doi: 10.1016/j.eurpolymj.2022.111700
2022	<u>Shaukat U.</u>; Sölle B.; Rossegger E.; Sravendra R.; Schlögl S. Vat Photopolymerization 3D-Printing of Dynamic Thiol-Acrylate Photopolymers Using Bio-Derived Building Blocks. *MDPI, Polymer.* **2022**, 14(24), 5377. doi: 10.3390/polym14245377
2022	<u>Shaukat U.</u>; Rossegger E.; Schlögl S. A Review of Multi-Material 3D-printing of Functional Materials via Vat Photopolymerization. *MDPI, Polymer.* **2022**, 14(12), 2449. doi: 10.3390/polym14122449
2021	<u>Shaukat U.</u>; Rossegger E.; Schlögl S. Thiol–acrylate based vitrimers: From their structure–property relationship to the additive manufacturing of self-healable soft active devices. *Elsevier, Polymer.* **2021**, 231(2), 124110. doi: 10.1016/j.polymer.2021.124110
2021	Moazzen K.; Rossegger E.; Alabiso W.; <u>Shaukat U.</u>; Schlögl S. Role of Organic Phosphates and Phosphonates in Catalyzing Dynamic Exchange Reactions in Thiol-Click Vitrimers. *Macromolecular, Chemistry and Physics.* 2021, doi: 10.1002/macp.202100072

Conferences and Workshops

2021	European Symposium of Photopolymer sciences (Virtual). Poster: Development of thiol-acrylate vitrimers using additive manufacturing.
2022	EPF European Polymer Congress, Prague, Czech Republic. Poster: Structure-property relationships of thiol–acrylate based vitrimers – From liquid resins to additive manufacturing of self-healable devices
2022	30th Leoben-Conference on Polymer Engineering and Science – Additive Manufacturing The role of photolatent catalysts on the exchange kinetics of dual-wavelength 3D printable and photopatternable thiol-click vitrimers.
2020	Workshop: Fundamentals of smart materials and soft-robotics (19th – 23rd October) Vrije University Brussels, Belgium. Presentation: 3D-printing of soft thiol-acrylate dynamic networks for soft-robotics
2021	Workshop: Integration smart materials in soft robotics (16th – 23rd March) EMPA – Swiss Federal Laboratories for Materials Science and Technology. Switzerland. Presentation: Smart materials for soft-robotics with DLP 3D-printing
2021	Winter training school: Smart Materials for Soft Robots (12th – 17th Dec) University of Cambridge, U.K. Poster: Self-healing soft materials with DLP 3D-printing.
2022	Workshop: Applications of smart materials and soft robotics (29th Aug – 1st Sep) BioRobotics Institute of Sant'Anna School of Advanced Studies in Pontedera, Pisa, Italy. Presentation: Bio-based vitrimers for DLP 3D-printing of soft-actuators.
2023	International symposium on SMART materials. Polymer Competence Center Leoben, Austria. Presentation: Multi-material DLP 3D-printing of SMART self-healing devices.